Effect of Surface Coatings and Treatments on Wear

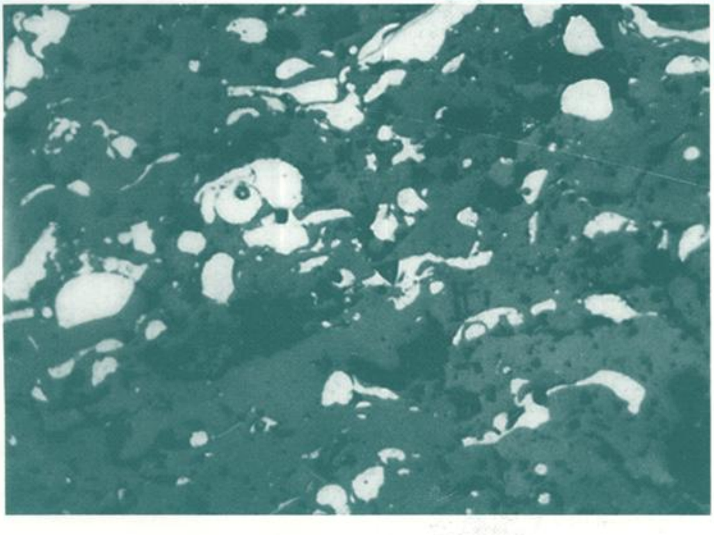

Shyam Bahadur, editor

ASTM

STP 1278

STP 1278

Effect of Surface Coatings and Treatments on Wear

Shyam Bahadur, editor

ASTM Publication Code Number (PCN):
04-012780-27

ASTM
100 Barr Harbor Drive
West Conshohocken
PA 19428-2959
Printed in the U.S.A.

Library of Congress Cataloging-in-Publication Data

Effect of surface coatings and treatments on wear / Shyam Bahadur, editor.
(STP ; 1278)
"ASTM publication code number (PCN): 04-012780-27."
Includes bibliographical references and index.
ISBN 0-8031-2036-2
1. Mechanical wear. 2. Protective coatings. 3. Coating processes. I. Bahadur, Shyam, 1934- II. Series: ASTM special technical publication ; 1278.
TA418.4.E32 1996
620.1'1292—dc20
96-14900
CIP

Photocopy Rights

Authorization to photocopy items for internal, personal, or educational classroom use, or the internal, personal, or educational classroom use of specific clients, is granted by the American Society for Testing and Materials (ASTM) provided that the appropriate fee is paid to the Copyright Clearance Center, 222 Rosewood Drive, Danvers, MA 01923, Tel: 508-750-8400 online: http://www.copyright.com/.

Peer Review Policy

Each paper published in this volume was evaluated by three peer reviewers. The authors addressed all of the reviewers' comments to the satisfaction of both the technical editor(s) and the ASTM Committee on Publications.

The quality of the papers in this publication reflects not only the obvious efforts of the authors and the technical editor(s), but also the work of these peer reviewers. The ASTM Committee on Publications acknowledges with appreciation their dedication and contribution to time and effort on behalf of ASTM.

Printed in Scranton, PA
June 1996

Foreword

The symposium on Effect of Surface Coatings and Treatments on Wear was held in Phoenix, Arizona, on 7 December 1994. ASTM Committee G2 on Wear and Erosion sponsored the Symposium. Shyam Bahadur, Iowa State University, presided as symposium chairman and is editor of this publication.

Contents

Overview

There is always an effort to increase the performance of mechanical systems. This has resulted in the components of the systems being subjected to higher stresses or aggressive environments and lead to the development of high performance materials. In this succession, ceramic materials have shown a great promise because of their high melting point, strength such as modulus of elasticity and hardness, and inertness to common atmospheres. The main drawback of these materials is the lack of ductility and fracture toughness, and poor thermal conductivity. Thus it is natural to think of the coatings of these materials over metals which compensate these materials for these drawbacks by providing the substrates with good toughness and high heat transfer characteristics. While coated systems enable the scientist to tailor the structures for specific applications, they introduce other complications because of porosity, dendritic grain structure, residual stresses, and interface shear stresses.

The understanding of the tribological behavior of even monolithic materials has been slow to evolve because of the complications from the interaction of sliding surfaces with their environment. Because of the later development of coated systems, it is not surprising that the tribological behavior of these has been of considerable interest. The latter has transpired because of the beneficial use of these coatings in advanced systems such as adiabatic diesel engine, coal fired engine, and gas turbine because higher operating temperatures provide higher thermal efficiency. These systems are subjected to a variety of tribological conditions which involve adhesion, abrasion, erosion, fretting, and others. Because of their high hardness, hard ceramic coatings in general exhibit high abrasion resistance. In the other modes of wear, problems often arise because of spalling of the coating due to the high shear stress induced between the coating and the substrate from high contact stresses and differential expansion resulting from localized temperature rise.

Purpose

This symposium was sponsored towards meeting the objectives of the ASTM G2 Committee, in particular the promotion of knowledge, stimulation of research, and the development of standards. The objective of this symposium was to provide a forum for the presentation of new research work related to the tribological behavior of hard coatings of the materials such as diamond, the carbides, nitrides and oxides of the elements and alloys, and explore the possibility of standards development activity based on this symposium.

ASTM has sponsored several symposia related to tribology. Of direct interest to the readers of this STP are the publications *ASTM STP 1010, Selection and Use of Wear Tests for Ceramics*, 1988 (Yust/Bayer, Eds.), *ASTM STP 1167, Wear Testing of Advanced Materials*, 1992 (Divakar/Blau, Eds.), and the *Tribology of Composite Materials*, 1991 (Rohatgi/Blau/Yust, Eds.).

Overview of Papers

The symposium was held on 7 December 1994 at Phoenix, Arizona. It was contributed by seven authors from USA and two from abroad, and one paper was not presented. It included papers on adhesive wear, abrasion, and fretting behaviors of the different kinds of coatings. The following is an overview of each paper.

The introduction to the symposium was provided by the opening paper by K. Budinski which reviewed the different surface treatment and coating processes such as plating, diffusion treatment, physical and chemical vapor deposition, ion implantation, thermal spray coatings, selective hardening, hardfacing, and the like. An overview of the wear processes was then presented to serve as a background information for the engineers in industry. It was followed by a discussion of the processes that were suited for different wear situations.

The next paper by Blau et al. discussed the development of self-lubricating ceramic coatings based on titanium nitride and MoS_2 and prepared by special chemical vapor deposition methods. The sliding of these coatings against silicon nitride counterfaces in the temperature range 20 to 700°C in air showed that the coefficient of friction was low (0.07 to 0.20) on initial sliding but varied considerably later on. It was particularly high at 400°C because of the changes occurring on the surface and the wear debris at this temperature. Further work is needed to study these changes and to explore the potential of these coatings for practical applications.

The paper by Bahadur and Yang studied the effect of laser surface melting on the detonation gun sprayed (W, Ti) C-Ni and WC-Co coatings on 1044 steel and Ti-6Aℓ-4V substrates. The study showed the variation in structure and hardness through the coating thickness because of laser treatment. Since laser treatment generated a lot of porosity, the use of these coatings in dynamic applications is questionable. The coefficient of friction and wear test data on these coatings is presented and the wear mechanisms are studied.

The paper by Vingsbo el al. reported the fretting results on three kinds of hard coatings: TiN and diamond-like carbon on steel substrates, and polycrystalline diamond on steel substrate. The displacement amplitudes selected in these experiments covered the partial slip regime and the lower part of the gross slip regime. Fretting maps were developed and the fretting mechanisms explained.

The paper by Mohrbacher et al. presented a conceptual framework for modeling laboratory fretting testing and applied the concepts to PVD TiN and CVD diamond coatings. The influence of the fretting conditions on the mechanical contact response as well as the materials modification induced in the contact zone are analyzed. The effects of third bodies, tribochemical reactions, and residual stress on the friction and wear behavior are also discussed.

The paper by Kennedy and Agarwala investigated whether thermally stable compounds such as oxides could be used as high temperature vapor phase ceramic lubricants. Towards this effort, they measured thermodynamic interactions between ceramics and the vapor phase of low sublimation temperature materials. They obtained thermodynamic data such as heat of adsorption, packing density, and reversibility of adsorption and related these data to the wear characteristics of these materials.

The paper by Ramalingam and Zheng studied the problem of hard coatings on light alloys which arises because the modulus of elasticity of the substrate is much lower than that of the coating. Loading in such a system produces differential displacements in the coating and the substrate thereby promoting debonding of the coating which contributes to severe wear. Using the displacement formulation solution approach, the authors have demonstrated that the film stresses can be managed to prevent coating failure by changing the coating material, contact condition, coating thickness, and film deposition conditions.

In the next paper Ruff studied the elastic, plastic, and cracking properties of the plasma sprayed coatings of ZrO_2, ZrO_2-metal composite, and Ni-NiO composite. In this study, from the continuous load versus nanoindentation depth data, material hardness, and elastic modulus are analyzed and the results for different indenter shapes compared. From the instrumented scratch test, the critical loads for severe cracking damage are also determined. The mechanisms responsible for damage in the above processes are then explained.

The last paper by Li and Qunji discussed the preparation of a coating by a high temperature synthesis process. The coating is prepared using a number of reactants such as CrO_3, Cr_2O_3, Al and C which comprise 98% of the total material. The resulting coating consisted of mainly Cr_7C_3, Cr, Cr_3C_2 and Al as revealed by X-ray diffraction. The coating deposited by this process on a steel substrate was found to have better adhesion and abrasion resistance than the Cr_7C_3 coating prepared by the chemical vapor deposition process.

As may be seen from the above, the papers covered a broad scope and were highly informative. The editor believes that this book will be a valuable and useful reference for both the scientists and engineers. Finally, the symposium chairman gratefully acknowledges the expert contributions of authors and reviewers. He would also like to express his deep appreciation for the help and cooperation of the ASTM staff in making this STP possible.

Shyam Bahadur

Professor, Mechanical Engineering Department, Iowa State University, Ames, IA 50011; symposium chairman and editor

Kenneth G. Budinski[1]

Overview of Surface Engineering and Wear

REFERENCE: Budinski, K. G., **"Overview of Surface Engineering and Wear,"** *Effect of Surface Coatings and Treatments on Wear, ASTM STP 1278,* S. Bahadur, Ed., American Society for Testing and Materials, 1996, pp. 4–21.

ABSTRACT: Surface engineering is a multidiscipline activity aimed at tailoring the properties or surfaces of engineering materials to improve their function or service life. As applied to metals, surface engineering includes processes such as plating, diffusion treatment, physical and chemical vapor deposition, ion implantation, thermal spray coatings, selective hardening, hardfacing, and a variety of less-used and proprietary processes. These processes will be described briefly and it will be shown that each process has a niche where it works better or is more cost effective than competing surface engineering treatments or bulk materials. This paper will review the various forms of wear that occur in industrial environments. Techniques will be described to match available surface engineering processes with wear situations. The goal is to present selection guidelines for machine designers and industrial operating personnel on the use of surface engineering to solve wear problems.

KEYWORDS: surface coatings, surface treatments, wear testing, surface engineering

Many industrial applications involve only the outermost atomic layers of a surface. Hard disk drives require relative motion to a magnetic head with a gap between the head and the disk of a fraction of a micrometer. If the two touch, there could be a catastrophic failure. "Up" surface features on both members must be less than the "fly" distance of 0.5 μm or thereabouts. Controlling these surfaces is surface engineering. Electrical contacts may require reduced oxides on contacting metal surfaces. Controlling the ohmic resistance of these surfaces is also surface engineering. Hardening the surface of steel to improve its abrasion resistance is a surface engineering process. Surface engineering is the engineering discipline that deals with the alteration of the surface properties to improve their serviceability or function. There are probably few people who call themselves surface engineers, but many engineers practice surface engineering.

It is the purpose of this paper to stimulate the awareness of design engineers of various surface engineering processes and to show how these surface treatments can be used to solve serviceability problems or design concerns associated with wear and friction. Tribological applications are only one part of surface engineering, but from the economic standpoint, they may be the most important. This paper will describe the more widely-used surface engineering processes and match these processes with various modes of wear.

Surface Engineering Processes

Figure 1 shows the spectrum of surface engineering processes that are available for tribological applications. Not included are processes like thin metal coatings on plastics to make them reflective, arsenic dopants diffused into germanium semiconductors, and zinc coating of fencing. These are surface engineering processes, but they are done for purposes other than

---

[1] Senior metallurgist, Eastman Kodak Company, Rochester, NY 14652.

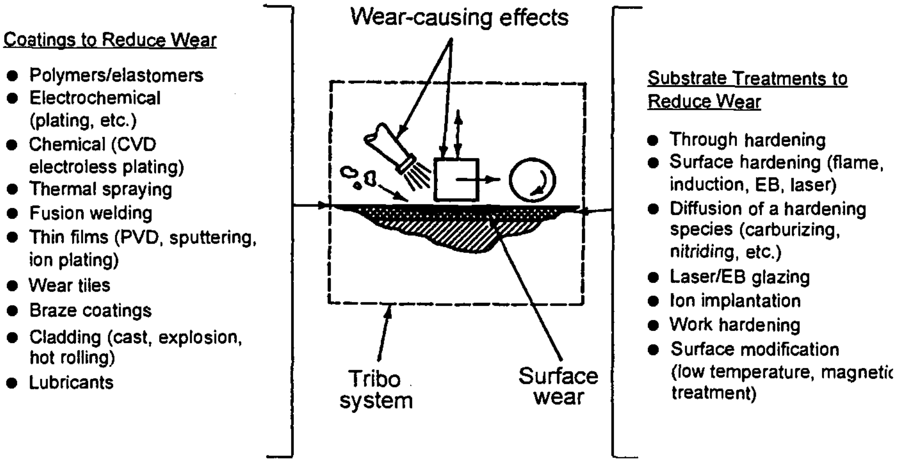

Coatings to Reduce Wear

- Polymers/elastomers
- Electrochemical (plating, etc.)
- Chemical (CVD electroless plating)
- Thermal spraying
- Fusion welding
- Thin films (PVD, sputtering, ion plating)
- Wear tiles
- Braze coatings
- Cladding (cast, explosion, hot rolling)
- Lubricants

Substrate Treatments to Reduce Wear

- Through hardening
- Surface hardening (flame, induction, EB, laser)
- Diffusion of a hardening species (carburizing, nitriding, etc.)
- Laser/EB glazing
- Ion implantation
- Work hardening
- Surface modification (low temperature, magnetic treatment)

FIG. 1—*Spectrum of surface engineering processes.*

modification of tribological applications. They are intended to alter physical or environmental resistance properties. The surface treatments that have utility for tribological applications can be classified into two categories: (1) those that form a coating, and (2) those that go into the substrate and do not produce a significant change in part dimension. The following is a brief description of these treatments:

Coatings

Polymers/Elastomers—Fluorocarbon enamels and dry film lubricant coatings are usually applied with a dry film thickness of less than 25 μm. Epoxy buildup cements can be applied centimetres thick, as can wear-resistant elastomer coatings.

Platings—Wear-resistant metallic coatings can be applied by electrodeposition or by autocatalytic plating. Chromium and nickel platings have been used for many years to increase surface hardness. Anodizing and hardcoating are wear-resistant coatings for aluminum.

Chemical Vapor Deposition—Many materials can be applied by chemical vapor deposition (CVD). Heavy nickel coatings can be applied from nickel carbonyl to a wide variety of substrates, chromium can be applied to a high carbon steel to make a hard surface or to soft steel to make a "low cost stainless steel," silicon carbide can be applied to add durability to optical disks, and diamond or hard diamond-like carbon can be applied to a variety of substrates to impart diamond-like characteristics.

Thermal Spray Processes—Thermal spray coatings are produced by melting various materials with welding techniques and spraying the melted material on a substrate to form a coating. The most widely used thermal spray processes fit into two categories: combustion gas processes and arc processes. The oldest combustion gas process involves introducing a wire consumable into an oxyacetylene flame. Newer processes use everything from laser to rocket fuel to melt the consumable. Arc processes include guns that use an arc between consumable wires as well as more complex plasma arc guns that melt powder in a plasma.

Fusion Welding—Fusing metal onto the surface of a substrate allows surfaces to take on the properties of whatever is melted onto the surface. The melting processes include arc welding, gas welding, laser, electron beam, electroslag, and even more exotic processes.

Thin Film Coatings—There is no official definition of a thin film coating, but the usual interpretation is coatings less than a few micrometers in thickness, applied with vacuum processes. Physical vapor deposition (PVD) is the most common process and titanium nitride is the most common coating. There are many PVD processes in use; many are proprietary.

Wear Tiles—Applying ceramic or cermented carbide tile to a surface, like tiling a bathroom floor, is a proven process for hardening surfaces. Tiles are usually cemented in place.

Cladding—Metal surfaces can have wear-resistant metals applied in substantial thickness with cladding techniques. These are solid-state joining processes and they include roll cladding, explosion bonding, and hipping, as well as proprietary techniques.

Substrate Treatments

A treatment that applies to a variety of metal substrates is through-hardening. This applies to ferrous metals that meet the requirements for quench hardening and some nonferrous metals that can be quench hardened or precipitation hardened. Though hardening is not surface engineering, just hardening the surface of a substrate is. The following paragraphs list the more common surface treatments to reduce wear.

Surface Hardening—This process is simply quench hardening the surface of ferrous metals by just heating the surface to the hardening temperature followed by a quench. This applies only to ferrous metals that have adequate carbon and alloy content. The surface heating processes include induction, flame, laser, and electron beam.

Diffusion Treatments—Non-hardenable metals can sometimes be hardened by diffusing some elemental species into the material, usually at elevated temperatures. This process normally applies to non-hardenable ferrous metals, but sometimes it is used to improve the surface properties of through-hardened metals. Applicable processes include nitriding, carburizing, carbonitriding, ferritic carbonitriding, and special processes that diffuse titanium and vanadium into surfaces.

Glazing—Rapid melting and solidification of surfaces is called glazing, and it is used to alter the microstructures of surfaces. If the quenching is rapid enough, amorphous surfaces can be obtained. Normally, this process simply produces a dendritic microstructure as applied to wrought steels, but the surface can also be harder than possible with normal quench hardening.

Ion Implantation—This is a vacuum process. An ion gun produces ions that are accelerated at a surface and either these ions or recoil atoms from a surface coating are implanted into a surface up to a depth of about 0.1 μm. These treatments can improve resistance to a variety of wear processes.

There are other surface engineering processes that have utility in tribological applications, but the ones mentioned are the most widely used. These are the surface engineering tools that are available to designers. Each process has unique advantages and applicability to the various forms of wear.

Wear Modes

The first step to take in addressing any wear problem is to identify the form of wear that will prevail in a tribosystem. Parts just do not wear out, they wear by one of a dozen or so different modes of wear that are agreed to by most tribology researchers [*1–5*] and as in the ASTM Standard for Terminology Relating to Wear and Erosion (G 40-94). Figure 2 illustrates wear processes broken down into four basic categories and 17 specific wear modes. The basis for this categorization is commonality in the tribosystems in which the wear occurs. All of the abrasive forms of wear involve the contact of a solid with a harder particle or sharp protuberance. The erosive forms of wear all involve at least a component of damage due to the me-

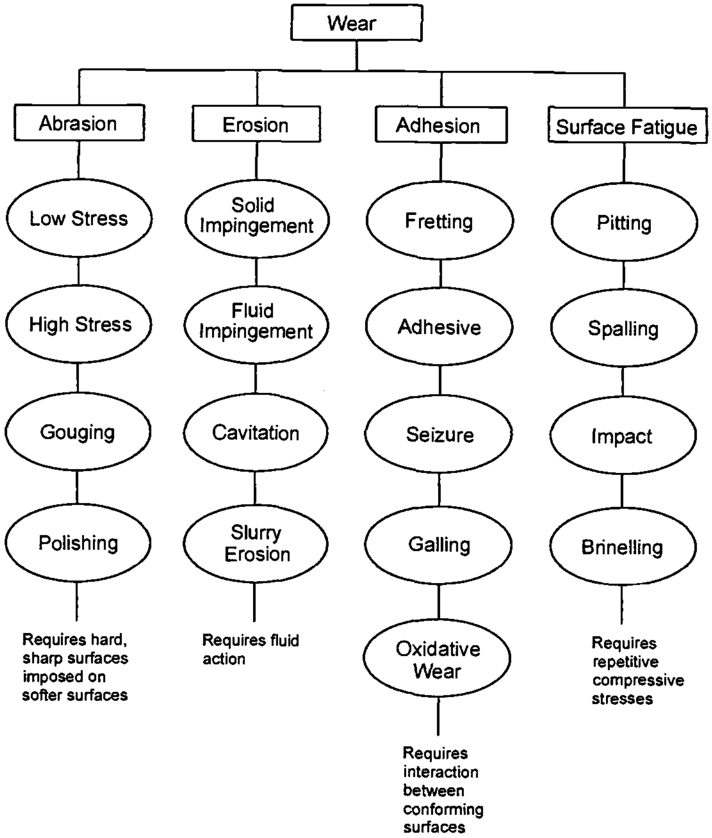

FIG. 2—*Basic categories of wear and specific wear modes.*

chanical action of a fluid in motion. Adhesive wear processes often occur in systems involving a solid sliding on another solid. Material removal by reaction with the environment may or may not occur conjointly with the adhesive wear process, but the major damage is produced by the adhesive interaction of the two surfaces. The surface fatigue category contains wear processes that involve repetitive compressive stressing of a surface. Relative motion parallel to the contacting surfaces is not necessarily intentional. It can be shown that these categories of wear processes are not succinct, but they serve the purpose of simplifying the subject of wear to some extent.

Each of these specific wear modes can usually be recognized by a simple visual inspection of the damage on a worn part. Each wear mode has a different solution, so it is important to address a wear problem by identifying the mode of wear that predominates or may predominate in a particular tribosystem. This is the first step in addressing a wear problem.

When to Use Various Surface Engineering Processes

Figure 1 lists the names of many surface engineering processes. The first question that a designer should address before using these processes is: Can I use a surface modification or should I use a material with bulk properties that resist a particular form of wear? A punch press die used for millions of parts is a good example of an application where through-hardening of tool steels or use of cemented carbides are usually required. In general, surface engineering usually allows the use of lower-cost materials. For some punch press die applications, it is possible to use a hard punch, to shear it into a soft die, and to harden the top surface of the die with a thin chromium plating. This has worked well on short-run jobs, and it is done with much lower cost than through-hardened punches and dies.

If through-hardening is selected as the appropriate system for an application, surface engineering may be used to further enhance the through-hardened part, but this usually is done only after one learns that the through-hardened part does not last as long as desired.

If the decision is made to consider a surface engineering process (as opposed to a through-hardened material), the next step is to decide on the appropriate surface engineering process. The following are guidelines on when to use the more important surface engineering processes.

Coatings

When to Use Platings—As mentioned previously, a unique advantage of metallic platings is that they can be applied to many different substrates. Suitable substrates for the common wear-resistant platings (chromium or nickel) are ferrous metals, copper-base metals, and some of the other nonferrous materials such as zinc. Anodizing and hardcoating are the related processes for aluminum alloys. They can perform the same function as a hard plating in addressing various wear modes. Figure 3 shows the entire spectrum of processes that apply a coating to the surface of a metal with an electrochemical or chemical process. Chromium is the hardest of the various metals that are commonly applied (Fig. 4) and it can be as thick as a millimetre, but it is most economical if it can be applied as a thick layer (1 to 2 μm); in this thickness range, it can be applied to finish machined parts. If a thickness of over 25 μm or so is thought to be necessary, it is likely that the plating will have to be ground after deposition.

If a plating process is under consideration for rebuilding of a worn surface, the rule of thumb that has been used for many years is that if the wear depth is less than 250 μm, plating processes are candidates for the rebuilding and chromium is by far the most wear-resistant plating. It has abrasion resistance that is often an order of magnitude better than that of electroless nickel.

On new parts, thin plating often excels as a surface-hardening process on soft metal shafts that may see abrasion from packing and the like. Plating is also the common choice for improving the durability of large rolls and machine components that are too big for furnace treatments and processes that require a part to be placed in some sort of reaction chamber. On the other hand, plating processes must be used with caution in situations involving Hertzian loading. They can spall. It is also advisable not to rely on platings for chemical resistance. Most platings have at least a few pinholes, which means they do not offer chemical resistance.

When to Use Thin-Film Processes—The definition of "thin film" is not agreed upon by workers in the field, but a practical definition is those coatings and treatments with a thickness or depth of penetration less than about 3 μm. Figure 5 illustrates the most widely used thin-film coating processes. The most widely used thin-film wear coatings are the PVD and CVD applied coatings of TiN-Ti-CN and the like. There are many job shops that will apply diamond-like carbon, diamond, TiN, titanium carbonitride, or graded versions with metals or ceramic interlayers or a combination thereof. TiN coating became popular on cutting tools in the late 1980s. Many cutting-tool suppliers sell complete lines of drills, milling cutters, lathe bits, and taps with TiN types of coatings. These coatings are applied to hardened substrates, and the typical thickness is about 2 μm. Suitable substrates are materials that can withstand a temperature of 425°C. TiN is significantly harder than its nearest competitive coating (thin chromium), and in machining it is said to prevent cratering caused by hot chips sliding on a tool.

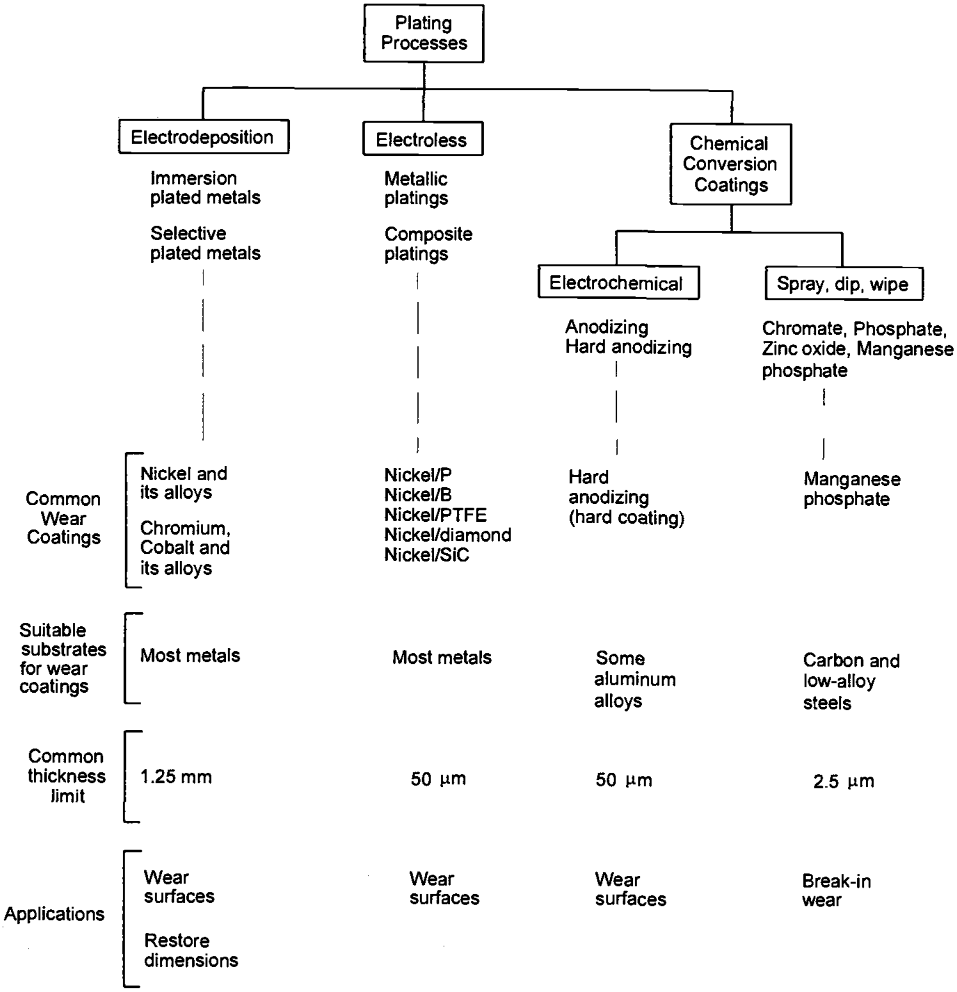

FIG. 3—*Use of platings for wear applications.*

These coatings have proven themselves in cutting tool applications, but their effectiveness in other applications usually has to be evaluated on a case-by-case basis. Many TiN coatings have significant roughness that comes from the coating process. This roughness is not a problem if the treated surface is destined to see only abrasion from sand or a similar particulate. On the other hand, if the treated surface is to run against a plain bearing, it may wear the bearing at a high rate. For this reason, it is still common practice to avoid thin-film coatings in situations where they will be sliding in contact with a softer counterface. These coatings would probably work fine in an application like a valve stem/packing tribosystem. It will resist low-stress abrasion. They are useful coatings to provide an additional measure of abrasion resistance to previously hardened tool materials.

Two other thin-film coatings/treatments are becoming more important—diamond coatings and ion implantation. Ion implantation will be discussed in the next section. Diamond coatings

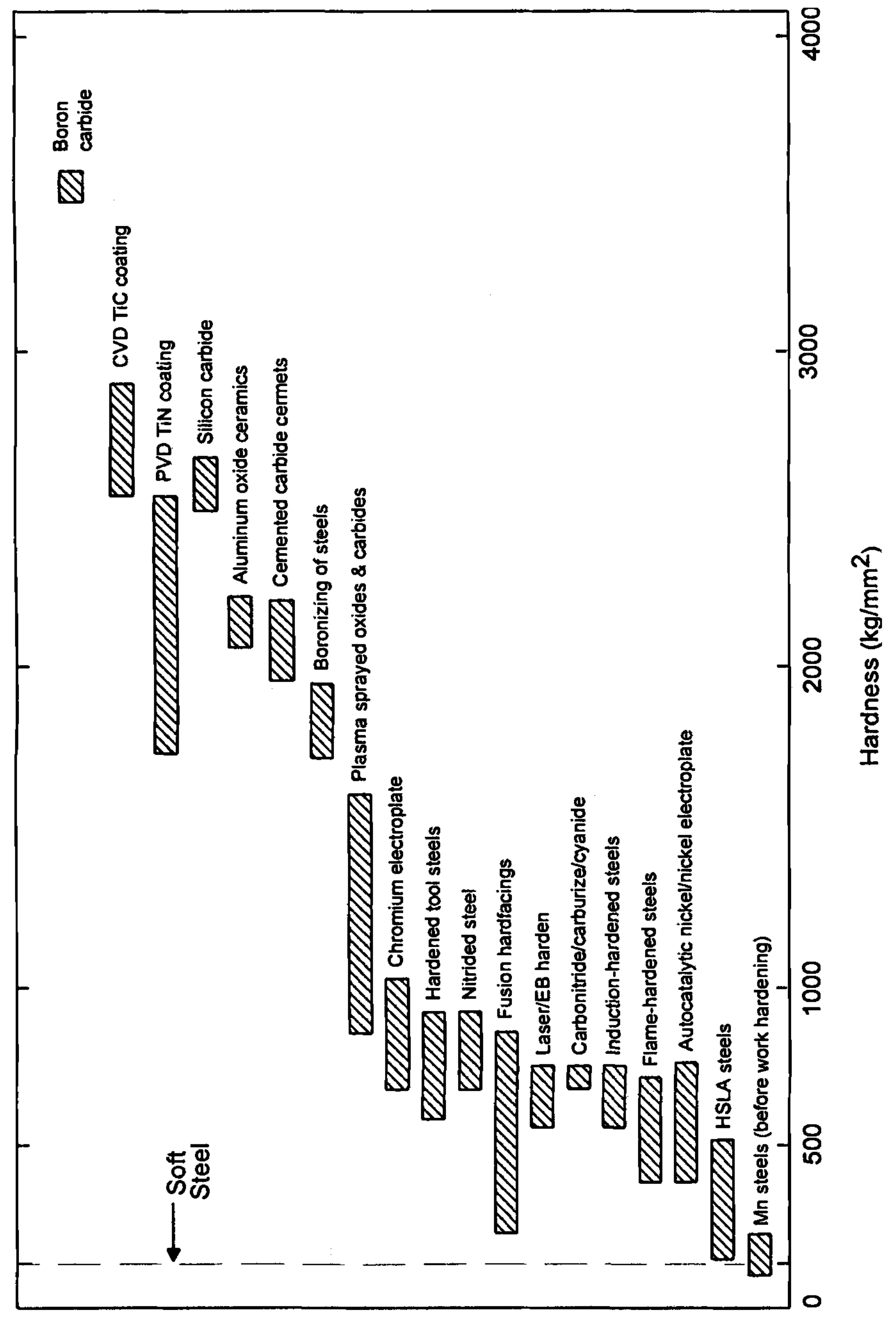

FIG. 4—Hardness ranges of various surface-engineering processes.

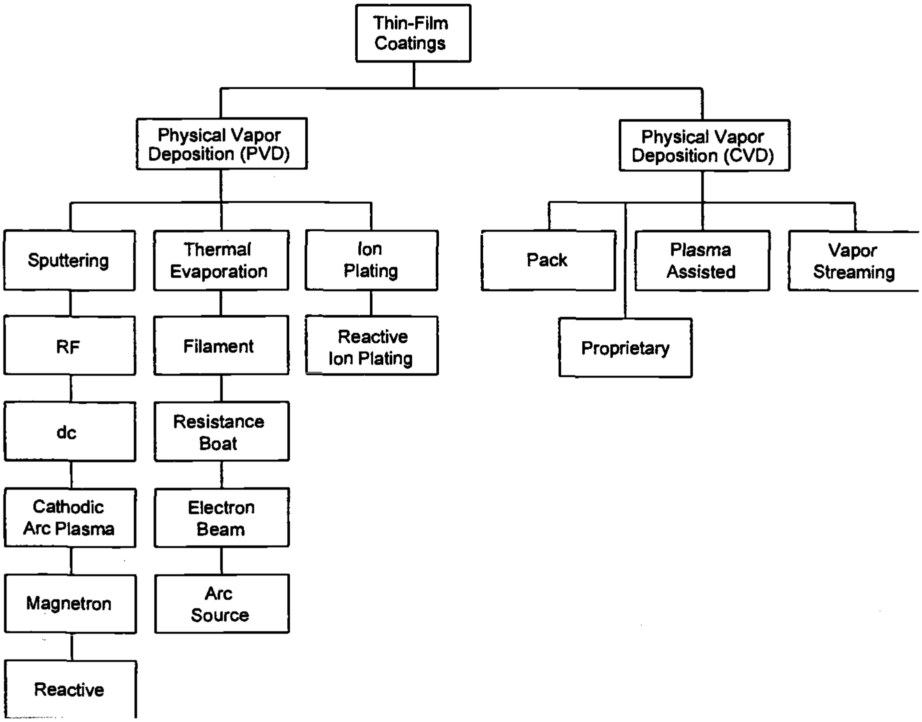

FIG. 5—*Processes for producing thin coatings.*

can be applied by PVD or CVD processes. Their current limitation is that they are difficult to coat onto some metal substrates. Adhesion is often inadequate. Some diamond coatings only adhere well on silicon nitride; some only adhere well on cemented carbide. This problem limits their utility. Users need to investigate coating adhesion when evaluating potential suppliers of these coatings.

When to Use Hardfacing—Hardfacing is probably the broadest category of surface engineering processes. By definition it is applying, with welding techniques, a material with properties that are superior to those of the substrate. The spectrum of specific processes that is included in hardfacing are illustrated in Fig. 6. They run the gamut from the traditional application of overlays with an oxyfuel torch to laser cladding, to thermal spraying of ceramics and cermets. Hardfacing is divided into two categories, and this division has significant consequences. Materials applied with fusion-hardfacing processes have a metallurgical bond to the substrate. They are bonded as if they were a traditional weld bead. In nonfusion processes, materials are bonded to the surface with a mechanical bond. In this case, the coatings are not melted into the surface; they adhere with the same types of bonds that hold electroplatings and adhesives to surfaces. There is some mechanical locking with surface roughness and there is some van der Waals-type atomic bonding. The bond strength of thermal spray coatings to substrates is usually measured by epoxy bonding another surface to the coating and pulling it off with a force measuring instrument. The strongest epoxy has a shear strength between 7 and 14 MPa. If the thermal spray coatings stay on and the epoxy fails, it is said that the coatings have a tensile shear strength to the surface of at least 7 MPa.

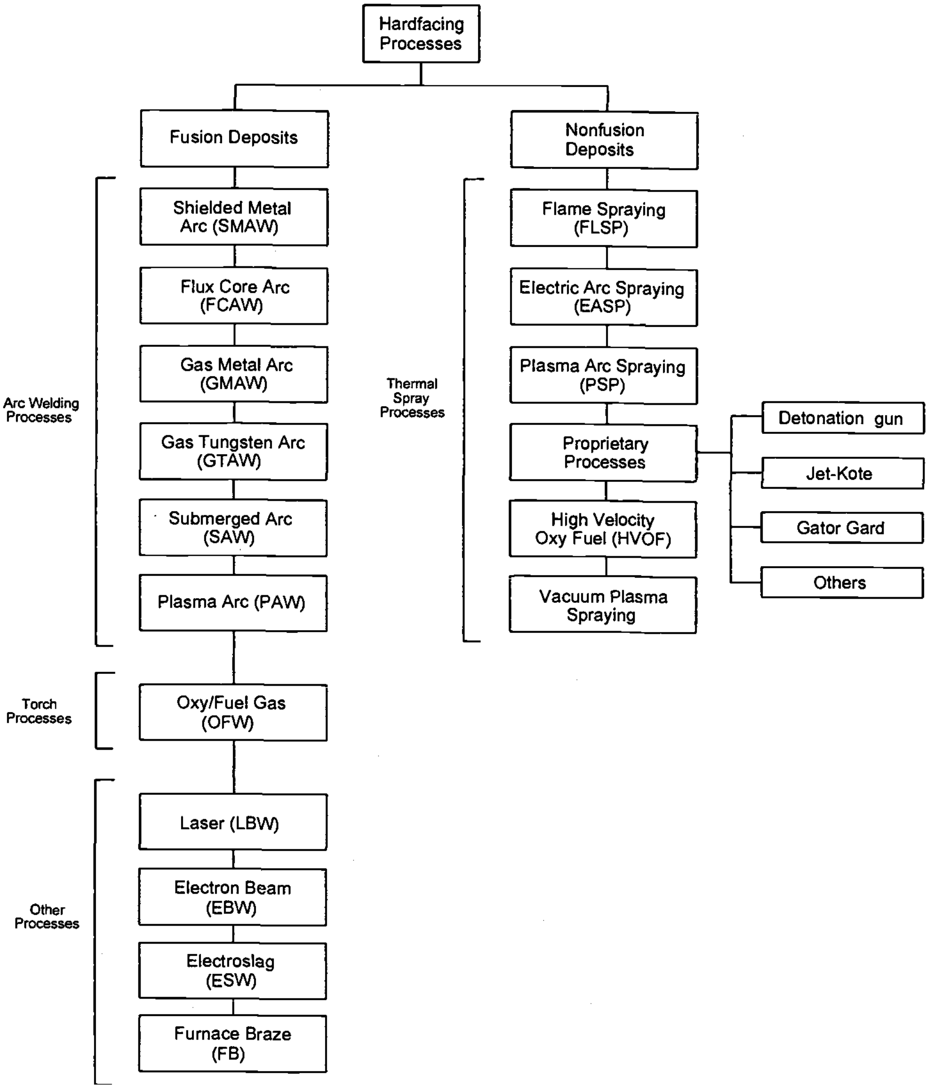

FIG. 6—*Hardfacing processes that require melting of the substrate (fusion) and those that do not (nonfusion).*

It is useful to keep this factor in mind when applying thermal spray coatings to surfaces that will be subjected to Hertzian stresses or to impact types of loads. If operating stresses approach 7 MPa, it may be well to use a fusion process. Surface adhesion is not usually a factor with fusion processes. Thus, the distinction between fusion and nonfusion hardening processes is that the fusion processes involve melting the surface and the nonfusion processes do not. Both categories involve a coating on the surface. There is no penetration into the substrate with the nonfusion processes; there is dilution of the hardfacing with the substrate in the fusion processes.

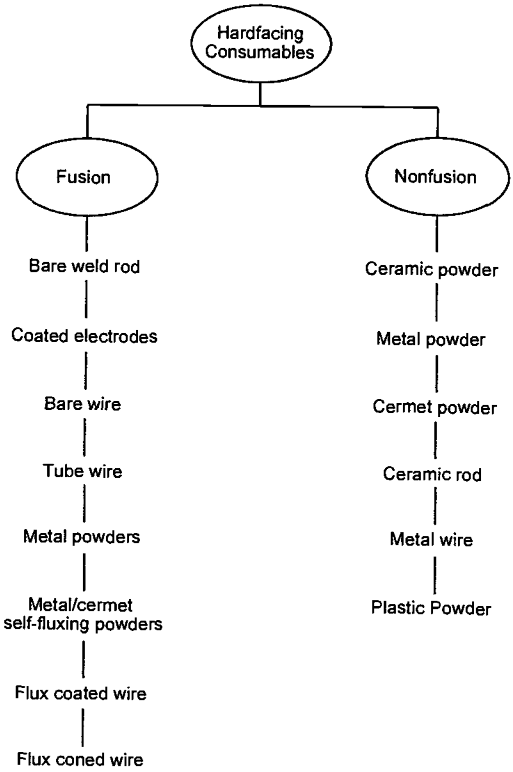

FIG. 7—*Available forms of fusion and nonfusion hardfacing consumables.*

The materials that can be applied with hardfacing processes are shown in Fig. 7. Fusion hardfacing consumables come in many product forms to accommodate various welding processes. Nonfusion consumables are mostly in powder form, but some processes use ceramic rods. There are many flame spray guns that use wire consumables. The largest fusion consumable from the tonnage standpoint is ferrous metals, but cobalt, nickel, and copper-base alloys are also widely used. Just about any material that can be made into a powder can be applied with thermal spray processes if it does not degrade in the spraying heat. Tungsten carbide/cobalt cermet, chromium oxide, and aluminum oxide ceramics are very popular plasma spray coatings. They are usually applied 125 to 175 μm thick and are finish ground to 75 to 125 μm. As-deposited thermal spray coatings can have a surface roughness of 6 μm. Most users need to grind the sprayed surface after coating.

There is no technological limit on the thickness of fusion deposits, but most users try to limit thickness to two layers, which means about 5 mm. These deposits are finished if the application requires it, but when applied to earth moving equipment and agriculture equipment, deposits are usually used as-applied. Deposits are not machined. Fusion hardfacing is widely used on extrusion screws (flights), on valves (seats, faces), on mineral handling and processing equipment (chutes, diggers, crusher rolls), dies (tool steel repair), and countless places in recovery industries. The iron chromium alloys are probably the most popular, and the most common substrate is weldable carbon steel. Cobalt and nickel-base alloys are very popular for metal-to-metal wear applications. Figure 8 compares the applicability of gas-combustion nonfusion pro-

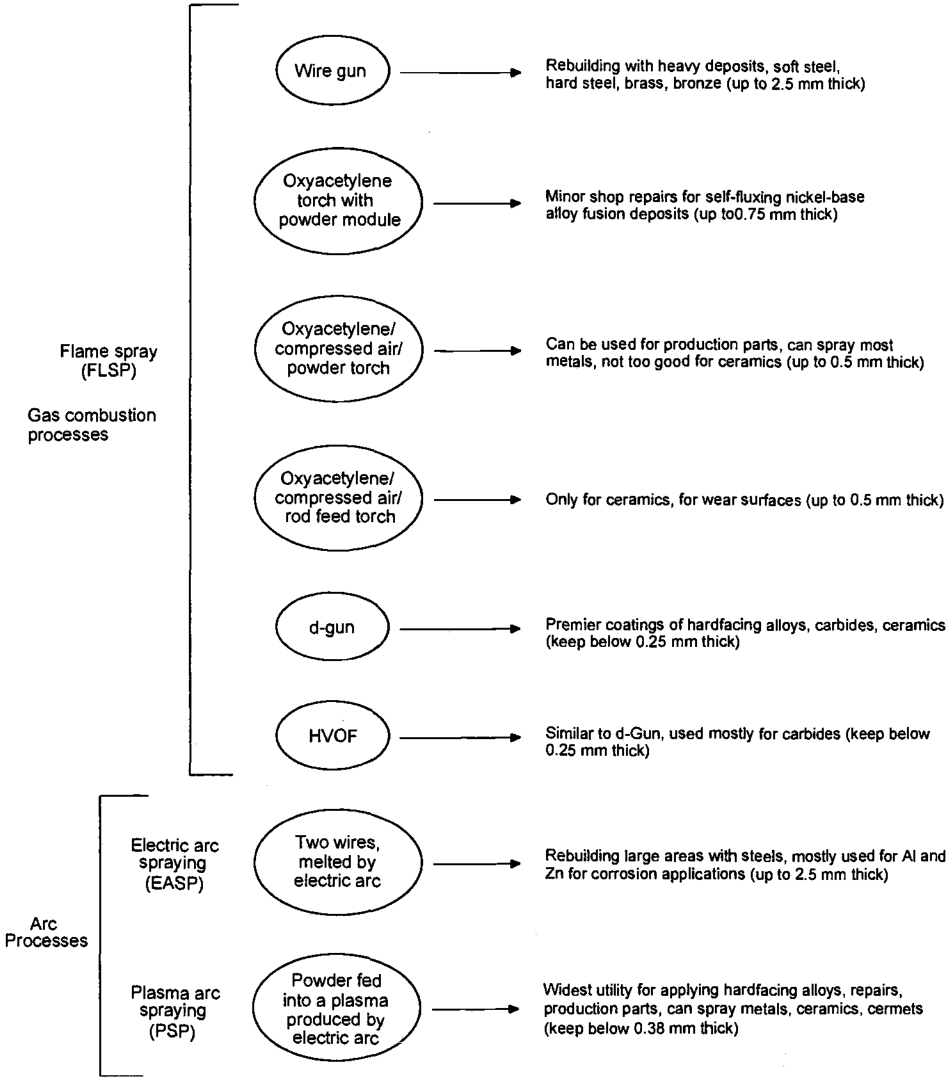

FIG. 8—*Flame-spray and arc-welding hardfacing processes.*

cesses and arc-spraying processes. Plasma spraying and high-velocity oxy fuel (HVOF) spraying are very popular nonfusion processes.

Each of the hardfacing processes listed have a niche where they are most cost effective. The same situation exists for the materials that can be applied. In general, hardfacing with fusion processes is applicable to systems where severe mechanical abuse or Hertzian loading takes place in service. The thermal spray coatings excel where just a few mils of protection will be adequate. Fusion hardfacings require a weldable substrate and high application temperatures. Thermal spray processes seldom get the substrate hotter than 200°C. All of the processes listed in Fig. 1 belong in the machine designer's repertoire of surface engineering processes. They are extremely useful.

When to Use Selective Hardening—The most important processes in this category of surface engineering are flame and induction hardening. Both processes require a suitable ferrous substrate. The steel or cast iron must have sufficient carbon in the matrix to allow quench hardening; parts must be raised to the austenitizing temperature and quenched. In selective hardening, these requirements are met only in a localized region. Either an oxy-fuel flame or an induction coil are the traditional ways of accomplishing selective hardening.

Flame hardening requires only a flame-heating system and a water-quenching system; induction heating requires that the parts fit into a water-cooled copper coil and an induction heating power supply is needed to produce induced current into the work. A distinct advantage of flame hardening is that it can be performed on parts of any size. Flights on a 12-m (40-ft) long plastic extrusion screw can be done with relative ease. Induction heating usually is restricted to small parts, and systems are often automated for high production. Both processes can produce surface hardening depths up to 10 mm or more. The minimum hardening depth on flame hardening is about 1.5 mm. Hardening depths as low as 0.25 mm are possible with induction techniques. Suitable substrates and attainable hardnesses are listed in Table 1.

Selective hardening is suitable for very large parts that would be difficult to heat in a furnace. It is preferred to one-of-a-kind parts as well as when heavy cases are desired. Gears, wheels, cams, and heavy-duty shafting are common applications. Selective hardening is usually performed on finish-machined parts. A disadvantage of both processes is that each requires the handling of individual parts. Flame and induction hardening are not batch processes.

When to Use Diffusion Treatments—The spectrum of diffusion hardening processes is shown in Fig. 9. The most common diffusion treatment is carburizing. Carbonitriding and nitriding are also widely used. Boronizing and the specialty treatments such as titanium carbide or vanadium carbide are less frequently used. These processes are normally restricted to ferrous metals.

Carburizing and nitriding produce slight surface growth, usually on the order of a few micrometers per surface. These processes are usually done on finished surfaces or surfaces that only have a small stock allowance for finishing. These processes are very well suited to metal-to-metal wear situations, and they are normally used for applications where another part will be rubbing on the diffusion-treated part. The carburized and nitrided parts should be used at their normal working hardness, 60+ HRC. They can have depths as much as a millimetre (or more) so they can be used for applications with a significant tolerance for wear.

The less-used processes (B, TiC, VC) are almost always done on finish-machined surfaces, and they normally produce case thicknesses of less than 3 μm. They can have hardnesses that

TABLE 1—*Materials that are commonly flame or induction hardened and their normal hardening ranges.*

Carbon Steels	HRC	Alloy Steels	HRC	Tool Steels	HRC	Cast Irons	HRC
1025-1030	40 to 45	3 140	50 to 60	01	58 to 60	Ductile, 80-60-03	55 to 62
1035-1040	45 to 50	4 140	50 to 60	02	56 to 60	Gray Class 30	45 to 55
1045	52 to 55	4 340	54 to 60	S1	50 to 55	Gray Class 45	55 to 62
1050	55 to 61	6 145	54 to 62	P20	45 to 50		
1145	52 to 55	52 100	58 to 62				
1065	60 to 63						

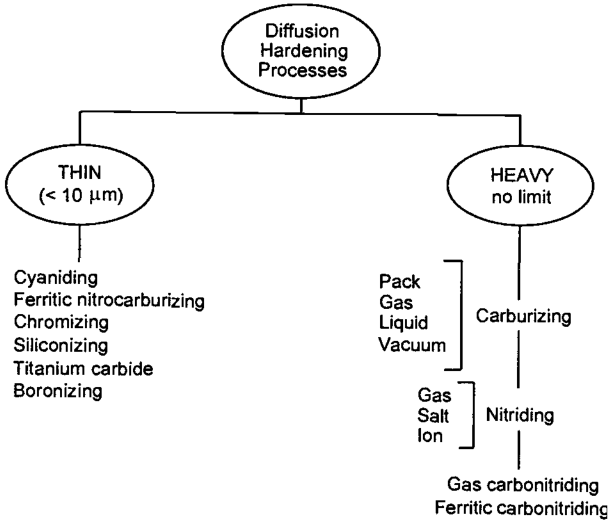

FIG. 9—*Categorization of diffusion hardening processes by case depth.*

are twice that of nitriding and carburizing. They are most suitable for applications where a thick and very hard coating is appropriate.

Another factor to consider in using these processes is if the part can tolerate the treatment temperature without significant distortion. As shown in Fig. 10, carburizing and other diffusion-treating processes are usually performed at temperatures in excess of 900°C. Heating to such a high temperature is likely to cause some part distortion. Carburizing and carbonitriding require a liquid quench from the treatment temperature. This can be an additional source of part distortion that must be dealt with. The final restriction on these processes is substrate compatibility. Carburizing works best on an alloy carburizing steel substrate. Nitriding develops the highest hardness on an alloy nitriding steel substrate; boronizing, vanadium carbide, and titanium carbide treatments are often performed on air-hardening tool steels such as AISI Type D2 that will air-harden on cooling from the process temperature.

The most common application of diffusion-treating processes is on parts that can be batch processed. Usually, small parts can be done without post-treatment finishing. The ideal diffusion treatment application is a job that requires many small parts that are used for metal-to-metal wear or low-stress abrasion applications. Carburizing and nitriding probably have the best availability of any surface-hardening processes.

When to Use High-Energy Processes—For the purposes of this discussion, high-energy processes mean electron beam, laser beam, and ion implantation. They are known as high-energy processes because the energy density in watts/unit area is usually higher than for many other surface engineering processes. Laser and electron beam are used to harden surfaces in a fashion that is identical to selective hardening except that quenching is usually performed by letting the mass of the treated substrate serve as the quenchant. Heating is usually confined to a small spot or pattern, so if a part has fairly large mass, it remains "stone cold" and conduction from the heated area produces the quench. Lasers and electron beam can harden suitable substrates (same as for flame and induction hardening) to a depth of about 1 mm under normal processing. The hardened patterns are usually strips, dots, or similar patterns generated by the numerically-controlled part moving (or gun moving) controls.

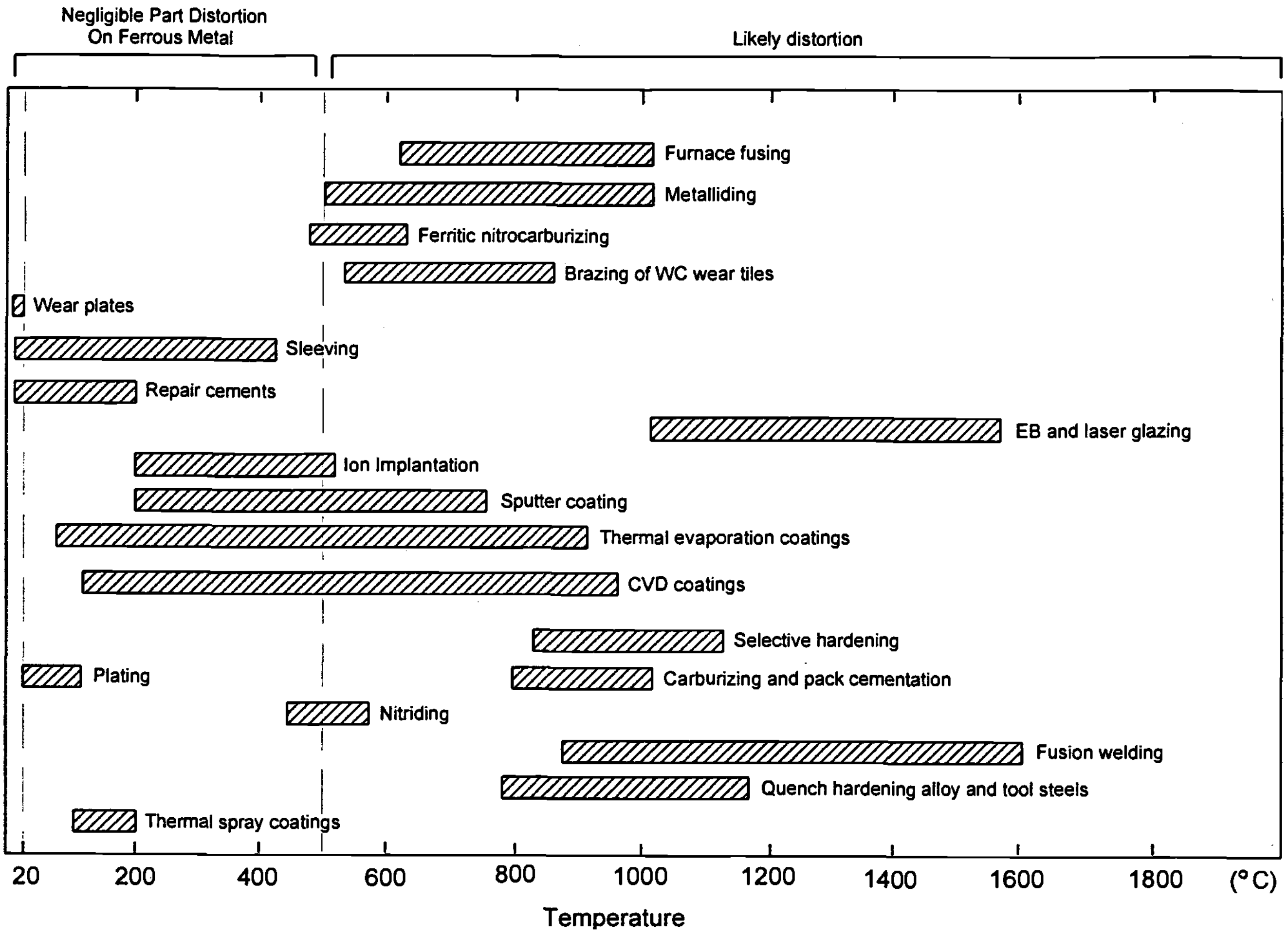

FIG. 10—*Temperatures encountered in various surface engineering processes.*

The other surface-improvement process that is offered with laser and electron beams is surface glazing. With both laser and electron beams, it is possible to rapidly bring the surface of the work to its melting temperature. It is believed that this melting and the subsequent quench can improve the tribological properties of a surface. This practice is not widely used, but it has been successfully used to produce structure refinement (elimination of massive carbides) in tool steel cutting edges. Surface melting by laser and electron beam is also done to melt thermal spray deposits so that they form a fusion bond to the substrate rather than the normal mechanical bond.

An advantage of laser surface treatments over electron beam surface treatments is that it is not necessary for the workpiece to be in a vacuum chamber as is the case with electron beam processes. An advantage of electron beam treatment over lasers is that the reflectivity of the surface is not a concern. Shiny metals reflect a significant portion of laser beams. In addition, electron beam equipment is much less expensive per unit of beam energy.

Ion implantation is performed in a vacuum chamber. A beam of ions is generated by a variety of techniques. This beam is rastered on the work, and the high-velocity ions penetrate the work to a depth of about 0.1 μm. As shown in Fig. 11, ion implanation produces the shallowest case depth of all of the surface engineering processes. It is claimed that the treatment of steel surfaces with carbon, nitrogen, chromium, and more recently boron, improves the tribological properties of metal surfaces. In some cases, compounds (such as nitrides) are thought to be formed. In other cases, the strengthening is thought to be analogous to diffusion strengthening. Carbon and nitrogen ions can diffuse into interstitial lattice positions like carbon does in quench hardening.

There are at least four vendors in the United States who perform this service on a commercial basis. The value of such treatments is reported in case histories in the literature, but applications are still being investigated.

Laser and electron beam hardening can be used wherever selective hardening is appropriate. Both processes will produce less distortion than flame and induction hardening if the hardened zone is kept to a minimum. Ion implantation is best used on tribosystems that need to have zero wear. If the treatment only penetrates to a depth of 0.1 μm, it is likely not to be helpful on a part that can tolerate 0.25 μm of wear.

Matching Materials and Processes to Wear Modes

Figure 12 is an attempt to present "preferred materials" of construction for various modes of wear. This illustration shows that nitrided alloy steel is very resistant to galling (self-mated), but a variety of surface engineering processes are also candidates for this form of wear.

Some of the "best-choice" materials are bulk materials rather than treated surfaces. This is where surface engineering should be considered. If one cannot afford to make a part from solid cemented carbide, a carbide surface coating can be applied with HVOF or one of the other thermal spray processes. The same situation exists with ceramics and many of the materials that were discussed.

Summary

In summary, using surface engineering to solve wear problems starts with the selection of the specific mode of wear that is anticipated in a system under design. The next step is to consider the surface engineering processes that can be used to address this form of wear (and which is compatible with the part requirements—distortion, tolerances, surface texture, etc.). Finally, the designer must decide on a process and material that will properly address the form

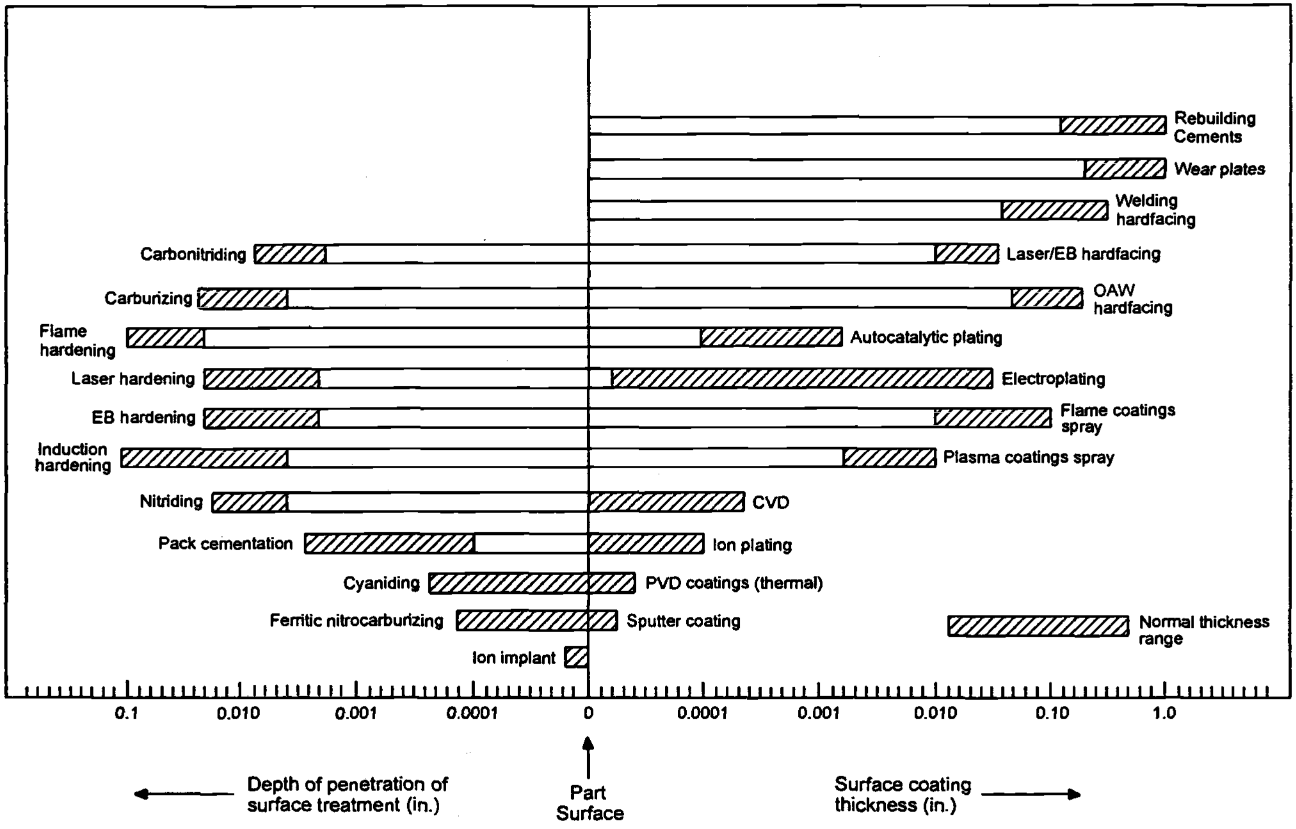

FIG. 11—*Normal thickness ranges for various surface-engineering processes.*

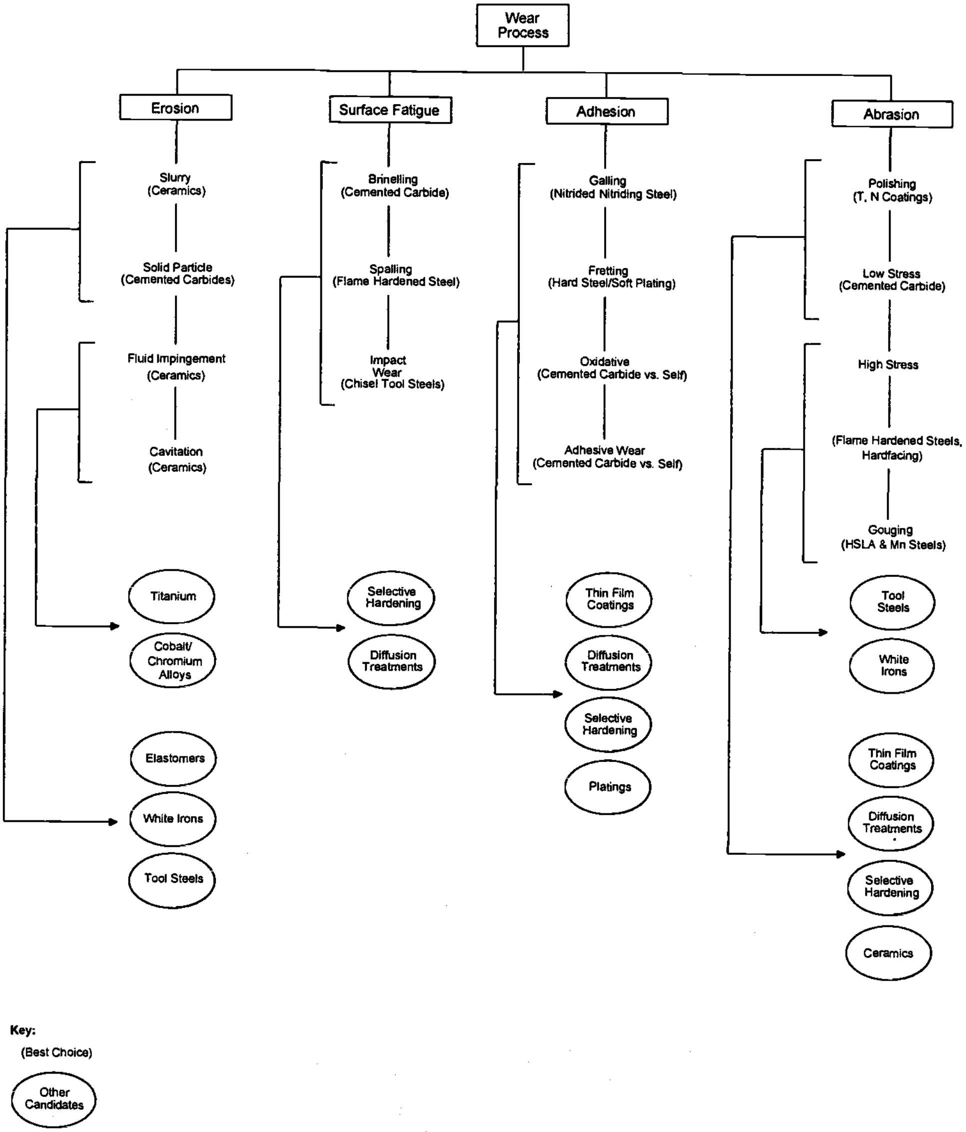

FIG. 12—*Wear processes showing preferred materials and candidate materials/treatments.*

of wear at hand. A few materials excel in combating each form of wear. Some of these are very expensive or hard to fabricate, or both. Surface engineering can often provide the means for using these materials only on the surfaces where they are needed. It is a cost-effective approach that should be tried wherever feasible.

References

[*1*] *ASM Handbook Volume 18, Friction, Lubrication and Wear Technology,* P. J. Blau, Ed., ASM International, Metals Park, OH, 1992, p. 176.

[2] Budinski, K. G., *Surface Engineering for Wear Resistance,* Prentice Hall, Inc., Englewood Cliffs, NJ, 1988, p. 16.

[3] *Wear Control Handbook,* M. B. Peterson and W. O. Winer, Eds., American Society of Mechanical Engineers, New York, 1980, p. 9.

[4] Samuals, L. E., *Metallographic Polishing by Mechanical Methods,* ASM International, Metals Park, OH, 1982, p. 31.

[5] Hutchings, I. M., *Tribology: Friction and Wear of Engineering Materials,* CRC Press, Inc., Boca Raton, FL, 1992, p. 77.

Peter J. Blau,[1] *Charles S. Yust,*[1] *Yong W. Bae,*[1]
Theodore M. Besmann,[1] *and Woo Y. Lee*[1]

Friction and Wear of Self-Lubricating TiN-MoS_2 Coatings Produced by Chemical Vapor Deposition

REFERENCE: Blau, P. J., Yust, C. S., Bae, Y. W., Besmann, T. M., and Lee, W. Y., **"Friction and Wear of Self-Lubricating TiN-MoS_2 Coatings Produced by Chemical Vapor Deposition,"** *Effect of Surface Coatings and Treatments on Wear, ASTM STP 1278,* S. Bahadur, Ed., American Society for Testing and Materials, 1996, pp. 22–34.

ABSTRACT: The purpose of the work reported here was to develop special chemical vapor deposition (CVD) methods to produce self-lubricating ceramic coatings in which the lubricating and structural phases were co-deposited on Ti-6A1-4V alloy substrates. These novel composite coatings are based on a system containing titanium nitride and molybdenum disulfide. The method for producing these coatings and their sliding behavior against silicon nitride counterfaces, in the temperature range of 20 to 700°C in air, are described. The initial sliding friction coefficients for the composite coatings at room temperature were 0.07 to 0.30, but longer-term transitions to higher friction occurred, and specimen-to-specimen test variations suggested that further developments of the deposition process are required to assure repeatable friction and wear results. Friction and wear tests at 300 and 700°C produced encouraging results, but tests run at an intermediate temperature of 400°C exhibited friction coefficients of 1.0 or more. Oxidation and a change in the nature of the debris layers formed during sliding are believed to be responsible for this behavior.

KEYWORDS: friction properties, wear testing, chemical vapor deposition, titanium nitride, surface coatings, molybdenum disulfide, self-lubricating materials, surface treatments

Coatings and surface treatments represent important strategies for affecting friction and wear improvements on load-bearing, sliding surfaces. There are a large number of such treatments currently available [*1–3*]. In fact, entire journals are devoted to the subject [*4*]. Coating processes involve adding material to the surface. Other treatments, like ion-implantation and diffusion treatments, involve modifying the composition or structure of the materials, or both, at and just below the surface.

Materials that contain an additive or additives that reduce friction during use are called self-lubricating materials. Examples of self-lubricating materials include polymer blends that contain tetrafluoroethylene and porous, oil-impregnated bronzes. Self-lubricating materials are useful for a number of reasons:

1. They can serve as fail-safe protection in a liquid lubricated system in case the liquid lubricant is lost or fails for some other reason.
2. They can lubricate parts of machinery where it is not practical to use external lubrication supply systems.

---

[1] Metals and Ceramics Division, Oak Ridge National Laboratory, Oak Ridge, TN 37831-6063.

3. They can operate in severe environments, such as high-temperatures, where liquid lubricants may not work.
4. They can be sealed into assemblies that must function effectively without having the opportunity to add more lubricant.
5. They may be a cost-effective alternative to other lubrication schemes.

In the present context, a self-lubricating coating consists of a matrix phase to provide a measure of wear resistance and load-bearing structure, and a solid lubricating phase to reduce friction. The coating should be so constructed such that there is sufficient quantity of lubricant to spread over the surface, yet not so much that the coating becomes too soft to support the load or to retain its integrity and adhesion to the substrate. In the ideal case, the wear of the coating should be low and just sufficient to continue to supply additional lubricating phase to the surface to replenish that which is lost by wear or transfer to the opposing surface.

For the matrix phase, we selected titanium nitride, a ceramic material whose success as a wear-resistant coating material for tooling and other tribological applications is well established. For the lubricating phase, we selected molybdendum disulfide, a solid lubricating material with moderate elevated temperature capabilities. At temperatures of approximately 350 to 400°C, MoS_2 tends to oxidize to form MoO_3 [*5*]. The challenge of this effort was to simultaneously deposit the matrix and lubricating phases by controlled chemical vapor deposition (CVD) so as to produce a functional coating.

Results of earlier microfriction studies indicated that the method of applying MoS_2 to surfaces affects the stability and nominal value of the friction coefficient when sliding against silicon nitride [*6*]. The current work presents results of sliding friction and wear tests of our composite coatings against silicon nitride that were conducted in air at temperatures between about 20 and 700°C.

Coating Synthesis and Characterization

Deposition of composite coatings of TiN-MoS_2 was carried out on polished Ti-6A1-4V alloy substrates in a cold-wall CVD reactor at 1073 K and a system pressure of 5.3 kPa. The precursor gases were composed of tetrakis (dimethylamino) titanium, $Ti((CH_3)_2N)_4$ (99.9%),[2] MoF_6 (99.9%),[3] NH_3 (99.95%),[4] and H_2S (99.5%).[4] The reaction chamber, constructed of a fused silica tube, was 61 cm long and 3.3 cm in inner diameter. Stainless steel flanges with compression O-ring fittings were used to seal the reactor assembly at both ends. Mass flow controllers were used to control gas flows, and the system pressure was controlled by using a mechanical pump with a solenoid flow valve coupled with a pressure controller and a capacitance manometer.

150 g of $Ti((CH_3)_2N)_4$ was contained in a 200-cm^3 bubbler maintained at a constant temperature of 338 K using a silicon oil bath with an immersion circulator. The vapor pressure of $Ti((CH_3)_2N)_4$ at this temperature is $\approx$200 Pa [*7*]. Argon at 20 cm^3/min at standard temperature and pressure was passed through the bubbler to carry the vapor into the reactor. The flow rate of NH_3 was 300 cm^3/min at standard temperature and pressure that was separately fed into the reaction zone using a dual-path, co-axial injector made of Inconel to prevent premature reaction with the titanium precursor. The flow rates of MoF_6 and H_2S were 6 and 60 cm^3/min at standard temperature and pressure, respectively. The titanium alloy substrates (1.8 by 2.5 cm) were

[2] Strem Chemicals, Inc., Newburyport, MA.

[3] Johnson & Matthy, Wardhill, MA.

[4] Alphagaz, Morrisville, PA.

placed on a 13-cm-long graphite susceptor that was inductively heated by a radio frequency field (164 kHz). A K-type thermocouple in contact with the graphite susceptor was used to measure temperatures. Film thicknesses of 3 to 4 μm were produced.

X-ray diffraction patterns such as that shown in Fig. 1 were obtained on the TiN-MoS_2 composite coatings to determine their structures and compositions. Peaks marked with asterisks in the figure arose from the substrate. While no preferred orientation was predominant in the case of TiN, MoS_2 was found to be textured such that its (002) planes were aligned parallel to the coating surface. This orientation is highly desirable to produce maximum lubricity. The deposition rate, estimated from the coating cross-sections analyzed by electron microprobe analysis, averaged ≈10 μm/h. Studies using Auger electron spectroscopy (AES) indicated that the MoS_2 content in the TiN-MoS_2 composite coatings increased as a function of the coating thickness. Selected-area, electron diffraction analysis indicated that the coating surface was primarily MoS_2, and both TiN and MoS_2 were identified near the substrate, in agreement with the results obtained by the AES analysis. A transmission electron micrograph of the composite coating in the transverse direction showed that MoS_2 was present as pockets dispersed in a matrix consisting of ≈50-nm TiN crystallites (see Fig. 2).

Friction and Wear Testing Procedure

Friction and wear testing was performed in a high-temperature pin-on-disk tribometer that is capable of continuous rotation in either clockwise or counter clockwise directions, or of

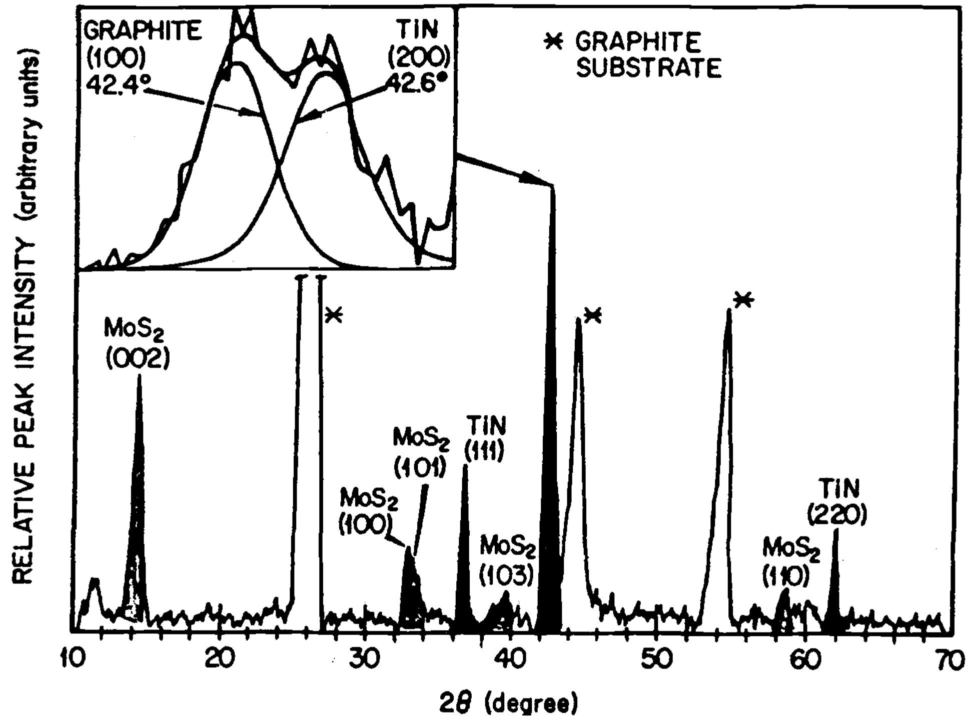

FIG. 1—*X-ray diffraction pattern of the TiN-MoS_2 coating deposited on Ti-6Al-4V alloy substrate.*

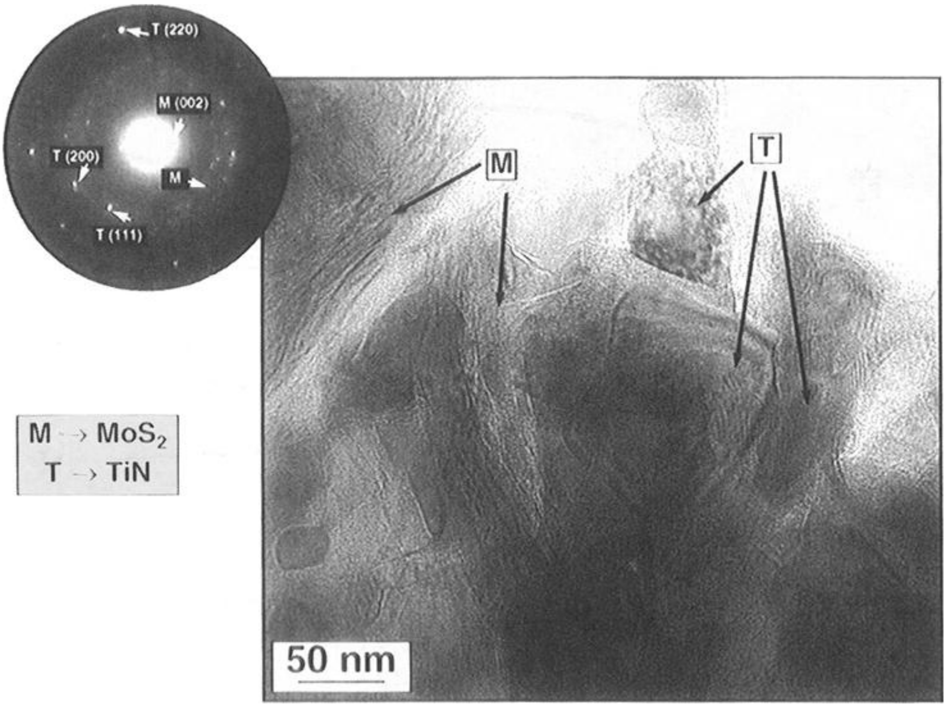

FIG. 2—*A transmission electron micrograph in the transverse direction of the TiN-MoS_2 composite coating.*

oscillation over a specified angular range. The latter mode was used for these experiments. The pin specimen, in these tests a 9.53 mm diameter silicon nitride (NBD200) sphere, was held in the end of a rod anchored in a strain-gaged collar arrangement which allowed recording both the normal and tangential forces during the test. The pin holder and the disk rotation system move along a vertical axis, bringing the pin and the disk into contact at the center of a resistance heated furnace. The furnace heating element is contained within quartz tubes, the outermost tube being gold-coated for reflection of radiation. A schematic illustration of the test configuration is shown in Fig. 3.

The present tests were done using oscillatory motion over an arc of 90°. The oscillation frequency was 40 cycles/min and the wear track diameter was 20 mm. The resultant average sliding velocity was approximately 20 mm/s. An applied force of 16.4 N was selected in order to provide an elastic, Hertzian contact pressure of 1 GPa for the silicon nitride sphere on the titanium alloy plane at the given test temperature. In one low-load test, the applied force was reduced to 1 N (0.37 GPa). The standard test duration was 500 cycles (12.5 min); however, additional tests of up to 4 h in duration examined the effect of more prolonged sliding. Tests were performed at room temperature and at temperatures up to 700°C. Ambient atmosphere was used in all the tests.

Tangential force and normal force were periodically sampled by a computer-driven data acquisition system. Data were recorded for 30 s at 2 min intervals at a rate of 125 s^{-1} during the 500-cycle tests, and at selected periods during more extended tests. A strip chart recorder was also used to display the general trend of both tangential and normal force in all tests. The

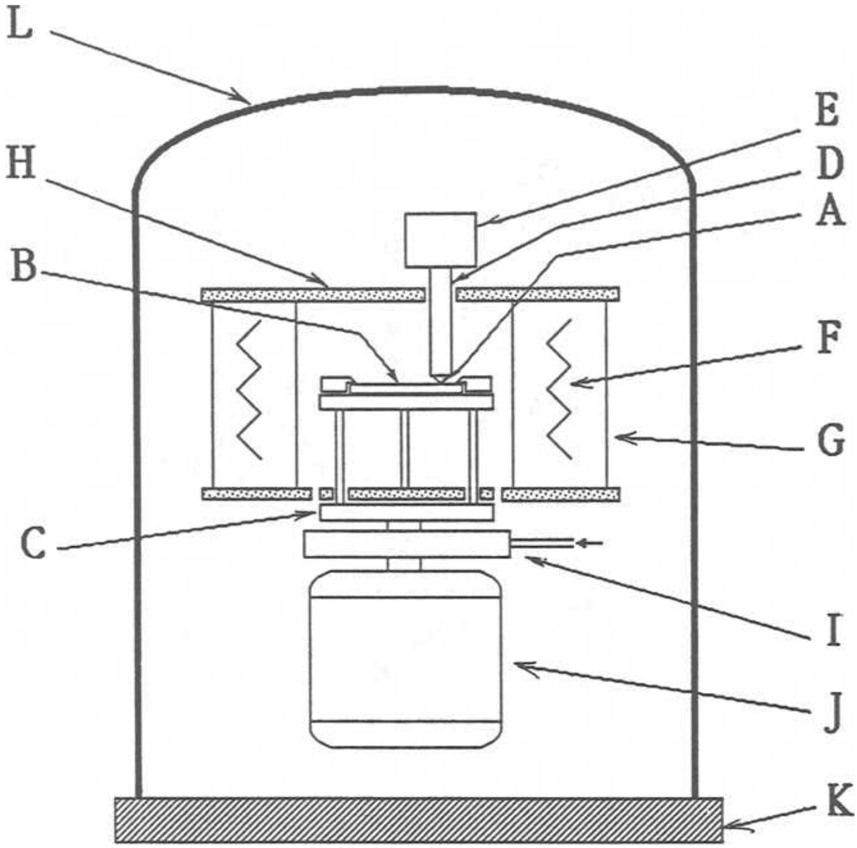

FIG. 3—*Schematic diagram of the high-temperature tribometer: A = ball specimen, B = flat specimen, C = base plate for flat specimen stage, D = mounting rod for ball specimen, E = dead weight, F = resistance heating coils, G = gold-coated reflector, H = insulating plate, I = water cooling for the base plate, J = drive motor, K = aluminum base plate for the machine, and L = glass bell jar.*

TABLE 1—*Friction and wear tests performed in this study.*

Composition	Temperature, °C	Test Time, min	Number of Tests
Polished Ti-6Al-4V alloy	20	12.5	1
TiN-rich coating	20	12.5	1
CVD MoS_2 coating	20	12.5	1
	20	240.0	1
Composite TiN-MoS_2 coating	20	12.5	5
	20	61.0	1
	20	90.0	1
	20	120.0	1
	20	230.0	1
	300	12.5	1
	400	12.5	2
	700	12.5	1

TABLE 2—*Friction results: room temperature tests (all tests at 1 GPa contact pressure, reciprocating, in air).*

Composition	μ, initial	Trend in μ	μ, final
Uncoated substrate	0.44	rapid decrease	0.40
TiN-rich coating	0.50	rising	0.80
MoS_2 coating	0.18 to 0.21	rising, highest for the 4-h test	0.20/0.32
Composite coating (12.5 min tests)	0.07 to 0.20	rise/drop/rise behavior was common	0.13 to 0.22 (0.6 for one test)
Composite coatings (>60 min tests)	0.09 to 0.30	rise/drop/rise behavior was common	0.40 to 0.60

figures depicting friction coefficient as a function of time presented here are all based on the computer-recorded data. The coatings and conditions used for these experiments are listed in Table 1.

Results of Friction and Wear Tests

Room Temperature Tests

Friction results for the room temperature tests are given in Table 2 and Fig. 4. The first three rows of Table 2 contain baseline data for a polished Ti-6A1-4V specimen, a TiN coating and

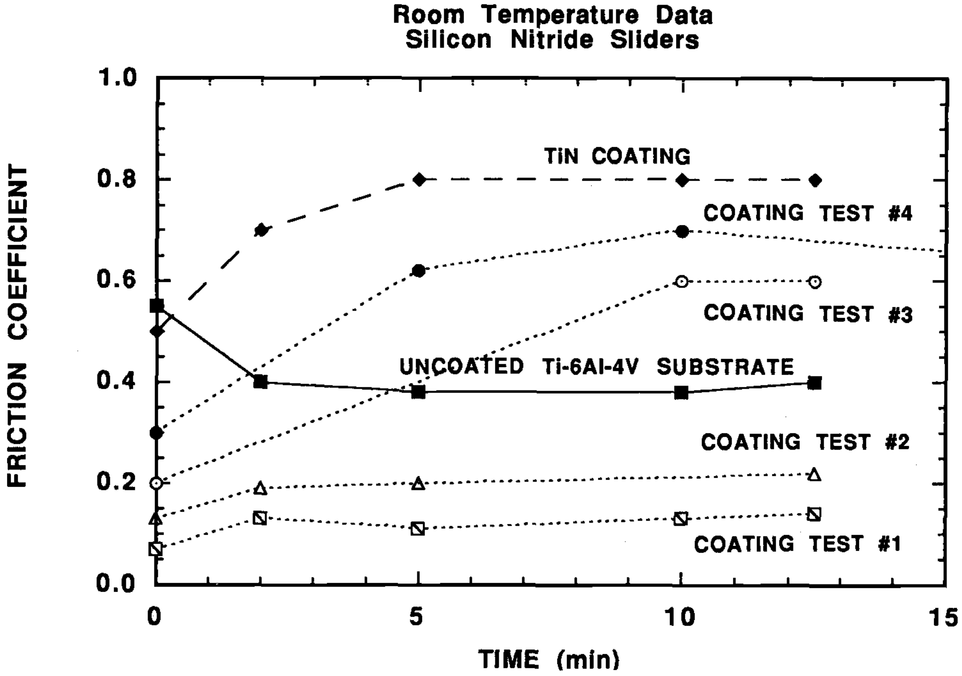

FIG. 4—*Summary of friction data from room temperature tests of various coatings.*

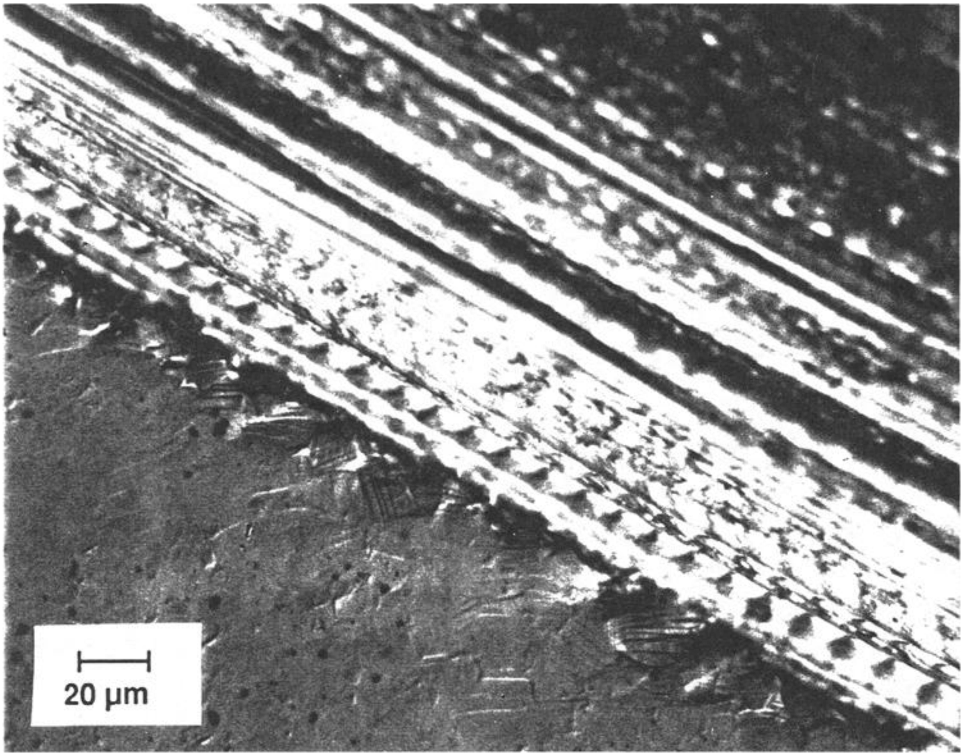

FIG. 5—*Photomicrograph of a wear track on the Ti-6A1-4V substrate material showing deformation twinning at the track edge and periodic features within the grooves.*

a MoS_2 coating (500 cycles, 12.5 min). As shown in Fig. 4, the friction coefficient for the bare substrate began at 0.55, decreased to 0.4 after 2 min of sliding, and remained at this value for the remainder of the test. The wear track was 10 μm deep (by profilometric measurement) with displaced material displaying deformation twinning at the track edge, as shown in Fig. 5. The tip of the slider was covered by adherent debris.

The friction coefficient of the TiN-coated specimen rose from 0.5 to 0.8 after only 5 min of sliding. The only evidence of wear was the flattening of the coating surface in the wear path caused either by the removal of prominent summits of the profile or filling of some of the profile valleys with wear debris, or both. Figure 6 shows the highly-fractured appearance of the track surface. A debris-free wear surface, 715 μm in diameter, was formed on the slider tip, suggestive of abrasive wear by the hard TiN coating.

The friction coefficient in the MoS_2 coating test remained at about 0.2 for the entire 500 cycles, but on the 4-h test reached 0.32. Because the starting film was about twice the thickness of the other coatings (8 μm), there was more material available to form a lubricating transfer film on the slider tip, and its effect lasted relatively long.

Composite coating specimens containing both TiN and MoS_2 were produced. Five tests of 500 cycles duration were conducted. The initial friction coefficients increased from about 0.07 to 0.20, in the first 2 min, to 0.13 to 0.22 for the remainder of the tests. In some specimens, the friction coefficient remained relatively low, but in others, it was higher and varied considerably during the test. Figure 7 shows the relatively smooth appearance of the wear track of one of the composite coating specimens that gave low friction results.

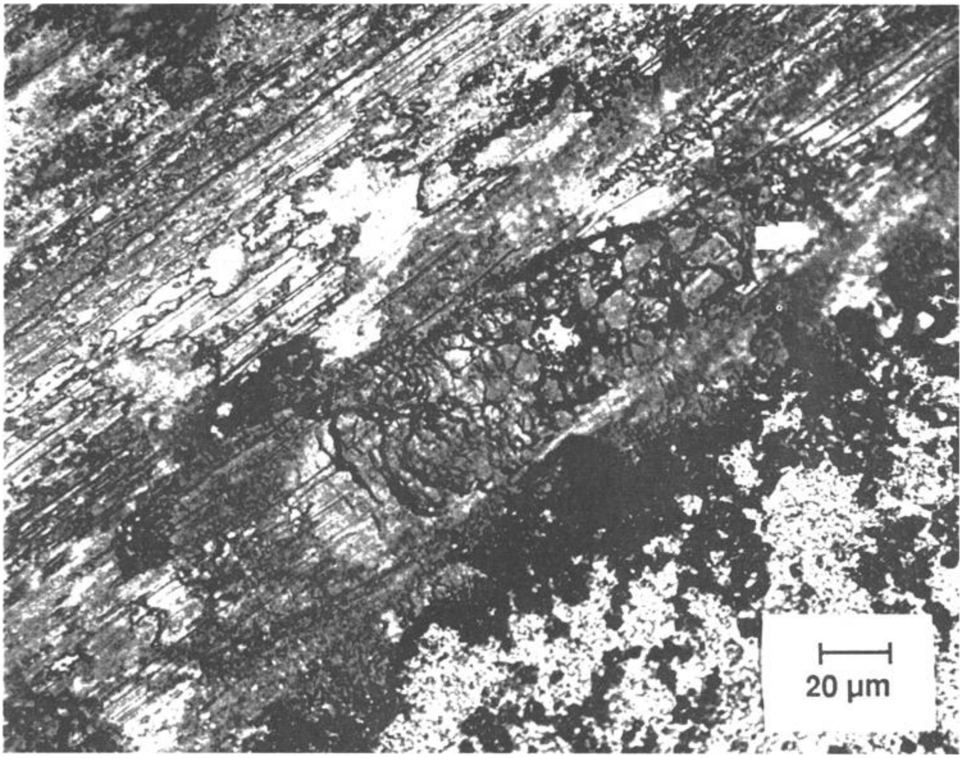

FIG. 6—*Fractured area on the surface of the TiN-coated specimen.*

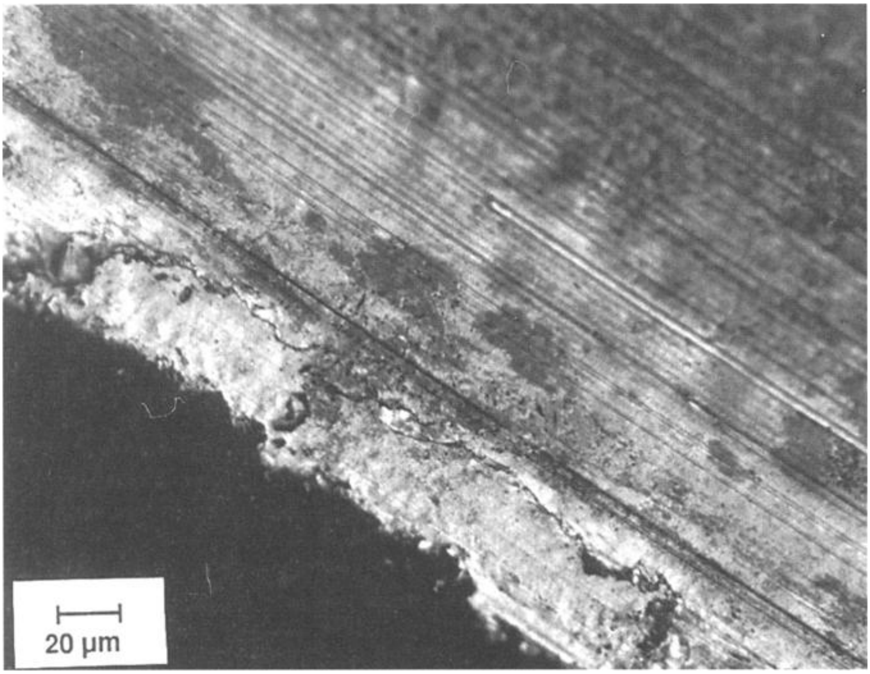

FIG. 7—*Smooth features on the composite coating surface.*

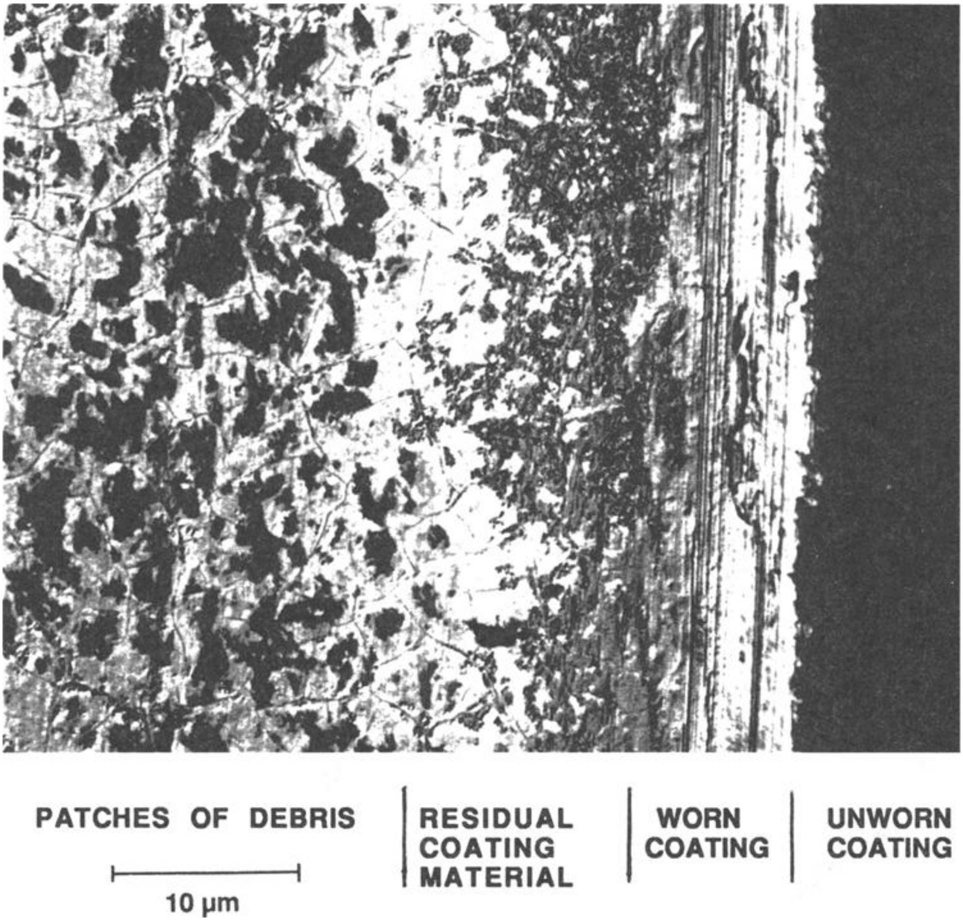

FIG. 8—*Optical micrograph of the wear track for a 230-min-long test showing three distinct regions.*

A longer run was conducted on the composite coating to investigate the effects of coating wear-through. The run was terminated at 3.83 h when there was clear evidence for wear-through (that is, transition to a high, erratic friction coefficient and a change in the appearance of the wear track). The structure of the wear track exhibited three zones: (1) a zone covered with dark patches at the center of the track, (2) a zone partially covered with residual coating material to each side of it, and (3) a narrow band suggestive of a still intact portion of the coating by the track edge (see Fig. 8). A profile of the wear track is shown in Fig. 9. The friction force record of this run exhibited an increasing trend as the proportion of the track width covered by the intact coating continued to decrease. Table 3 lists wear track depths for room temperature tests.

Elevated Temperature Test Results

Coatings were tested at temperatures of 300, 400, and 700°C in air. Results are shown in Fig. 10. Tests at 300°C behaved similarly in friction and wear to those run at room temperature.

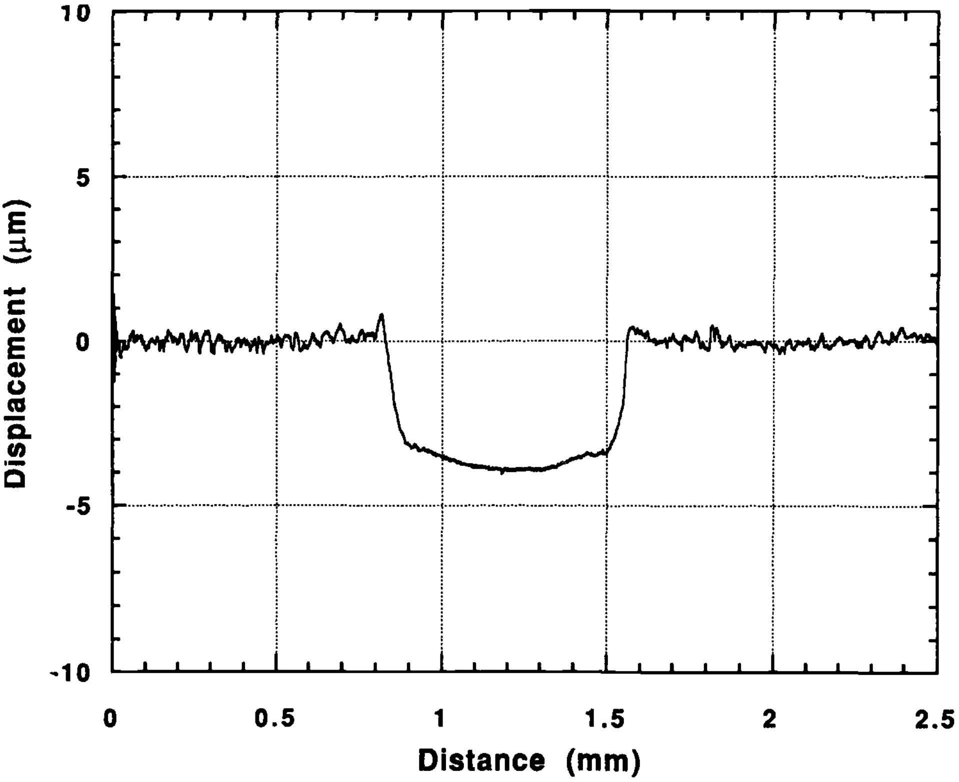

FIG. 9—*Stylus profile (2-μm tip radius) of the wear track shown in Fig. 9.*

Tests at 400°C, however, did not produce the same low friction and wear. The same specimen that exhibited friction coefficients from 0.1 to 0.14 at room temperature was tested at 400°C in an air atmosphere. The initial friction coefficient value was 0.35, but it increased very rapidly to 0.62 at the end of 1 min and reached a final value of 0.75 at 12.5 min. To assess the possibility that lower friction coefficients would be obtained under reduced contact stress, this coating was tested again at 400°C, but at 1 N applied normal force (0.37 GPa). The initial friction coefficient was 0.7, and it increased continually to reach 1.0 at the end of the 12.5-min test. Despite the difference in initial friction values, the elevated temperature response of the coating in two tests was similar, as shown in Fig. 10. Relatively debris-free wear surfaces, surrounded by some

TABLE 3—*Wear track depths for room temperature tests.*

Disc Specimen	Test Time, min	Approximate Track Depth, μm
Ti alloy	12.5	10.0
MoS_2	12.5	20.0
$TiN-MoS_2$ coating	12.5	1.0
	120.0	40.0

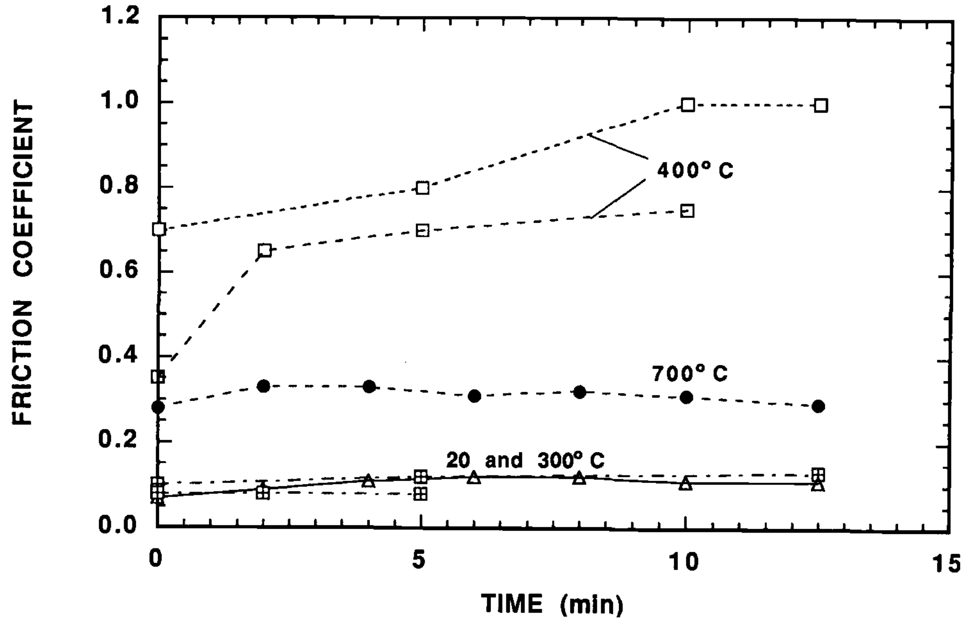

FIG. 10.—*Friction results for coatings tested at various temperatures. Symbol key: squares containing crosses = 20°C tests, triangles = 300°C tests, open squares = 400°C tests, and closed circles = 700°C tests.*

adhered debris, were formed in both 400°C tests. A final run was conducted at 700°C. Friction coefficients for this run were lower than those for the 400°C.

Discussion

A primary issue involved in developing any new tribological surface treatment or coating is that of performance repeatability. Three tests with the same load, speed, and duration were performed on the same specimen, but friction and wear results were not similar, suggesting place-to-place variations in the composition or microstructure within a given coating. Visual inspection of the coating surfaces indicated the likelihood of this variability (for example, a nodular appearance in some regions, or a powdery appearance in others). Auger analysis and depth profiling of the composite coatings indicated that the MoS_2 content decreased with depth. This composition gradient probably contributed to the increase in friction as the coatings wore.

Studies of the friction versus time records for the room temperature coating tests, including the longer duration runs, revealed that friction force tended to follow a complex series of changes before reaching what might be termed the steady-state condition. Friction curve analysis is an established method to assess the repeatability of test conditions as well as the uniformity of the starting materials and scheme of lubrication [*8*]. A commonly-observed behavior in the coating tests would be for the friction force to climb rapidly at first, level off, experience a sharp drop, and finally rise to a steady-state value. Steady state, in the present sense, involved considerable fluctuations in friction force about a mean value. Other types of frictional variations were also observed, reinforcing the idea that the composition and microstructure of the coatings varied from place-to-place on the specimens. This suggests a sequence of evolving interfacial processes: initial abrasion and transfer of material to the slider, smoothing of the as-formed coating features, texturing of the surface layers, and finally, gradual break-through to expose the substrate below. Even when the substrate was exposed, microscopic evidence suggested that some residual coating material, mixed with wear debris, remained on the wear track to modify its frictional behavior.

Elevated temperature friction results were encouraging for high and low temperature tests but not for intermediate temperatures. Friction coefficients were low at 300°C and relatively low at 700°C, but not at 400°C. At 400°C, friction coefficients quickly rose to unacceptably high levels ($\mu \approx 0.8$ to 1.0). It was hoped that tying the MoS_2 up in a very fine-grained composite with TiN might help retain its lubricating qualities at the higher temperatures, but in light of the current results, is suspected that the MoS_2 was oxidized to form MoO_3, a compound not known to be an effective lubricant.

The decrease in friction at 700°C is encouraging for higher temperature applications. It might initially be suspected that TiO_{2-x}, a candidate solid lubricant, might have helped reduce the friction at 700°C, but earlier results from Gardos on the friction of rutile single crystals at various temperatures and partial pressures indicated that friction coefficients of about 0.6 to 0.8 were typical of that material in air at 700°C [9].

No chemical analysis data were available for the high-temperature wear-tested specimens, and the specific composition of the wear surface layers from the elevated temperature tests must remain for future study. Nevertheless, there is good reason to suspect that the tribochemistry of the elevated temperature wear surfaces was a major influence in the coating behavior. In particular, the formation of lubricious oxides on the surface is known to reduce sliding friction in metals and some ceramics, however, it is not clear that such oxides, once formed, would resist wear very well.

Finally, a comment should be made regarding the type of tests used to evaluate these coatings. The contact conditions in the present experiments were relatively severe (ball-on-flat). It is possible that the composite coatings would perform better in a conformal contact situation, like that of journal bearing, face seal, or bushing. Thus, the current results suggest that the coatings may not be appropriate for highly-concentrated sliding conditions as might occur in non-conformal contacts unless improvements in homogeneity are made through further process development.

Summary and Conclusions

Composite, self-lubricating coatings have been produced by CVD on titanium alloy substrates. The coatings contained very fine-grained mixtures of TiN and MoS_2. The composite composition seemed to adhere better compared to MoS_2 CVD coatings alone. While low initial friction coefficients (0.07 to 0.20, typically) were obtained against silicon-nitride sliders, longer-term behavior was quite variable. The latter result is attributed to coating heterogeneity, a subject that needs to be addressed in future development of this coating system.

Friction force-time traces indicate that the wear-through of the coating usually is not an instantaneous event, but rather progresses through a series of stages. Thus, the benefits of the lubrication with the coating persist even when some of the substrate has been exposed.

While the composite coatings show promise for room and elevated temperature applications at 300 and 700°C, test results at 400°C indicate that use at this temperature is not favored from a high-friction standpoint. Differences in the oxide compositions and the debris layers formed at different temperatures are suggested as the reason for this behavior. In particular, the formation of lubricious oxides may reduce friction coefficients at 700°C, but experimental validation of this hypothesis and data on the durability of the oxide films at that temperature have yet to be obtained.

Acknowledgments

This research was sponsored by the Department of Energy, Division of Advanced Energy Projects, under Contract DE-AC05-84OR21400 with Martin Marietta Energy Systems, Inc. The authors wish to thank the internal reviewers at Oak Ridge National Laboratory and at ASTM for their useful comments on this manuscript.

References

[*1*] "Surface Treatments and Coatings for Friction and Wear Control," *ASM Handbook,* 10th ed., Vol. 18, *Friction, Lubrication, and Wear Technology,* ASM International, Metals Park, OH, 1992, pp. 829–883.

[*2*] Budinski, K. G., *Surface Engineering for Wear Resistance,* Prentice Hall, Englewood Cliffs, NJ, 1988.

[*3*] Peterson, M. B. and Ramalingam, S., "Coatings for Tribological Applications," *Fundamentals of Friction and Wear of Materials,* ASM International, Metals Park, OH, 1981, pp. 331–372.

[*4*] *Surface Coatings and Technology,* Elsevier Sequoia, Lausanne, Switzerland.

[*5*] Lancaster, J. K., "Solid Lubricants," *CRC Handbook of Lubrication,* Vol. II, E. R. Booser, Ed., CRC Press, Boca Raton, FL, 1983, pp. 269–286.

[*6*] Blau, P. J. and Yust, C. S., "Microfriction Studies of Model Self-lubricating Surfaces," *Surface and Coatings Technology,* Vol. 62, 1993, pp. 380–387.

[*7*] Katz, A., Feingold, A., Pearton, S. J., Nakahara, S., Ellington, M., Chakrabarti, U. K., Geva, M., and Lane, E., *Journal of Applied Physics,* Vol. 70, No. 7, 1991, p. 3666.

[*8*] Blau, P. J., "Shapes and Other Attributes of Friction Break-in Curves," *Friction and Wear Transitions in Materials,* Noyes Publications, Park Ridge, NJ, 1992, pp. 271–288.

[*9*] Gardos, M. N., Hong, H.-S., and Winer, W. O., "The Effect of Anion Vacancies on the Tribological Properties of Rutile (TiO_{2-x}), Part II: Experimental Evidence," *Tribology Transactions,* Vol. 22, No. 2, 1990, pp. 209–220.

Shyam Bahadur[1] *and Chien-Nan Yang*[1]

Laser Surface Melting of Carbide Coatings and Their Tribological Behavior

---

REFERENCE: Bahadur, S. and Yang, C.-N., **"Laser Surface Melting of Carbide Coatings and Their Tribological Behavior,"** *Effect of Surface Coatings and Treatments on Wear, ASTM STP 1278,* S. Bahadur, Ed., American Society for Testing and Materials, 1996, pp. 35–53.

ABSTRACT: The effect of laser surface-melting on the friction and wear of detonation gun-sprayed (W, Ti)C-Ni (tungsten and titanium carbide-nickel) and WC-Co (tungsten carbide-cobalt) ceramic coatings on AISI 1044 steel and Ti-6A1-4V substrates was studied. The coated surfaces were melted using a 1.5 kW CO_2 laser with a power setting of 1.4 kW and travel speed of 0.01 m/s. The changes in microstructure and microhardness due to the laser treatment were examined. The melted layers were found to be full of dispersed pores that started 65 to 70 μm below the surface. The surface hardness of (W, Ti)C-Ni coated specimens either decreased or remained constant after surface melting; however, the hardness of WC-Co coated specimens increased. Dry sliding friction and wear tests were conducted in a block-on-ring wear tester, with the coated specimens as block specimens and hardened tool steel as the ring specimen. The width of both the ring and the block was 6.35 mm. The test conditions were 4 m/s sliding speed and 4.9 N load. It was found that as a result of laser treatment the wear resistance of WC-Co coating increased, but that of (W, Ti)C-Ni coating decreased. Scanning electron microscopy of the wear surfaces showed that the micromechanisms of wear were cracking and material disintegration from the edges of the cracks and holes.

KEYWORDS: carbide coatings, laser treatment, friction properties, wear testing, microstructure, hardness testing, wear mechanisms, surface coatings, surface treatments

Laser treatment is particularly suitable for surface alloying by using preplaced powder or a coating and then melting the surface by a laser beam. When hard carbide particles were introduced into the melted surface layers of titanium and aluminum alloys, the composite surface layers consisting of hard carbide phases embedded in the matrix of the base materials were formed [*1*]. These surface treatments were found to improve the wear resistance.

The effect of laser surface treatment on plasma-sprayed alumina and zirconia coatings has been studied. It was reported that the laser-treated layer of the coating recrystallizes and becomes denser [*2,3*]. In the case of thin coatings (3 μm thickness or less), laser surface treatment has been reported to harden the substrate without destroying the coating [*4*]. It would also be expected that laser heating would enable the coating material to diffuse into the substrate and thus produce a stronger bond.

In our earlier study [*5*] on the friction and wear behavior of (W, Ti)C-Ni (tungsten and titanium carbide-nickel) and WC-Co (tungsten carbide-cobalt) coatings on steel and titanium substrates, it was found that the coatings were very effective in improving the wear resistance. Since delamination was found to be the dominant mechanism of material removal, it was decided in the present work to melt these coatings into the substrate by laser heating and thereby

---

[1] Professor and graduate student, respectively, Mechanical Engineering Department, Iowa State University, Ames, IA 50011.

achieve a stronger bond between the coatings and the substrate materials. This treatment was expected to reduce delamination and thereby enhance the wear resistance.

Experimental Procedure

Two types of ceramic coatings were deposited by the Union Carbide Corporation by D-Gun process on 1044 steel and Ti-6A1-4V surfaces. The WT-1 coating consisted of 83% (W, Ti) carbide with 17% Ni as binder, and the LW-1N40 coating had 83% W, 3% C, and 14% Co as binder. These percentages are by weight. The thickness of the coatings was 325 to 400 μm. The porosity of as-deposited coatings was not more than 1% by volume. The coated specimens were in the form of blocks with dimensions as 6.35 by 12 by 10 mm where the 6.35 by 12 mm face had the coating on it.

The coated surfaces were melted using a continuous-wave 1.5-kW CO_2 laser with the power setting of 1.4 kW and travel speed of 0.01 m/s. The laser beam was focused on the specimen surface with a lens of 190.5 mm focal length and oscillated by the scanner. It focused to a small spot of 0.25 mm diameter. As the beam was oscillated by the scanner, the spot rotated in an elliptical path of 3 by 2 mm. The heated surface region was shielded by argon gas.

The laser-melted surface was afterwards ground to a depth of 100 μm. It was then finished with 600 grit silicon-carbide wet paper for wear testing.

Sliding wear tests were run in a block-on-ring configuration in which the block with the treated surface rode on the periphery of the ring. The size of the ring was 70 mm diameter and 6.35 mm thick. The ring was made of tool steel that was heat treated to a hardness of 58 to 62 HRC. The conditions used for wear tests were a sliding speed of 4 m/s and a normal load of 4.9 N. The tests in duplicate were run for 8 h that corresponded to a sliding distance of 115.2 km. The tests were run in ambient air with about 35% relative humidity (RH).

The worn block surfaces were coated with a thin layer of gold and studied by scanning electron microscopy. For microhardness measurements and metallographic examination, the specimen cross sections were polished using silicon-carbide wet paper and diamond paste. The hardness measurements were made using a load of 9.8 N (1 kg). The polished specimens were etched for microstructural studies of both the coating and the substrate. The etchants for the coatings and the steel and titanium substrates were Murakami's reagent, nital, and Keller's reagent, respectively.

Results and Discussion

Microstructure

The laser-melted surfaces were shiny and full of striations and ripples. There was neither cracking nor coating segmentation apparent on these surfaces. The cross sections of the coated specimens before and after laser treatment are shown in Figs. 1 to 4. Prior to laser treatment, the coatings exhibited a lamellar structure that resulted from the detonation gun-spraying process. There is a distinct boundary between the coating and the substrate with no indication of diffusion between the two from detonation gun spraying.

In the case of the 1044 steel substrate specimens (Figs. 1 and 2), neither the lower part of the coating nor the substrate was affected by laser surface-melting. The laser treatment affected the coatings to a depth of 175 to 275 μm. The affected layers are full of dispersed pores that start at a small depth below the surface. The lamellar structure of the coating became more iostropic within the affected layer. The carbide size distribution in the laser-melted region of the WT-1 coating is more uniform than that in the as-received specimen (Fig. 5). Such a

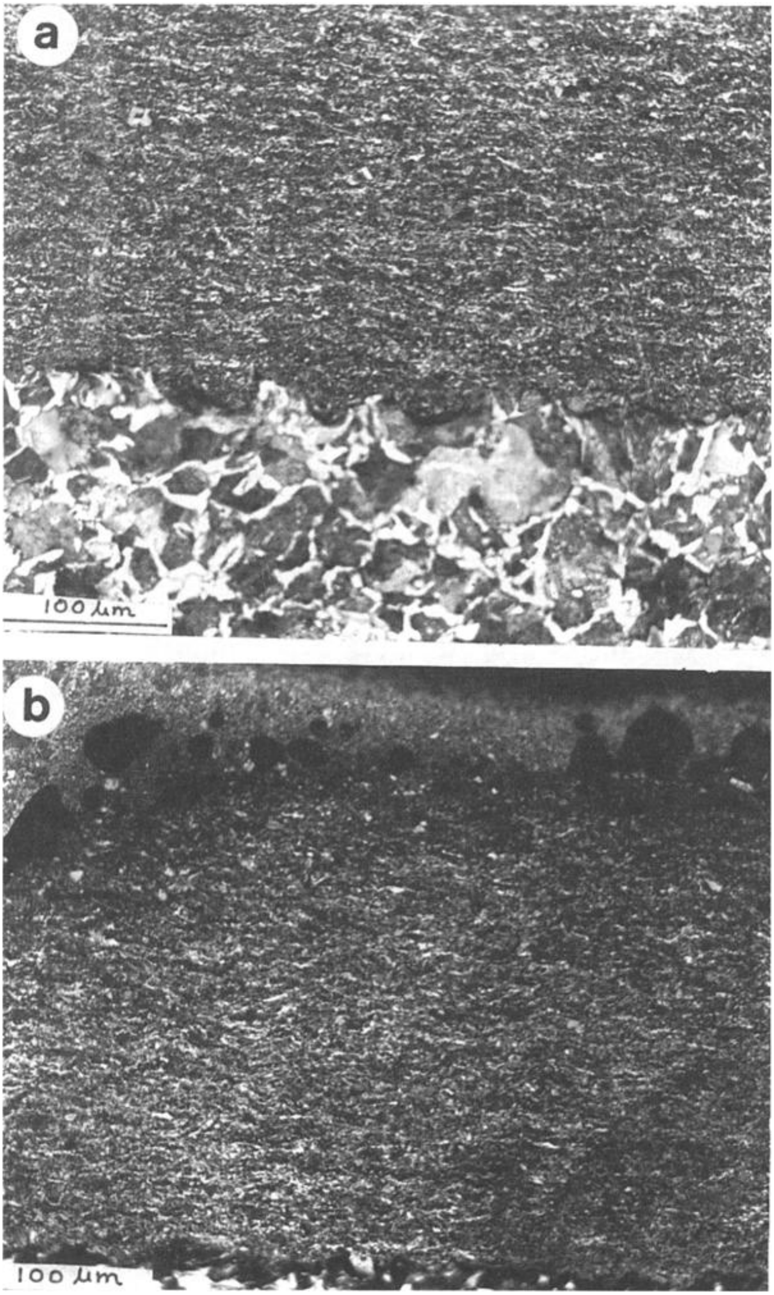

FIG. 1—*Cross sections of the WT-1 coated specimens with the 1044 steel substrate:* (a) *as-received,* (b) *laser surface-melted.*

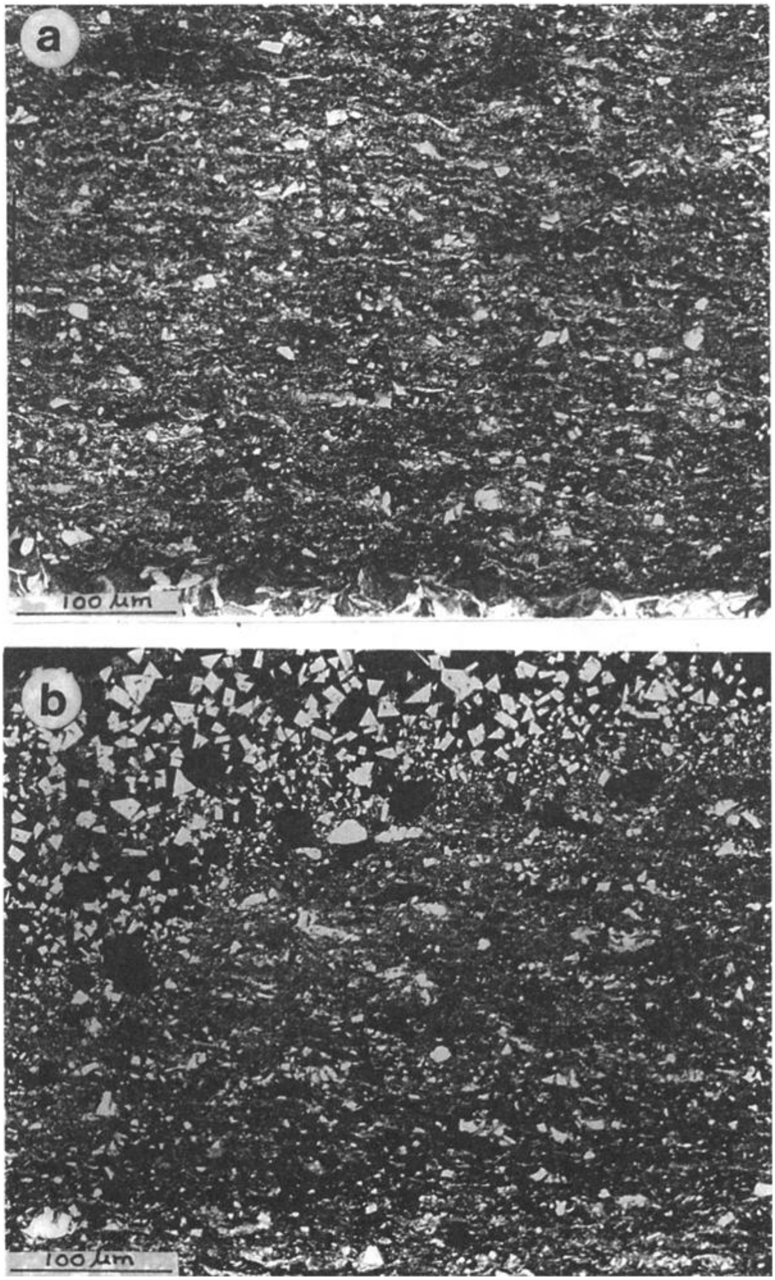

FIG. 2—*Cross sections of the LW-1N40 coated specimens with the 1044 steel substrate:* (a) *as-received and* (b) *laser surface-melted.*

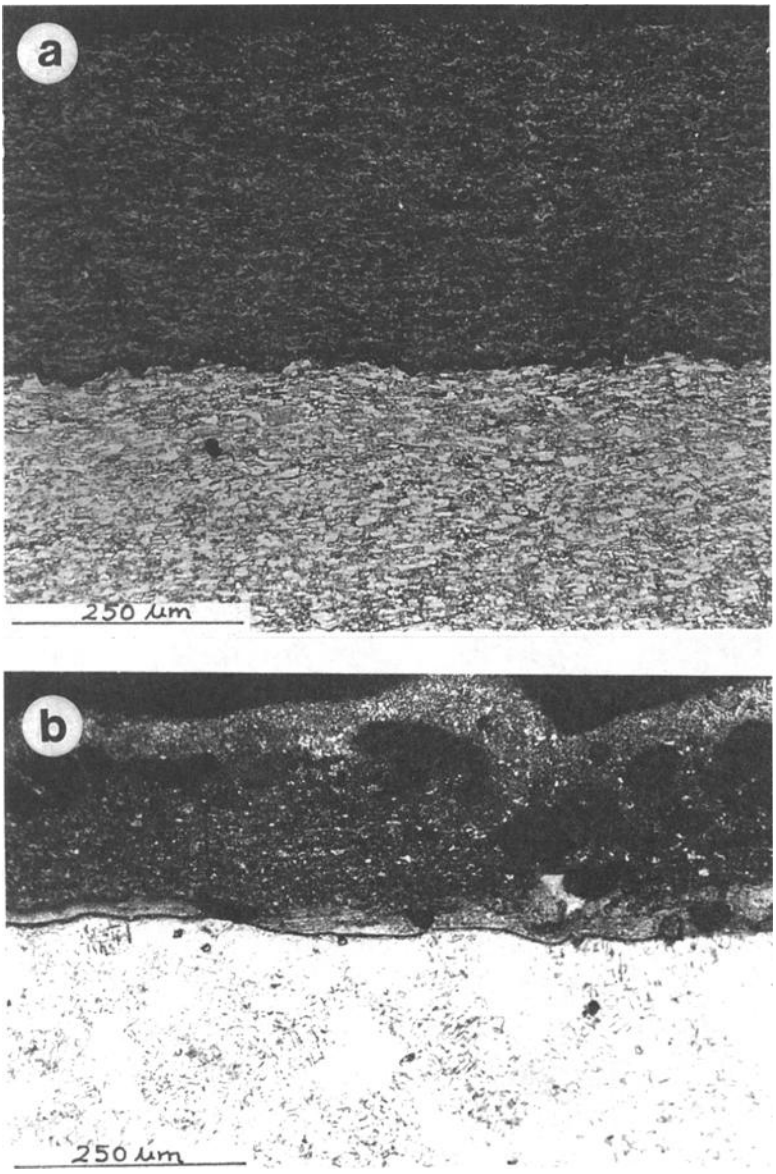

FIG. 3—*Cross sections of WT-1 coated specimens with the Ti-6Al-4V substrate: (*a*) as-received and (*b*) laser surface-melted.*

homogenization has been reported [*6*] to occur because of the dissolution of nonequilibrium complex (W, Ti)C phases in the binder during melting and later the precipitation of equilibrium carbide phases on cooling. The dendritic carbide grains are also seen in this region. Figure 6 shows the laser-melted LW-1N40 coating in which the size of angular tungsten carbide grains

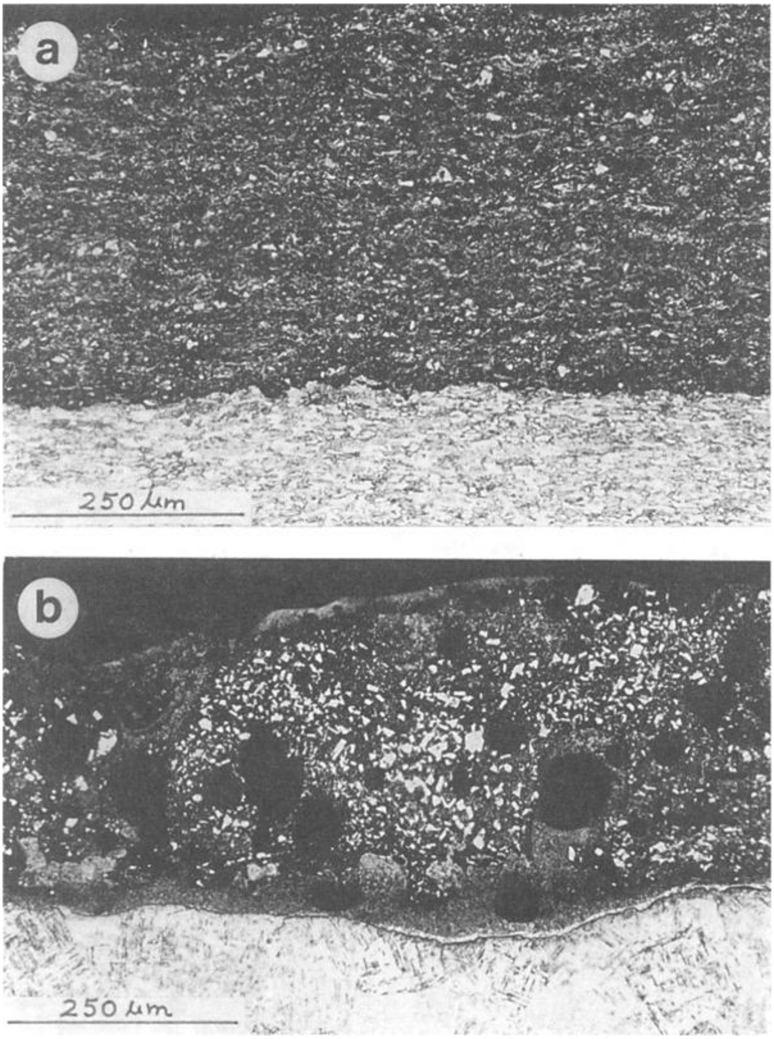

FIG. 4—*Cross sections of the LW-1N40 coated specimens with the Ti-6A1-4V substrate:* (a) *as-received and* (b) *laser surface-melted.*

formed on resolidification is larger than that seen in the untreated coating. It also shows finely dispersed η-carbide precipitates within the binder material. The precipitation occurred because of the supersaturation of tungsten and carbon in the binder as a result of the fast cooling following laser melting [*6,7*].

In the case of specimens with Ti-6A1-4V substrate, laser melting affected both the coatings and the substrate, as seen in Figs. 3*b* and 4*b*. Three regions can be seen here: the coating, the interlayer, and the substrate. The coating is full of dispersed pores that start at a depth of 65 to 70 μm below the surface. The top surface of the WT-1 coating on the Ti-6A1-4V substrate (Fig. 3*b*) exhibits recrystallization and homogenization similar to that observed for this coating

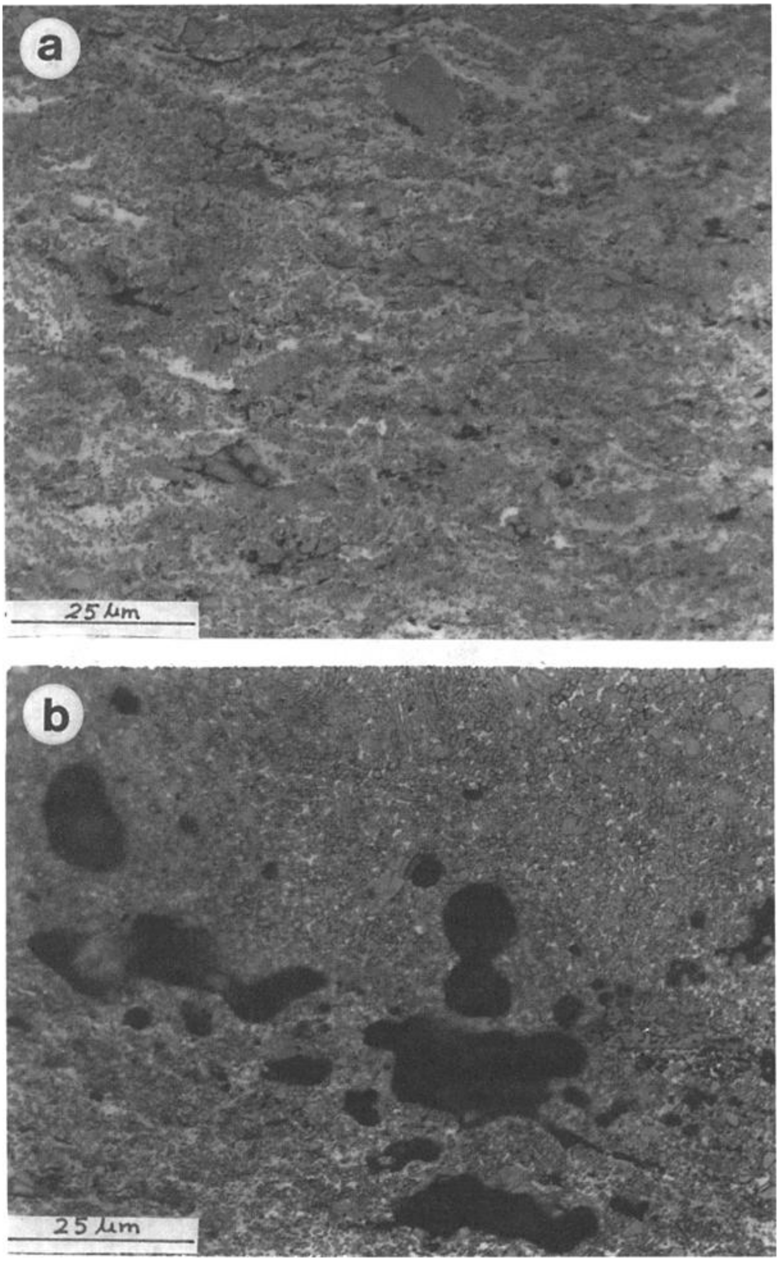

FIG. 5—*Micrographs showing the cross sections of the WT-1 coating on the 1044 steel substrate: a) as-received and (b) laser surface-melted.*

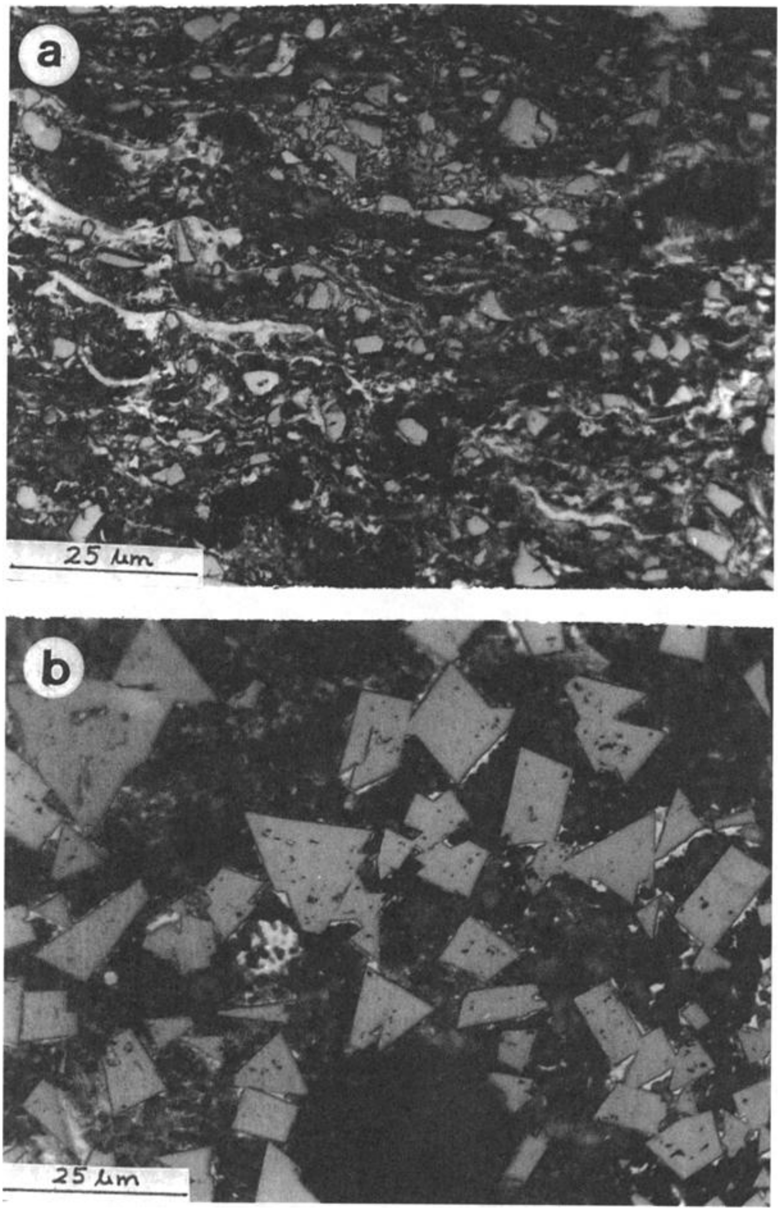

FIG. 6—*Micrographs showing the cross sections of the LW-1N40 coating on the 1044 steel substrate:* (a) *as-received and* (b) *laser surface-melted.*

on the 1044 steel substrate. Beneath this uniform layer are located the pores of different sizes and then the coating with a somewhat reduced lamellar structure, as seen by the comparison between Fig. 3*a* and *b*. The interlayer is less than 25 μm thick, and its structure is produced as a result of diffusion between the coating and the substrate material. There are some pores present in this layer as well.

The substrate microstructure transformed to a α' martensite because of rapid cooling after heating. Figure 4*b* shows the cross section of the laser-melted LW-1N40 coating on the Ti-6Al-4V substrate. The carbide grain growth and η-carbide phase precipitation in the cobalt binder are similar to those described earlier for the LW-1N40 coating on the steel substrate. The dispersed pores, an interlayer, and α' martensite in the substrate were also observed.

Hardness

The microhardness profiles for the as-received coated and laser surface-melted specimens are shown in Figs. 7 to 10. For the WT-1 coating on steel and titanium substrates (Figs. 7 and 8), the surface hardness of the laser-treated specimens is either equal to or lower than that of the original coating hardness. The decrease in hardness in the laser-melted coating region results from excessive porosity in the upper layers. For the LW-1N40 coating (Figs. 9 and 10), the coating hardness increases on laser melting. Since the hardness of the WC-Co alloy decreases with increasing carbide size [*8*], as was also observed in this work, the increased hardness must be due to the precipitation of the fine η-phase in the cobalt binder.

Friction and Wear

Sliding tests were run on the laser-melted surfaces after grinding to a depth of 100 μm followed by polishing, because the melted surfaces were too rough. The wear behavior of the as-received and the laser surface-melted specimens is shown in Figs. 11 and 12. It can be seen that the wear resistance of the WT-1 coating decreases while that of the LW-1N40 coating increases as a result of laser melting and the coefficient of friction increases slightly (Fig. 13).

Since the hardness of the WT-1 coated specimen on the titanium substrate remained the same for laser melting (Fig. 8), the increase in wear rate of the laser-melted WT-1 coatings on both the titanium and steel substrates is attributed to the high porosity produced in the melted regions. Because most of the pores were located at about a 100-μm depth below the laser-treated surface, specimen preparation by grinding virtually exposed these holes to the finished surface that was subjected to sliding wear. For the LW-1N40 coating, the hardness of the laser-treated coating layer was larger than that of the untreated coating (Figs. 9 and 10). The decrease in wear rate from laser treatment is thus attributed to the increased hardness because of η-carbide precipitation in the binder material. There was porosity in this coating too, but the pores were distributed fairly uniformly throughout the thickness, and the surface that resulted after removal of a 100-μm-thick layer from grinding was not affected by porosity as much as the WT-1 coating. The coefficient of friction also increased for laser treatment, possibly because the increased porosity made the surface rougher. Because of this, the deformation component of friction increased.

The wear volumes of the laser-treated blocks and the tool-steel rings are compared in Fig. 14. The ring wear is invariably higher than the block wear and is about the same in all cases. This is so because the carbide coatings are more wear-resistant than the tool steel, as would be expected.

Wear Mechanisms

The wear mechanisms were investigated by examination of the wear surfaces. Figure 15 shows cracks and holes on a laser-treated WT-1 coating surface. Cracks were observed all over the surface as well as material disintegration. The holes presumably resulted from the porosity that developed during laser melting. The cracks seem to have developed as an interconnecting network between the holes, as seen in Fig. 16. Energy-dispersive X-ray analysis (EDXA) indicated the transfer of ring material in the location of the dark spots in Fig. 16. Similar features

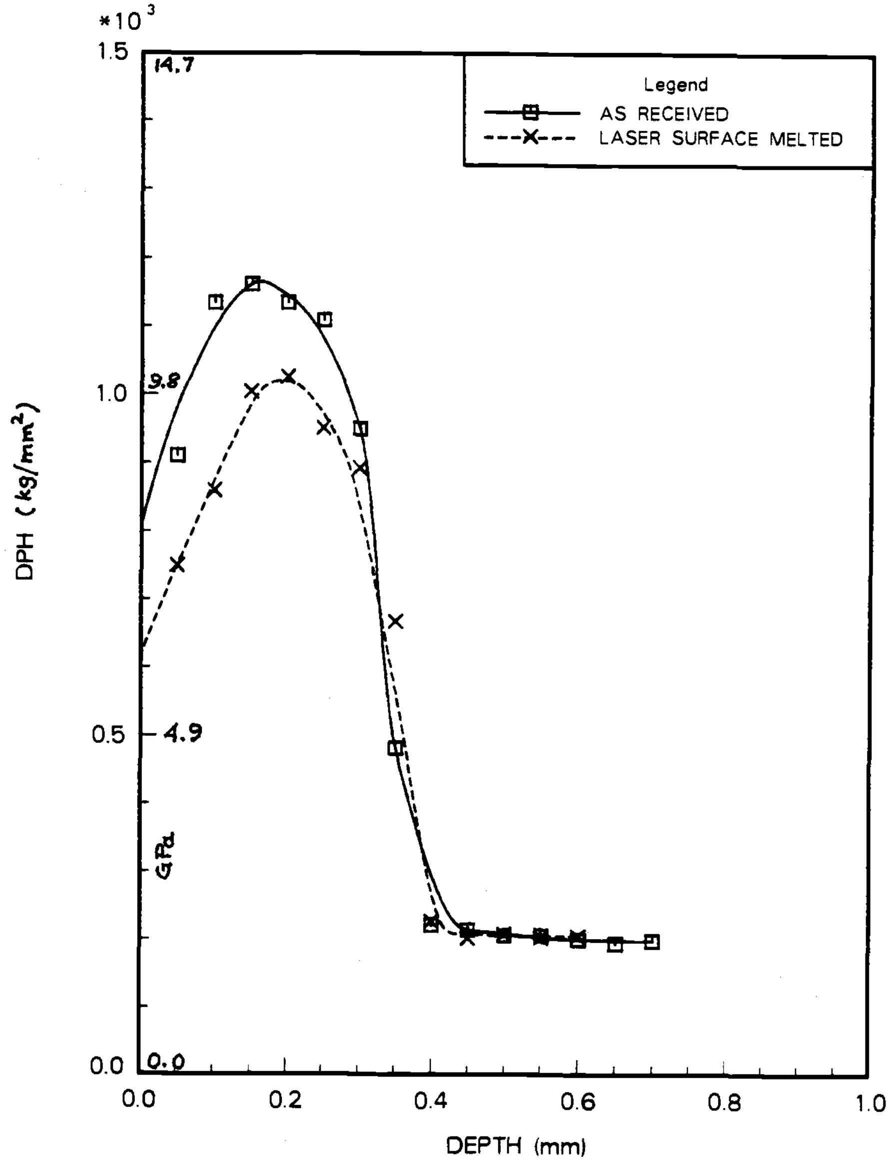

FIG. 7—*Microhardness profiles of the as-received and laser surface-melted WT-1 coated 1044 steel specimens.*

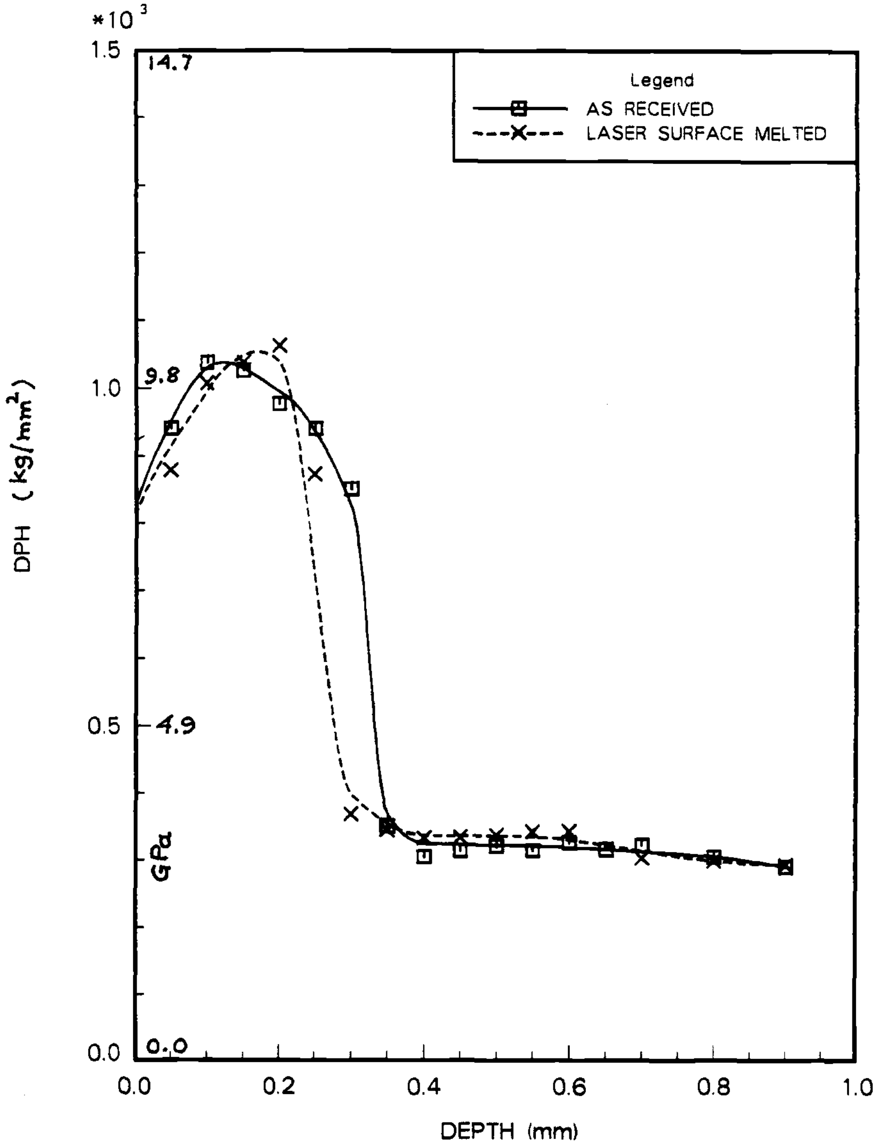

FIG. 8—*Microhardness profiles of the as-received and laser surface-melted WT-1 coated Ti-6Al-4V specimens.*

were also observed on the worn surface of the laser-treated WT-1 coating on the Ti-6Al-4V substrate. From these observations, it was concluded that the wear mechanisms were cracking and material disintegration from the edges of the cracks and holes.

Figure 17 shows the features on the worn surface of the laser-treated LW-1N40 coating on the 1044 steel substrate. The surface exhibits intensive carcking. EDXA of Location A indicated

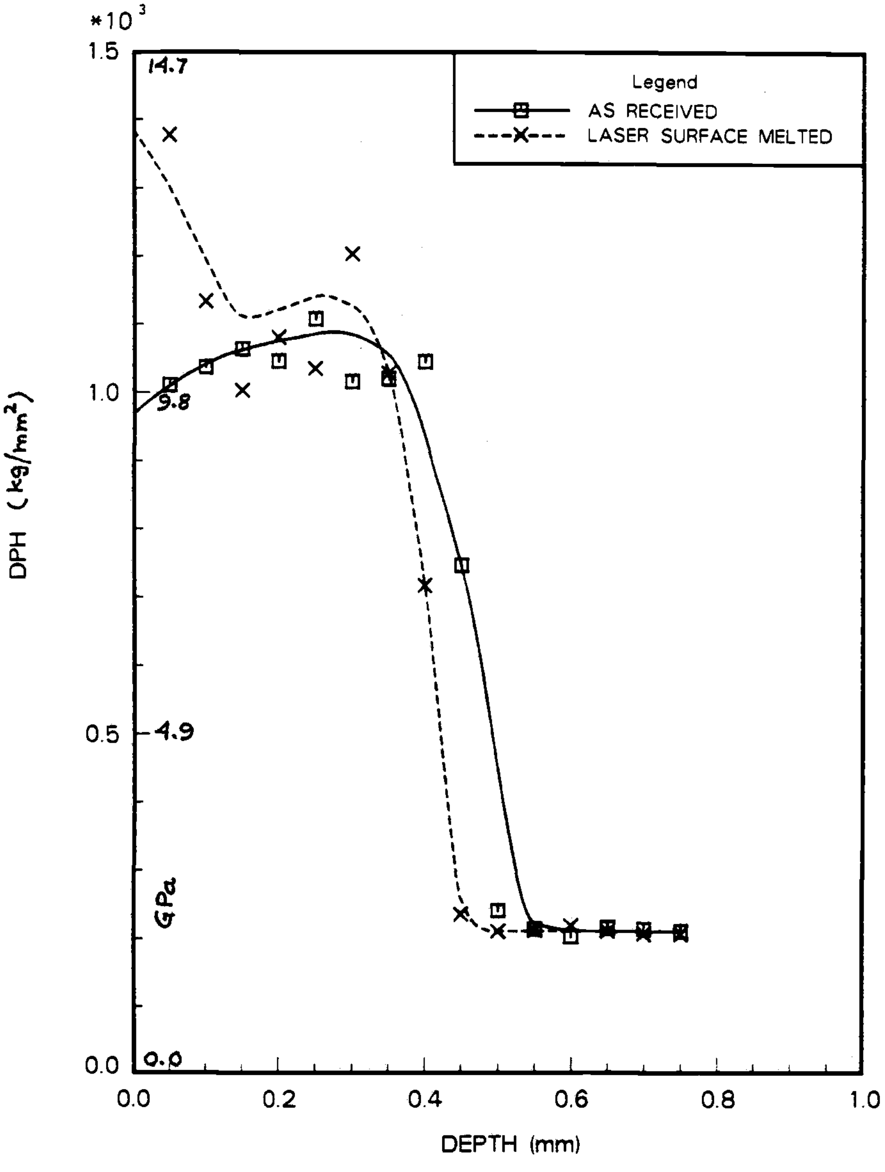

FIG. 9—*Microhardness profiles of the as-received and laser surface-melted LW-1N40 coated steel specimens.*

the presence of tungsten, iron, and oxygen. This led us to conclude that material was transferred from the tool steel ring to the block surface and was oxidized in the process. The transferred material helped in reducing the damage on the block surface during sliding. There is no indication of material disintegration from the crack edges, as was observed for the WT-1 coating.

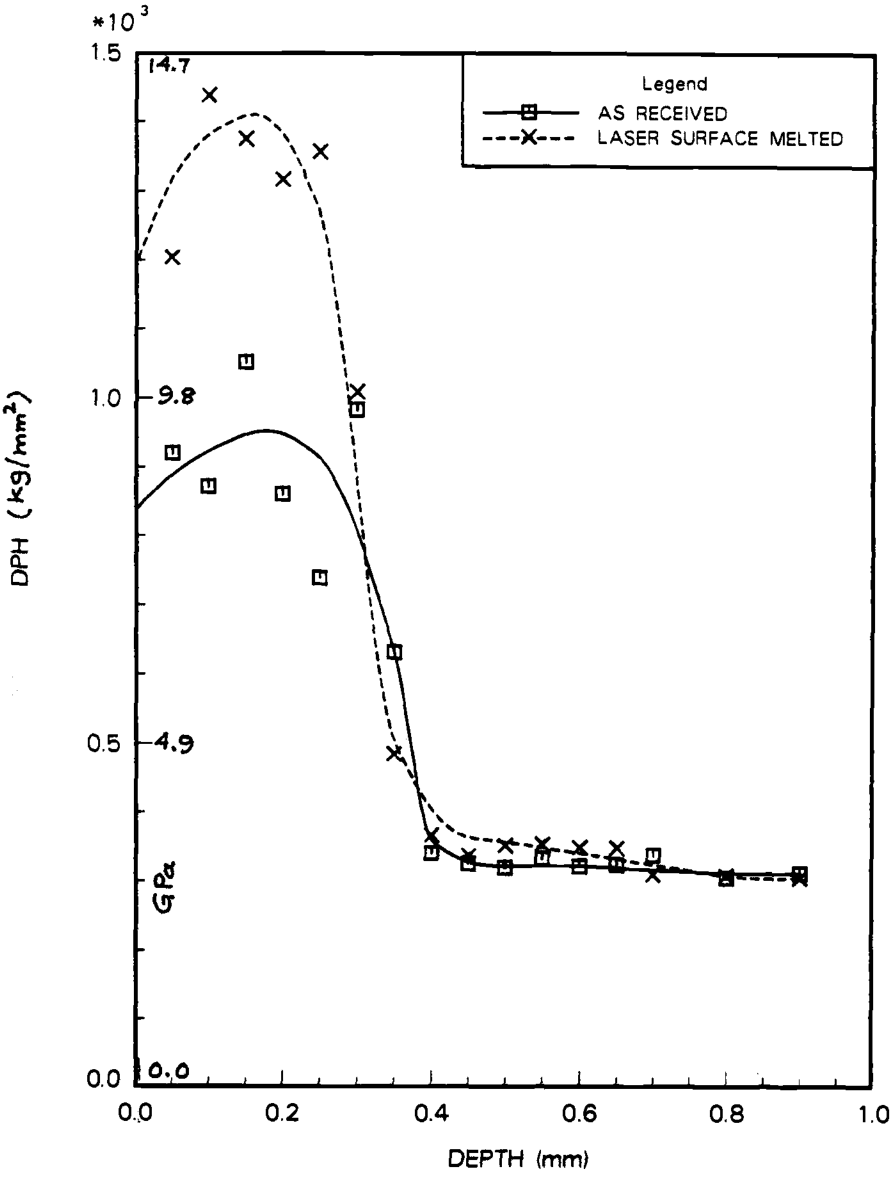

FIG. 10—*Microhardness profiles of the as-received and laser surface-melted LW-1N40 coated Ti-6A1-4V specimens.*

Even though porosity was observed in the laser-treated LW-1N40 coating, no holes can be seen on the worn surface. The holes were probably filled and covered with the material transferred from the mating surface. Similar features were also observed on the worn surface of the laser-treated LW-1N40 coating on the Ti-6A1-4V substrate. Based on these observations, it was

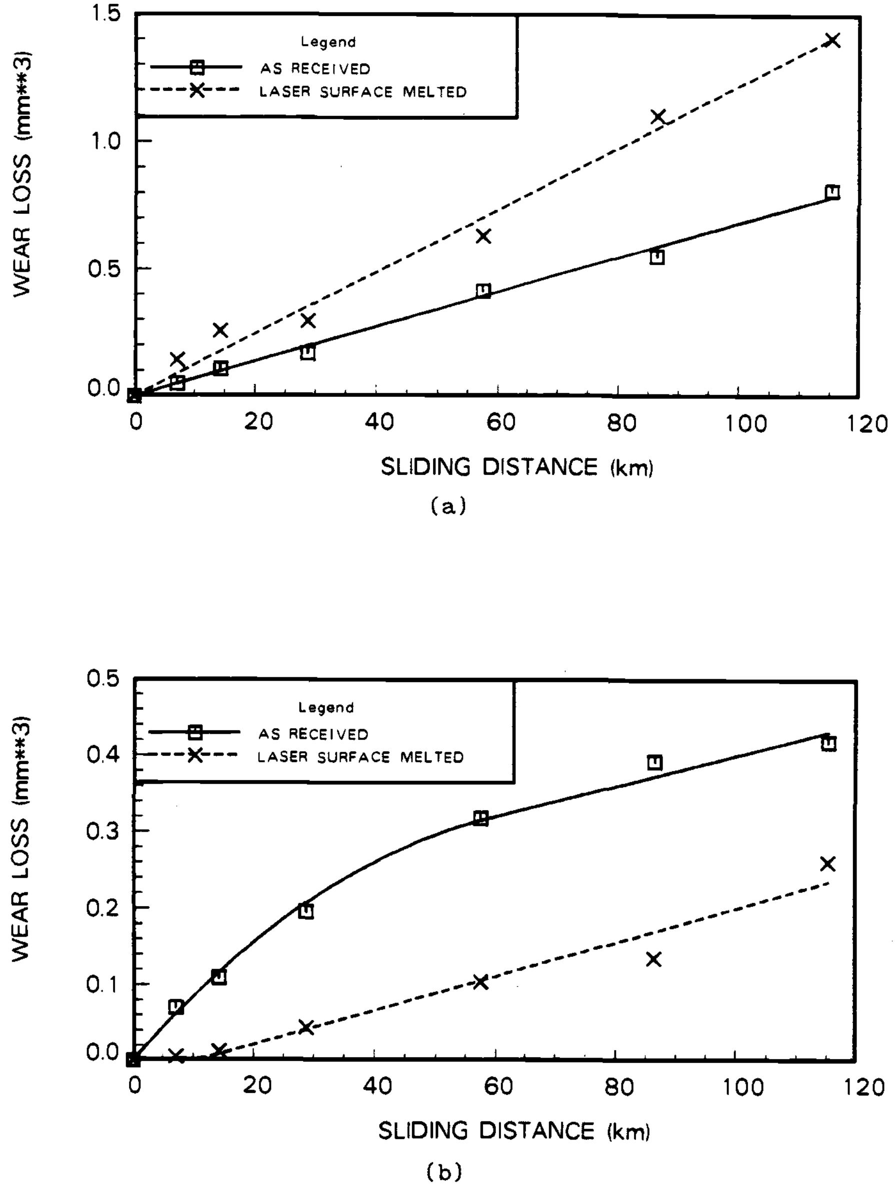

FIG. 11—*Comparison between the wear for the coated steel specimens with and without laser surface-melting:* (a) *WT-1 and* (b) *LW-1N40 (sliding speed = 4 m/s and normal load = 4.9 N).*

concluded that wear of the laser-melted LW-1N40 coating was reduced because of increased hardness, carbide precipitation in the binder material, and protection from material transferred from the ring. Furthermore, the mechanisms of wear were adhesion, cracking, and compaction of the transferred material.

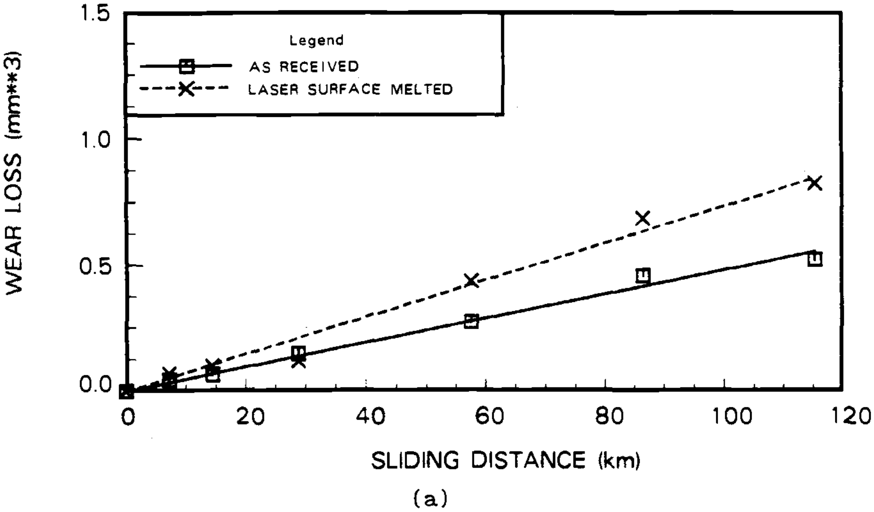

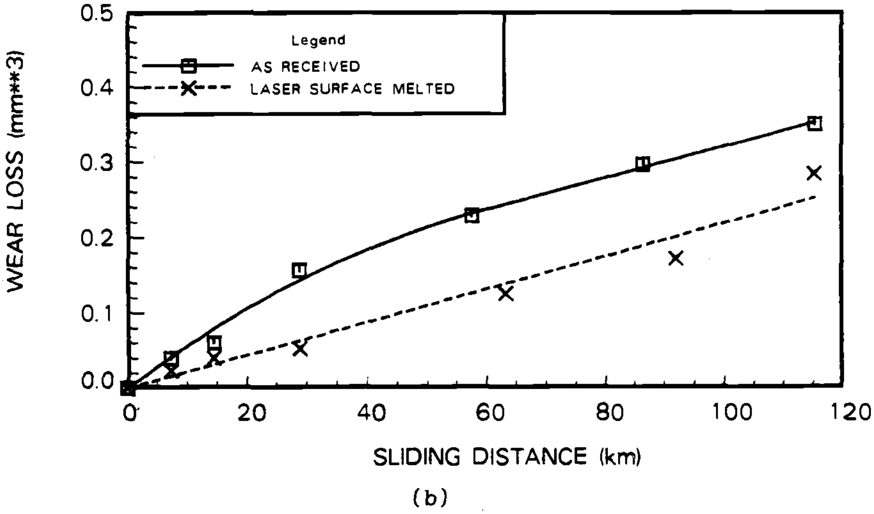

FIG. 12—*Comparison between the wear loss versus sliding distance behaviors for the coated Ti-6Al-4V specimens with and without laser surface-melting:* (a) *WT-1 and* (b) *LW-1N40 (sliding speed = 4 m/s, normal load = 4.9 N).*

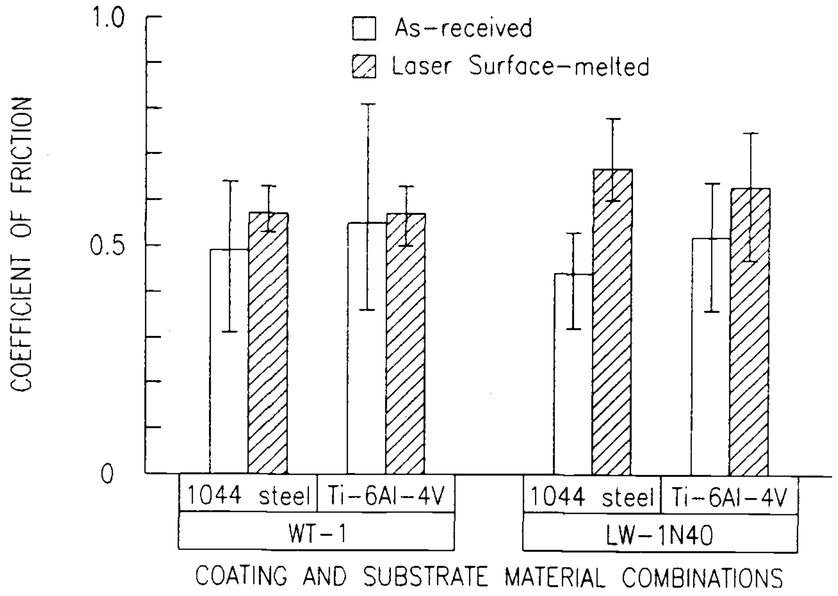

FIG. 13—*Comparison between the coefficients of friction for the as-received and laser-treated specimens.*

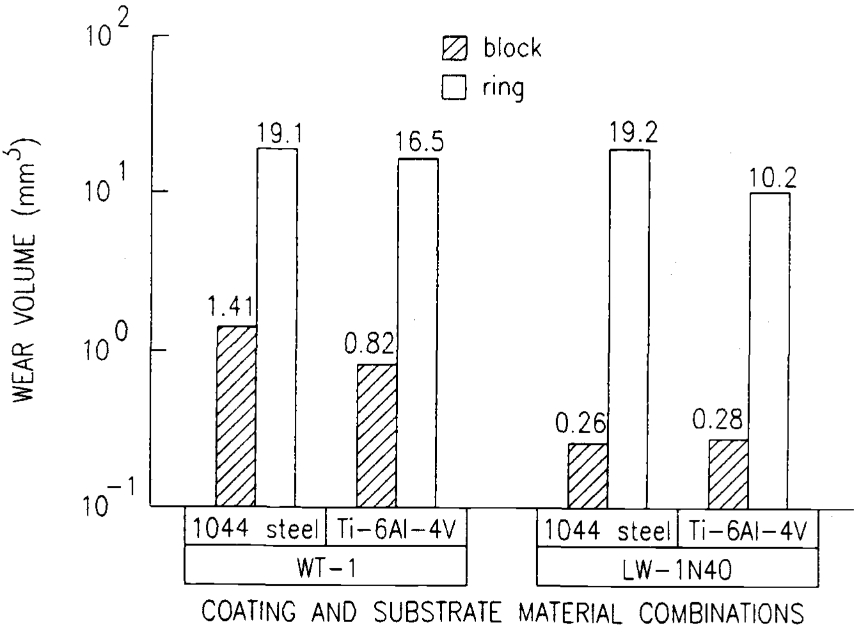

FIG. 14—*Wear volumes of the blocks and rings for a sliding distance of 115.2 km (sliding speed = 4 m/s and normal load = 4.9 N).*

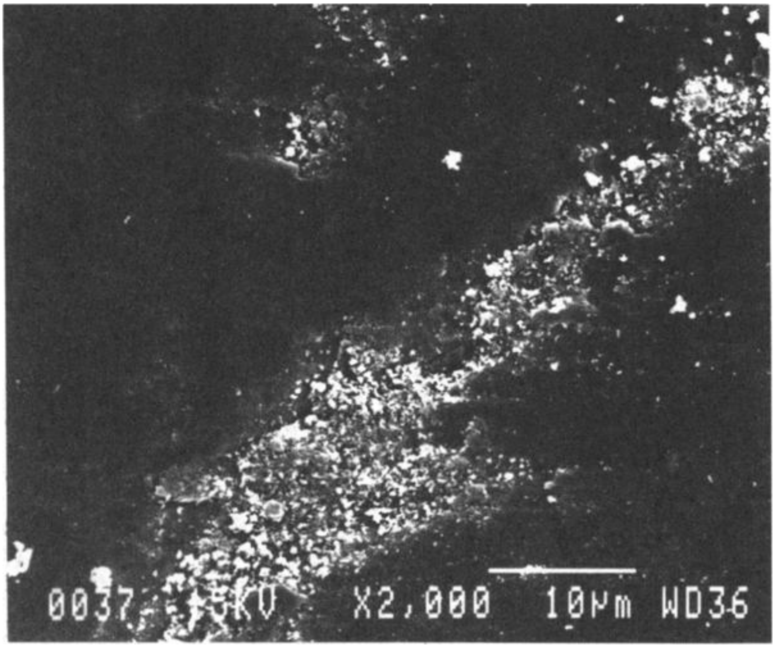

FIG. 15—*SEM micrograph showing the worn surface of the laser-melted WT-1 coating on the 1044 steel substrate (sliding direction of the mating surface is from left to right).*

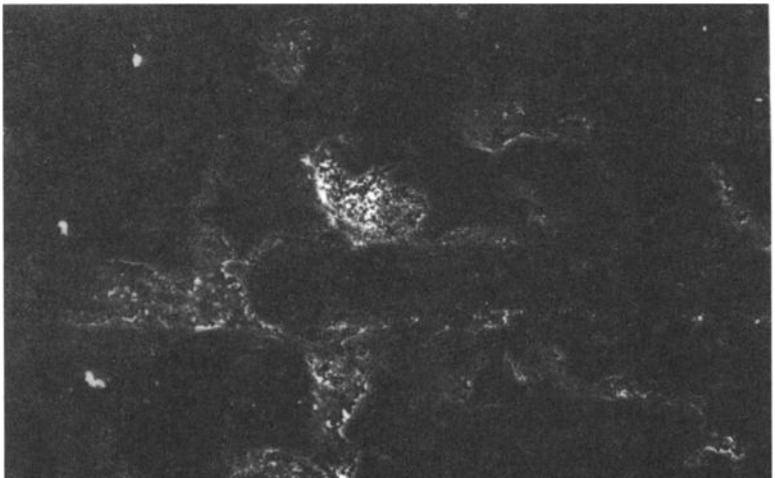

FIG. 16—*SEM micrograph showing the worn surface of the laser-melted WT-1 coating on the 1044 steel substrate (sliding direction of the mating surface is from left to right).*

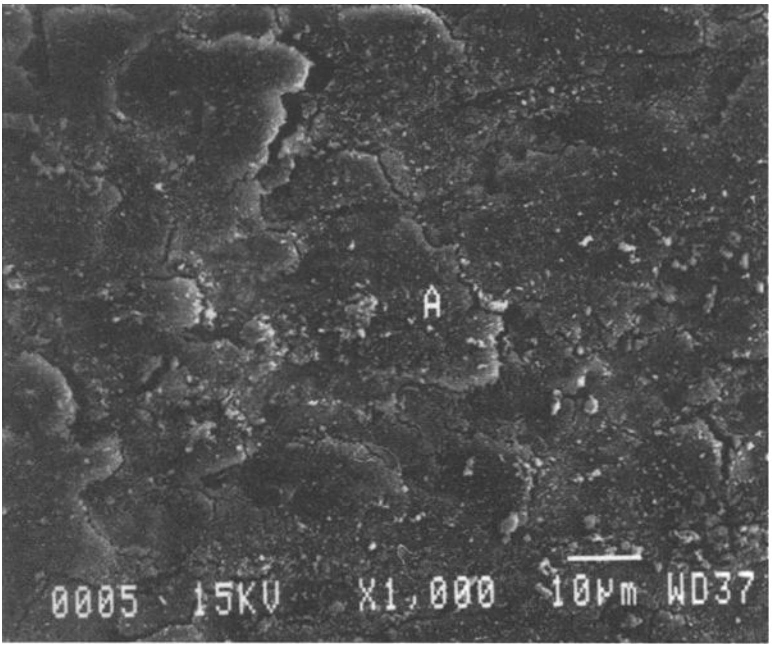

FIG. 17—*SEM micrograph showing the worn surface of the laser-melted LW-1N40 coating on the 1044 steel substrate (sliding direction of the mating surface is from right to left).*

Conclusions

1. Laser surface melting of the carbide coatings on a Ti-6Al-4V substrate resulted in alteration of the lamellar coating structure, the development of an interlayer, the transformation to α' martensite in the near-coating substrate, and the generation of porosity in the melted region. When the substrate was a 1044 steel, neither the development of an interlayer nor martensitic transformation in the substrate microstructure occurred.
2. The hardness of the WT-1 coated surface either decreased or remained unaltered after laser melting while the hardness of the LW-1N40 coated surface increased.
3. As a result of laser treatment, the wear of the WT-1 coated surface increased while that of the LW-1N40 coated surface decreased. The transfer of material from the tool steel ring to the coated surface of the block occurred in both cases.
4. The mechanisms of sliding wear for the laser-treated WT-1 coating were cracking and material disintegration from the edges of the cracks and holes. For the LW-1N40 coating, the mechanisms of wear were adhesion, cracking, and compaction of the transferred material.

Acknowledgments

We would like to thank Dr. M. Naim of the Union Carbide Co. for supplying the specimens with carbide coatings, Prof. P. A. Molian for helping with the laser treatment, and Mr. J. Zhou for the scanning electron microscopy work.

References

[*1*] Ayers, J. D., "Wear Behavior of Carbide-Injected Titanium and Aluminum Alloys," *Wear,* Vol. 97, 1984, pp. 249–266.

[*2*] Iwamoto, N., Umesaki, N., Katayama, Y., and Kuroki, H., "Surface Treatment of Plasma-Sprayed Ceramic Coatings by a Laser Beam," *Surface and Coatings Technology,* Vol. 34, 1988, pp. 59–67.

[*3*] Zaplatynsky, I., "Performance of Laser-Glazed Zirconia Thermal Barrier Coatings in Cyclic Oxidation and Corrosion Burner Rig Tests," *Thin Solid Films,* Vol. 95, 1982, pp. 275–284.

[*4*] Wiiala, U. K., Sulonen, M. S., and Korhonen, A. S., "Laser Hardening of TiN-Coated Steel," *Surface and Coatings Technology,* Vol. 36, 1988, pp. 773–780.

[*5*] Yang, C., "Friction and Wear Behavior of Tungsten and Titanium Carbide Coatings," Masters thesis, Department of Mechanical Engineering, Iowa State University, Ames, 1990.

[*6*] Exner, H. E., "Qualitative and Quantitative Interpretation of Microstructures in Cemented Carbides," *Proceedings,* International Conference on the Science of Hard Materials, 23–28 Aug. 1981, R. K. Viswanadham, D. J. Rowcliffe, and J. Gurland, Eds., Plenum, New York, 1983, pp. 233–259.

[*7*] Lai, H. and Yang, J., "Investigation of Heat Treatment of WC-Co Hardmetals and Transformation Temperature of Cobalt Binder Phase," *Modern Developments in Powder Metallurgy,* Vol. 19, P. U. Gummeson and D. A. Gustafson, Eds., Metal Powder Industries Federation, Princeton, NJ, 1988, pp. 23–29.

[*8*] Exner, H. E. and Gurland, J., "A Review of Parameters Influencing Some Mechanical Properties of Tungsten Carbide-Cobalt Alloys," *Powder Metallurgy,* Vol. 13, 1970, pp. 13–31.

Olof Vingsbo,[1] *Murugu Venkatachalam,*[1] *Martin Sundquist,*[2] *and Kris Schouterden*[3]

Low-Amplitude Fretting of Hard Coatings of TiN, Diamond-Like Carbon, and Polycrystalline Diamond

REFERENCE: Vingsbo, O., Venkatachalam, M., Sundquist, M., and Schouterden, K., **"Low-Amplitude Fretting of Hard Coatings of TiN, Diamond-Like Carbon, and Polycrystalline Diamond,"** *Effect of Surface Coatings and Treatments on Wear, ASTM STP 1278,* S. Bahadur, Ed., American Society for Testing and Materials, 1996, pp. 54–75.

ABSTRACT: Three different hard surface coatings, that is, TiN, so-called diamond-like carbon (DLC) on steel substrates, and polycrystalline diamond on cemented carbide substrates, have been tested and compared under conditions of low-amplitude fretting. The displacement amplitudes were chosen to cover the partial slip regime and the lower part of the gross slip regime, with some emphasis on identifying the critical conditions for incipient gross slip (IGS). A giant-magnetostrictive actuator has been used, allowing extremely well-controlled testing conditions, typical of the partial-slip fretting regime. The relative displacement between the vibrating specimens was measured with an optical technique, capable of a resolution of 2 nm. The displacement and the tangential forces active in the contact surface were recorded as functions of time. Based on these data, post-experiment off-line computation was used for identifying IGS parameter values. Two- and three-dimensional fretting maps were constructed. The fretting scar morphology was studied by scanning electron microscopy. Fretting mechanisms were clarified by comparisons between the recorded test data and the structural damage revealed by the surface studies.

KEYWORDS: surface coatings, surface treatments, wear testing, fretting, fretting maps, low-amplitude fretting, partial slip, gross slip, incipient gross slip, scanning electron microscopy, scar morphology

Mechanical vibrations can enhance the surface damage of contacting bodies due to oscillatory relative motion in the contact zone. At low displacement amplitudes, this is referred to as "fretting." According to the elastic model for contacting surface elements, suggested by Cattaneo [*1*] and Mindlin [*2*], the size of the contact zone is related to the normal load in the contact and the radii of curvature of the contact elements. Normal contact between engineering surfaces is established at a number (three or more) of contact patches scattered over the nominal contact area. For a sphere-on-flat contact configuration, after the application of a tangential force, f_x, the contact circle of radius, a, is subdivided into a central stick zone of radius, $a' < a$, surrounded by a slip annulus of width, $a\text{-}a'$ (Fig. 1). The radius, a', of the stick zone can be expressed in f_x as

$$a' = a\{1 - f_x/\mu f_z\}^{1/3} \tag{1}$$

---

[1] Professor and graduate student, respectively, Department of Mechanical Engineering, University of Houston, Houston, TX 77204–4792.

[2] Lecturer, University of Karlstad, Department of Technology, S–650 09, Karlstad, Sweden.

[3] Graduate student, Catholic University of Leuven, Department Metaalkunde en Toegepaste Materiaalkunde, B–3001, Leuven, Belgium.

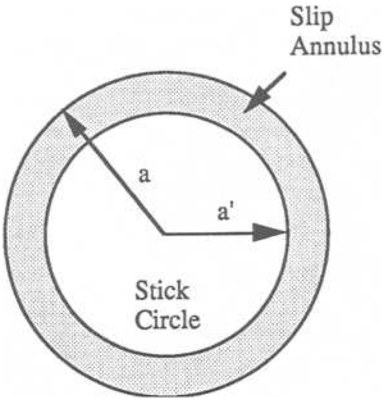

FIG. 1—*Mixed stick-slip contact conditions for circular geometry.*

where f_z is the normal force and μ is the coefficient of friction. If the applied tangential force is a function, $f_x(t)$, of time, t, and oscillates at a frequency, v (see Eq 5), a' will oscillate with the same frequency. These are the contact conditions characteristic of the partial slip regime in fretting. The radius of the stick zone decreases with increasing f_x, and will become zero for forces above a critical value, $f_{x,\mathrm{cr}}$, given by

$$f_{x,\mathrm{cr}} = \mu f_z \tag{2}$$

The vanishing of the stick zone is referred to as incipient gross slip (IGS) and constitutes the transfer from conditions of partial slip to conditions of gross slip. If the amplitude of $f_x(t)$ is higher than the critical value, a' will vanish and gross slip will be reached once per half-cycle.

The mixed stick-slip conditions are characterized by high stress concentrations at the stick-slip boundary [*c*], promoting nucleation and growth of contact fatigue cracks, while the gross slip conditions above IGS will correspond to fretting wear.

Hard surface coatings are widely used for reduction of sliding wear. Recent studies have shown, however, that the damage of TiN coatings under low-frequency fretting conditions can be severe [*4*]. There is a general lack of information about the behavior of hard coatings under fretting conditions, and the present report deals with a study of the fretting properties of a number of hard coatings: TiN, diamond-like carbon (DLC), and polycrystalline diamond. In the characterization of tangential surface vibrations, the type of damage that prevails for a certain vibrational amplitude is often of central interest, and therefore, there is a need for testing within a range that covers the transition from partial to gross slip. The results are summarized and discussed in terms of fretting maps.

Fretting Test Matrix and Fretting Maps

In addition to parameters related to materials and environment, there are five main variables/parameters that control fretting testing. They can be described in a Cartesian system, with the x-y plane in the contact surface, and the x axis in the direction of the applied tangential force. The testing parameters then are: the normal force, f_z; tangential force, f_x; displacement, d; applied frequency, v; and number of cycles, n. These five parameters define the fretting matrix. The characterization of the multi-parameter dependence in the fretting process is complex, and the simulation is generally done with one parameter varied at a time, having all the others fixed.

The determination of the critical IGS parameters for different combinations of testing variables enables the construction of fretting maps, showing the fretting damage regimes, as a function of selected parameters in the fretting matrix. A "fretting map" is any two-dimensional or three-dimensional section through the fretting matrix, with the critical IGS conditions represented by a curve or a surface, separating a regime of partial slip from a regime of gross slip [*5,6*]. Once the relevant fretting maps for a tribosystem are established, in principle, it is possible to control the fretting process by parameter selection to confine the damage characteristics.

Experimental Procedure

Materials

The TiN and DLC coatings were deposited on flat substrates of high-speed tool steel (ASP23) heat treated to HRC 66. The substrates were mechanically polished before deposition. The TiN coating was deposited by a triode ion-plating process to a nominal thickness of 5 μm and a surface roughness 0.045 μm R_a. The DLC coating was deposited to a nominal thickness of 1.6 μm in a radio frequency plasma-assisted chemical vapor disposition (PACVD) system. The diamond coating was deposited on a cemented carbide substrate to a nominal thickness of 1 μm, using the hot-flame method [*7*]. The counter bodies used in the fretting tests were corundum (α-Al_2O_3) spheres of 10-mm diameter.

Equipment and Testing Parameters

The fretting simulator, described in detail elsewhere [*8*], was designed for vibrations of low-amplitude displacements. It consists of a computer-controlled actuator for tangential displacements in the order of 0.1 to 10 μm and 3 kHz frequency response. It can generate and record displacements with a resolution of 2 nm. The actuator is based on a giant-magnetostrictive vibrator rod, the elongation of which can be accurately controlled by an alternating current through a coil, surrounding the rod. The upper limit of the displacement amplitude depends on the applied normal load and frequency. Frequency and displacement amplitude can be varied independently in the simulator.

The specimen configuration is a vibrating alumina sphere (the "vibrating specimen") pressed against a flat, coated specimen (the "stationary" specimen) by a normal force applied as a dead weight by a lever system. The tangential displacements of both the vibrating and the stationary specimens are recorded by two optical probes, measuring variations in the intensity of light reflected against polished parts of the specimen surfaces. The normal and tangential forces are recorded by a piezoelectric strain gage situated in the stationary specimen holder.

The mechanical system, designed to support the machine elements and to transfer loads, is optimized to reduce all system-induced vibrations of the stationary specimen, and particularly to minimize resonances at frequencies close to the externally applied testing frequency, υ. Nevertheless, the fretting contact itself will necessarily generate vibrations of the applied frequency, υ. These effects, however, are eliminated by recording the difference between the two displacement signals, representing the true relative specimen-to-specimen displacement. It is of vital importance to measure the "relative" displacement in the case of low-amplitude fretting, since the test-induced vibrations can have amplitudes of the same order as that of the vibrating specimen.

The five active input/output variables of the simulator are as follows:

The Applied Frequency, υ—The applied frequency, ν, is a pre-set constant for each test run, and is an input to the simulator. However, machine-induced vibrations of other frequencies may occur.

The Number of Applied Cycles n—During a test, the number of applied cycles, n, is proportional to the time, t, according to

$$n = v \cdot t \tag{3}$$

where t is the independent variable in all recordings.

The Normal Force, f_z—The normal force, f_z, although generally considered equal to the constant, externally applied dead weight, is a function of time according to

$$f_z(t) = L + g(t) \tag{4}$$

where L represents the dead weight, and $g(t)$ represents induced vibrations of frequency, v, from the applied tangential force, f_x, and of other frequencies from stick-slip phenomena in the test zone and from remaining machine-induced vibrations.

The Tangential Force, f_x, *and Displacement*—The tangential force, f_x, and displacement, d, are the recorded raw data in the experiments. They have sinusoidal components

$$f_x(t) = F_x \cdot \sin\omega t \qquad (\omega = 2\pi v) \tag{5}$$

$$d(t) = D \cdot \sin(\omega t + \Phi) \qquad (\Phi = \text{phase difference}) \tag{6}$$

with amplitudes F_x and D. Both are controlled by the actuator coil current of the vibrator. The analogue $f_x(t)$ and $d(t)$ signals are filtered and recorded as digital storage for post-experiment off-line analysis.

Testing

It is obvious from the preceding review of the five-dimensional test space that the measurables in the present type of testing are the forces and the relative displacement, and all experimental information is, in fact, contained in the recorded and stored $f_z(t)$, $f_x(t)$, and $d(t)$ curves. Other types of information must be retrieved by post-experiment, off-line computer calculations from the recorded data. Therefore, the experiments must be so designed that the relevant changes in the recorded variables, which are strongly interrelated, really are covered within the experimental ranges.

The basic IGS criterion is that the transition from partial slip to gross slip implies a corresponding drop in friction coefficient from the (higher) static value to the (lower) kinetic value. This should be detectable by comparing the successive and interrelated development of the tangential force, F_x, and displacement, D, amplitudes, respectively, during an experiment with gradually increasing D. In order to make sure that IGS criteria could be identified off-line, the following experimental procedure was chosen.

For each constant pre-set pair of L and v, a series of programmed tests were carried out, starting with a low-displacement amplitude, set to be safely below the critical value, D_{cr}. The amplitude was then increased incrementally, and the experiment was continued to a displacement amplitude, D_{max}, set to be safely above D_{cr}, or until the maximum coil current was reached. The frequency was varied from 70 to 3000 Hz, and four different normal loads at 2.8, 4.3, 5.7, and 8.7 N were maintained. Each experiment was repeated from four to ten times to obtain statistical significance in critical parameters. The same series of tests was then repeated for each coating. All tests were performed in air of ambient pressure, a temperature of 25°C, and a relative humidity of 60%.

On-Line Measurements

The basic raw data measured and recorded are the $f_x(t)$ and $d(t)$ curves. The measurement is continuous, but the recording is intermittent due to the memory constraints of the controller. Examples of typical $d(t)$ and $f_x(t)$ curves are given in Figs. 2 and 3. The $d(t)$ curves generally have a nearly undistorted sinusoidal shape, whereas the $f_x(t)$ curves may display a variety of distortions. However, the amplitudes can always be retrieved from the stored data.

Because of the interest in the transition from partial slip to gross slip, that is, the critical IGS parameter values, the amplitudes of the force and displacement signals were recorded over the whole span of the experiment at known intervals. In the beginning of an experimental run, the time between recording of signals was kept short to allow for observation of changes in the contact area, whereas later in the experiment a longer time interval could be used without losing information about onset of IGS, etc.

Off-Line Analysis

The critical parameters can be deduced by retrieving the F_x and D amplitude values, and plotting their development during a test. Once the critical parameter values were calculated for the fretting matrix, fretting maps were constructed as a function of frequency, v, and normal load, L.

As *ex situ* characterization, scar morphology studies were done with light optical microscopy and scanning electron microscopy. The DLC coatings were gold plated for scanning electron microscopy (SEM) studies to avoid charging.

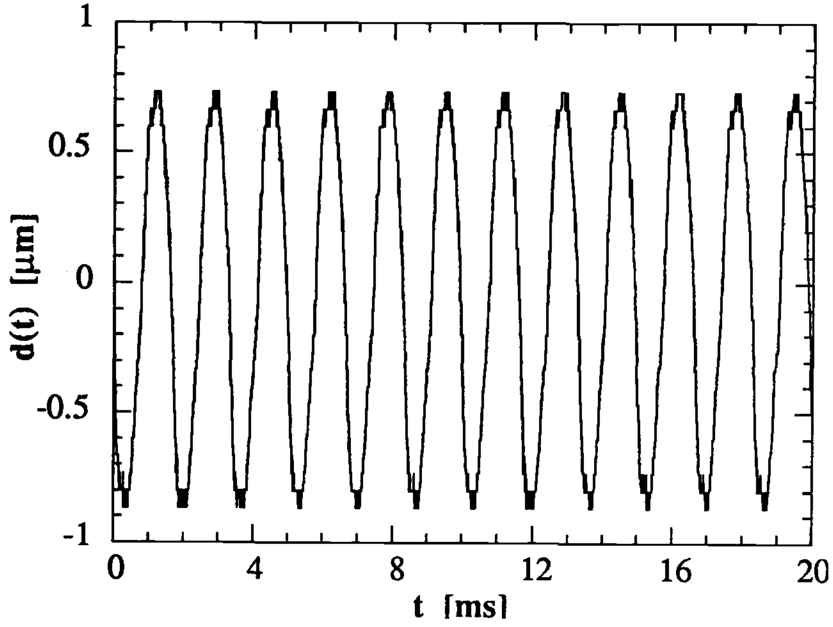

FIG. 2—*Example of* d(t) *curve for TiN coating, in partial slip conditions, after 2.3 × 10^5 cycles; v = 600 Hz and* L *= 8.7 N.*

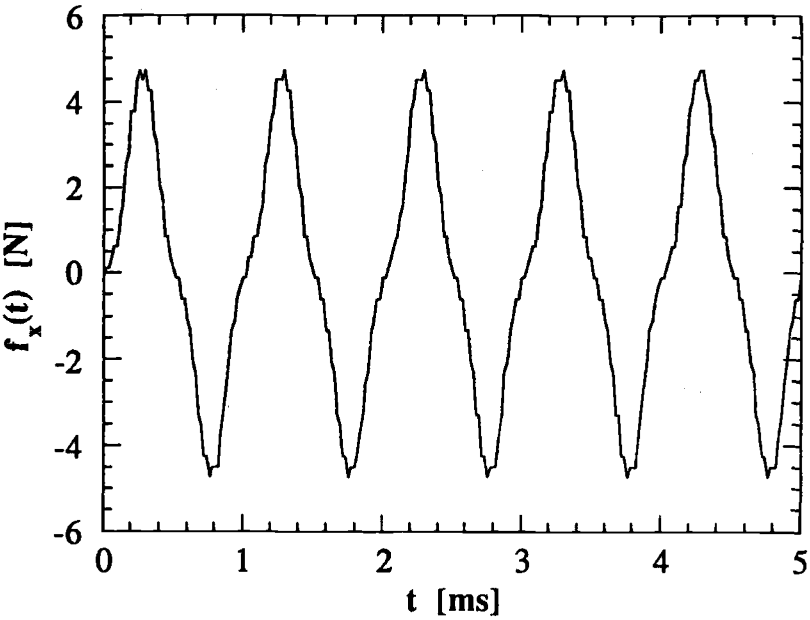

FIG. 3—*Example of* $f_x(t)$ *curve for DLC coating, in partial slip conditions, after 2.1* × 10^5 *cycles;* υ = *1 kHz and* L = *8.7 N.*

Results

IGS Criteria

The reduction in friction coefficient for a continuously increasing actuator coil current is revealed as follows. At the beginning of the test run, both the F_x and D amplitudes will increase with coil current amplitude. When IGS conditions are reached, F_x will approach a constant value or decrease more or less abruptly, while D continues to increase. Two different data representations can be used to visualize this F_x-D interrelationship: $F_x(n)$ - $D(n)$ amplitude co-plots, and $F_x(D)$ plots.

$F_x(n)$ *and* D(n) *Co-Plots*

Figure 4 shows a typical amplitude co-plot of F_x and D versus number of cycles, n, for a TiN specimen fretted with 8.7 N applied normal load and a frequency of 600 Hz. It can be seen that the force amplitude (dashed curve) increases with the coil current until it reaches a peak value of 10.1 N after about 435 000 cycles. At that point, the displacement amplitude (full curve) reached 1.9 μm, and continued to increase, whereas the force curve becomes increasingly scattered after a steep drop. Thus, the critical IGS coordinates are $F_{x,cr}$ = 10.1 N and D_{cr} = 1.9 μm.

Because the applied amplitudes were gradually increased during the experiment, this type of figure also, implicitly, contains information about the influence of the increasing number of

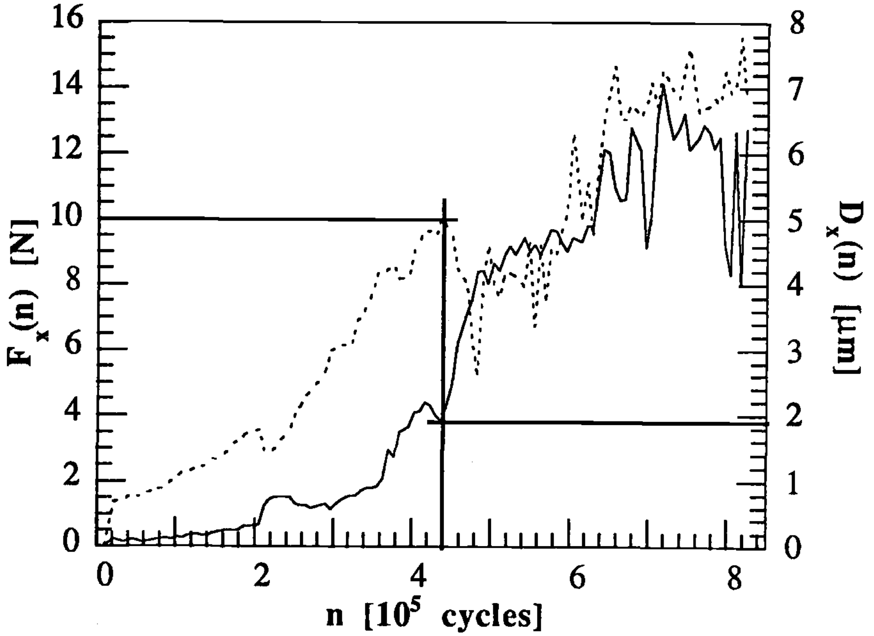

FIG. 4—*Example of* $F_x(n)$-$D(n)$ *amplitude co-plot for TiN coating;* ν = *600 Hz and* L = *8.7 N.*

cycles, *n*. It is seen in Fig. 4 that both curves become more and more irregular and display strong serrations after 435 000 cycles. This reflects the fact that, after IGS is reached, the transition of mechanism from predominantly contact fatigue to fretting wear will generate a gradual degradation to a rougher topography of the contact surfaces.

$F_x(D)$ *Plots*

Figure 5 is based on the same data points as Fig. 4, but plotted as an F_x versus D diagram. The critical IGS coordinates correspond to the commencement of a plateau in the $F_x(D)$ curve, as indicated in the figure. The increasing fretting wear for displacements above IGS gives rise to the increasing scatter of the data points. It should be pointed out, though, that the D axis does not correspond directly to the n axis of Fig. 4. A later cycle may incidentally have a smaller displacement amplitude than an earlier cycle, and the interpretation has to be performed with some care.

The $F_x(n)$ - $D(n)$ amplitude co-plots and $F_x(D)$ plots for the DLC coatings have essentially the same features as those of the TiN coatings.

Figures 6 and 7 show critical parameter diagrams for the diamond coating, tested at a normal load of 8.7 N, and at an applied frequency of 200 Hz. In this case IGS is reached around 55 000 cycles from the start, and F_x then stays constant for another 50 000 cycles. After 100 000 cycles, however, unlike the case of the previous coatings, F_x begins a second period of increase. This is probably due to an increase in contact area, caused by wear of the corundum sphere, as verified by SEM studies. The critical IGS coordinates are $F_{x,\mathrm{cr}}$ = 1.6 N and D_{cr} = 0.5 μm, obtained using both Figs. 6 and 7.

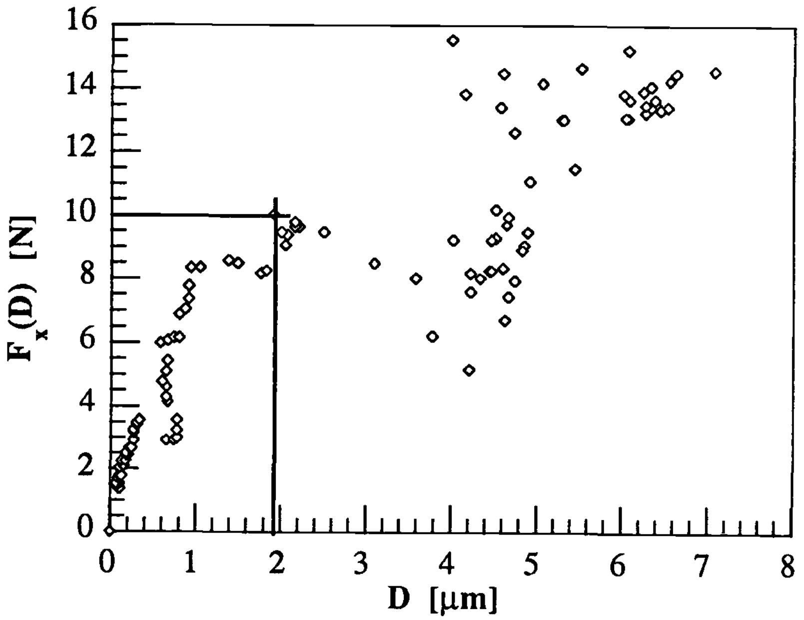

FIG. 5—*Example of* $F_x(D)$ *plot, for TiN coating;* $\upsilon = 600$ *Hz and* $L = 8.7$ *N.*

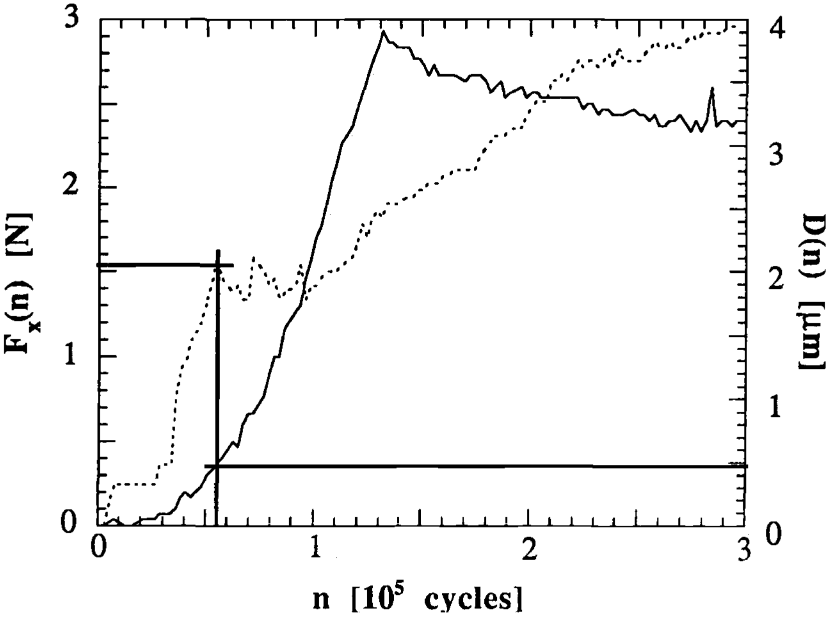

FIG. 6—*Example of* $F_x(n)$-$D(n)$ *amplitude co-plot, for diamond coating;* $\upsilon = 200$ *Hz and* $L = 8.7$ *N.*

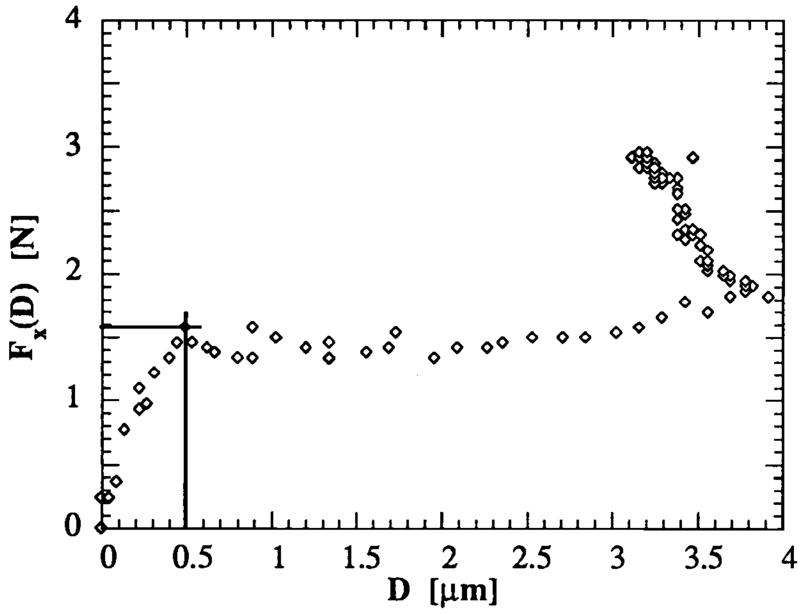

FIG. 7—*Example of* $F_x(D)$ *plot, for diamond coating;* $v = 200$ *Hz and* L $= 8.7$ *N.*

Scanning Electron Microscopy

The aim of the scar morphology studies is to clarify the relationships between the properties of the coating material and its response to the vibrating contact in terms of the mechanisms of surface damage. Three SEM micrographs of scars from the DLC coating have been selected to demonstrate the influence of fretting regime on surface damage characteristics. Figure 8 represents a very low displacement amplitude, with stick conditions prevailing over the whole contact zone (essentially no slip annulus). It can be seen that the vibrations have had a smoothing effect on the coating, removing the "blistered" morphology of the unfretted background surface, probably by plastic deformation. Figure 9 represents the partial slip regime, close to the regime boundary. The coating has cracked and is being broken up. Some debris remain in the contact zone. The effect of gross slip, finally, is shown in Fig. 10. The coating is worn to a crater, at the center of which, where the contact pressure is highest, the substrate has been uncovered and subjected to substantial fretting wear.

Fretting Maps

The applied vibration frequency, v, was varied in steps from 70 to 3000 Hz. For each material, the critical amplitudes for IGS, determined using both types of diagrams (Figs. 4 or 5), can be summarized as functions of frequency in $F_x(v)$ and $D(v)$ two-dimensional fretting maps (for constant applied normal load). Based on the definition of IGS, this type of fretting map shows the extension of the two fretting regimes, with the IGS curve representing the regime boundary between partial slip (below) and gross slip (above). The resulting maps are reproduced in Figs 11 through 14 for the TiN coatings, and Figs. 15 through 18 for the DLC coating. Each figure represents one normal load and displays a pair of $D(v)$ and $F_x(v)$ maps. A map is generally based on ten tests for each frequency, the scatter being indicated by maximum and minimum values (dashed curves), surrounding the mean value (full curve).

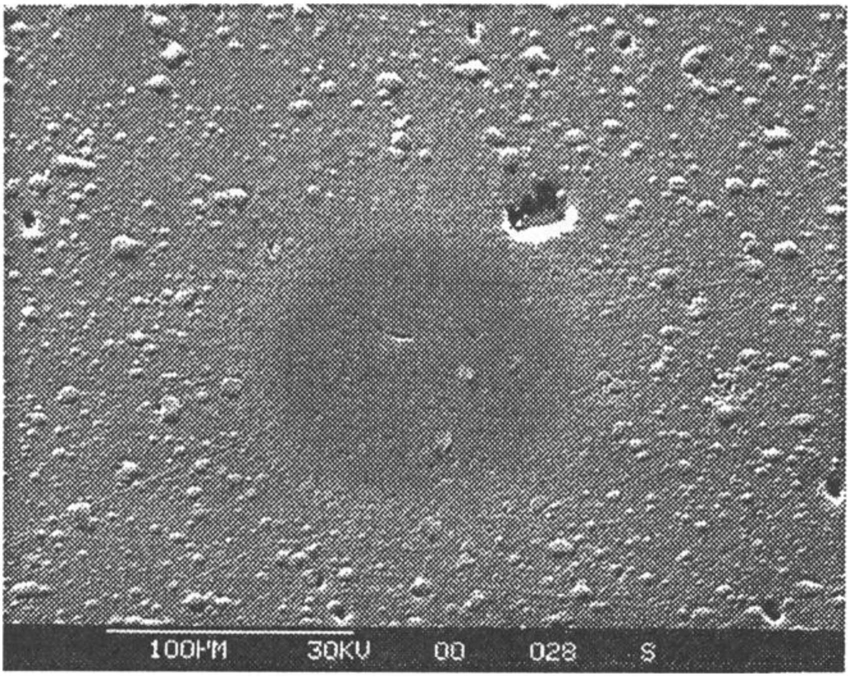

FIG. 8—*SEM micrograph of DLC coating under stick conditions;* $\nu = 1500$ *Hz and* $L = 2.8$ *N.*

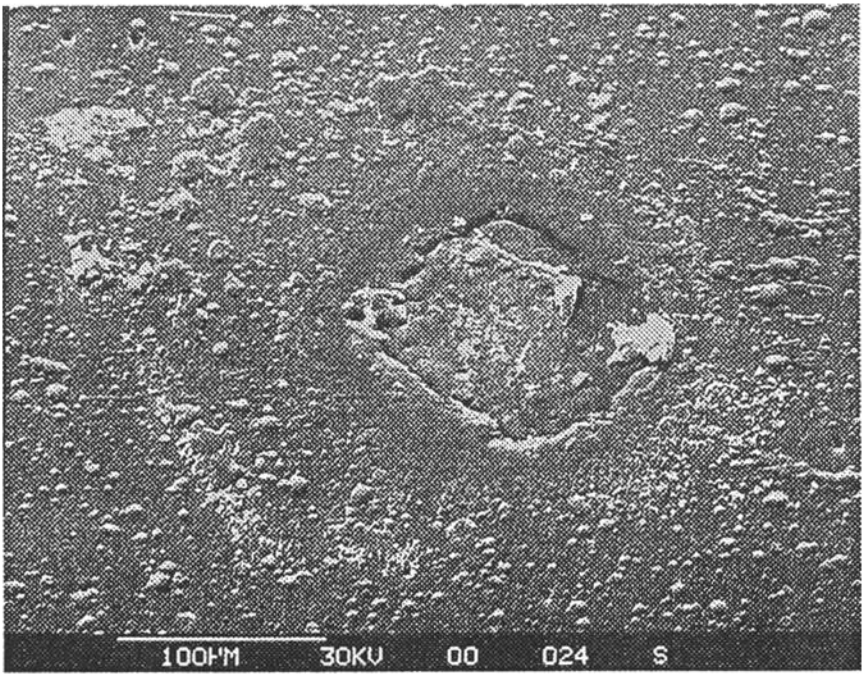

FIG. 9—*SEM micrograph of DLC coating, partial slip regime;* $\nu = 200$ *Hz and* $L = 8.7$ *N.*

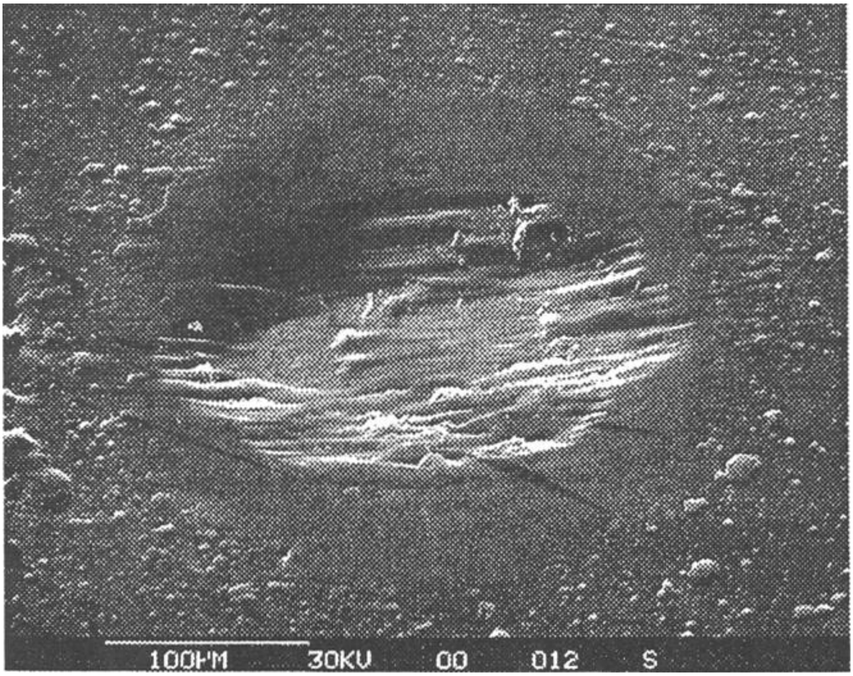

FIG. 10—*SEM micrograph of DLC coating, gross slip regime;* $\nu = 200$ *Hz and* $L = 8.7$ *N.*

The investigation of the diamond coatings is in an early stage. The scatter of the results is not yet statistically verified, and only mean value regime boundary curves are given. The result is presented as three-dimensional fretting maps (Figs. 19 and 20), in which the regime boundary is a surface in the $F_x(v,L)$ or $D(v,L)$ space. Thus, each map represents all four normal loads, L, as well as all the applied frequencies.

Discussion

Equation 1 is based on an elliptic stress distribution under elastic conditions, as assumed by the Cattaneo-Mindlin model [*1–3*]. However, on a microscale, the yield stress—and often also the fracture stress—is exceeded in asperity contact bridges. Plastic deformation will also occur on a macroscale in practice in fretting, since the bulk yield stress is lowered by the simultaneous action of both normal and tangential applied stresses [*9*]. A further weakness of the elastic model is that it only describes homogeneous bodies and, thus, does not consider the departure from Hertzian stress distribution in layered structures [*10*]. Nevertheless, the model is an excellent tool for understanding the mechanics of fretting, and also works well for semi-quantitative relationships between damage mechanisms and materials parameters. In the present project, it forms the basis for working out fretting maps.

The ultimate scope for developing fretting maps is to make them available, via data bases, to designers of machines or other tribo systems. Their primary application will be to provide data, already at the design level, for control of the fretting damage with respect to the predominant fretting process to be expected: fretting wear or contact fatigue.

In addition to this engineering goal, fretting maps also provide a background for gaining

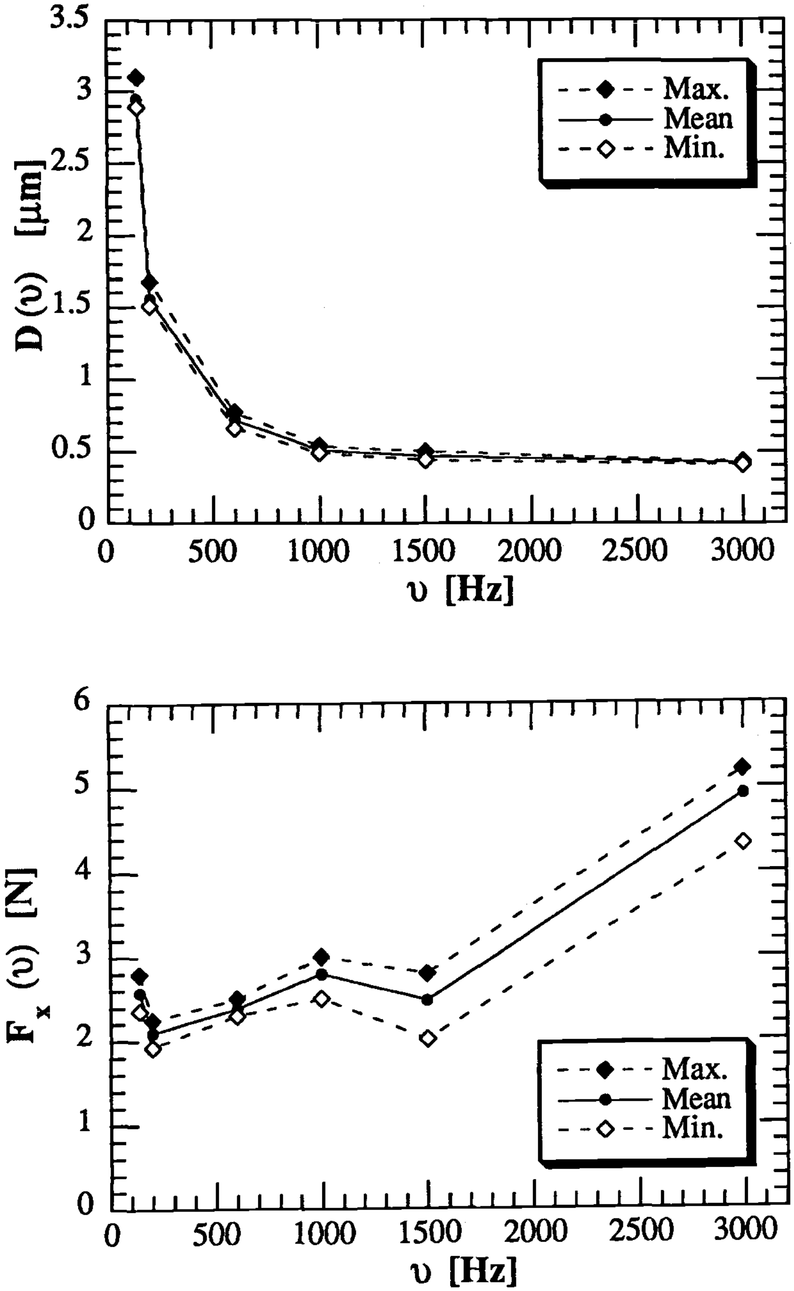

FIG. 11—*Two-dimensional* D(υ) *and* F_x(υ) *fretting maps for TiN coating;* L = *2.8 N.*

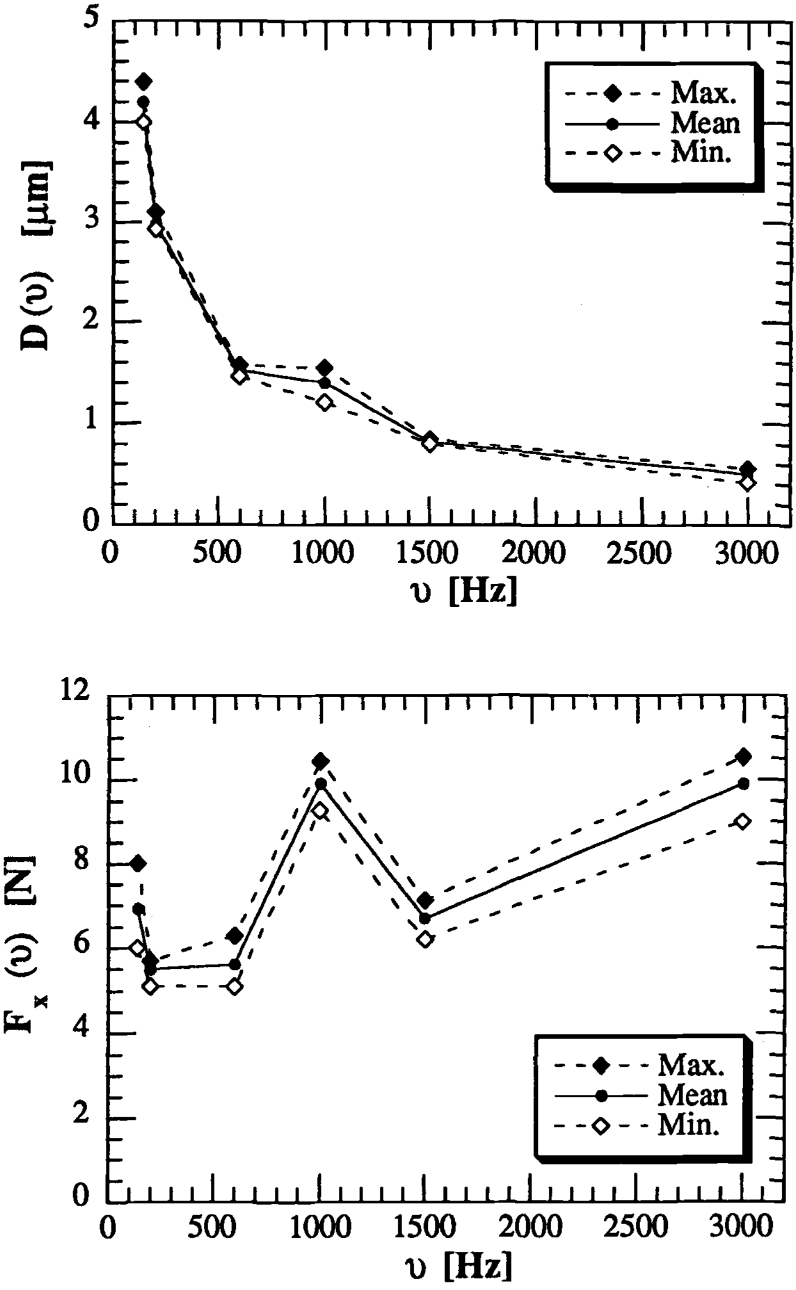

FIG. 12—*Two-dimensional* D(υ) *and* F_x(υ) *fretting maps for TiN coating;* L = *4.3 N.*

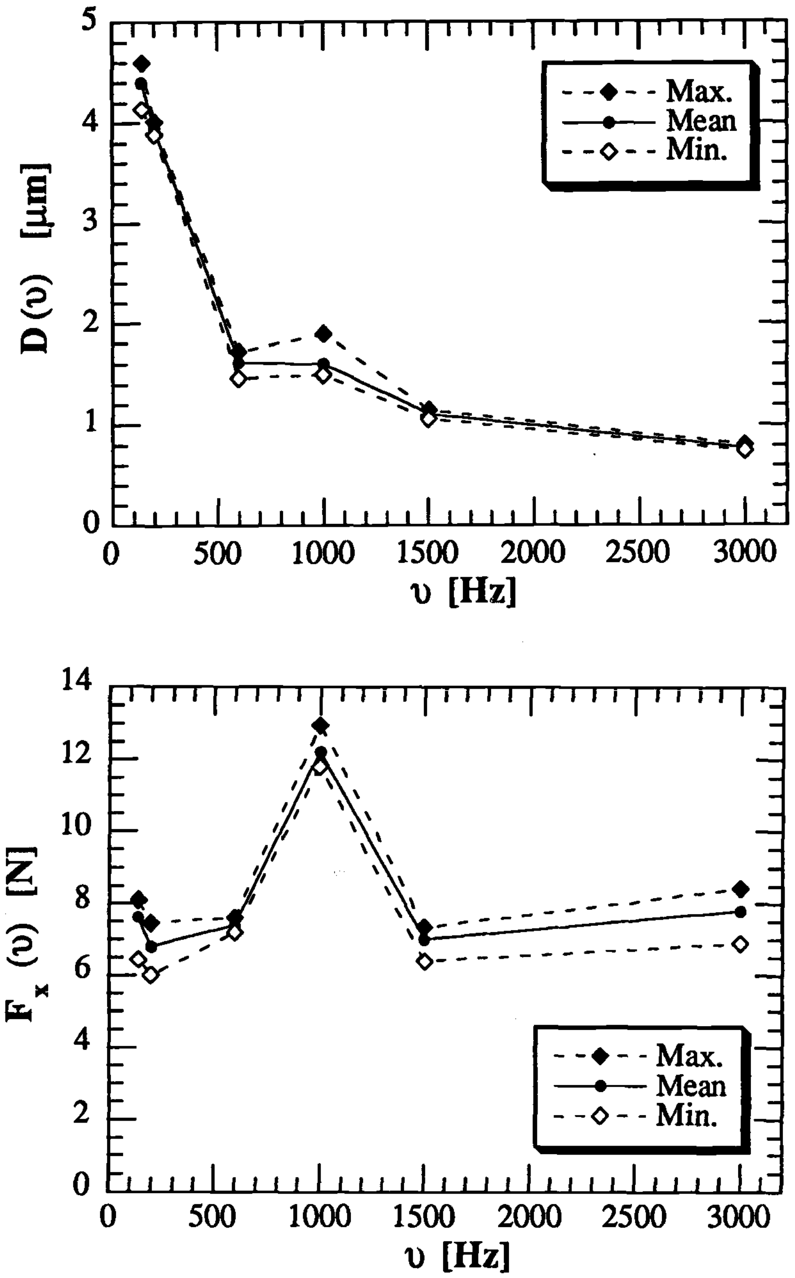

FIG. 13—*Two-dimensional* D(υ) *and* F_x(υ) *fretting maps for TiN coating;* L = *5.7 N.*

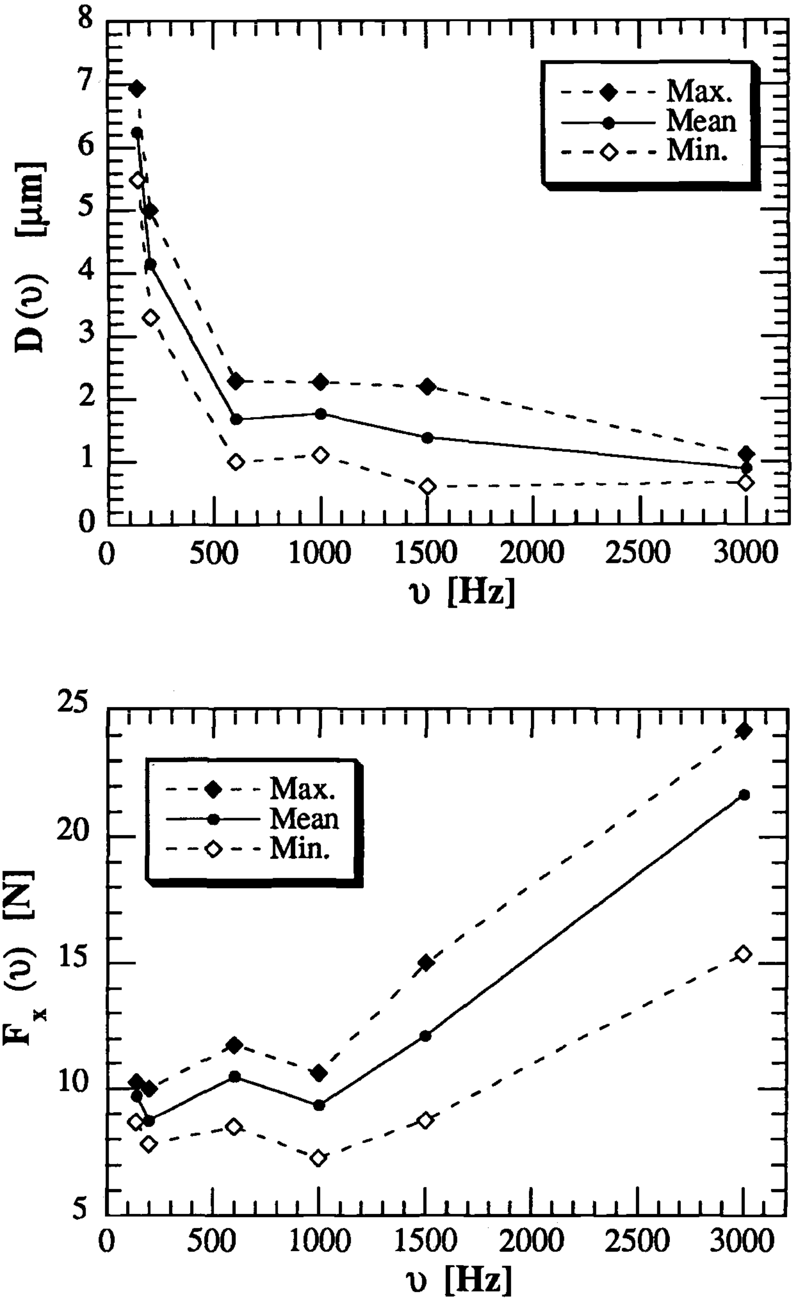

FIG. 14—*Two-dimensional* D(υ) *and* F_x(υ) *fretting maps for TiN coating;* L = *8.7 N.*

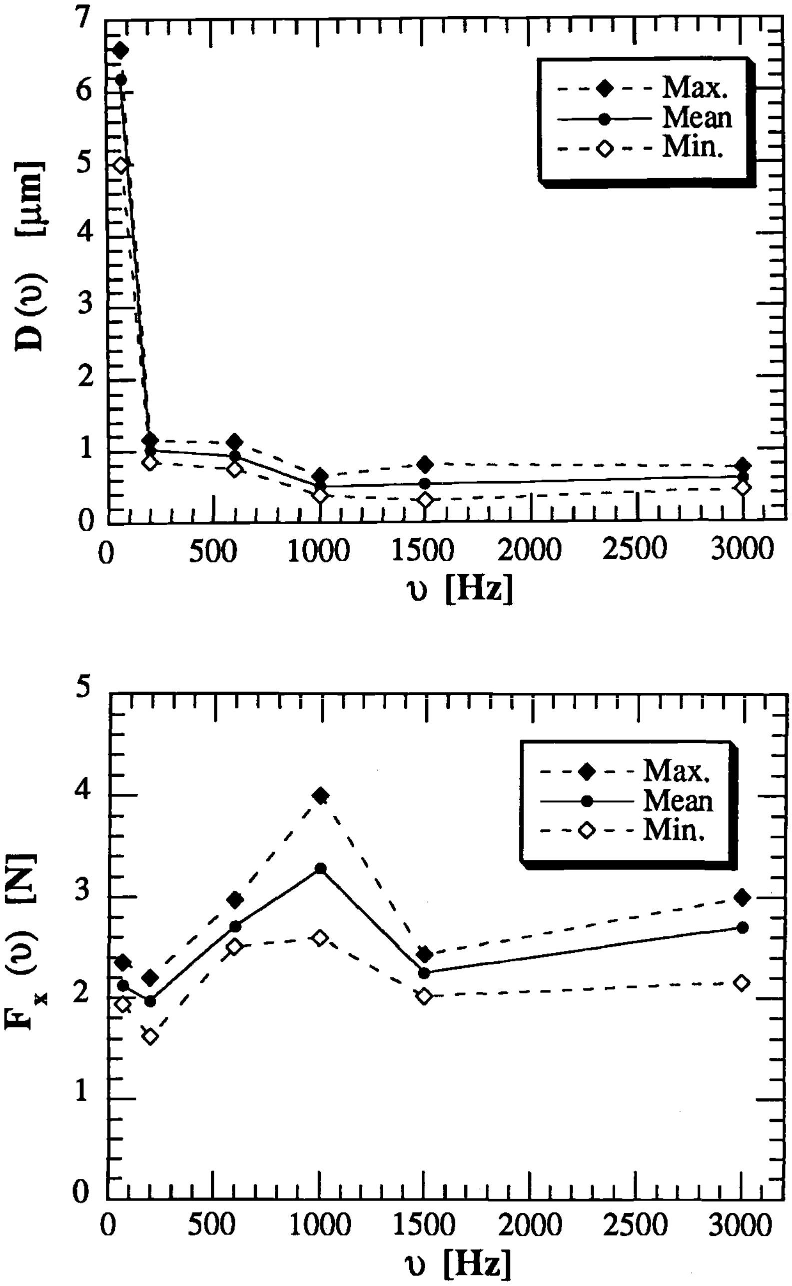

FIG. 15—*Two-dimensional* D(υ) *and* F_x(υ) *fretting maps for DLC coating;* L = *2.8 N.*

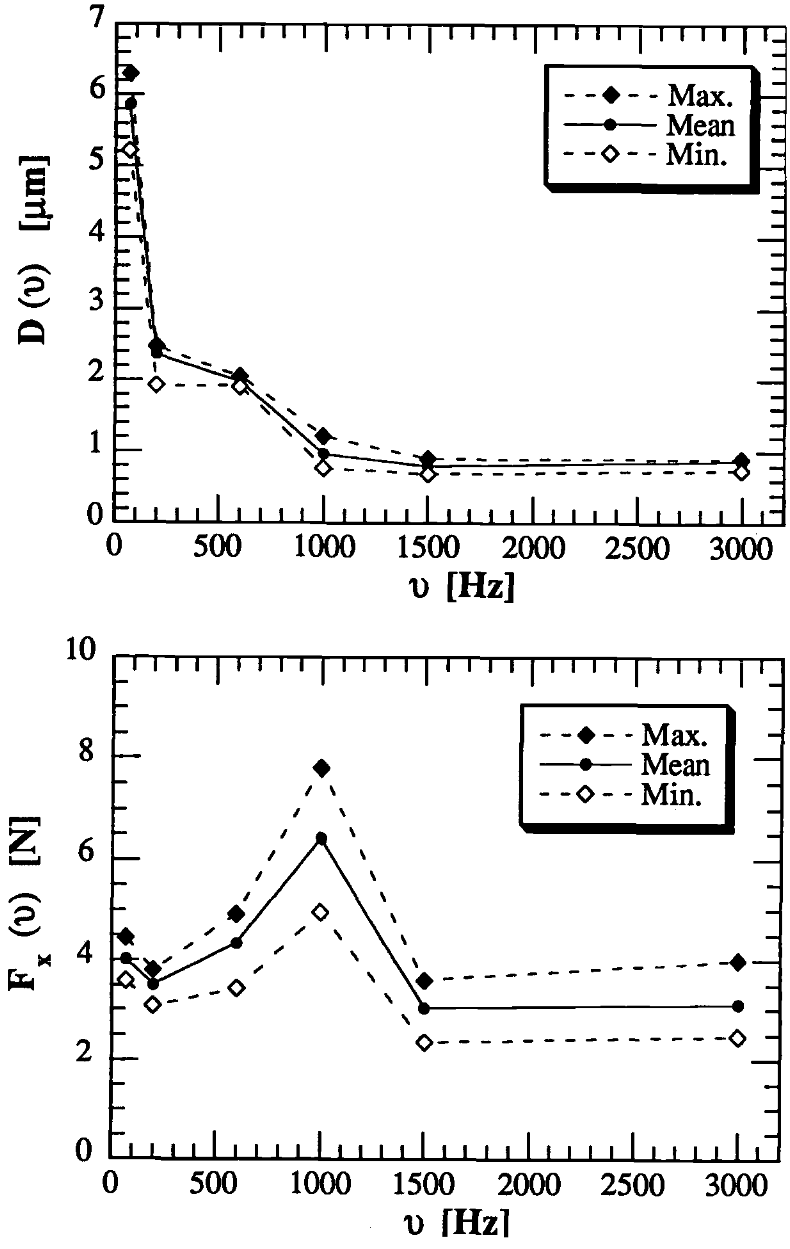

FIG. 16—*Two-dimensional* $D(\upsilon)$ *and* $F_x(\upsilon)$ *fretting maps for DLC coating;* $L = 4.3$ *N.*

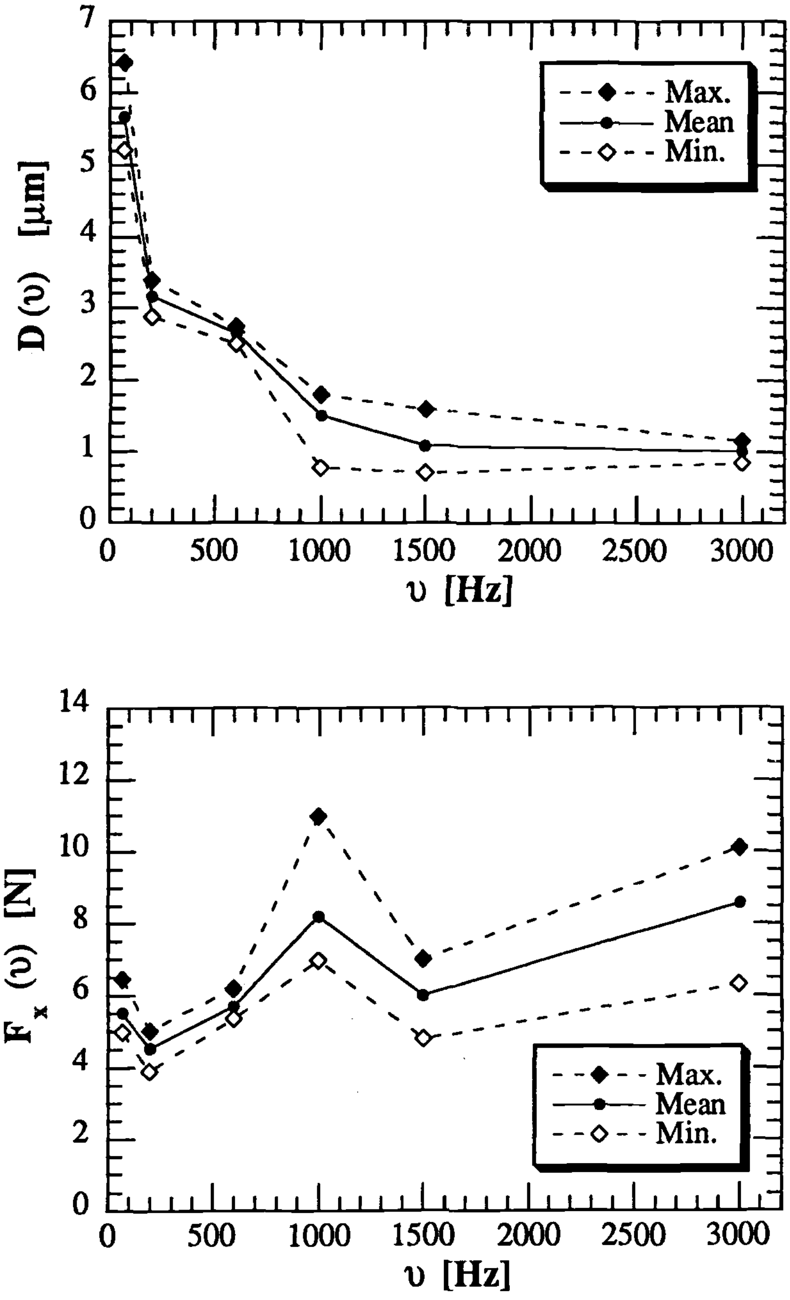

FIG. 17—*Two-dimensional* D(υ) *and* F_x(υ) *fretting maps for DLC coating;* L = 5.7 N.

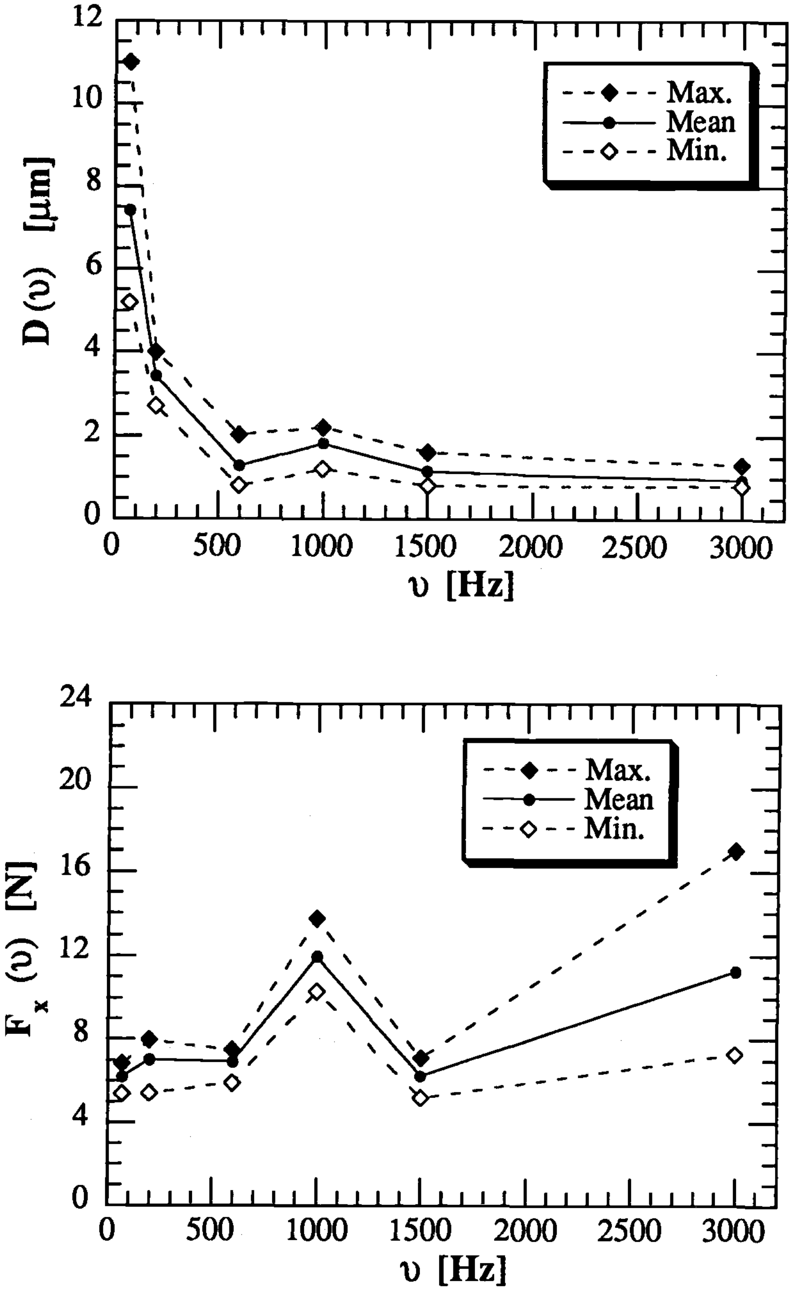

FIG. 18—*Two-dimensional* $D(\upsilon)$ *and* $F_x(\upsilon)$ *fretting maps for DLC coating;* $L = 8.7$ *N.*

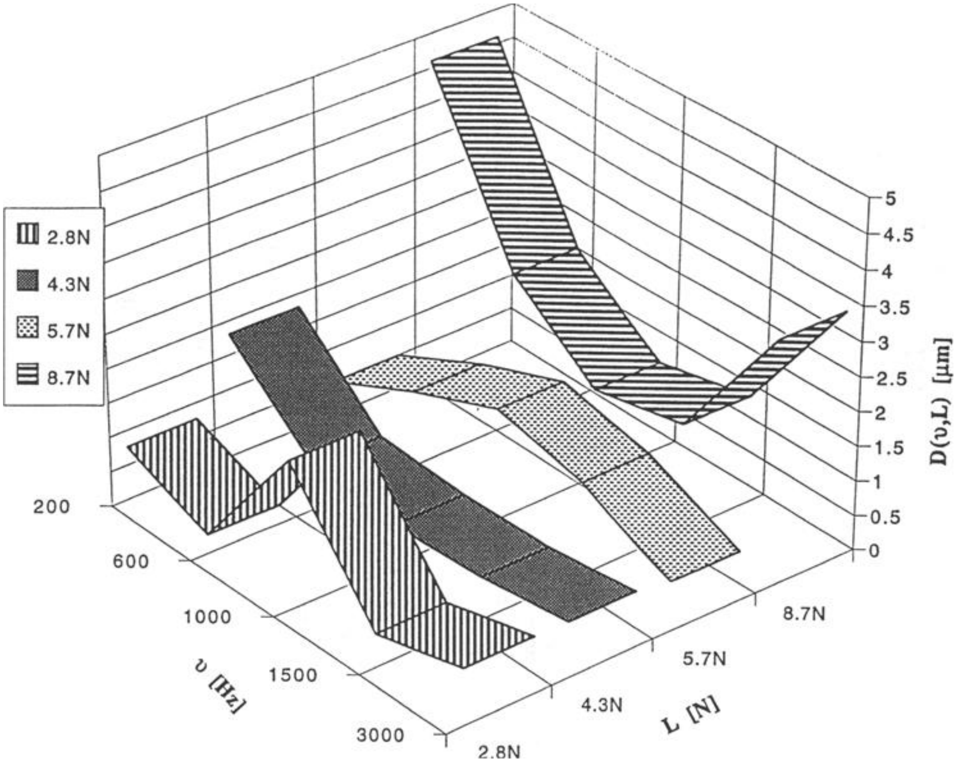

FIG. 19—*Three-dimensional* D(v,L) *fretting map for diamond coating.*

basic insight into the behavior of materials under oscillating surface contacts. As an example of this approach, compare the $D(v)$ and $F_x(v)$ map pairs in each of Figs. 11 through 18. In most of the $F_x(v)$ maps, there is an initial amplitude drop in the very lowest interval. In the 200 to 1000 Hz interval, however, there is always a steep increase in force amplitude with increasing frequency. In all the $D(v)$ maps, on the contrary, the displacement amplitude drops rapidly in this frequency interval. This observation is valid for both materials, irrespective of normal load, although the effect is less pronounced for the lowest and the highest loads in the TiN coating (Figs. 11 and 14). This interrelationship between tangential force and displacement amplitudes with respect to vibration frequency can be interpreted in terms of strain rate dependence. With increasing frequency, the displacement velocity, and thereby the rate at which deformation takes place or cracks propagate in the contact zone or both, the strain rate, will increase. The observed decrease in displacement amplitude, related to an increase in the force amplitude with increasing v, indicates that the adhesively bonded coating material in the stick zone is subjected to strain rate hardening for amplitudes in the partial stick regime, where plastic deformation of the contact zone is important. Correspondingly, the decrease in displacement will be associated with a decrease in fracture strain for amplitudes in the gross slip regime, indicating a strain rate embrittlement effect within this frequency range.

A similar, but reversed, effect is observed in the 1000 through 1500 Hz frequency range in both materials and for all normal loads. Here, the force amplitude decreases with increasing

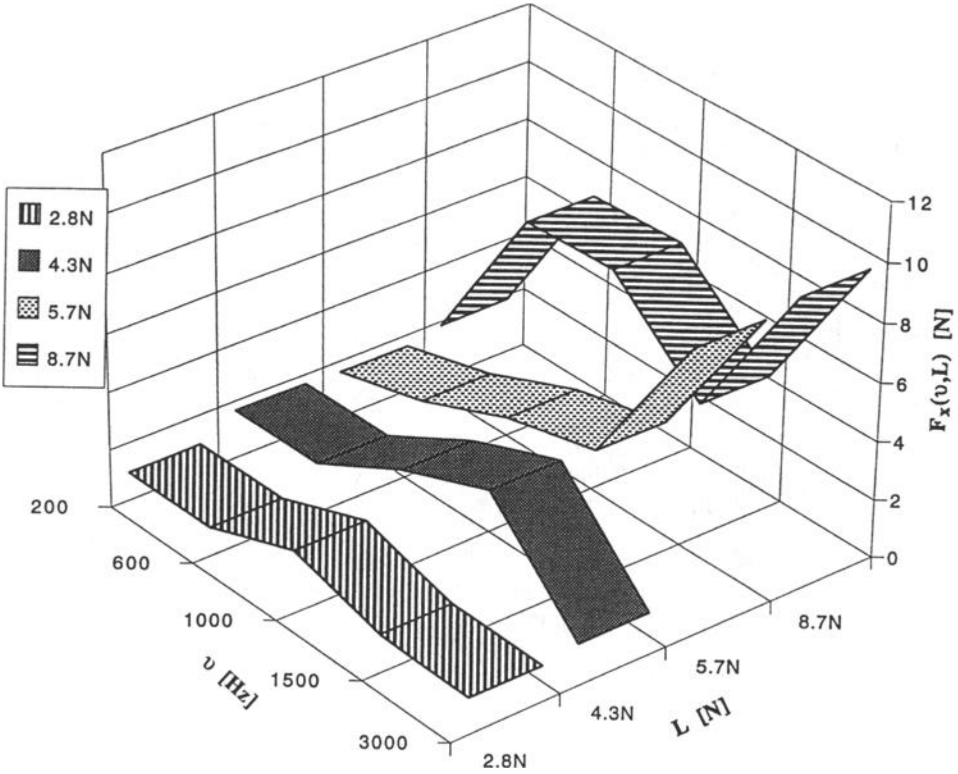

FIG. 20—*Three-dimensional* $F_x(\upsilon,L)$ *fretting map for diamond coating.*

strain rate, for a mainly unchanged, or slightly decreasing, displacement. An explanation can be sought in the fact that the increase in frequency also implies an increase in power consumption in the contact zone, leading to a temperature rise. The observed decrease in force amplitude, necessary to achieve the unchanged strain (displacement amplitude), indicates a thermal softening effect.

According to this successive hardening-softening model, the $F_x(\upsilon)$ "bump" in the 500 through 1500 Hz interval is an example of the well-known effect of two competing mechanisms, both depending on the same variable (the frequency in the present case), but each dominating and having opposite effects in adjacent intervals.

The suggested thermal softening can also be discussed in terms of the actual temperature increase, induced by the mechanical work, done on the contact zone during fretting. The "fretting work" can be calculated as the surface area of the fretting loop, that is, the hysteresis loop defined by one cycle of a $f_x(d)$ plot. This is done on a routine basis by off-line calculations in our equipment, and the values obtained are of the order of μJ/cycle under the present conditions. Standard temperature calculations, taking heat conduction to the entire test body into account, generally render practically negligible temperature increases. However, it is well known that the "flash temperature" of so-called hot spots, representing momentary asperity contacts and measured by pyrometric methods, can be quite high. This favors the assumption that, during a short time, most of the fretting energy is dissipated only in the small volume of material in a contact bridge (asperity). The present indications of thermal softening in certain frequency intervals are in agreement with the idea that flash temperatures can reach substantial fractions of the melting temperature even in hard materials such as those of the present coatings.

Conclusions

The results prove that it is possible to identify criteria for incipient gross slip in fretting based on changes in tangential force amplitude during experiments with gradually increasing diplacement amplitude. The validity of these criteria could be verified by SEM studies of damage mechanisms in the fretting scars. The critical amplitudes for IGS can be used to plot fretting maps, describing the boundary between the partial slip and the gross slip regimes in two- and three-dimensional graphs. Comparisons between different fretting maps can render information on mechanical behavior and deformation phenomena such as thermal softening, and strain rate hardening and embrittlement.

Acknowledgment

Partial financial support of this work from the Swedish agency, NUTEK, is acknowledged.

References

[*1*] Cattaneo, C., "Sul contatto di due corpi elastici," *Rendiconti dell'Accademia nazionale dei Lincei,* Series 6, Vol. 27, 1938, pp. 342–348.

[*2*] Mindlin, R. D., "Compliance of Elastic Bodies in Contact," *Journal of Applied Mechanics,* Vol. 16, 1949, pp. 259–268.

[*3*] Johnson, K. L., "Surface Interaction between Elastically Loaded Bodies under Tangential Forces," *Proceedings,* Royal Society, A230, 1955, pp. 531–548.

[*4*] Roos, J. R., Celis, J. P., Franck, M., and Pattyn, H., "Fretting Wear of Carbon-Ion-Plated Physical-Vapour-Deposited TiN Coatings," *Surface Coatings Technology,* Vol. 45, 1991, pp. 89–98.

[*5*] Vingsbo, O. and Soderberg, S., "On Fretting Maps," *Wear,* Vol. 126, 1988, pp. 131–147.

[*6*] Vingsbo, O., "Fretting and Contact Fatigue, Studied with the Aid of Fretting Maps," M. H. Attia and R. B. Waterhouse, Eds., *Standardization of Fretting Fatigue Test Methods and Equipment, ASTM STP 1159,* American Society for Testing and Materials, Philadelphia, 1992, pp. 49–59.

[*7*] Alahelisten, A., Olsson, M., and Hogmark S., "Mechanical and Tribological Properties of Hot Flame Deposited Diamond on Cemented Carbide Substrates," *Proceedings,* Sixth International Congress on Tribology, Vol. 3, M. Kozma, Ed., Hungarian Society of Mechanical Engineers, Hungarian Chemical Society, Hungarian Academy of Sciences, Budapest, 1993, pp. 280–283.

[*8*] Vingsbo, O. and Schon, J., "A Giant-Magnetostrictive Vibrator for Fretting Testing at Low Amplitudes," *Wear,* Vol. 162–164, 1993, pp. 1129–1138.

[*9*] Odfalk, M. and Vingsbo, O., "An Elastic-Plastic Model for Fretting Contact," *Wear,* Vol. 157, 1992, pp. 435–444.

[*10*] Gupta, P. K. and Walovit, J. A., "Contact Stresses between an Elastic Cylinder and a Layered Elastic Solid," *Journal of Lubrication Technology,* Vol. 96, 1974, pp 250–257.

Hardy Mohrbacher,[1] *Bart Blanpain,*[1] *and Jean-Pierre Celis*[1]

Friction and Wear Mechanisms on CVD Diamond and PVD TiN Coatings under Fretting Conditions

---

REFERENCE: Mohrbacher, H., Blanpain, B., and Celis, J.-P., **"Friction and Wear Mechanisms on CVD Diamond and PVD TiN Coatings under Fretting Conditions,"** *Effect of Surface Coatings and Treatments on Wear, ASTM STP 1278,* S. Bahadur, Ed., American Society for Testing and Materials, 1996, pp. 76–93.

ABSTRACT: Laboratory fretting testing is an appropriate method to investigate the friction and wear behaviors of hard coating materials in vibrating contacts under specified conditions. Such testing can help to select the most suitable coating for a specific application. Furthermore, it can assist in optimizing the coating deposition process. A conceptual framework for modeling laboratory fretting testing is presented together with test equipment and experimental methods for on-line mechanical analysis and off-line material degradation analysis. The application of these concepts is demonstrated for two hard coating types, namely, physical vapor deposition (PVD) TiN and chemical vapor deposition (CVD) diamond coatings. The influence of the fretting conditions on the mechanical contact response as well as on the materials modification induced in the contact is analyzed. The effect of third bodies, tribochemical reactions, and residual stress on the friction and wear behavior of these hard coatings is discussed.

KEYWORDS: surface coatings, surface treatments, wear testing, hard coatings, fretting wear protection, friction properties, contact fatigue, tribochemistry

Material contacts subjected to vibrations can respond with a small oscillatory relative displacement at the contact interface resulting in wear or in the initiation of cracks by cyclic contact stresses [*1,2*]. The material degradation due to sliding in vibrating contacts is also known as fretting wear. Crack initiation, on the other hand, is attributed to contact fatigue. The practical importance of these material degradation processes attracts widespread concern in industry. Fretting wear and contact fatigue cause problems in, for example, aerospace, power generation, ground transportation, and medical implants. The use of hard coatings is considered to be a promising approach to control friction and to reduce wear in vibrating unlubricated contacts [*3*]. Nevertheless, practical experience as well as laboratory simulations have shown that hard coatings can degrade in vibrating contacts [*4*]. It is therefore of interest to identify critical fretting conditions for hard coatings by laboratory testing. Coating selection criteria in view of a specific application can then be developed from such tests.

In this work, the potentiality of fretting testing in evaluating the tribological behavior of hard coatings is demonstrated for physical vapor deposition (PVD) TiN and chemical vapor deposition (CVD) diamond coatings. The observed mechanical contact response as well as the materials modification are interpreted using established and newly developed modeling con-

---

[1] Research associate, post-doctoral researcher, and professor, respectively, Department of Metallurgy and Materials Engineering (MTM), Katholieke Universiteit Leuven, de Croylaan 2, B-3001 Leuven, Belgium.

cepts in fretting. Friction and wear mechanisms under various testing conditions are derived. The effect of third bodies (particle debris, transfer layers), tribochemical reactions, and residual stress in that respect is discussed.

Concepts in Fretting Research

The friction and wear behaviors of materials in vibrating contacts are determined by mechanical contact conditions, environmental conditions, and material properties. Each of these aspects introduces a number of basic fretting variables making fretting a true system property. The simultaneous interaction of many fretting variables has to be encountered in practical applications. Such a condition matrix can usually not be identically simulated in laboratory experiments. A considerable simplification is required to achieve a high reproducibility and to permit the detailed analysis of the mechanical contact response and the material degradation. Therefore, a conceptual framework is defined in the following to assist the setup of laboratory fretting tests and to support the evaluation of these experiments.

Fretting Modes

Contact vibrations are often induced by cyclic accelerations, cyclic stresses, acoustical noise, or by thermal cycling. The displacement field of an arbitrary vibration can be decomposed into three basic "fretting modes" characterized by a linear, radial, or circumferential trajectory. These trajectories and the possible methods of actuation are schematically shown in Fig. 1 for a ball-on-flat model contact [*5*].

Most of the laboratory fretting experiments reported in the literature have been performed with a linear displacement trajectory (Mode I). The imposed normal force, displacement stroke, and vibration frequency are the external mechanical variables in such vibrating contacts. Mode I fretting is likely to occur in systems with one degree of freedom such as linearly guided components.

A contact vibration with radial displacement trajectory (Mode II) can be induced by a periodically varying contact load. The induced relative displacement stroke is zero in the contact center and reaches a maximum value at the contact periphery. The maximum displacement stroke for a given materials contact depends on the minimum contact load as well as on the load amplitude [*5*]. Mode II fretting is encountered in practice, for example, in ball bearing applications and is also known as "false brinelling."

A relative displacement field of circumferential trajectory (Mode III) is induced when an oscillating torsional couple is applied. The circumferential displacement stroke gradually increases from zero at the pivot point to a maximum value at the contact periphery. Mode III fretting experiments have been reported by Kennedy el al. [*6*].

The fretting mode, the size of the contact area, and the contact dynamics determine the exposure time of the contact zone to the surrounding test atmosphere during a vibration cycle [*7*]. Modes I and II, the contact exposure, t_{exp}, approaches a value corresponding to the vibration period, $1/f$, at the contact periphery whereas it remains zero over the whole contact zone in the case of Mode III fretting. The minimum contact exposure in Mode I fretting is determined by the contact radius, a, the linear displacement stroke, D, and the vibration frequency, f (Fig. 1). It becomes zero when the displacement stroke is smaller than the contact diameter ($D < 2a$). In this respect, it is important to clearly define these variables when simulating contact vibrations occurring in field practice.

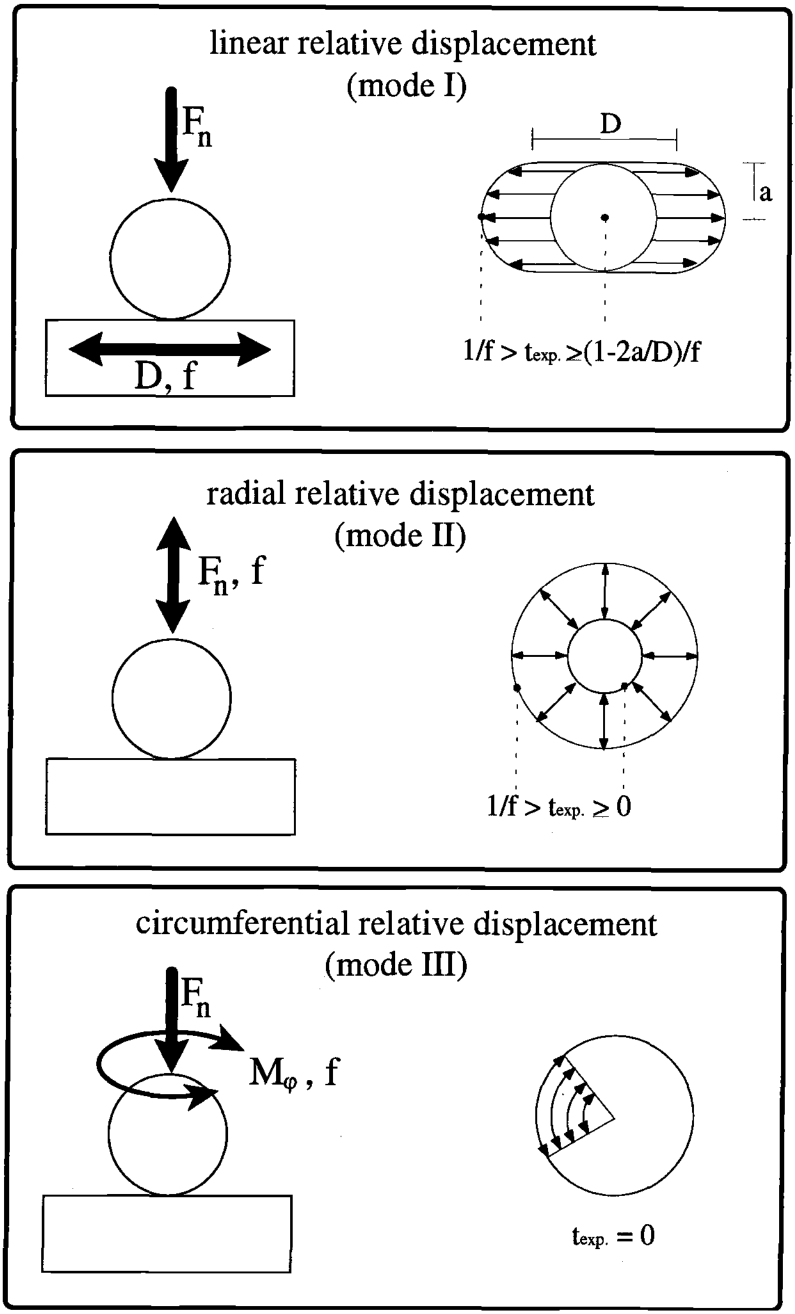

FIG. 1—*Definition of the three basic fretting modes for a ball-on-flat model contact and methods of actuation (*D = *linear displacement stroke,* F_n = *normal force,* M_φ = *torsional couple,* f = *vibration frequency,* a = *contact radius, and* t_{exp} = *contact exposure).*

Fretting Regimes

Analysis of the mechanical response and the damage morphology developed in Mode I fretting testing has led to the definition of three fretting regimes [*8–10*]. In the gross-slip regime, sliding between the mating solids occurs across the whole contact interface. In the partial-slip regime, sliding is confined to an outer ring-shaped zone called "slip annulus" whereas the inner contact zone called "stick zone" deforms only elastically. The elastic-stick regime becomes dominant when the width of the slip annulus approaches zero. The occurrence of these regimes in a vibrating materials contact depends on the combination of the normal force, displacement stroke, and vibration frequency. The gross-slip regime is generally not to be observed for Modes II and III contact vibrations since the relative contact displacement gradually approaches zero towards the contact center and, consequently, some part of the contact zone remains sticking. Generally, a decreasing displacement stroke and an increasing contact load promote the occurrence of sticking in vibrating contacts [*9*]. In contacts subjected to partial-slip, wear does not occur uniformly across the fretting zone but is confined to the slip annulus.

Velocity Accommodation Mechanisms

The tangential force opposing the relative velocity in a vibrating contact is determined by the active velocity accommodation mechanism and by the properties of the materials involved [*10–12*]. Velocity accommodation either occurs directly between the mating solids or involves a third body present in the contact zone in the form of transfer layers, surface reaction layers, or wear particles. Berthier et al. [*12*] have developed a unique classification of velocity accommodation mechanisms in a vibrating contact. Four basic accommodation modes such as elastic deformation, normal breaking, shearing, and rolling are distinguished. These modes can be active at five different sites in the contact, namely, in the surface near bulk of the first bodies, at the boundary between the first bodies, in the bulk of the third body, and at the boundaries between the first and third bodies. The combination of four modes and five sites leads to a variety of 20 velocity accommodation mechanisms. The friction behavior of a vibrating contact can only be understood when the active velocity accommodation mechanisms are identified. These, however, can change due to wear-induced material modifications in the contact so that an evolution of the friction behavior during testing is usually observed.

Material Degradation Mechanisms

The mechanisms of material degradation in vibrating contacts may be generalized into two classes, namely energy-dissipative and stress-induced mechanisms. The generation of material damage due to mechanical or tribochemical wear always requires the dissipation of frictional energy and, thus, the occurrence of partial or gross sliding of the vibrating contact. Oscillating contact stresses result in cracking and rupturing of the materials. Damage occurs instantly when the stress amplitude reaches a critical value or by fatigue failure when it is subcritical. A similar classification of material degradation mechanisms was suggested by Vincent et al. [*10*] who distinguished "overstraining" and "overstressing" mechanisms. The damage induced by energy dissipative mechanisms covers large parts of the fretting zone and progresses gradually with a particular wear rate. The wear rate of an active wear mechanism relates the amount of removed material volume to the friction energy dissipated during one cycle. The dissipated energy accounts mainly for contact heating and the activation of mechanical deformation and tribochemical processes in the contact. Accordingly, the total wear damage is expected to be proportional to the cumulative friction energy dissipated over the test duration [*13,14*]. Stress-induced mechanisms, on the contrary, result in highly localized damage often leading to a sudden failure of the material. The exact prediction of time and location of materials failure in the vibrating contact is difficult and requires the detailed analysis of the contact stress field. Wear mechanisms involving fracturing and fragmentation processes can be promoted by residual tensile stresses present in the contacting materials [*1,2*].

Experimental

Fretting Simulation and Analysis Equipment

Fretting Simulation Device—Contact vibrations with a linearly oscillating displacement (Mode I) were induced by a newly developed test system with a friction-free actuation mechanism [*5*]. This actuator allows one to accurately control the linear displacement stroke and the vibration frequency over a wide range. The ball-shaped counterbody was loaded on top of the vibrating hard-coated flat specimen at variable normal forces induced by a spring system. The test duration was varied from a few hundred to several thousand fretting cycles to study the initiation of wear damage and the coating durability, respectively. The relative humidity (RH) in the test atmosphere was stabilized at selected values between 10 and 80% using a climate control system as described previously [*7*]. All tests were performed without lubrication in ambient air at a temperature of 23°C.

On-line Monitoring—The tangential force, contact displacement, and normal force were continuously monitored by appropriate sensors. A computer software routine was used for the acquisition and on-line analysis of force-displacement hysteresis loops measured over individual vibration cycles [*5*]. Quantities characterizing the mechanical contact response can be extracted from such hysteresis loops as shown in Fig. 2. The open loop width enclosed by the zero crossings of the tangential force represents the sliding distance, s, in the fretting contact. The maximum loop extension corresponds to the imposed displacement stroke, D. The ratio of the sliding distance to the imposed displacement stroke is called the fretting regime indicator, r, (Fig. 2) and has been proposed recently as a convenient numerical criterion for the on-line monitoring of the operative fretting regime in a vibrating contact [*5*]. The value of this ratio ranges from zero when the applied stroke results only in elastic contact deformation (elastic-stick regime) to unity when the applied displacement stroke is fully accommodated by contact sliding (gross-slip regime). At the transition from partial-slip to gross-slip, the fretting regime indicator has values around 0.33. The area enclosed by the force-displacement loop represents the friction energy, E_d, dissipated in the contact. The value of the dissipated friction energy approaches zero when elastic-stick becomes the dominating fretting regime. In the gross-slip regime, the average coefficient of friction is obtained from the dissipated energy, the sliding distance, and the normal force as indicated in Fig. 2. On-line monitoring of these quantities over the test duration can be used to characterize the evolution of the mechanical contact response.

Off-Line Characterization—Laser stylus profilometry was used to quantitatively determine the wear depth as well as the planimetric and volumetric wear on the coatings [*4*]. Damage features and the morphology of third body material were examined by optical and scanning electron microscopy. Chemical material modifications induced by fretting wear were investigated by surface analysis techniques such as micro-Raman and X-ray photoelectron spectroscopy (XPS) [*15,16*].

Hard Coating Preparation and Counterbody Materials

Diamond coatings were grown on flat WC-Co (tungsten-carbide-cobalt) and SiAlON cutting tool inserts by hot filament chemical vapor deposition (CVD). The CVD reactor was operated

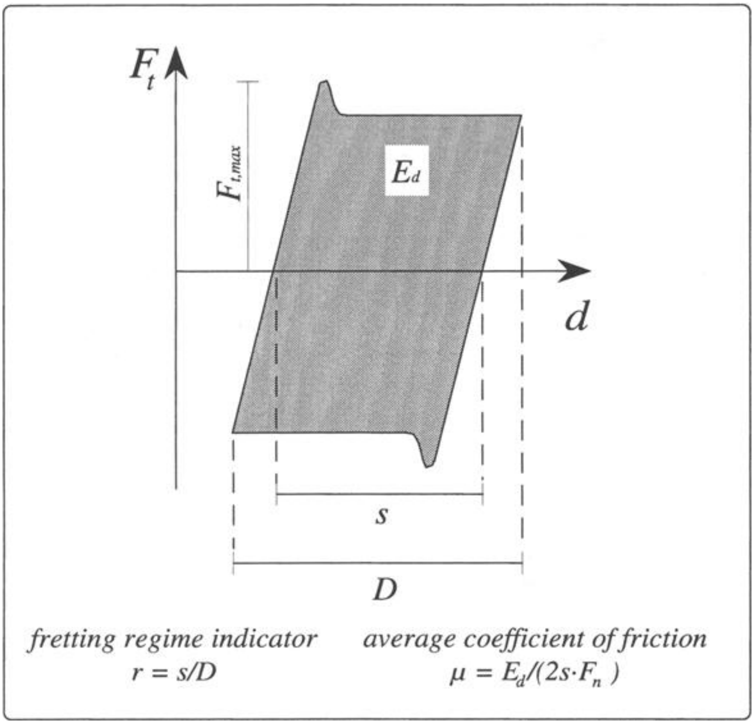

FIG. 2—*Schematic representation of a tangential force-displacement hysteresis loop;* s = *contact sliding,* D = *displacement stroke,* $F_{t,max}$ = *maximum tangential force,* F_n = *applied normal force,* E_d = *dissipated friction energy,* r = *fretting regime indicator, and* μ = *coefficient of sliding friction.*

with a tungsten filament (~2000°C) in a hydrogen diluted methane (CH_4:H_2 = 1:100) atmosphere at 50 mbar pressure.[2] Coating thicknesses of 6 and 18 μm were deposited at substrate temperatures of 860 and 940°C, respectively. The coating roughness was around 0.2 μm (R_a) on most of the samples. Some coatings had an increased roughness of 0.5 μm (R_a). Characterization of the mechanical properties of these diamond coatings using the nano-indention technique indicated hardness values of around 80 GPa and values for the Young's modulus of approximately 1300 GPa.

TiN was deposited on flat ASP 23 tool steel substrates by PVD in an industrial Balzers triode ion-plating equipment.[3] The steel substrates had a hardness of 1100 HV and were highly polished before the TiN deposition. The substrates were held at a bias voltage of −150 V during deposition. The TiN coatings were approximately 5 μm thick and had a roughness of around 0.03 μm (R_a). The coating hardness was evaluated by micro-Vickers indentation as around 2300 HV [*14*].

The counterbody materials used in the present fretting experiments were corundum (α-Al_2O_3) and chromium steel (100Cr6) with a hardness of 2000 HV and 63 HRC, respectively. The counterbodies were ball shaped (10 mm diameter) and had a highly polished surface finish.

---

[2] CemeCon, Aachen, Germany.

[3] WTCM, Diepenbeek, Belgium.

Results and Discussion

Fretting Behavior of CVD Diamond Coatings

Corundum balls were loaded on top of the diamond coatings with normal forces of 4 and 6 N. The diamond-coated flats were oscillated at displacement strokes of 100 and 50 μm at frequencies of 10 and 20 Hz, respectively, corresponding to a relative velocity of 1 mm/s. The friction and wear behavior of CVD diamond coatings under different fretting regimes are discussed.

Gross Slip—The evolution of friction on a smooth and on a rough diamond coating in the gross-slip regime is shown in Fig. 3. Two stages are recognized in each curve. During an initial high friction phase, the coefficient of friction has values around 0.6 for the rough and around 0.4 for the smooth diamond coating. After a few hundred cycles, a transition phase is observed at which the coefficient of friction decreases to values below 0.1 where it remains stable. The transition from high to low friction proceeds faster on the diamond coatings characterized with a low roughness.

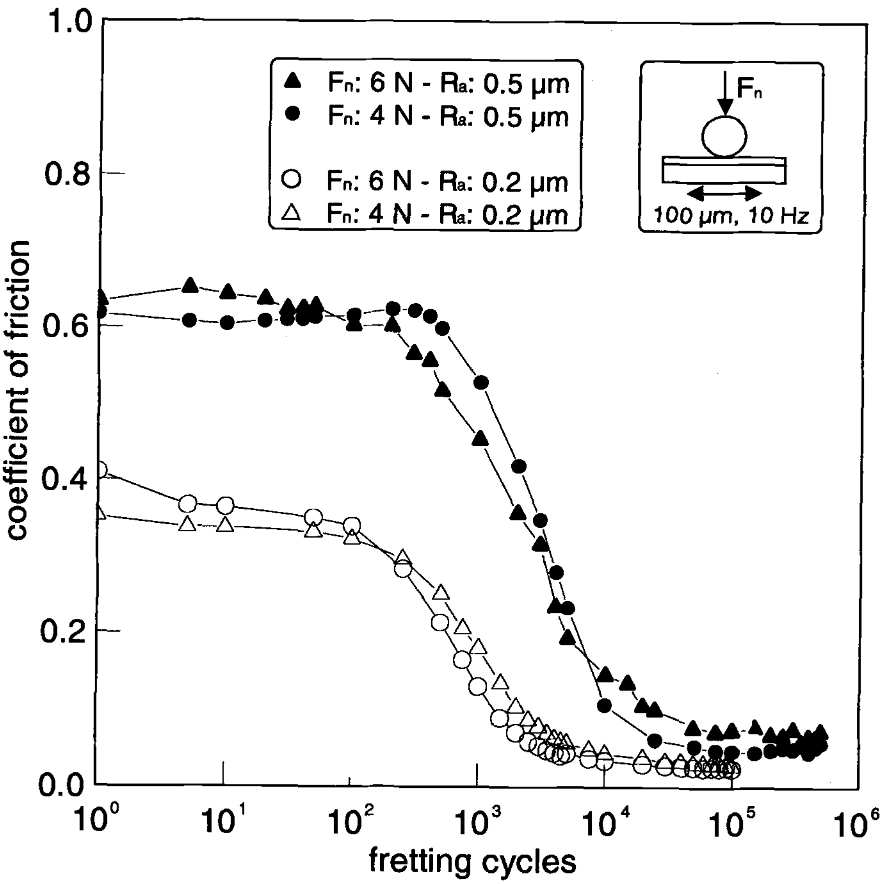

FIG. 3—*Evolution of the coefficient of friction on CVD diamond coatings of various surface roughness vibrating against corundum.*

The observed transition in the friction behavior is indicative of a change in the velocity accommodation mechanism and is closely related to the wear behavior. During the high friction phase, the velocity is accommodated directly between the first bodies. A high tangential force results in the detachment of particles by asperity shearing and fracturing mechanisms [*13*]. The coefficient of friction evolves to a low value as the coating roughness is being reduced by wear [*17*]. The establishment of the low friction state is delayed when the initial coating roughness is high (Fig. 3). The particle debris originating from the diamond coating and the corundum counterbody is trapped in the contact leading to a polishing effect by further wear. Very smooth regions can develop in the wear track after sufficiently long testing (Fig. 4). Particle rolling starts playing an increasing role as a velocity accommodation mechanism on the smoothened coating surface.

The wear volume measured on diamond coatings was found to be proportional to the cumulative friction energy dissipated in the vibrating contact [*13*]. Wear on the diamond coating by the sliding corundum counterbody progresses at a very low rate of about 400 $\mu m^3/J$. This relationship was also found for other counterbody materials such as CVD diamond-coated Si_3N_4 balls sliding versus a CVD diamond-coated flat [*13*]. These results indicate that the wear behavior of diamond coatings subjected to gross-slip conditions becomes stable and predictable after a short running-in phase.

Partial Slip—Reducing the displacement stroke from 100 to 50 μm resulted in a characteristic mechanical response that is shown in Fig. 5. Transitions in the tangential force amplitude and in the fretting regime indicator are observed after approximately 45 000 cycles. The partial-slip regime ($r < 0.33$) is dominant during the initial test phase (Fig. 5*a*). The maximum tangential force remains nearly constant at a value of 3 N. The transition to gross slip ($r > 0.33$) is accompanied by a drop in the tangential force amplitude to values below 1 N. In the partial slip regime, sliding between the contacting surfaces is restricted by asperity interlocking. The tangential force amplitude results from the elastic deformation of the interlocked contact interface due to the imposed displacement stroke. This force is not high enough to instantly break the interlocked asperities as observed in tests with a displacement stroke of 100 μm. The asperities are now subjected to contact fatigue induced by the cyclic tangential force. Asperity failure occurs thus only after a sufficient number of fatigue cycles. The progressive damage during this phase of gross-failure is seen as a peak in the evolution of the dissipated friction energy (Fig. 5*b*). Once the transition to gross-slip has occurred, a smooth wear track is being formed under the abrasive action of wear debris.

Fretting tests performed under the same set of conditions were repeated on a number of similar CVD diamond coatings deposited on SiAlON substrates. The mechanical contact response was equivalent to that shown in Fig. 5, that is, a transition from partial slip to gross slip was observed. Although the tangential force amplitude was kept at 3 N in these tests, the duration of the partial-slip regime ranged from only 13 000 to more than 90 000 cycles. Different residual stress levels present in the diamond coatings are assumed to influence the progress of fatigue failure in the interlocked contact interface [*1*]. The residual stress in diamond coatings can be evaluated from X-ray diffraction or Raman spectroscopy measurements [*18,19*]. Tensile stresses up to 700 MPa were observed in these diamond coatings depending on the substrate material and the deposition parameters. The duration of the partial-slip regime, that is, the fatigue life of the interlocked contact interface is plotted versus the tensile residual stress in Fig. 6. It is observed that the failure of interlocked asperities and, thus, the transition from partial slip to gross slip occurs faster as the tensile residual stress in the diamond coatings increases. Such a relationship, however, can only be established when the mechanical contact conditions are well known. Thus, the reliable prediction of the friction and wear behaviors of diamond coatings subjected to varying contact vibrations in the partial slip regime remains difficult.

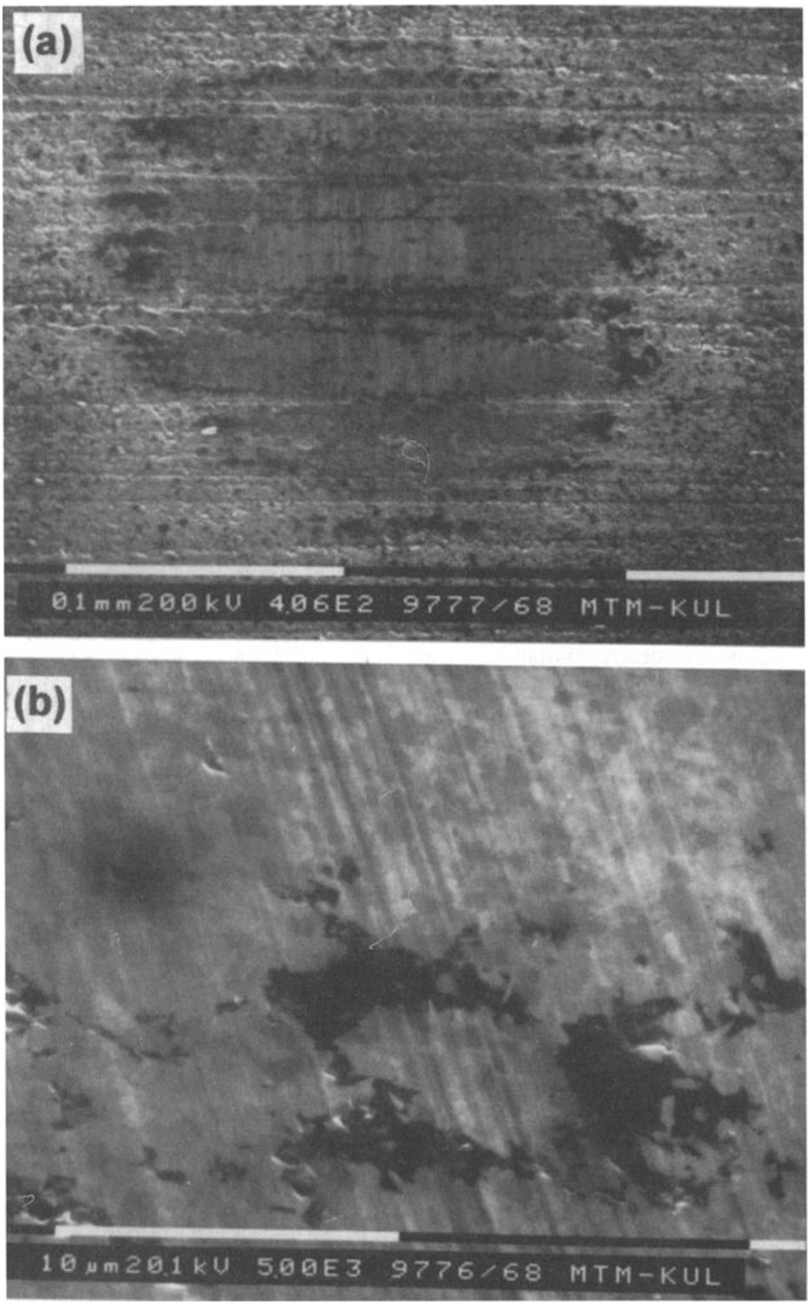

FIG. 4—*SEM micrographs of wear damage induced on a CVD diamond coating after 5* × 10^5 *fretting cycles against corundum (*D = *100* µm*,* F_n = *6 N, and* f = *10 Hz). (*a*) Damage zone on the diamond coated flat showing the reduction of the original coating roughness. (*b*) Close-up of a wear plateau in the damage zone exhibiting sliding marks parallel to the fretting direction.*

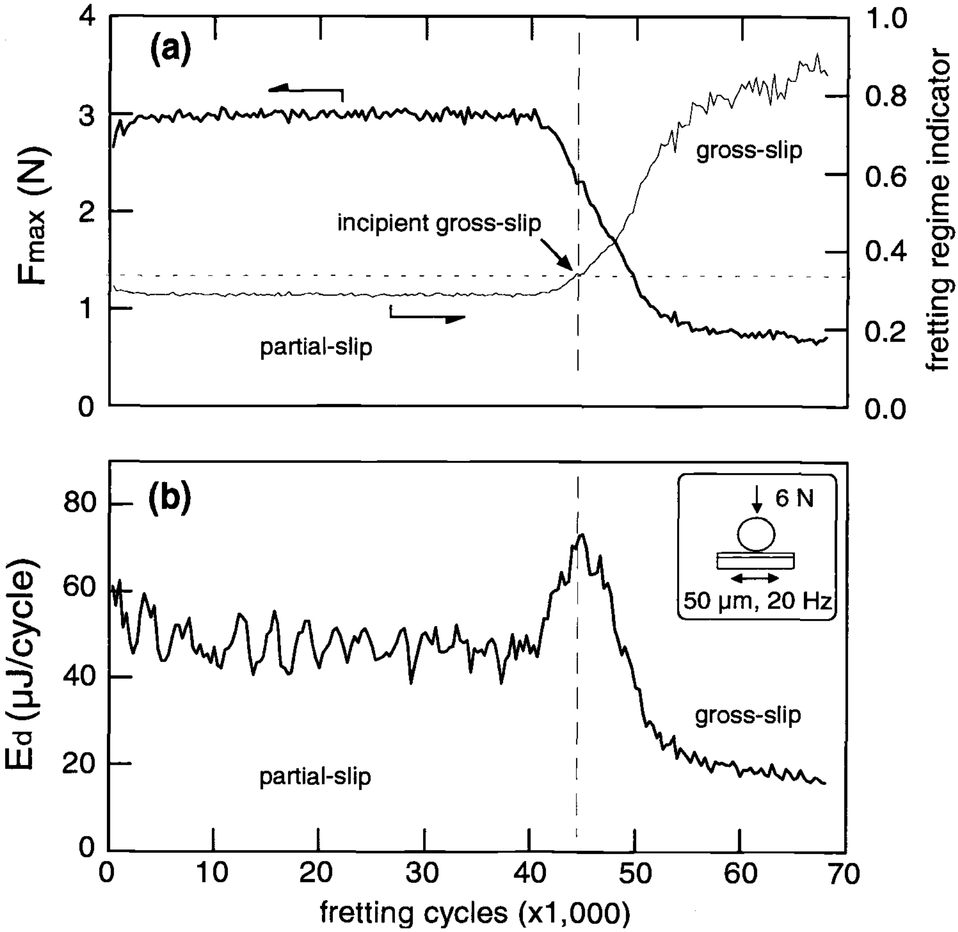

FIG. 5—*Changes in the mechanical response of a vibrating contact between CVD diamond and corundum during the transition from partial-slip to gross-slip. (*a*) Evolution of the maximum tangential force and the fretting regime indicator (see Fig. 2). (*b*) Evolution of the friction energy (area of the force-displacement loop) dissipated during each fretting cycle.*

Fretting Behavior of TiN Coatings

The humidity in the test atmosphere has to be considered when evaluating the tribological performance of ceramic coatings such as TiN. The relative humidity can vary in practice over a range of about 5 to 95%. Fretting Mode I experiments on TiN coatings were performed with a displacement stroke of 100 μm and frequencies of 2, 5, and 10 Hz. Normal forces of 1, 2, and 4 N were applied to corundum and chromium steel counterbodies. Gross slip was prevailing in these vibrating contacts.

TiN versus Corundum—The evolution of the coefficient of friction at different humidity levels is displayed in Fig. 7. The coefficient of friction remains at low values ($\mu < 0.25$) over the whole test duration when the relative humidity is high (RH > 70%). At low humidity, the coefficient of friction strongly increases after the first few hundred cycles, reaching peak values

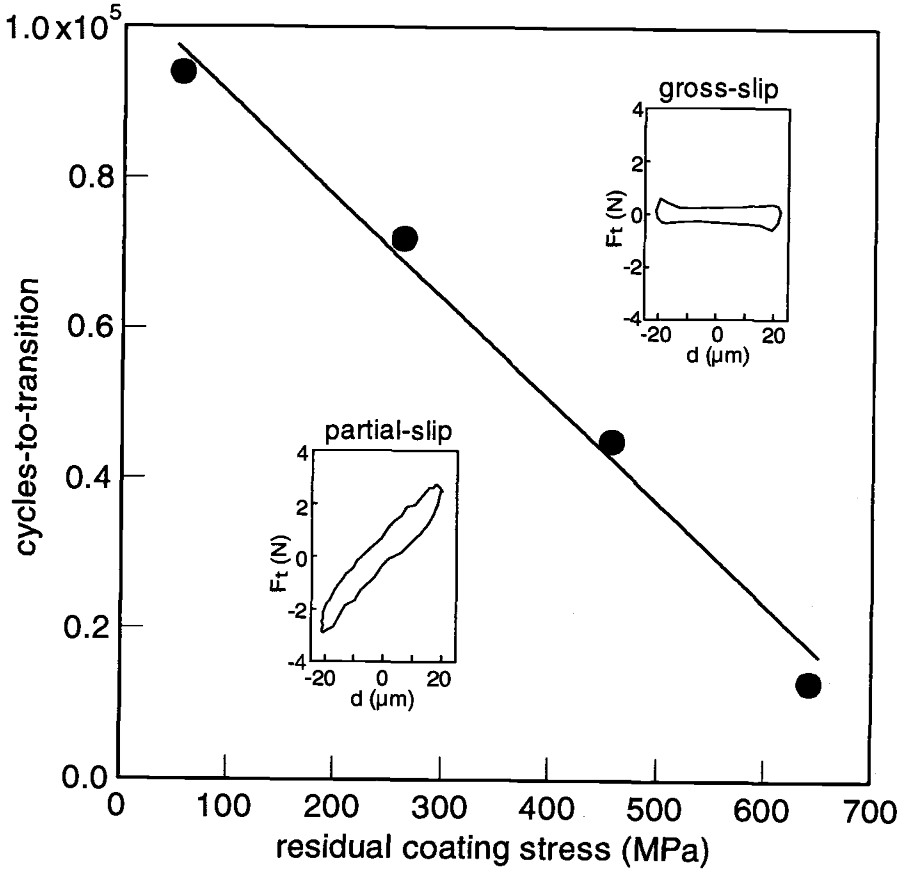

FIG. 6—*Influence of tensile residual stress in diamond coatings on the duration of the partial-slip regime under contact vibrations against corundum* (D = *50* μ*m*, F_n = *6 N, and* f = *20 Hz).*

in the range of 0.7 to about 1.5 The extent of the high friction phase is limited at medium humidity (RH = 40 to 60%). Under these conditions, the coefficient of friction returns to values below 0.25 where it remains stable. In dry air (RH < 30%), however, the coefficient of friction remains at a rather high level over the whole test duration.

The duration of the high friction phase is not only sensitive to the relative humidity but also to mechanical fretting variables. An increasing vibration frequency as well as an increasing normal force tend to extend the high friction phase in medium humid air (Fig. 8). An increase in one of these variables generally decreases the contact exposure to the test atmosphere [*7*]. As a consequence, the reduced access of oxygen and moisture to the surfaces in the vibrating contact has to be considered. TiN coatings subjected to contact vibrations were found to degrade by oxidational wear [*14*]. Moisture in the test atmosphere can then interact with the wear debris generated in the vibrating contact. Micro-Raman and XPS analysis have revealed that the wear debris consists of titanium oxide compounds of different Ti:O stoichiometry. The onset of low friction in the contact can be related to the accumulation of a bed of defective rutile (TiO_{2-x}) debris in the contact area [*7,14,16*]. Fine-grained defective oxide debris is assumed to aggregate

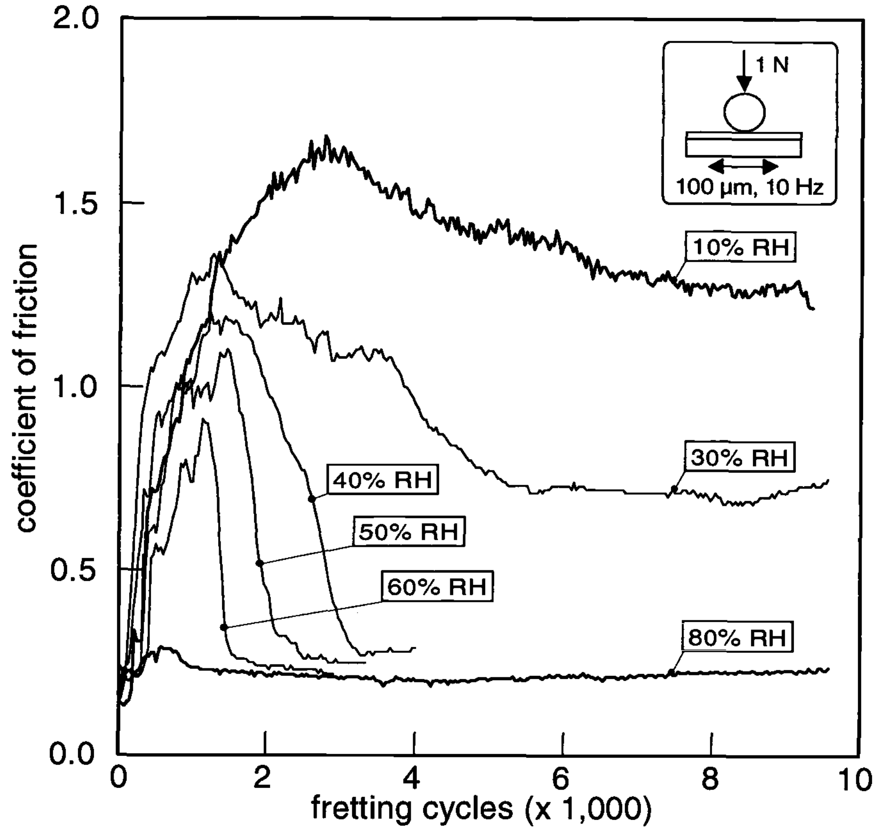

FIG. 7—*Evolution of the coefficient of friction on a TiN coating vibrating against corundum at different levels of relative humidity in the test atmosphere.*

by a weak bridge-bonding due to the absorption of moisture from the environment. Such bridge bonds usually offer a low resistance against shear stresses. Bulk shearing across the debris bed as a velocity accommodation mechanism would then result in a low tangential force accounting for the observed low coefficient of friction. The absorption of moisture is the rate controlling step in the formation of such a lubricious reaction layer. It is expected that the formation should be promoted by an increased relative humidity and an extended contact exposure.

The humidity also has an effect on the wear scar morphology on the coating. Fretting in a dry atmosphere results in a considerable lateral expansion of the damage area and in a high wear volume. At high humidity, wear proceeds preferentially into the coating depth generating a comparably small wear volume [7]. Figure 9 displays the increase of the wear volume as a function of the cumulative friction energy dissipated in the corresponding fretting tests. A linear relationship is maintained during the high and the low friction phases implying that the same degradation mechanism, namely, oxidational wear, is operative during both phases. This mechanism proceeds at a rate of about 18 000 $\mu m^3/J$ that holds for a wide range of fretting conditions. Therefore the possibility exists of a micrograph estimation of the wear volume on the TiN coating based on the on-line measured friction energy.

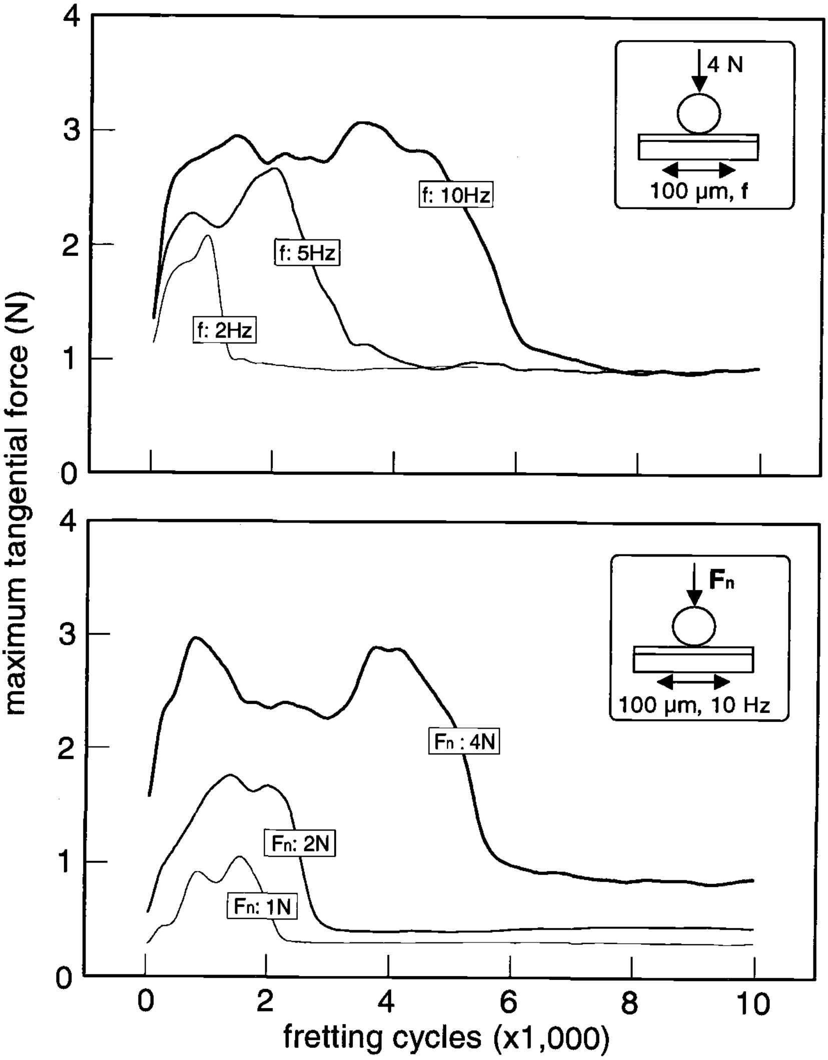

FIG. 8—*Influence of vibration frequency and normal force on the duration of the high friction phase on a TiN coating vibrating against corundum at medium relative humidity (50% RH) in the test atmosphere.*

TiN versus Chromium Steel—The relative humidity also affects the evolution in cases where TiN coatings vibrate against chromium steel counterbodies (Fig. 10). Although the friction behavior is similar to that observed with corundum counterbodies, differences are found during the running-in period as friction is instantly high. The magnitude of the coefficient of friction during the high friction phase is slightly lower, whereas it is nearly equal during the low friction phase as compared to corundum counterbodies. These deviations indicate that different wear and velocity accommodation mechanisms are active in the vibrating contact. Figure 11 displays the wear damage generated on the TiN coating under a normal force of 2 N at medium relative

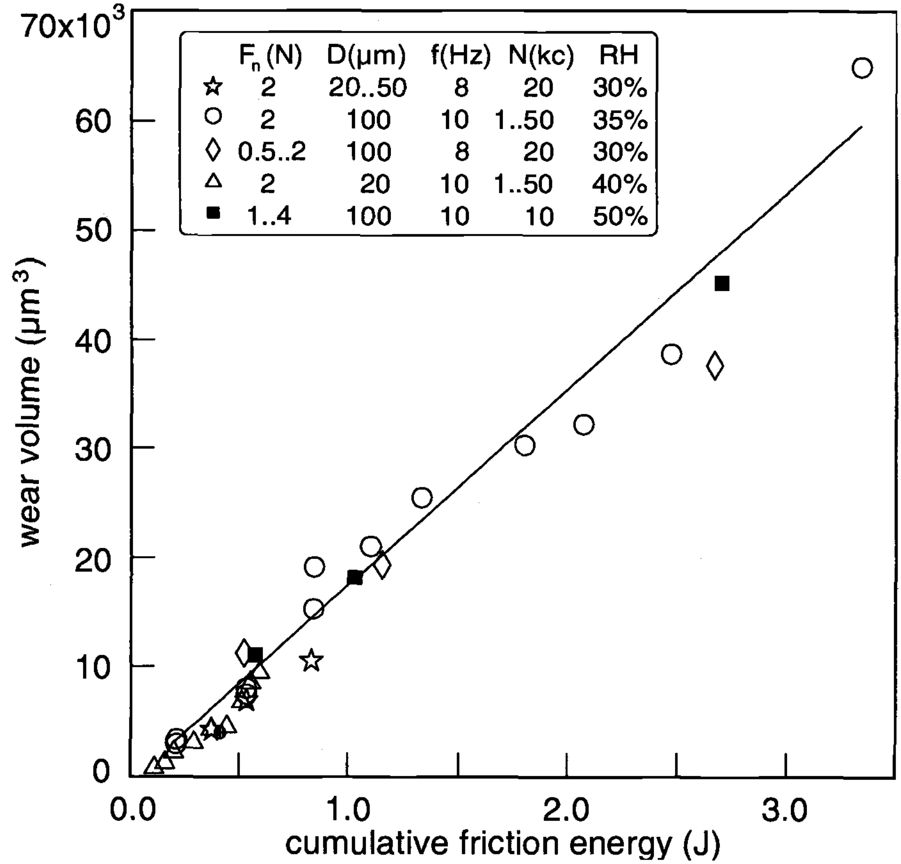

FIG. 9—*Wear volume measured on a TiN coating as a function of the cumulative friction energy dissipated during contact vibrations against corundum under various fretting conditions.*

humidity (50% RH). The Nomarski micrograph (Fig. 11*a*) reveals that the central part of the fretting scar is covered by a thin transfer layer protecting the TiN coating from being worn. Wear damage on the TiN coating occurs, however, in the peripheral regions of the fretting zone [*7*]. A close-up of the transfer layer by scanning electron microscopy shows features of extensive plastic deformation (Fig. 11*b*). Thin sheets of the counterbody material are smeared onto the coating along the sliding direction. The activation of velocity accommodation by plastic displacement requires that the tangential stress exceeds the yield limit of the counterbody steel [*12*]. This condition occurs most likely in the contact center where the Hertzian contact pressure has its maximum value. The coefficient of friction is determined as the ratio of the yield stress to the contact pressure. The latter decreases when the steel counterbody is flattened due to wear. Plastic sliding is then gradually replaced by other velocity accommodation mechanisms. The same low coefficient of friction ($\mu < 0.25$), as observed with corundum counterbodies, indicates that the lubricating effect provided by the defective TiO_{2-x} debris becomes active when sufficient moisture is present in the atmosphere. Therefore, titanium oxide debris generated in the peripheral region must spread to the central region. In the latter, the access of oxygen and

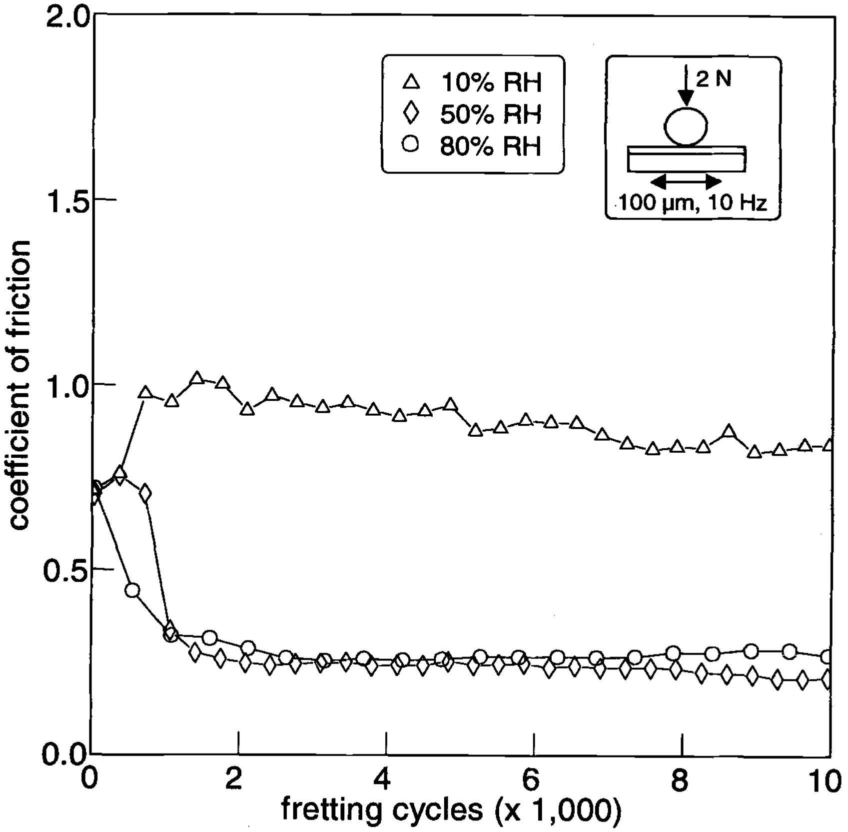

FIG. 10—*Evolution of the coefficient of friction on a TiN coating vibrating against chromium steel at different levels of relative humidity in the test atmosphere.*

moisture towards TiN is limited by the steel transfer layer. Partial oxidation of the transfer layer results in reddish iron-oxide particles, as observed by optical microscopy. Although the TiN coating wears only locally at the contact periphery, a linear relationship between the coating wear volume and the cumulative friction energy is also noticed. The wear rate of TiN (~20 000 $\mu m^3/J$) is quite comparable to that found with corundum counterbodies. The considerable wear of the hard TiN coating by the comparably soft chromium steel counterbody confirms the important role of tribochemical wear.

Conclusions

The potentiality of laboratory fretting testing as a method to evaluate the tribological performance of hard coatings in linearly vibrating contacts (Mode I fretting) was demonstrated. The critical influence of the linear displacement stroke, normal force, vibration frequency, and relative humidity on the mechanical and materials response of hard coatings was shown.

The friction and wear behavior of diamond coatings subjected to gross-slip vibrations against corundum become stable and predictable after a short running in phase. Coating degradation

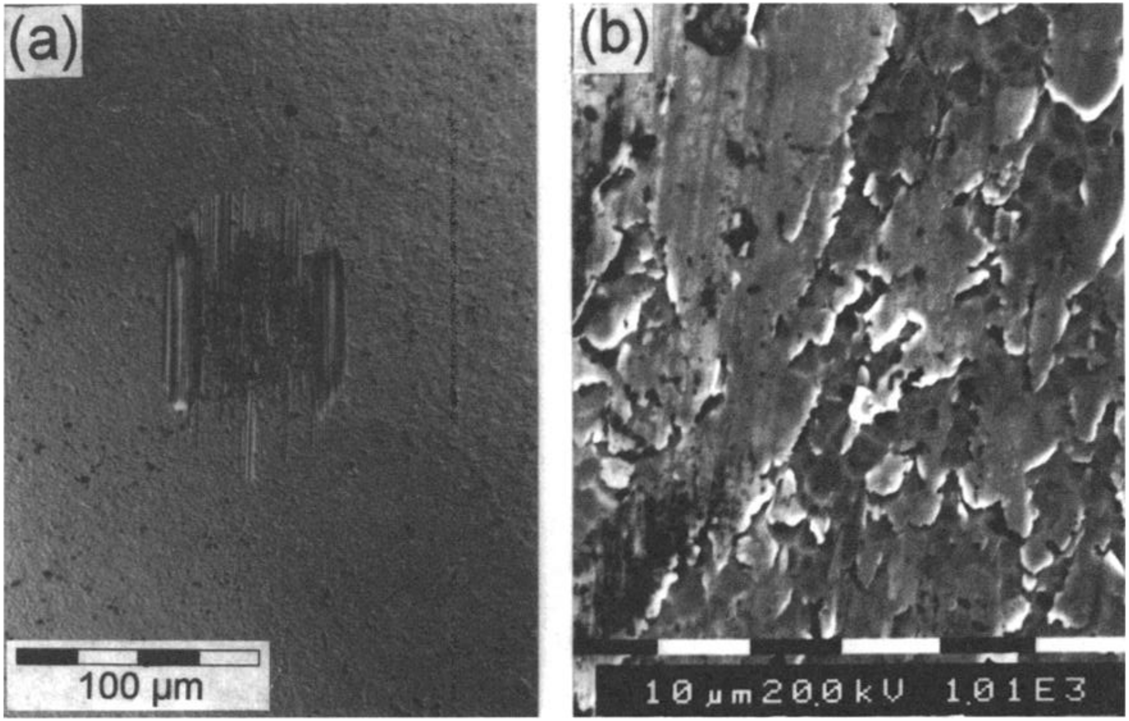

FIG. 11—(a) *Nomarski micrograph of a wear scar on a TiN coating after 10^4 fretting cycles against chromium steel* (D *= 100* µ*m,* F_n *= 2 N,* f *= 10 Hz, and 50% RH);* (b) *SEM micrograph of the steel transfer layer in the scar center.*

progresses by abrasive wear leading to a smooth coating surface. Velocity accommodation by debris particle rolling in the smoothened wear track results in low friction. Under partial-slip conditions, the diamond coating is subjected to contact fatigue. Fatigue failure in the contact zone results in a sudden significant alteration of the friction and wear behaviors. Variations in the onset of fatigue failure were explained by the level of residual stress present in the diamond coatings.

Friction and wear on TiN coatings subjected to gross-slip vibrations against corundum as well as chromium steel are controlled by tribochemical reactions in the fretting zone. The contact exposure and the relative humidity in the surrounding environment play an important role in this case. Titanium-oxide wear debris was found to form a lubricious layer in the contact after sufficient absorption of moisture from the environment. This tribochemical process is promoted by increased relative humidity and prolonged contact exposure. Velocity accommodation by shearing of the lubricious debris results in a reduction of friction. Coating wear is not observed when the access of oxygen and moisture towards TiN is limited by a transfer layer resulting from plastic wear of the steel counterbody.

The wear volume on both coating materials was shown to be proportional to the dissipated friction energy under gross-slip conditions. This energy-related wear rate permits an a priori estimation of the coating wear damage if the contact conditions can be specified.

Acknowledgments

Sincere thanks are addressed to Dr. T. Leyendecker (CemeCon GmbH, Aachen, Germany) and to M. Van Stappen for providing the diamond coatings and TiN coatings, respectively. The authors are indebted to the Commission of European Communities for providing a Human Capital and Mobility fellowship (HM) and to the National Fund for Scientific Research (NFWO, Belgium) for providing a postdoctoral fellowship (BB). This work was partly financed by a BRITE/EURAM project (BRE2-CT92-0224). The text presents research results by the Belgian program on Interuniversity Poles of Attraction initiated by the Belgian state.

References

[*1*] Waterhouse, R. B., "Fretting Wear," *ASM Handbook,* Vol. 18, ASM International, Metals Park, OH, 1992, pp. 242–256.

[*2*] Waterhouse, R. B., "Fretting Fatigue," *International Materials Reviews,* Vol. 37, No. 2, 1992, pp. 77–97.

[*3*] Holmberg, K., "A Concept for Friction Mechanisms of Coated Surfaces," *Surface and Coatings Technology,* Vol. 56, 1992, pp. 1–10.

[*4*] Blanpain, B., Celis, J. P., Roos, J., Ebberink, J., and Smeets, J. "A Comparative Study of the Fretting Wear of Hard Carbon Coatings," *Thin Solid Films,* Vol. 223, 1993, pp. 65–71.

[*5*] Mohrbacher, H., Celis, J. P., and Roos, J., "On the Laboratory Testing of Displacement and Load Induced Fretting," *Tribology International,* accepted for publication.

[*6*] Kennedy, P., Peterson, M. B., and Stallings, L., "An Evaluation of Fretting at Small Slip Amplitudes," *Materials Evaluation under Fretting Conditions, ASTM STP 780,* S. R. Brown, Ed., American Society for Testing and Materials, Philadelphia, 1982, pp. 30–48.

[*7*] Mohrbacher, H., Blanpain, B., Celis, J. P., and Roos, J., "The Influence of Humidity on the Fretting Behaviour of PVD TiN Coatings," *Wear,* Vol. 180, 1995, pp. 43–52.

[*8*] Vingsbo, O., "Fretting and Contact Fatigue Studied with the Aid of Fretting Maps," *Standardization of Fretting Fatigue Test Methods and Equipment, ASTM STP 1159,* M. H. Attia and R. B. Waterhouse, Eds., American Society for Testing and Materials, 1992, pp. 49–59.

[*9*] Vingsbo, O. and Söderberg, S., "On Fretting Maps," *Wear,* Vol. 126, 1988, pp. 131–147.

[*10*] Vincent, L., Berthier, Y., Dubourg, M. C., and Godet, M., "Mechanics and Materials in Fretting," *Wear,* Vol. 153, 1992, pp. 135–148.

[*11*] Vincent, L., Berthier, Y., and Godet, M., "Testing Methods in Fretting Fatigue: A Critical Appraisal,"

Standardization of Fretting Fatigue Test Methods and Equipment, ASTM STP 1159, M. H. Attia and R. B. Waterhouse, Eds., American Society for Testing and Materials, Philadelphia, 1992, pp. 33–48.

[*12*] Berthier, Y., Vincent, L., and Godet, M., "Velocity Accommodation in Fretting," *Wear,* Vol. 125, 1988, pp. 25–38.

[*13*] Mohrbacher, H., Blanpain, B., Celis, J. P., and Roos, J., "Low Amplitude Oscillating Sliding Wear on Chemically Vapour Deposited Diamond Coatings," *Diamond and Related Materials,* Vol. 2, 1993, pp. 879–884.

[*14*] Mohrbacher, H., Blanpain, B., Celis, J. P., Roos, J., Stals, L., and Van Stappen, M., "Oxidational Wear of TiN Coatings on Tool Steel and Nitrided Tool Steel in Unlubricated Fretting," *Wear,* in press.

[*15*] Mohrbacher, H., Blanpain, B., Celis, J. P., and Roos, J., "Frictional Behaviour of Diamond-Like Carbon and Diamond Coatings in Oscillating Sliding," *Surface and Coatings Technology,* Vol. 62, 1993, pp. 583–588.

[*16*] Mohrbacher, H., Blanpain, B., Celis, J. P., and Roos, J., "Raman Spectroscopy on Defective Wear Debris Generated by Contact Vibrations," *Journal of Materials Science Letters,* Vol. 14, 1995, pp. 279–281.

[*17*] Hayward, I. P., "Friction and Wear Properties of Diamonds and Diamond Coatings," *Surface and Coatings Technology,* Vol. 49, 1992, pp. 554–559.

[*18*] Van Acker, K., Mohrbacher, H., Blanpain, B., Van Houtte, P., and Celis, J. P., "Internal Stress Measurement on CVD Diamond Coatings by X-Ray Diffraction and Raman Spectroscopy," *Proceedings,* Materials Research Society Symposium, Materials Research Society, Pittsburgh, PA, Vol. 308, 1993, pp. 677–682.

[*19*] Mohrbacher, H., Van Acker, K., Blanpain, B., Van Houtte, P., and Celis, J. P., "Comparative Measurement of Residual Stress in Thin Diamond Coatings by Low-Incident-Beam-Angle-Diffraction and Micro Raman Spectroscopy," *Journal of Materials Research,* accepted for publication.

Paul J. Kennedy[1] *and Vinod S. Agarwala*[1]

Absorption of Organic Compounds and Organometallics on Ceramic Substrates for Wear Reduction

REFERENCE: Kennedy, P. J. and Agarwala, V. S., "**Absorption of Organic Compounds and Organometallics on Ceramic Substrates for Wear Reduction,**" *Effect of Surface Coatings and Treatments on Wear, ASTM STP 1278,* S. Bahadur, Ed., American Society for Testing and Materials, 1996, pp. 94–105.

ABSTRACT: The concept of employing thermally stable compounds (that is, metal oxides) as high temperature vapor phase ceramic lubricants was investigated. A major part of this study was devoted to the development of various calorimetric and tribological techniques that could be used to determine interfacial reactions between thermally stable compounds and ceramic substrates such as zirconia and alumina. This interaction is pivotal in understanding the mechanism of high temperature lubricity. The approach consisted of selecting low sublimation temperature materials and measuring their thermodynamic interactions as vapors with the ceramic substrates. The materials studied included two easily sublimable organic compounds (that is, naphthalene and salicylic acid) and several organometallics (for example, copper phthalocyanine). Thermodynamic data such as heat of adsorption, packing density, and reversibility of the adsorption were obtained on some of these compounds and were related to wear characteristics. All of these compounds provided effective lubrication at room temperature. Copper phthalocyanine was an effective lubricant at temperatures up to 400°C.

KEYWORDS: surface coatings, surface treatments, wear testing, high temperatures, lubricants, ceramics, organometallics, vapor phase lubrication, sublimation, bearing lubrication, adsorption, heat of adsorption, alumina

The lubrication of moving parts, achieved through either surface modification procedures, solid film coatings, or conventional lubrication techniques, represents a critical and limiting technological barrier. Old lubrication concepts need to be replaced so that we can begin operating in higher, more efficient temperature ranges. Over the last several decades, internal combustion engines have singularly relied on liquid (that is, oil-based) lubricant systems. This present-day reliance on lubricating oils is based on their inherent advantage of being able to maintain a liquid state over a wide temperature range. Liquid lubrication is based on the film forming properties of this state (that is, to act as a clean hydrodynamic film that prevents metal-to-metal contact). Under the more extreme conditions typically found in the internal combustion engine, the use of liquid lubricants is also dictated by the need to effectively act as both a heat sink and as a vehicle that can rapidly supply additives capable of modifying the wear characteristics of a surface. All of these properties are closely tied-in with the amenability of liquid lubricants to external cooling and filtration. The down-side to liquid lubrication is that present-day gas turbine engines are severely pushing the upper lubrication temperature limit of organic materials. Alternative lubrication concepts are needed.

---

[1] Research chemist and staff scientist, respectively, Aerospace Materials Division, Naval Air Warfare Center, Aircraft Division, Patuxent River, MD 20670-5304

Present-day gas turbine engines rely on basically the same lubrication principles that were initially developed for internal combustion engines except that turbine engine oil formulations depend on a more thermally stable, synthetic hydrocarbon base fluid. In the future, gas turbine engines will operate at much higher temperatures. More advanced generations of gas turbine engines will eventually operate in the adiabatic gas temperature range in order to achieve theoretical goals such as a 50% increase in thrust-to-weight ratio and a 100% increase in fuel efficiency. The primary problem in extending the operating temperature of turbine engine oils is that the carbon-carbon bond begins to breakdown at temperatures as low as 350°C. Presently, turbine engine oils are being pushed beyond this temperature limit through cooling and recirculation of the oil. In present-day turbine engines, bearing seal temperatures can approach 650°C. Future engines will definitely exceed the thermal capability of liquid lubricant systems (>800°C) and will require a new lubricant technology.

One approach that would negate the need to develop a new lubrication discipline would be to replace existing turbine engine bearings with either air foil or magnetic bearings. However, even in these cases, lubrication of support bearings would still be a factor. A considerable amount of work is also being done on the development of high temperature lubrication systems for conventionally designed ceramic bearings. One of several promising approaches involves the use of a vapor phase lubrication system. In vapor lubrication, a constant stream of a gas, vapor, or a vapor in a carrier gas is directed onto moving mechanical assemblies in order to reduce wear. Work has shown that nickel-coated alumina components, when exposed to ethylene gas at 500°C, will catalytically decompose the hydrocarbon forming a lubricious microcrystalline graphitic carbon coating [*1,2*]. Another approach involves the use of tricresyl phosphate (TCP) as a vapor-delivered lubricant for temperatures ranging from 500 to 800°C. Again, metals would be needed as a source of catalytic activity [*3,4*]. This vapor lubrication approach has been extended to a rig simulating an advanced diesel engine [*5*]. Other areas of research involve the use of solid lubricants for high temperature applications. Present-day solid lubricants such as molybdenum and tungsten disulfides decompose at temperatures of 400°C, however, there are several compounds such as tungsten trioxide and cerium fluoride that have melting points in excess of 1000°C. These compounds have been shown to provide good lubricity [*6*]. Other approaches involve incorporation of friction-modifying substances into the surface structure of ceramics by ion implantation. Boron ion implantation has been shown to significantly reduce wear [*7*]. Another area of research involves investigating the possibility of transferring lubricating material from bearing ball retainers to the ball/raceway area [*8*].

Our intent was to extend our knowledge of vapor lubrication systems, to investigate other unusual materials as vapor phase lubricants, and to lay the groundwork for the development of a lubricant system that could operate from ambient to 800°C. The decision to investigate vapor lubrication systems was based on the assumption that effective lubrication would require constant replenishment. Nonreplenishable systems would include techniques such as surface modification procedures or the use of bonded solid coatings. It was planned to establish fundamental concepts of interfacial reactions for the selection of vapor lubrication systems capable of providing low friction and wear at elevated temperatures and high contact pressures. Thermodynamic data collected from selected vapor lubrication systems would then be correlated with tribological data in order to develop the foundation for a vapor lubrication model. The vapor phase lubrication system should be similar to a liquid lubrication system in that they would both be dependent upon the adsorption of anti-wear additives. The major penalty associated with this approach is the loss in the hydrodynamic component of lubrication, but this component is relatively small during high load conditions. The advantage of this approach is that the temperature restrictions imposed by the liquid state are no longer relevant.

Experimental Details

Specimens

The ceramic substrates that were studied include alumina, zirconia, and silicon nitride wear specimens. A high surface area adsorption alumina (that is, 232 m^2/g) was used in most of the adsorption experiments. This powder was dried at either 130 or 400°C to eliminate adsorbed water [*9*].

Analytical Techniques

Interactions between a lubricant in the vapor phase and a ceramic substrate are defined by such parameters as heat of adsorption, surface packing density, adsorption constants, and reversibility of the adsorption process. Four techniques that were investigated included gas chromatography, differential scanning calorimetry, vapor phase flow calorimetry, and liquid phase flow calorimetry. A gas chromatograph (GC) was used to measure naphthalene vapor concentrations. Temperature was maintained at 100°C for 1 min and ramped to 250°C and 6°C/min. The helium flow rate was 20 mL/min. A thermal analyzer and differential scanning calorimeter (DSC) was used to measure heats of adsorption. A flow calorimeter (Fig. 1) equipped with two syringe pumps was used to measure additive adsorption from the vapor and liquid phase. The calorimeter consists of a large steel block containing a central channel approximately 8 mm in diameter. An insert that fits into the base of the calorimeter serves as the base for a small column (typically 0.12 cm^3) of ceramic powder. The temperature of the column is measured by means of a four-thermistor bridge. Two thermistors are inserted into the column and two are located in the block. The primary function of the steel block is to act as either a heat sink or source. Prior to a measurement, the column and block are at thermal equilibrium and the thermistor bridge is in balance. After achieving thermal equilibrium, a solvent such as cyclohexane is slowly passed through the central channel at a rate slow enough to allow the solvent to reach block temperature (for example, 6.6 mL/h). When the solvent reaches the column and percolates through, no heat effects other than an initial heat of wetting are noted since the

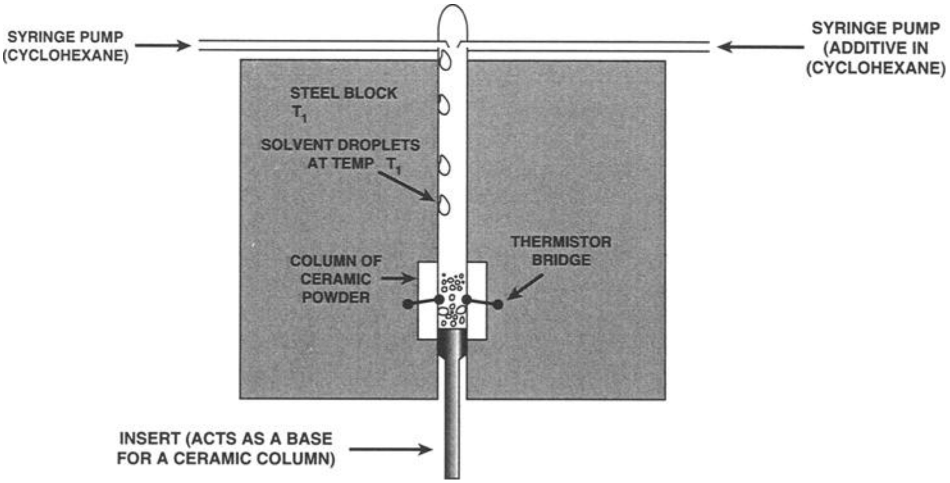

FIG. 1—*Flow calorimeter for measuring heats of adsorption.*

solvent, block, and column are at thermal equilibrium. When an additive in the solvent is present, it will adsorb and create a heat effect that will be detected by the thermistor bridge. The calorimeter can also be used with gas phases containing adsorbable vapors.

Wear Testing

The anti-wear characteristics associated with a given monolayer are quantified using a ball-on-flat wear test device (Fig. 2). The device provides for the mounting of a 12.7-mm-diameter ball against a stationary 38 by 6 mm flat specimen. The ball is attached to a movable arm that is driven by means of a reciprocating air motor. This arm is attached to the rig by means of a double-axes universal joint. The wear scar that is formed on the surface of the flat, is in the shape of an arced wear path and is approximately 50 mm in length. This path is transversed at a rate of approximately 20 cycles/min. Load, speed, and temperature can be varied. The load calculated at the ball/flat contact point, is applied by counterbalancing the weight of the arm and can range from 5 to 100 N. The temperature is controlled by cartridge heating elements above the ball and below the flat specimen. The device can be operated at temperatures up to 800°C. During high temperature operation, set screws that hold the ball in place need to be tightened in order to prevent rotational motion of the ball specimen. The coefficient of friction is determined by measuring the tangential force with a strain gage attached at the point where the air motor is connected to the movable arm. After testing, wear scars are quantified using a three-dimensional surface profilometer.

Results

Experiments were performed to determine if a vaporized compound would behave similarly to that of an antiwear additive in an oil-based lubricant. Primary interests were in the ability of vapors to adsorb on ceramic substrates and produce significant reductions in wear rates. Concerns were (1) the concentration of the material in the vapor phase as a function of temperature, (2) the adsorption equilibrium constant for the vapor on the ceramic, and (3) the ability of the adsorbed material to reduce the wear rate of the ceramic below that of the unlu-

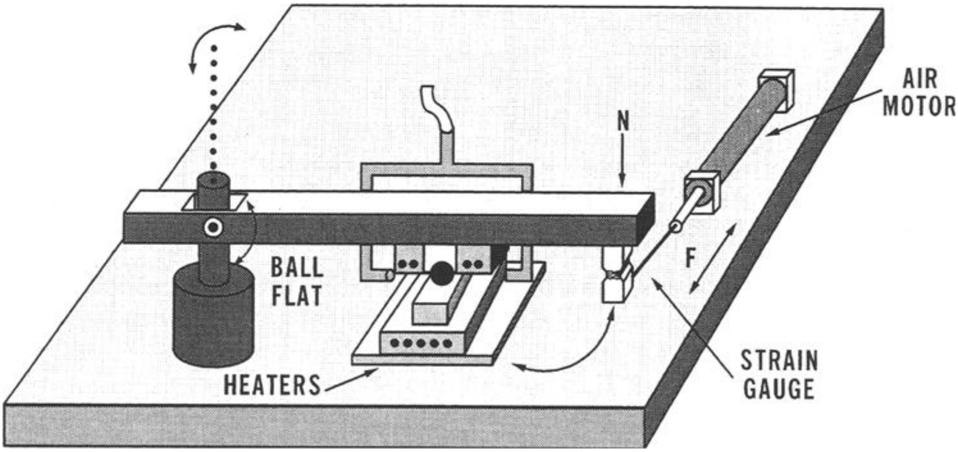

FIG. 2—*Wear test device for measuring coefficient of friction.*

bricated material. Initially, concerns were with developing techniques that would allow determination of heats of adsorption, reversibility of adsorption, adsorption equilibrium constants, and packing density.

Several systems of varying complexity were investigated. The first system consisted of naphthalene vapor on alumina. This system was chosen because naphthalene (melting point of 82°C) sublimes and has a significant vapor pressure at room temperature. In addition, its structure is similar to naphthenic oils that are known for their excellent lubricating properties. Most of these studies were done with a high-surface-area alumina powder to maximize surface-related effects. Different experimental approaches were used in the measurement of adsorption constants. These included the use of gas chromatography (GC) for measuring equilibrium concentrations of vapors, a calorimeter for measuring heats and the reversibility of adsorption, and a DSC for measuring surface concentrations. The coefficient of friction and wear were measured using the wear test defice. Gas chromatography proved to be the most limited technique. Liquid flow calorimetery techniques did provide data on a limited number of systems. The most successful technique was a method that was developed for the DSC. All candidate materials could be evaluated for their ability to reduce the coefficient of friction and wear rate.

Gas Chromatographic Studies

Adsorption constants for naphthalene vapor on alumina powder were investigated by using standard absorption isotherm techniques. The procedure consisted of introducing known amounts of naphthalene vapor into 5-mL vials containing various amounts of alumina powder. After equilibration, vapor equilibrium concentrations were re-analyzed to determine the amount of naphthalene adsorbed on the surface of the alumina. The initial calibration of GC using dilute solutions of naphthalene in cyclohexane indicated a lower limit of detection of less than 0.1 μg. Analysis of the vapor drawn from a bottle of naphthalene at room temperature indicated a concentration of 0.4 μg/mL. The calculated equilibrium vapor concentration for naphthalene at room temperature is 0.6 μg/mL. This technique should be able to measure moderately small changes in vapor concentration and provide a means of determining equilibrium constants and maximum packing densities. Actual experiments consisted of adding 2.5 mL of 0.28 μg/mL naphthalene vapor into vials that contained amounts of alumina ranging from 0 to 100 mg. The measured equilibrium concentrations were in the 0.01 to 0.02 μg/mL range and were essentially independent of the amount of alumina in the vial. The difficulty with this approach was that the internal surface area of the syringe and vial was sufficient to adsorb a significant amount of the naphthalene in the vapor phase. Assuming a moderate molecular packing density (that is, 1 nm^2/molecule), a relatively small amount of exposed glass surface (that is, an area of approximately 14 cm^2) could possibly reduce the initial vapor concentration to zero. Another approach consisted of coating glass beads with small amounts of alumina powder and using these coated beads to make adsorption columns. Air saturated with naphthalene vapor was then passed through the column, collected and analyzed using GC. Results indicated that the glass wool plugs that held the column in place adsorbed most of the naphthalene vapor and reduced the vapor concentration to approximately 0.05 μg/mL. Equilibrium concentrations after adsorption were close to this amount, and it was difficult to distinguish if adsorption was on the glass beads, alumina, or the plug material. Later studies involved injecting naphthalene vapor through an alumina column directly into the GC. These studies indicated that all of the naphthalene vapor was strongly and irreversibly adsorbed on the alumina column.

Vapor Flow Calorimetry

The possibility of directly measuring the heat of adsorption of naphthalene vapor on alumina was investigated using a flow calorimeter modified for gas usage. This calorimeter contained a small column of alumina that weighed approximately 100 mg. The temperature of the column relative to that of the block was measured by means of a four-thermistor bridge. Nitrogen gas was passed through the column at a rate of 8.5 mL/min and, after attaining equilibrium, air saturated with naphthalene vapor was introduced into the nitrogen flow at a rate of 1 mL/min. The calorimeter can detect a sustained heat effect of 1 mJ/min or possibly an instantaneous heat effect as small as 4 μJ. Results showed minimal heat effects of about 1 mJ/min during the adsorption of naphthalene of alumina. It was difficult to determine if these observed heat effects were due to the failure of the carrier gas in attaining thermal equilibrium or if these effects were due to adsorption. A significant problem with this approach was that the flow rates of naphthalene vapor limited adsorption to less than 0.4 μg/min. Vapors associated with other compounds having potential lubricating properties were investigated to establish the viability of this approach. Vapors of compounds such as salicylic acid, benzophenone, and phenol gave no response. Quinone, camphor, adipic acid, and "lab" air gave questionable responses. Octadecylmercaptan, dioctylamine, tert-octylamine, naphthalacetic acid, 1,2, dodecanediol, menthol, and water-saturated air gave possible responses. Compounds such as hexanoic acid, tridecanoic acid, iodine, 2-hydroxylmyristic acid, and *t*-butanol showed relatively small, but definite, heat effects associated with vapor adsorption. Of the different materials tested, hexanoic acid vapor at room temperature showed the largest heat effect.

Solution Flow Calorimetry

The relatively low vapor pressure of most solids at room temperature limits the effectiveness of vapor phase calorimetry for determining adsorption characteristics. However, it should be possible to obtain similar data using a solution flow calorimeter approach. The primary assumption is that heats of adsorption from the liquid phase should approximate heats of adsorption from the vapor phase if the material of interest is dissolved into an inert solvent. Hydrocarbons such as cyclohexane should not adsorb on a ceramic substrate to any appreciable extent since they lack double bonds and polar functional groups. Through the use of nonpolar solvents, initial concentrations and related heat effects associated with adsorption can be increased by a factor of 10^4. Figure 3 shows heat of adsorption data for 5% naphthalene in dry cyclohexane on an alumina column. Naphthalene from cyclohexane solution was initially adsorbed on a 0.18-g column. Adsorbed naphthalene was then desorbed using pure cyclohexane. This adsorption and desorption process was repeated several times on the same column in order to determine if the adsorption process was reversible. The heat effect associated with adsorption was 3.7 J/g and was essentially constant in repeat adsorption experiments. This would indicate that naphthalene adsorption on alumina was completely reversible. Although *n*-butanol is not considered a good lubricant, tests on a freshly prepared column of alumina indicated a stronger heat effect associated with adsorption. Initially, this heat effect was about 10.5 J/g, but each subsequent desorption/re-adsorption cycle resulted in a decrease in the measured heat effect. In this case, a fraction of the alcohol is irreversibly adsorbed on the surface of the alumina.

In the preceding procedure, a liquid having a known initial concentration of naphthalene is percolated through a column of alumina powder for an extended period of time. The subsequent heat effect is produced from an equilibrium concentration nearly equal to the initial concentration of naphthalene. The major drawback of this technique is that the amount of naphthalene adsorbed from solution can not be measured and this makes it difficult to estimate heats of adsorption. Another approach involves injecting small amounts of naphthalene into the cyclohexane carrier stream. Using this type of approach (that is, 25 μL injections of 5% naphthalene) and assuming that all naphthalene injected into the column is adsorbed, the heat of adsorption can be directly measured. The heat of adsorption for naphthalene using the injection technique was found to be 1.5 kJ/mol. In this study, naphthalene was an ideal candidate since relatively high concentrations could be dissolved in a nonpolar solvent (that is, cyclohexane) that would

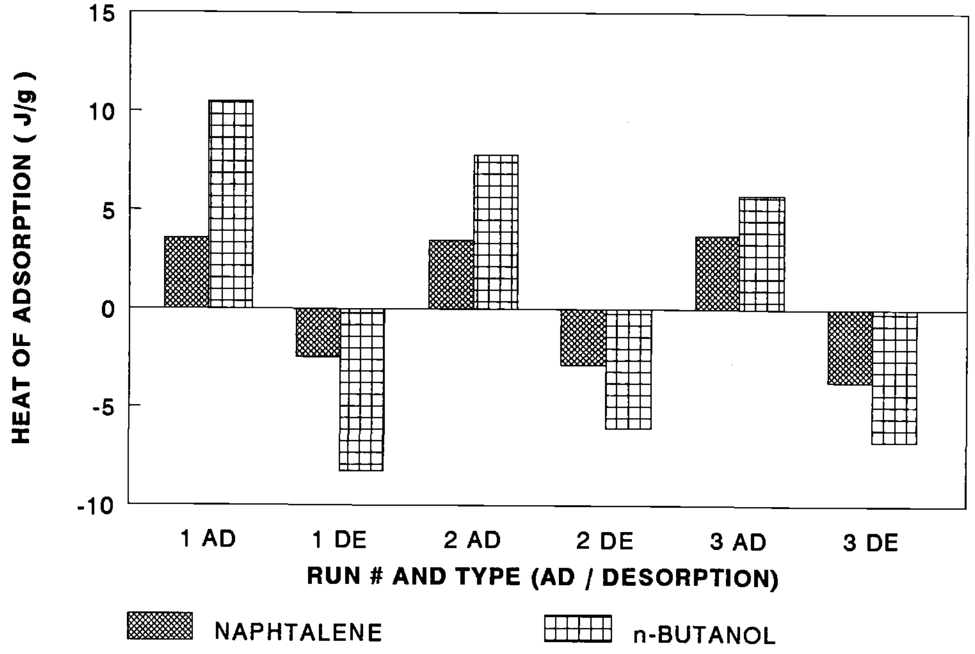

FIG. 3—*Heat of adsorption from a 5%* C_6H_{12} *solution of naphthalene on alumina.*

not compete for adsorption. The other compound of particular interest, salicylic acid, also sublimes at fairly low temperatures, but studies on this material were limited because of its relatively low solubility in nonpolar solvents. Similar measurements with salicylic acid were difficult to quantify because of the extremely low solubility of this material in cyclohexane. The heat of adsorption for salicylic acid (that is, 25-μL injection of 0.05% salicylic acid) was estimated as 3.4 kJ/mol. These results are shown as footnotes in Table 1.

Another class of materials, organometallics, were also investigated for solubility in nonpolar

TABLE 1—*Adsorption characteristics of naphthalene and salicylic acid on alumina.*

Adsorbate Concentration in Al_2O_3, % by weight	Amount Adsorbed per Unit Area (μmol/m^2)	
	Naphthalene[a]	Salicylic Acid[b]
10%	3.49	...
20%	...	7.75
30%	7.79	7.45
40%	...	7.55
50%	7.78	5.03
60%	...	7.09
70%	...	7.49
80%	...	6.86

[a] Flow calorimetry studies indicated that the heat of adsorption on alumina was 1.5 kJ/mol (from 25 μL of 5% naphthalene solution in C_6H_{12}).

[b] Flow calorimetry studies indicated that the heat of adsorption on alumina was approximately 3.4 kJ/mol (from 25 μL of 0.05% salicylic acid solution in C_6H_{12}).

and then in polar solvents. At higher temperatures, these materials may have sufficient vapor pressure to provide lubrication to ceramic bearings. These adsorbed vapors might then decompose under load and higher temperatures to form small amounts of solid stable oxides that would be effective in reducing friction and wear. These materials included selenourea, copper phthalocyanine, vanadium oxide tetraphenylporphine, quaternary amine molybdata, manganese phthalocyanine, copper tetraphenylporphine, iron dicyanophenanthroline, nickel trimethylpyridine *t*-sulfonate, copper salicylaldehyde ethylene diimine Schiff base, and copper salicylaldehyde phenylene diimine Schiff base. Solvents investigated included water, methanol, isopropanol, acetone, xylene, toluene, heptane, dimethylformamide (DMF), and mineral oil. The most promising solvent was DMF. Most of the organometallics dissolved to some extent in DMF to form highly colored solutions, but the concentrations of dissolved material were less than 0.05%. This low solubility was true for most of the solvents tested. For example, copper tetraphenylporphine dissolved to form a rose-colored solution at a concentration of less than 0.001% in cyclohexane. Testing of these materials was primarily limited to studying their effect on the coefficient of friction and wear inhibition.

Differential Scanning Calorimetry

Another approach to studying the thermodynamic interaction of potential vapor lubricants with ceramics involves the use of a DSC. Of all of the analytical techniques used in this study, this approach appears to be the most universally applicable. In this technique, alumina and the vapor phase lubricant (that is, salicylic acid or naphthalene) are mixed and stored overnight in a sealed vial. Approximately 10 mg of this mixture was then analyzed in the DSC. Typical results are shown for salicylic acid (Fig. 4). The heat of fusion of salicylic acid was found to

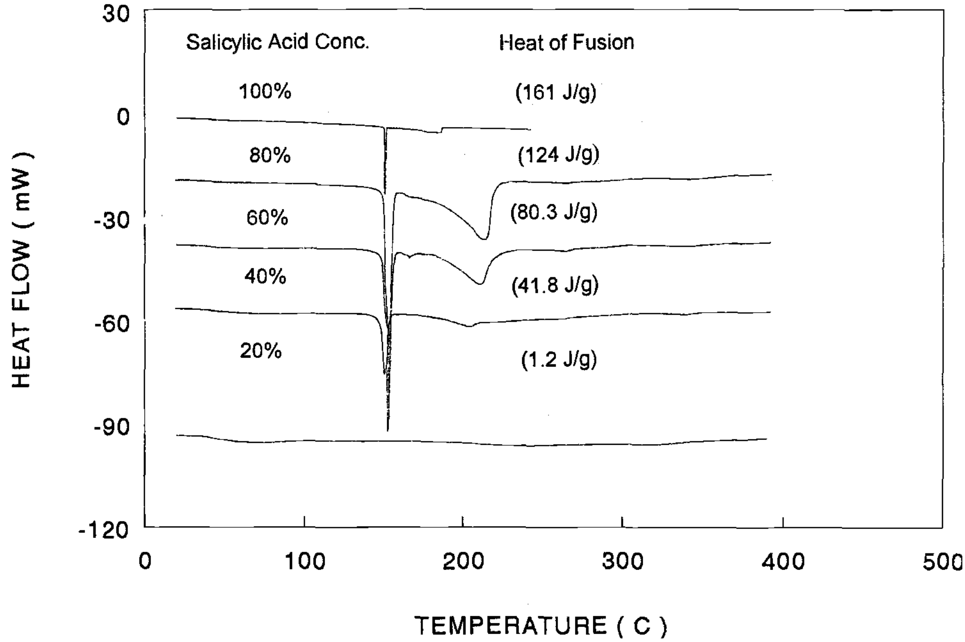

FIG. 4—*Effect of alumina on the measured heat of fusion of salicylic acid.*

be 161 J/g. The traces of several mixtures by weight of salicylic acid and alumina shows the "instrument calculated" heat of fusion that is equal to the measured heat effect divided by the weight of material in the sample pan. If it is assumed that there is no interaction between the salicylic acid and the alumina, then the heat of fusion would be equal to the "instrument calculated" heat multiplied by the fraction of salicylic acid in the mixture. For example, the instrument calculated heat of fusion for the 20% mixture of salicylic acid with alumina should be 36.2 J/g. The measured value of 1.2 J/g indicated that only 3% of the salicylic acid in the mixture was available to contribute to the heat of fusion. In general, as the percent of salicylic acid in the mixture decreased, the amount adsorbed increased. The calculated value for the maximum packing density for salicylic acid on alumina (Table 1) and was found to be 7.75 μmol/m^2.

The naphthalene vapor/alumina system was also studied using the DSC and the preceding technique. The heat of fusion for naphthalene was reported in the International Critical Tables as 148.9 J/g that compares favorably with our measured value of 144 J/g. Heat of vaporization was reported as 316 J/g, which is higher than our measured value of 258 J/g. Since the alumina is submicron (232 m^2/g), 50% by weight mixtures of naphthalene and alumina powder should provide monolayer or less coverage. It was assumed that pre-adsorbed naphthalene would not contribute to the heat of fusion and the experimentally measured heat of fusion would be an indirect measure of the amount of naphthalene adsorbed on the alumina. A series of experiments at different mole fractions of naphthalene indicate that the packing density for naphthalene on alumina is 7.8 μmol/m^2. The packing densities for salicylic acid and naphthalene are similar. The organometallics were also investigated using DSC techniques. Some of the compounds such as iron dicyanophenanthroline, copper tetraphenylporphine, and manganese phthalocya-

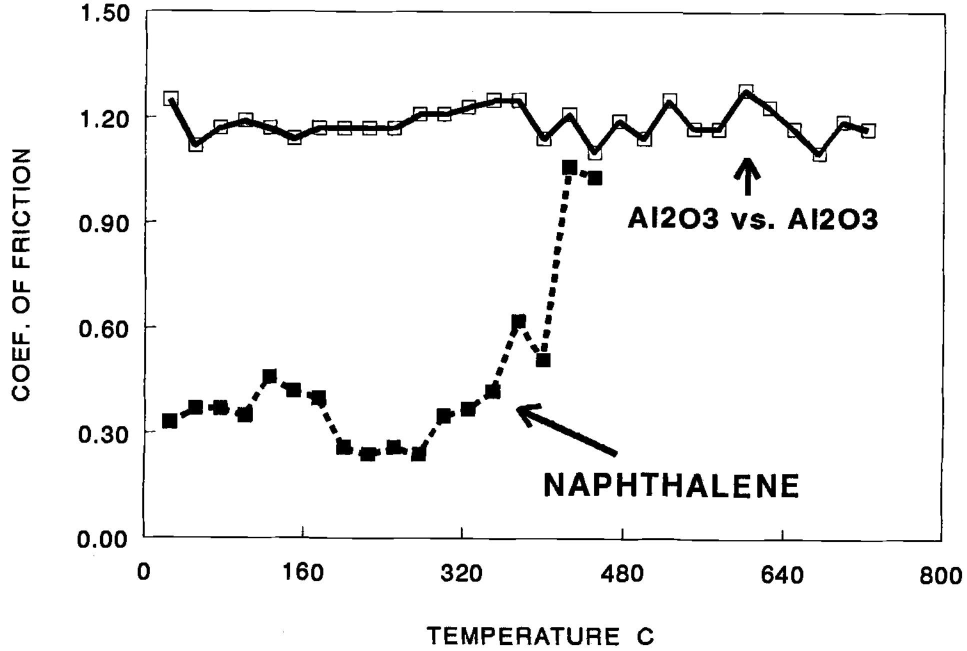

FIG. 5—*Effect of naphthalene on friction of alumina sliding on alumina.*

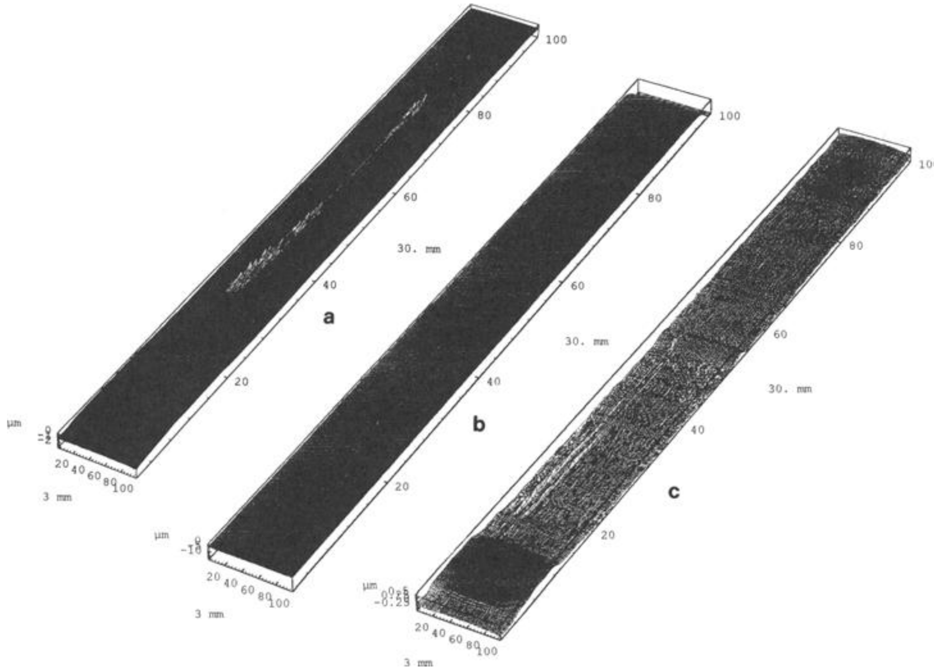

FIG. 6—*Wear scars formed at room temperature on* (A) *unlubricated* ZrO_2 *and on* ZrO_2 *lubricated with* (B) *powdered naphthalene and* (C) *powdered salicylic acid.*

nine had melting points between 400 and 500°C. Nickel trimethylpyridine *t*-sulfonate underwent a thermal transition at 200°C. Future DSC studies of these compounds are planned.

Wear Testing

Friction measurements from the ball-on-flat wear tester (Fig. 5) are shown for an alumina ball sliding against an alumina flat when lubricated with naphthalene. Since naphthalene crystals were spooned onto the ball/flat contact region as needed, naphthalene was effective at temperatures much higher than its melting point of 82°C. The application of naphthalene reduced the coefficient of friction from 1.2 to 0.3 for temperatures up to 300°C. Figure 6 shows several tracings of wear scars formed at room temperature using a zirconia ball on a zirconia flat. Figure 6*a* shows the wear scar formed under unlubricated conditions. Figure 6*b* shows the effect of naphthalene lubrication, and Fig. 6*c* shows the effect of salicylic acid lubrication. Salicylic acid was slightly less effective than naphthalene in reducing the amount of wear. Figure 7 shows the effect of copper phthalocyanine on the lubrication process at a temperature of 400°C. In this study, lubricant was only added at the start of the high temperature test. Copper phthalocyanine was highly effective in reducing wear at higher temperatures.

Discussion

Initially, we decided to investigate materials that were capable of subliming at or near room temperature and were soluble in hydrocarbon solvents. Our goal was to eventually study stable

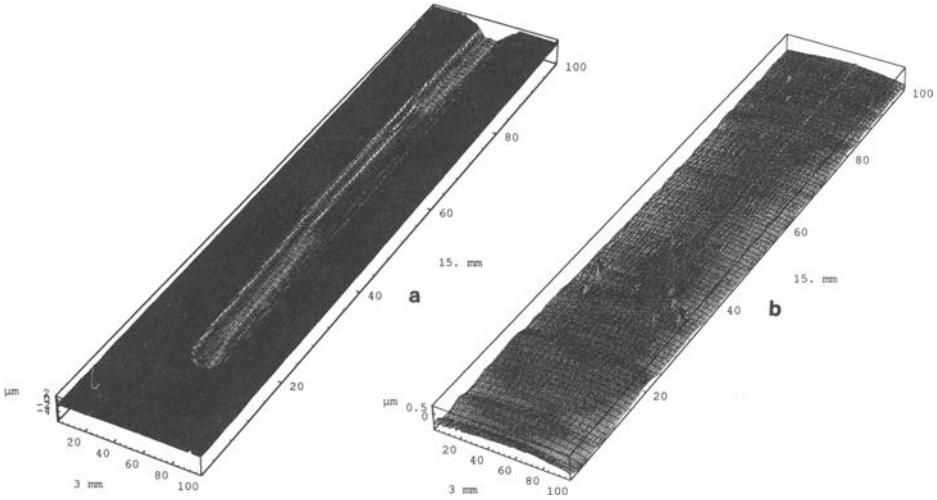

FIG. 7—*Wear scars formed at 400°C on* (A) *unlubricated ZrO_2 and on* (B) *ZrO_2 lubricated with powdered copper phthalocyanine.*

metal oxides as high temperature lubricants using techniques developed during these lower temperature studies. As an intermediate step, some work was done with organometallics as a possible mechanism for transporting a metal oxide to a hot surface at temperatures much less than the melting point of the metal oxide. Copper phthalocyanine was found to be a highly effective lubricant at higher temperatures but no correlation was made with its adsorption characteristics. A significant amount of success was achieved with the naphthalene/alumina and salicylic acid/alumina systems in correlating adsorption data with wear data. Parameters that were of primary interest were the amount of material adsorbed per unit area, the reversibility of adsorption, and heat of adsorption. The packing density of naphthalene was relatively low with a surface concentration of 7.8 $\mu mol/m^2$ that corresponds to a surface coverage of approximately 20 nm^2/molecule. The heat of adsorption was a relatively low 1.5 kJ/mol and the adsorption was reversible. Wear tests under heavy load indicated that naphthalene was effective at reducing the coefficient of friction from 1.2 to 0.3 and that it also prevented wear when tested at room temperature. The packing density of salicylic acid was similar with a surface concentration of 7.75 $\mu mol/m^2$. The heat of adsorption was approximately 3.4 kJ/mol and significantly higher than that found for naphthalene. Surprisingly, salicylic acid was not quite as effective as naphthalene in reducing wear. Compounds such as molybdenum telluride were initially studied and were found to be very effective. Such materials, however, were not studied further because of potential experimental and health risks.

Conclusions

Thermodynamic data obtained for adsorption of naphthalene and salicylic acid on alumina indicated relatively weak interactions (that is, less than 4 kJ/mol) and significantly less than the theoretical packing density in the adsorbed monolayers. The friction and wear measurements showed that these compounds served as highly effective lubricants on ceramics. This suggests that the lubrication of ceramics does not necessarily require strong surface adsorption and close packing in the monolayer. Wear studies also show that copper phthalocyanine was an effective lubricant on alumina and zirconia at temperatures up to 400°C.

References

[*1*] Lauer, J. L. and Dwyer, S. R., "Continuous High Temperature Lubrication of Ceramics by Carbon Generated Catalytically formed Hydrocarbon Gas," *Tribology Transactions*, Vol. 33, No. 4, 1990, pp. 529–534.

[*2*] Lauer J. L., Vlcek, B. L., and Sargent, B. L., "Wear Reduction by Pyrolytic Carbon on Tribosurfaces," *Wear*, Vol. 162-164, 1993, pp. 498–507.

[*3*] Makki, J. and Graham, E., "Formation of Solid Films from the Vapor Phase on High Temperature Surfaces," *Lubrication Engineering*, Vol. 47, No. 3, 1992, pp. 199–206.

[*4*] Graham, E. E. and Klaus, E. E., "Lubrication from the Vapor Phase at High Temperatures," *Transactions*, American Society of Lubrication Engineers, Vol. 29, No. 2, 1986, pp. 229–234.

[*5*] Groeneweg, M., Hakim N., Barber, G. C., and Klaus, E., "Vapor Delivered Lubrication of Diesel Engines—Cylinder Kit Rig Simulation," *Lubrication Engineering*, Vol. 47, No. 12, 1991, pp. 1035–1039.

[*6*] Murray, S. F. and Calabrese, S. J., "Effect of Solid Lubricants on Low Speed Sliding Behavior of Silicon Nitride at Temperatures to 800° C," *Lubrication Engineering*, Vol. 49, No. 12, 1993, pp. 955–964.

[*7*] Kobel, W. and Sate, A., "Effect of Boron Ion Implantation on Tribological Properties of CAD Silicon Nitride," *Lubrication Engineering*, Vol. 46, No. 10, 1990, pp. 645–650.

[*8*] Ruff, A. W. and Peterson, M. B., "Wear of Selected Materials and Composites Sliding against Molybdenum Disulfide Films," *Wear*, Vol. 162–164, 1993, pp. 492–497.

[*9*] Ravikiran, A. and Pramila Bai, B. N., "Water-Lubricated Sliding of Alumina against Steel," *Wear*, Vol. 171, 1993, pp. 33–39.

Subbiah Ramalingam[1] *and Lanshi Zheng*[1]

Coating-Substrate Interface Stress Management in Wear Protection of Light Alloy Components

---

REFERENCE: Ramalingam, S. and Zheng, L., "**Coating-Substrate Interface Stress Management in Wear Protection of Light Alloy Components,**" *Effect of Surface Coatings and Treatments on Wear, ASTM STP 1278,* S. Bahadur, Ed., American Society for Testing and Materials, 1996, pp. 106–123.

ABSTRACT: Hard coating light alloys for wear protection presents an interface stress problem due to mismatch in elastic constants across the film-substrate interface. The displacement formulation method is used in this work to calculate interface stresses as a function of contact parameters, coating/substrate properties, and coating thickness. Quantitative results obtained suggests that interface stresses can be managed with a judicious choice of coating materials, film thickness, contact parameters, and film deposition conditions.

KEYWORDS: surface coatings, surface treatments, wear testing, wear protection film-substrate interface, hard coatings

Components made of light alloys of aluminum, magnesium, and titanium tend to fail by excessive wear when used in tribological applications. This problem is difficult to avoid even with lubrication when the contact stresses are high. Thin coatings of hard materials may be used to overcome this difficulty. However, the use of hard coatings on light alloys introduces a new problem. The substrate is much more compliant than the coating. For TiN on aluminum alloys, the Young's modulus ratio of titanium nitride to aluminum is approximately eight. When the coated material is loaded, the differential displacements generated in the substrate and the coating, due to differences in elastic moduli, can lead to high stresses in the film and at the film-substrate interface. Film fracture and film-substrate debonding can then occur leading to severe wear in closed tribological systems. Film-substrate interface stresses will have to be managed to avoid this difficulty. The problem of calculating interface stresses is first considered, and an approach is developed that yields quantitative results. With the calculated stresses, it is shown that interface stresses can be managed through a choice of contact conditions, coatings, coating thickness, and film deposition conditions.

Overview of Earlier Studies

Although tribo-contacts are three-dimensional in character, a great deal can be understood with two-dimensional modeling. Plane-strain modeling is commonly used [*1*]. We follow, and formulate the layered solid contact problem from the plane-strain perspective (Fig. 1).

---

[1] Professor and graduate research assistant, respectively, Department of Mechanical Engineering, University of Minnesota, Minneapolis, MN 55455.

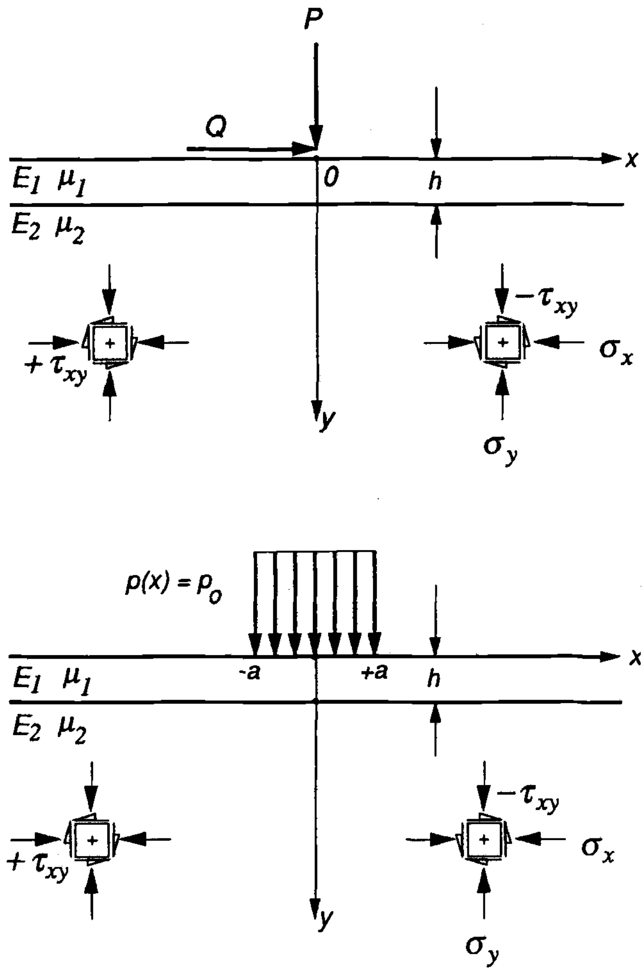

FIG. 1—*Problem geometry for plane-strain modeling of a layered semi-infinite solid.*

In terms of the Airy stress function, $\chi\,(x, y)$, the stresses, σ_x, σ_y, and σ_{xy}, are

$$\frac{\partial^2\chi\,(x, y)}{\partial y^2} = \sigma_x;\ \frac{\partial^2\chi\,(x, y)}{\partial x^2} = \sigma_y;\ \frac{\partial^2\chi\,(x, y)}{\partial x\,\partial y} = -\sigma_{xy} \tag{1}$$

Sneddon [2] has shown that problems involving semi-infinite solids, $-\infty \leq x \leq +\infty$; $y \geq 0$, with boundary loading along $-\infty \leq x \leq +\infty$; $y = 0$, can be solved with Fourier transforms. The principle is that if $G(\alpha, y)$ is the Fourier transform of $\chi\,(x, y)$

$$G(\alpha, y) = F\{\chi(x, y);\ x \rightarrow \alpha\} = \frac{1}{\sqrt{2\pi}} \int_{-\infty}^{+\infty} \chi(x, y)e^{i\alpha x}\,dx \tag{2}$$

once $G(\alpha, y)$ is determined, $\chi(x, y)$ can be recovered with the inverse transform

$$\chi(x, y) = \frac{1}{\sqrt{2\pi}} \int_{-\infty}^{+\infty} G(\alpha, y) e^{-i\alpha x}\, d\alpha \tag{3}$$

and stresses are calculated with Eq 1. Displacements, u and v are determined with similar equations.

For a homogeneous, semi-infinite solid with edge tractions along $y = 0$, $G(\alpha, y)$ has the form

$$G(\alpha, y) = [A(\alpha) + B(\alpha)y]e^{-|\alpha| y} \tag{4}$$

where A and B are determined from the boundary conditions. For tractions imposed along $-\infty \leq x \leq +\infty$; $y = 0$, that is, for $\sigma_y = -P(x)$ along $y = 0$ (or a part of it) and $\sigma_{xy} = 0$ along its remainder, from Eq 1 and taking the derivatives of Eq 2

$$\sigma_y(\alpha,0) = -\alpha^2 G = -p_\alpha \text{ and } \sigma_{xy}(\alpha,0) = i\alpha \frac{\partial G}{\partial y} = 0 \tag{5}$$

The constants of Eq 4 evaluated with Eq 5, are $A(\alpha) = \{p_\alpha / \alpha^2\}$ and $B(\alpha) = \{p_\alpha / \alpha\}$, where p_α is the transform of the boundary traction.

Stress functions, $G(\alpha, y)$ and $\chi(x, y)$, in terms of p_α are

$$G(\alpha, y) = \left\{\frac{p_\alpha}{\alpha^2}(1 + \alpha y)\right\} r^{-|\alpha| y} \tag{6}$$

and

$$\chi(x, y) = \frac{1}{\sqrt{2\pi}} \int_{-\infty}^{+\infty} \frac{p_\alpha}{\alpha^2}(1 + |\alpha| y)\, e^{-|\alpha|(y+ix)}\, \partial\alpha \tag{7}$$

From Eqs 7 and 1, the stresses are

$$\sigma_x = -\frac{1}{\sqrt{2\pi}} \int_{-\infty}^{+\infty} p_\alpha(1 + |\alpha| y)\, e^{-|\alpha|(y+ix)}\, \partial\alpha \tag{8}$$

$$\sigma_y = -\frac{1}{\sqrt{2\pi}} \int_{-\infty}^{+\infty} p_\alpha(1 + |\alpha| y)\, e^{-|\alpha|(y+ix)}\, \partial\alpha \tag{9}$$

and

$$\sigma_{xy} = -\frac{iy}{\sqrt{2\pi}} \int_{-\infty}^{+\infty} \alpha\, p_\alpha\, e^{-|\alpha|(y+ix)}\, \partial\alpha \tag{10}$$

Displacements v and u are determined similarly.

Using the convolution theorem, stress and displacement integrals can be written in closed form for some cases. When it is not possible to do so, Green's function for an isolated line load applied at the origin is determined and the principle of superposition invoked to calculate stresses for any combination of surface tractions [*1*]. Mixed boundary value problems are handled by calculating surface displacements and matching them to those imposed. Here, two integral equations are solved simultaneously. Sneddon [*3*] has obtained solutions for several cases.

A solid covered with a layer of finite thickness, h, requires a transform of the form

$$G(\alpha, y) = [A + B\, y]\, e^{-|\alpha| y} + [C + D\, y]\, e^{|\alpha| y} \tag{11}$$

When the layer covering the solid is bonded to a rigid substrate, layer displacements, u and v, are zero at $y = h$. If the interface is perfectly lubricated, shear stress and normal displacement, v, in the layer must vanish at the interface. These requirements and the boundary conditions at $y = 0$ allow $G(\alpha, y)$ to be determined.

If the substrate is elastic, two transformed stress functions are needed to calculate the stresses and displacements in the layer and in the substrate.

$$\begin{aligned} G_1(\alpha, y) &= [A_1 + B_1\, y]\, e^{-|\alpha| y} + [C_1 + D_1 y]\, e^{\,|\alpha| y} \\ G_2(\alpha, y) &= [A_2 + B_2\, y]\, e^{-|\alpha| y} \end{aligned} \tag{12}$$

Substrate function is simpler, since stresses and displacements must vanish at $y = \infty$. The unknowns of Eq 12 are determined as before. If the layer is perfectly bonded, the two displacements, u and v, and the two stresses, σ_{xy} and σ_y, must be continuous at $y = h$. These requirements, in terms of derivatives of G_1 and G_2, are given in Gupta and Walowit [*4*]. A matrix equation to solve for the constants of Eq 12 is also given there for an isolated normal load applied at the origin. Corresponding equations for an isolated shear load applied at the origin have been determined by Kannel and Dow [*5*].

Barkovich et al. [*6*] have determined the constants for an elliptical contact stress distribution applied over a part of the boundary in terms of transcendental functions. The case of axisymmetric loading of a layer on a rigid substrate has been treated by Ling [*7*], and Wu and Ling [*8*] using Hankel transforms. In the cited references, integrals for stresses and displacements are generally expressions with intractable kernels. Numerical integration is necessary. For a cylinder on an elastic layer over a rigid substrate, asymptotic solutions have been found by Meijers [*9*].

The works cited focus mainly on stresses within the coated body along the load axis, $x = 0$, or on the extent of deviation from Hertzian stress distribution at the contact surface due to indentor or substrate elasticity. The mixed boundary value problem encountered with indentors of specified geometry is difficult to solve but has been treated satisfactorily [*4*]. The stress function method used leads to cumbersome integral expressions that can not be inverted or fractions containing transcendental functions in the numerator and denominator. The numerical integration carried out tends to converge slowly or not at all for some contact geometries and combinations of loading parameters.

Displacement Formulation

Recognizing that the layered solid problem will require numerical integration, displacement formulation is used here to calculate film-substrate interface stresses. Navier equations are first solved in the absence of body forces. Stress components are then determined from displacements.

The two-dimensional Navier equations of elasticity are

$$(\lambda + G)\frac{\partial \varepsilon}{\partial x} + G\,\nabla^2 u = 0;\ (\lambda + G)\frac{\partial \varepsilon}{\partial y} + G\,\nabla^2 v = 0 \tag{13}$$

where

$$\lambda = \frac{\mu E}{(1 + \mu)(1 - 2\mu)} \text{ and } G = \frac{E}{2\,(1 + \mu)} \tag{14}$$

Here, λ and G are the Lamé constants defined with Young's modulus, E, and the Poisson's ratio, μ. The ε term is the sum of normal strains, $\varepsilon = (\varepsilon_x + \varepsilon_y)$, and ∇^2 is the two-dimensional Laplacian. Applying the Laplacian to Navier equations (Eq 13), since $\nabla^2\,(\varepsilon_x + \varepsilon_y) = 0$, it is evident that $\nabla^4 u(x, y) = 0$ and $\nabla^4 v(x, y) = 0$, that is, u and v are biharmonic.

Displacement formulation requires two transforms, $U(\alpha, y)$ and $V(\alpha, y)$

$$\begin{aligned} U(\alpha, y) &= F[u(x, y); x \rightarrow \alpha] = \frac{1}{\sqrt{2\pi}} \int_{-\infty}^{\infty} u(x, y)\, e^{i\alpha x}\, dx \\ V(\alpha, y) &= F[v(x, y); x \rightarrow \alpha] = \frac{1}{\sqrt{2\pi}} \int_{-\infty}^{\infty} v(x, y)\, e^{i\alpha x}\, dx \end{aligned} \tag{15}$$

to satisfy the two biharmonic equations for u and v (homogeneous solid). It can be shown that U and V have the form

$$U(\alpha, y) = [a_1 + a_2\,\alpha\,y]\,e^{-|\alpha|y} \text{ and } V(\alpha, y) = [b_1 + b_2\,\alpha\,y]\,e^{-|\alpha|y} \tag{16}$$

Inverting Eq 16, the displacements are

$$u(x, y) = \frac{1}{\sqrt{2\pi}} \int_{-\infty}^{\infty} U(\alpha, y)\, e^{-i\alpha x}\, d\alpha \text{ and } v(x, y) = \frac{1}{\sqrt{2\pi}} \int_{-\infty}^{\infty} V(\alpha, y)\, e^{-i\alpha x}\, d\alpha \tag{17}$$

Since an even normal boundary traction at $y = 0$ will lead to an odd displacement, $u(x, y)$, and an even displacement, $v(x, y)$, Eq 17 is written in terms of Fourier sine and cosine transforms

$$u(x, y) = \sqrt{\frac{2}{\pi}} \int_0^{\infty} U \sin(\alpha x)\, d\alpha \text{ and } v(x, y) = \sqrt{\frac{2}{\pi}} \int_0^{\infty} V \cos(\alpha x)\, d\alpha \tag{18}$$

The stress components are therefore

$$\begin{aligned} \sigma_x &= \sqrt{\frac{2}{\pi}} \int_0^{\infty} \left\{(\lambda + 2G)\,\alpha\,U + \lambda\frac{dV}{dy}\right\} \cos(\alpha x)\, d\alpha \\ \sigma_y &= \sqrt{\frac{2}{\pi}} \int_0^{\infty} \left\{\lambda\,\alpha\,U + (\lambda + 2G)\frac{dV}{dy}\right\} \cos(\alpha x)\, d\alpha \\ \sigma_{xy} &= \sqrt{\frac{2}{\pi}} \int_0^{\infty} \left\{G(\frac{dU}{dy} - \alpha\,V)\right\} \sin(\alpha x)\, d\alpha \end{aligned} \tag{19}$$

Once the a_1, a_2, b_1, and b_2 constants of U and V are determined, solution with displacement formulation is complete.

To determine the constants, two equations are obtained from the equations of equilibrium and two more from boundary conditions. Shear stress evaluated and equated to zero at $y = 0$ satisfies the first boundary condition. Traction $\sigma_y = -p(x)$ along $y = 0$, taken as even, satisfies the second, that is

$$\sigma_y(x,0) = -p(x) = \sqrt{\frac{2}{\pi}} \int_0^\infty p_\alpha \cos(\alpha x)\, d\alpha \tag{20}$$

Equations to determine a_1, a_2, b_1, and b_2 become

$$\begin{bmatrix} 1 & 2(1-2\mu) & -1 & 1 \\ 1 & -1 & -1 & 4(1-\mu) \\ 1 & -1 & 1 & 0 \\ \lambda & 0 & -(\lambda + 2G) & (\lambda + 2G \end{bmatrix} \begin{bmatrix} a_1 \\ a_2 \\ b_1 \\ b_2 \end{bmatrix} = - \begin{bmatrix} 0 \\ 0 \\ 0 \\ 1 \end{bmatrix} \frac{p_\alpha}{\alpha} \tag{21}$$

Solving Eq 21 and substituting into Eq 18, the displacement functions are

$$\begin{aligned} u &= \frac{(1+\mu)}{E} \int_0^\infty \left\{ \frac{p_\alpha}{\alpha} (2\mu - 1 + \alpha y) \right\} e^{-\alpha y} \sin(\alpha x)\, d\alpha \\ v &= \frac{(1+\mu)}{E} \int_0^\infty \left\{ \frac{p_\alpha}{\alpha} (2 - 2\mu + \alpha y) \right\} e^{-\alpha y} \cos(\alpha x)\, d\alpha \end{aligned} \tag{22}$$

For odd boundary tractions, first and second equations of Eq 18 are written as Fourier cosine and sine transforms, respectively. When the traction boundary conditions are not complicated, Eq 22 and the stress equations obtained can be integrated. Closed-form solutions are obtained.

Displacement Formulation for Coated Solids

For a semi-infinite solid covered with a thin film coating of thickness, h, two transforms, $U_1(\alpha, y)$ and $V_1(\alpha, y)$, for the film and two more, $U_2(\alpha, y)$ and $V_2(\alpha, y)$, for the substrate are needed

$$\begin{aligned} U_1(\alpha, y) &= [A_1 + A_2\, \alpha\, y]\, e^{-|\alpha| y} + [A_3 + A_4\, \alpha\, y]\, e^{|\alpha| y} \\ V_1(\alpha, y) &= [B_1 + B_2\, \alpha\, y]\, e^{-|\alpha| y} + [B_3 + B_4\, \alpha\, y]\, e^{|\alpha| y} \end{aligned} \tag{23}$$

$$\begin{aligned} U_2(\alpha, y) &= [C_1 + C_2\, \alpha\, y]\, e^{-|\alpha| y} \\ V_2(\alpha, y) &= [D_1 + D_2\, \alpha\, y]\, e^{-|\alpha| y} \end{aligned} \tag{24}$$

For even boundary tractions at the surface, displacement functions, that is, $u_1(x, y)$ and $v_1(x, y)$ in the film and $u_2(x, y)$ and $v_2(x, y)$ in the substrate, are identical in form as Eq 18 with $U_1(\alpha, y)$ and $V_1(\alpha, y)$ replacing $U(\alpha, y)$ and $V(\alpha, y)$ for the film, and $U_2(\alpha, y)$ and $V_2(\alpha, y)$ replacing $U(\alpha, y)$ and $V(\alpha, y)$ for the substrate. There are 12 constants in the four displacement equations. A set of 12 equations are needed. As in the case of the homogeneous semi-infinite solid, a matrix equation corresponding to Eq 21 is needed.

Equations to construct the matrix are obtained as before. Stress equilibrium equations along x and y yield two equations for the film and two more for the substrate. But, since $u_1(x, y)$ and $v_1(x, y)$ contain both positive and negative exponential terms, to satisfy equilibrium equations everywhere in the film, coefficients of positive and negative exponentials are equated to zero. Equilibrium requirements in the film alone, therefore, lead to four equations. Two more are obtained from the substrate.

For well-bonded films, continuity of displacements is required along x and y at the film-substrate interface, that is, $u_1 = u_2$ and $v_1 = v_2$ at $y = h$. In addition, two components of stresses must also be continuous at $y = h$, that is, $\sigma_y^1 = \sigma_y^2$ at $y = h$, and $\sigma_{xy}^1 = \sigma_{xy}^2$. Thus, displacement and stress continuity provide four equations.

The final two equations are obtained from the traction boundary conditions. When only normal loads are applied, shear traction at the film surface is zero. This gives the eleventh equation. The normal traction applied on the free surface of the film, here taken to be even, provides the last equation.

Calculating the displacements and stresses in a layered solid is now reduced mainly to one of solving a set of 12 equations to determine the constants of displacement functions. Writing these equations in matrix form, with $[K]$ designating the coefficients of the equations, $[A]$ the vector of constants to be determined, and $[I]$ a vector containing only one non-zero term, we obtain

$$[K]\,[A] = [I]\,\frac{p_\alpha}{\alpha} \tag{25}$$

where

$$[A]^T = (A_1, A_2, A_3, A_4, B_1, B_2, B_3, B_4, C_1, C_2, D_1, D_2)$$
$$[I]^T = (0, 0, 0, 0, 0, \cdots, 0, 1)$$

inverting

$$[A] = [K]^{-1}\,[I]\,\frac{p_\alpha}{\alpha} \tag{26}$$

Terms of the coefficient matrix, [K, are primarily numeric constants, numbers given by the problem geometry, or properties of materials. Matrix inversion to determine $[A]$, as a function of loading, is straight forward. Numerical integration, to calculate displacements and stresses, can then be carried out.

Displacements and stresses in the film ($j = 1$) and in the substrate ($j = 2$) are

$$\begin{gathered}
u_j(x, y) = \sqrt{\frac{2}{\pi}}\int_0^\infty U_j \sin \alpha \times d\alpha,\; v_j(x, y) = \sqrt{\frac{2}{\pi}}\int_0^\infty V_j \cos(\alpha x)\, d\alpha \\
\sigma_x^j = \sqrt{\frac{2}{\pi}}\int_0^\infty \left\{(\lambda j + 2G_j)\,\alpha\, U_j + \lambda j \frac{dV_j}{dy}\right\}\cos(\alpha x)\, d\alpha \\
\sigma_y^j = \sqrt{\frac{2}{\pi}}\int_0^\infty \left\{\lambda_j\,\alpha\, U_j + (\lambda_j + 2G_j)\frac{dV_j}{dy}\right\}\cos(\alpha x)\, d\alpha
\end{gathered} \tag{27}$$

$$\sigma^j_{xy} = \sqrt{\frac{2}{\pi}} \int_0^\infty \left\{ G_j \left(\frac{dU_j}{dy} - \alpha\, V_j \right) \sin(\alpha x)\, d\alpha \right.$$

Solution for even forward problems, that is, problems involving normal traction boundary conditions on the film surface, is now complete.

For shear loading, cosine and sine transforms are used in Eq 18 for displacement functions $u(x, y)$ and $v(x, y)$, respectively, with $U_j(\alpha, y)$ and $V_j(\alpha, y)$; $j = 1,2$ given by Eqs 23 and 24. Matrix $[K]$ differs and is determined as for the case with normal tractions. The first ten equations corresponding to those for the normal load are obtained using identical reasoning. When only shear tractions are applied, the film surface must be free from normal tractions. This yields the eleventh equation. Finally, the shear traction applied on the free surface of the film provides the twelfth equation. Calculating the constants of the displacement equations with the $[K]$ matrix and computation of displacements and stresses proceeds as for the previous case. Since the principle of superposition holds, the case of a general surface traction is handled by summing calculated results for normal and shear tractions. Alternately, Fourier exponential transforms may be used.

Calculated Results

When hard coats are used to protect light alloys of aluminum, titanium, etc., substrate modulus, E_2 is lower than that of the film, E_1. To evaluate the significance of variations in elastic properties, calculations have been made with $E_1 = 1.0$ and letting E_2 vary between 0.2 and 5.0. Substrates more compliant than the film are characterized by $E_2/E_1 < 1$, and stiffer substrates have $E_2/E_1 > 1$. Poisson's ratios also differ, with hard materials possessing $\mu \cong 0.25$ and metallic alloys between 0.3 and 0.35. Poisson's ratio is taken here as 0.25 or 0.33 for the film. That of the substrate is kept always at 0.33. Typically, physical vapor deposition (PVD) hard coatings in use range in thickness between 5×10^2 and 10×10^3 nm. In most calculations, film thickness is taken to be 1000 nm.

Calculations have been made here for isolated normal and shear tractions (line loads, P and Q, shown in Fig. 1) applied at the origin. Representing these as delta functions, it can be shown that the transform of the loading function, p_α, needed for displacement and stress calculations is $p_\alpha = P/\pi$ or $p_\alpha = Q/\pi$, for the normal and shear line tractions, P and Q, shown in Fig. 1. For a normal strip load of intensity, p_0, applied between $-a$ and $+a$ and directed along y, p_α is given by

$$p_\alpha = p_0 \left\{ \frac{\sin(\alpha\, a)}{\pi\, \alpha} \right\} \tag{28}$$

Transforms for shear loading, flat punch indentation, Hertzian contact, etc., are known [*1–9*]. In Hertzian contacts, stresses vanish at contact extremeties. The case of a strip load is expected to be more severe on film-substrate interface stresses than Hertzian loading. We have therefore used line loads and strip loads as principal contact loadings to examine interface stress issues. Extending this to elliptic contact stress distribution involves use of Bessel functions and it is straightforward.

Film flexure stress, σ_x, generated at the film-substrate interface of a coated solid by a unit normal line load (P in Fig. 1 and $p_\alpha = 1/\pi$) applied at the origin are shown in Fig. 2*a* for (E_2/

E_1) ratios ranging between 0.2 and 5.0. Stresses have been determined for x/h values to 4, where h is the film thickness. Since the Young's modulus of titanium nitride is ~ 560 GPa, titanium alloys ~ 120 GPa, and aluminum alloys ~ 70 GPa, calculated results presented in most of the figures generally span the property ranges that would be of interest. For the light alloy coating, $E_2/E_1 < 1$ range applies, and here the flexure stresses in the film, immediately below the line load, are tensile (positive values signify tension). Peak tensile stresses increase with increasing substrate compliance.

Calculated interface bearing stresses, σ_y, are shown in Fig. 2*b*. The bearing stress is compressive everywhere with lower peak values in more compliant substrates. Since displacements due to surface loading are distributed over a larger volume of the substrate in more compliant substrates, bearing stresses are lower.

When the bearing stress at the interface is tensile, this stress component tends to separate the film from the substrate. In subsequent sections, the term "lift-off stress" is sometimes used to designate tensile bearing stresses.

The "isometric" or three-dimensional representation of flexure stress, σ_x, as a function of substrate modulus, shown in Fig. 3*a*, is presented to emphasize the significance of substrate compliance. The case of $E_2/E_1 = 1$ that approximately (approximate because film $\mu = 0.25$ and substrate $\mu = 0.33$) represents an uncoated solid, is included to provide a reference basis. Displacements distributed over a larger volume of the substrates will tend to lower the film-substrate interfacial shear stress. This is confirmed by the calculated results shown in Fig. 3*b*.

High film flexural stresses can lead to film failure by fracture processes, since most hard coating materials used are refractory metal compounds with a limited capacity to relax occasional overstressing with plastic flow. Film fracture and the fragments generated in a tribo-conjunction of a closed tribological system can defeat the purpose of coating. High film flexure stresses are therefore undesirable.

High tensile stresses at the film-matrix interface can be lowered by raising the film thickness. That this is feasible is clear from the calculated results shown in Fig. 4*a* for a compliant substrate with $E_2 = 0.25$ and $\mu = 0.25$. There is a sharp drop off in peak tensile stresses as the film thickness is raised from 500 to 1500 nm. To demonstrate this better, calculations have been extended to 5000 nm. Results are shown in Fig. 4*b*. Raising the film thickness offers a viable means of relocating the vulnerable interface at a less severely stressed part of the coated solid. The needed increase in film thickness is not unrealistically high (within the cost-effective range of PVD processes).

Stresses generated at the film-substrate interface by a unit shear line load applied at the origin (Q in Fig. 1 and $p_\alpha = 1/\pi$ are shown in Fig. 5. To evaluate the significance of substrate elastic properties, film-substrate interface stress components, σ_x, and σ_y, and τ_{xy}, have been calculated for a very compliant substrate ($E_2/E_1 = 0.2$) and for a relatively stiff substrate ($E_2/E_1 = 5$). Film thickness is taken to be 1000 nm, and Poisson's ratios are assumed to be equal, with $\mu = 0.33$.

As in the case of a normal line load, substrate displacements now span larger lateral dimensions when the substrate is more compliant. Shear stresses induced at the film-substrate interface are also lower. Two problems are noted; tensile flexural stresses, σ_x, are generated in the contact wake and the bearing stress, σ_y, becomes positive (that is, a lift-off stress) in the same region. Flexural stresses induced are very significant when the substrate is elastically much softer than the film. On the other hand, lift-off stress is much higher when the substrate is stiffer than the film.

Distributed tractions are much more common in tribological contacts than the ideal line loads considered so far. The simplest of these involve uniform loading over a contact width, $2a$, as shown in Fig. 1. Two contact classes of interest in tribological applications are the narrow

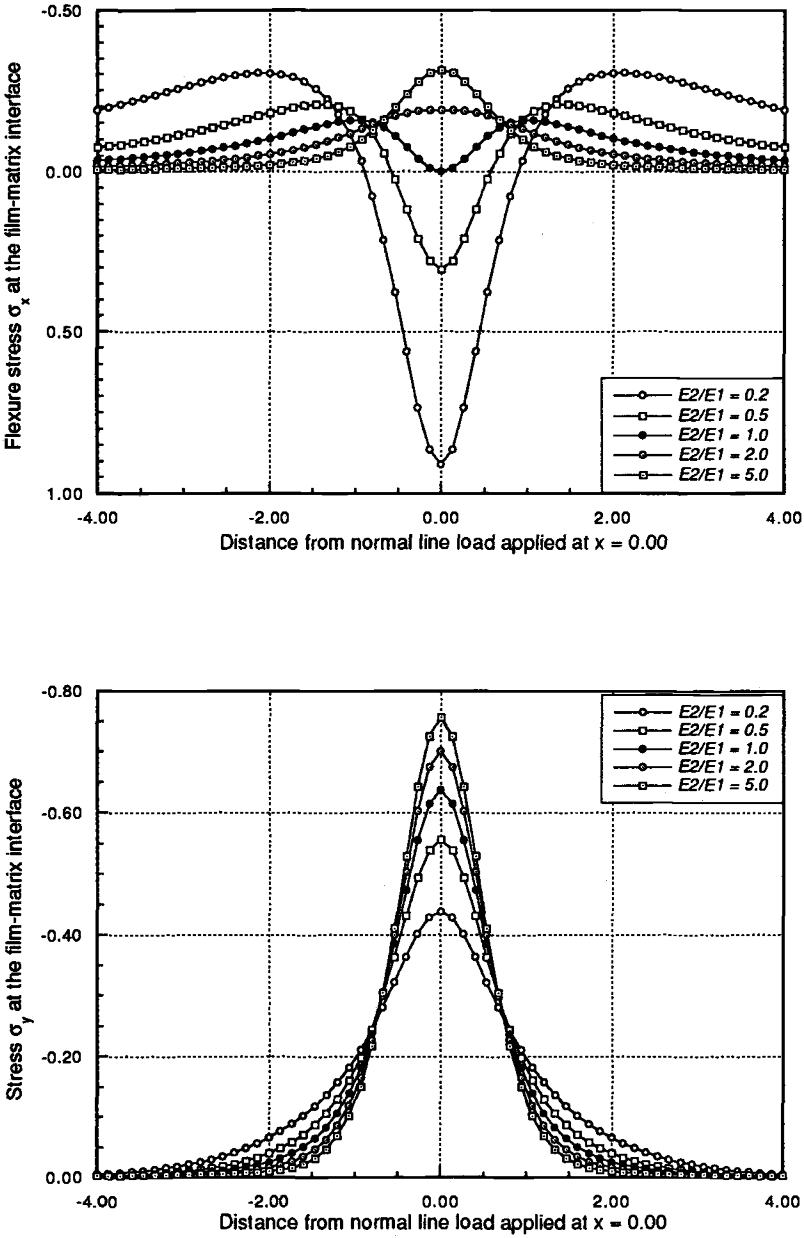

FIG. 2—*Calculated interface stresses as a function of modulus ratio,* E_2/E_1. *Unit normal line load applied at the origin:* (a) *variation of flexure stress,* σ_x *and* (b) *variation of bearing stress,* σ_y, (h = *1* μm*;* μ *= 0.33 for the film and the substrate).*

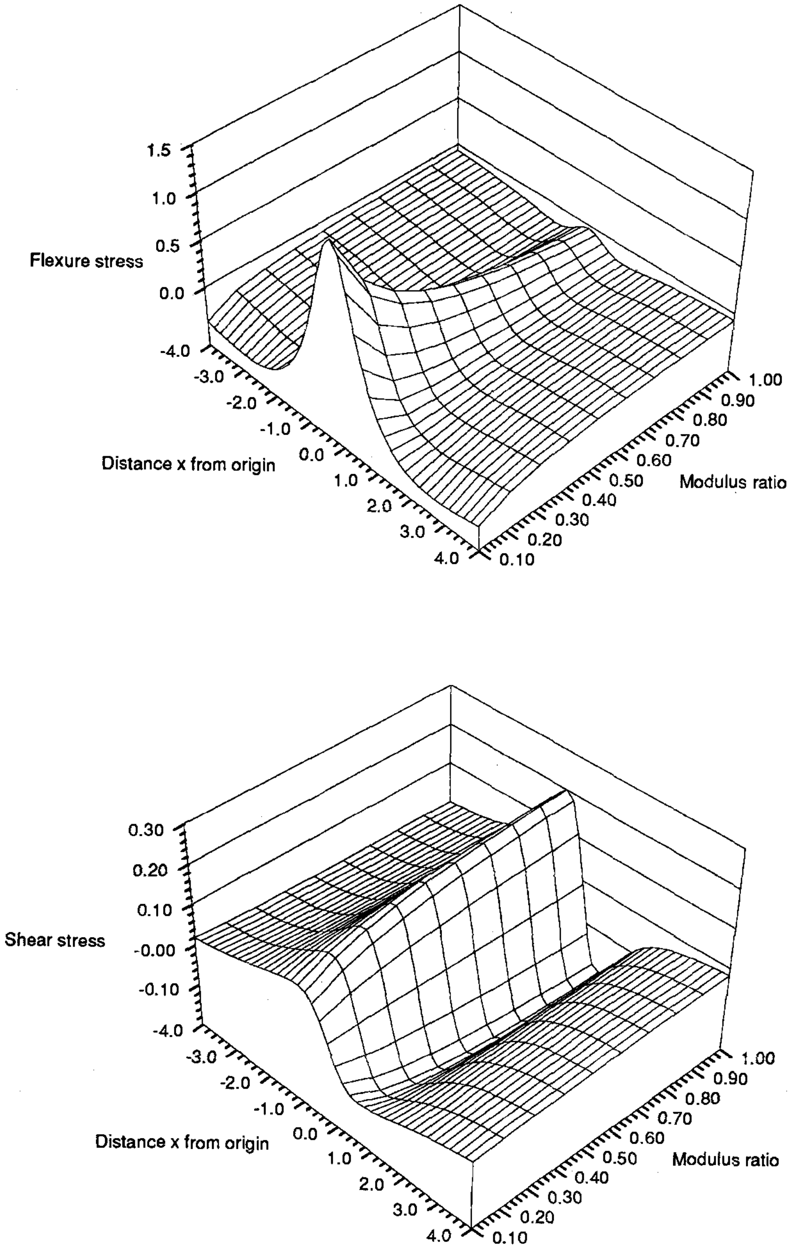

FIG. 3—*Calculated interface stresses as a function of modulus ratio,* E_2/E_1. *Unit normal line load applied at the origin:* (a) *variation of flexure stress,* σ_x, *and* (b) *variation of shear stress,* σ_{xy} (h = *1* μ*m;* μ = *0.25 for the film and 0.33 for the substrate).*

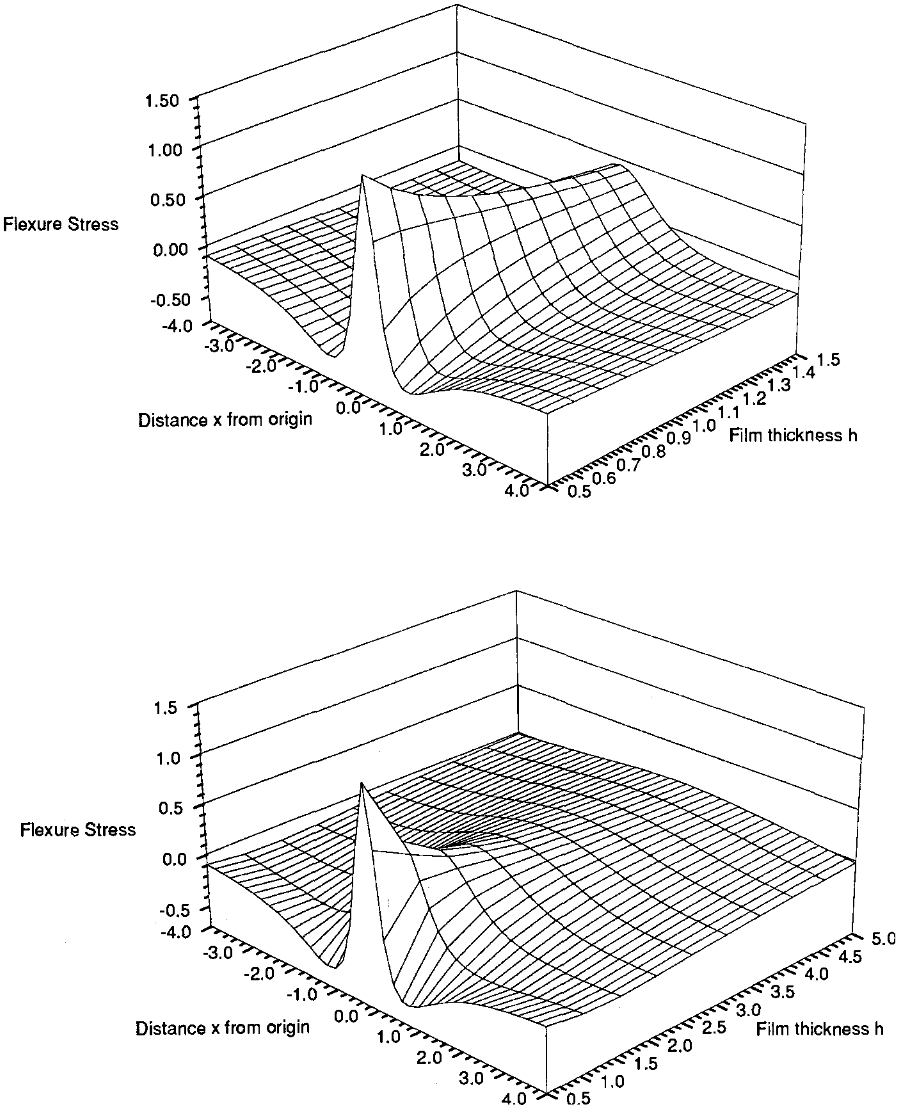

FIG. 4—*Variation of flexure stress,* σ_x, *at the film-substrate interface as a function of film thickness for a modulus ratio of* $E_2/E_1 = 0.25$: (a) *film thickness range: 0.50 to 1.50* μm *and* (b) *film thickness range: 1.0 to 5.0* μm (μ *= 0.25 for the film and 0.33 for the substrate).*

contacts where the contact width is a small multiple of the film thickness and wide contacts. The narrow contacts approximate high stress contacts as, for example, those that occur when small hard particles impact a surface at high velocities (erosive contact). Wider contacts are common in boundary-lubricated and hydrodynamically-lubricated tribological conjunctions.

Calculated flexure stresses at the interface due to a uniform normal load in a narrow contact ($a/h \approx 3$) and a wider contact ($a/h \approx 10$) are shown in Figs. 6*a* and *b*. In both cases, the film

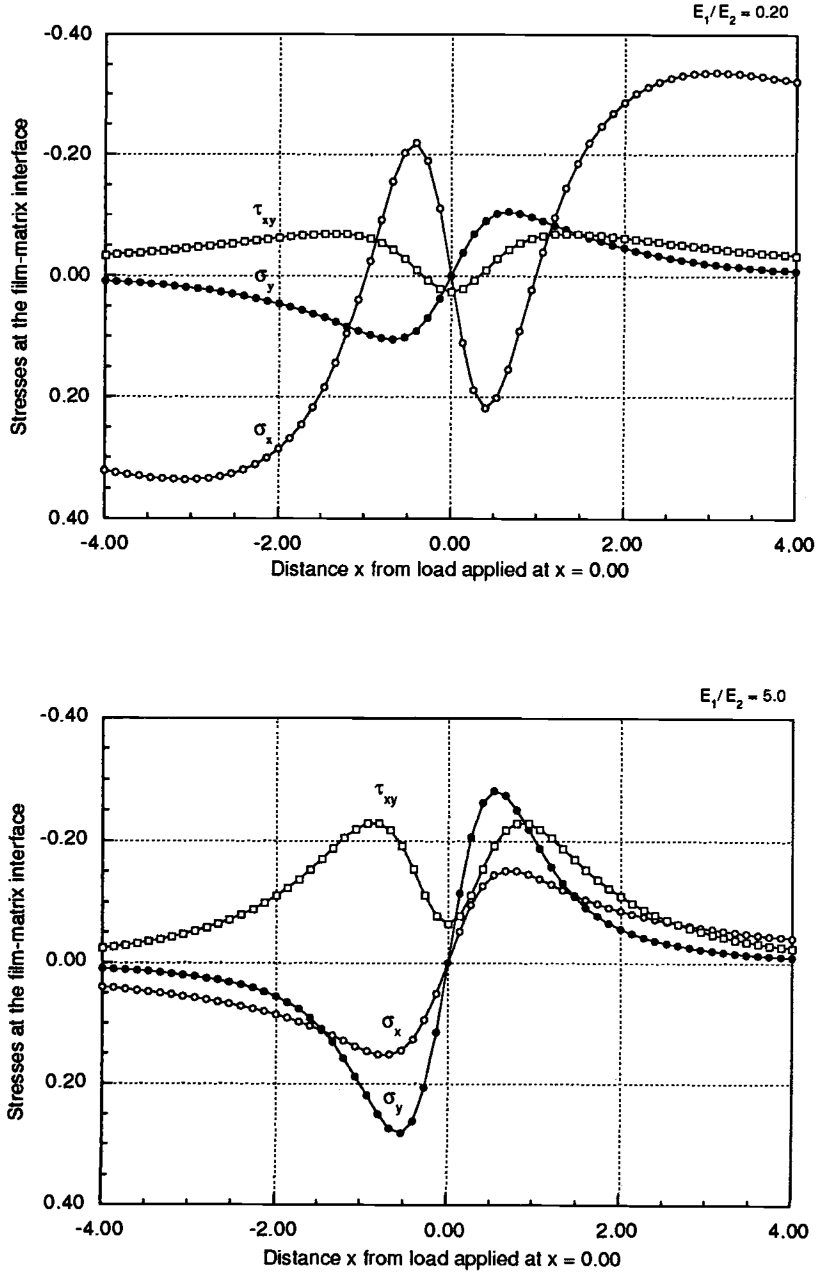

FIG. 5—*Calculated interface stresses,* σ_x, σ_y, *and* τ_{xy}, *due to an isolated unit shear line load applied at the origin. Tensile flexural stress (*top*) dominates in a compliant substrate. Bearing or lift-off stress (*bottom*) dominates in the contact wake in a stiff substrate (*$h = 1$ μm; $\mu = 0.33$ *for the film and the substrate).*

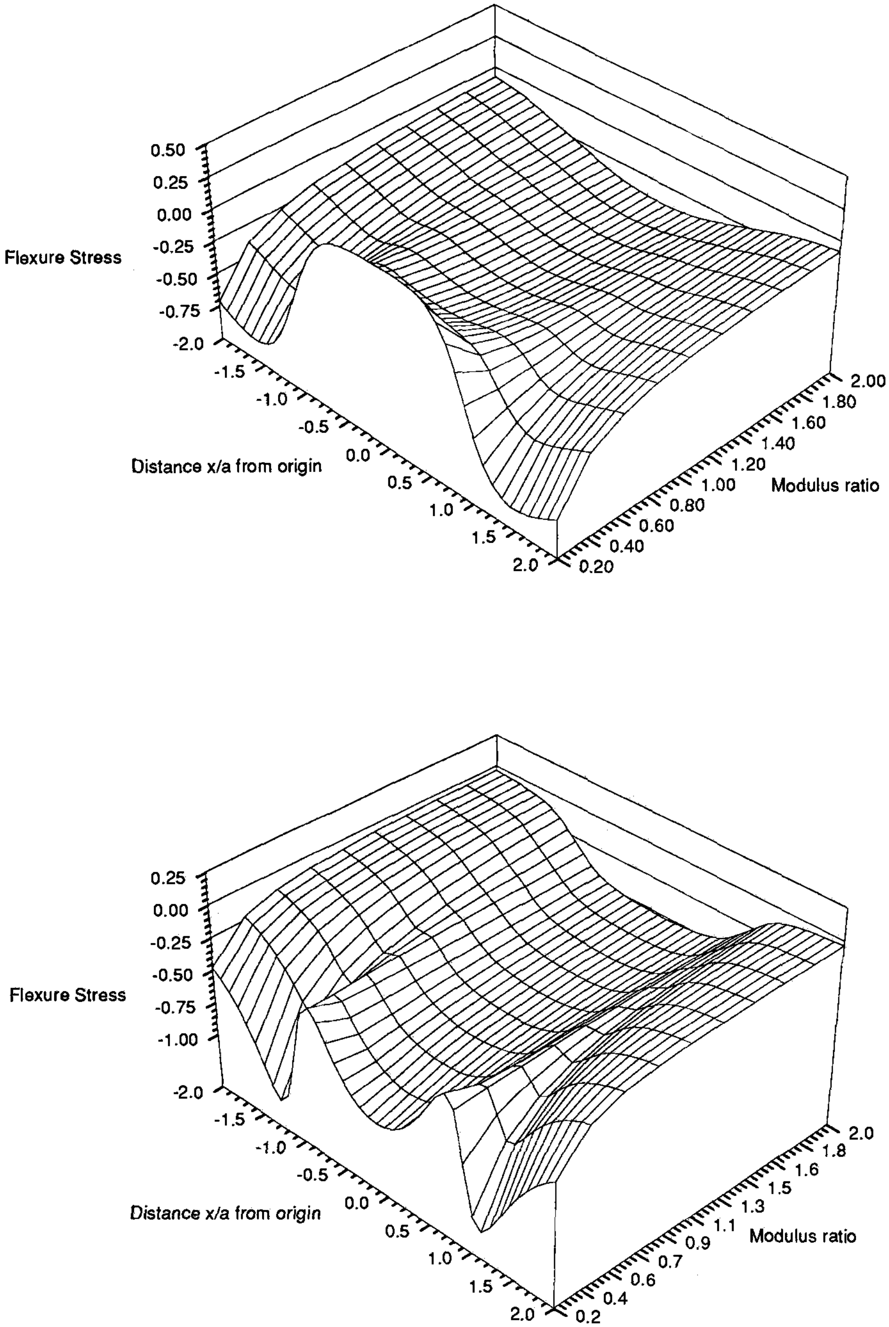

FIG. 6—*Flexure stress, σ_x, at the interface due to a unit normal strip load at the origin as a function of film-substrate modulus ratio, E_2/E_1. Flexural stress, σ_x, changes sign as the substrate modulus is raised:* (a) *narrow contact: contact width = 3* h *and* (b) *wide contact: contact width = 10* h (h *= 1* μm*;* μ *= 0.25 for the film and 0.33 for the substrate). Note the stress reversals in compliant substrates.*

thickness is 1000 nm. Results presented span the substrate modulus range of 0.2 to 2.0. Corresponding results for distributed shear tractions are shown in Figs. 7 and 8. As before, the film thickness is 1000 nm. Contact width and substrate compliances have been varied.

In narrow contacts, as when $a/h \approx 3$, flexural stresses in the film are highly tensile even with distributed normal tractions if the substrate is more compliant than the film. The bearing stress, σ_y, and the shear stress, τ_{xy}, at the film-substrate interface pose no special problems. As in the case of isolated line load, it may be possible to remedy the tensile flexural stress problem with a judicious choice of the film thickness.

Whenever the contact dimensions are much larger, as when $a \approx 10\ h$, film flexural stresses are not tensile within or outside the contact for uniform normal tractions. Flexural stresses are compressive regardless of the substrate modulus as long as contact occurs over a region much larger than the film thickness. Stress reversals observed in wider contacts involving compliant substrates can have more adverse consequences in applications involving periodic contact or cyclic loading.

If transverse forces are applied to obtain relative motion, a frictional resistance to movement appears at the contact as a shear stress with a magnitude proportional to the normal stress. The proportionality constant is the friction coefficient. In a coated part, distributed shear loading gives rise to large, tensile flexural stresses in the film and at the film-substrate interface. Calculated results for $a/h = 3$ and $a/h = 10$ are shown in Figs. 7 and 8. The stress component, σ_y, at the film-substrate interface, tending to separate the film from the substrate, also becomes tensile in the wake of the contact, that is, for negative x/a values. Softer substrates are, however, less hazardous in this regard than stiffer substrates.

The calculated results show that in extended contacts adverse stresses are induced primarily by the tangential component of surface tractions. Flexural stress, σ_x, is high in the contact wake, with severity rising with decreasing substrate modulus. The lift-off stress, tending to separate the film from the substrate, rises when the substrate is stiffer. But for realistic bearing stresses in well-engineered sliding contacts, flexure stresses in the film and film-substrate separation stresses due to tangential tractions are unlikely to be particularly hazardous. This is so since bearing stresses are limited to low values (usually less than 10 MPa, and the prevailing friction coefficient is also low due to, at a minimum, boundary lubrication (with a typical numerical value around 0.15).

Discussion

Film-substrate interface stress calculations show that hard coating is a viable solution for wear protection in extended contacts even when the substrate modulus is much lower than that of the film. The film used must, however, be a hard coating in order to reduce the wear coefficient to small values. To prevent wear of the counterface, both surfaces in contact will require hard coating.

When hard coats are used for erosion protection, since the eroding species are small, the width of the contact between the erodant and the solid is small as well. At the small a/h ratios that tend to prevail, tensile flexural stresses in the film can be a problem in normal erosive impact, if the substrate modulus is much lower than that of the hard coat. Under low-angle erosion conditions, the tangential component of the contact load can generate large film-substrate separation stresses in the wake (trailing side) of the contact, especially when the substrate is less compliant than the hard coat. In instances where the substrate is more compliant than the film, tensile flexural stresses are rather high in the wake of the contact. Film fracture is possible. Use of a higher film thickness may offer a viable solution.

From the results of the calculations, it is clear that residual compressive stresses in coated

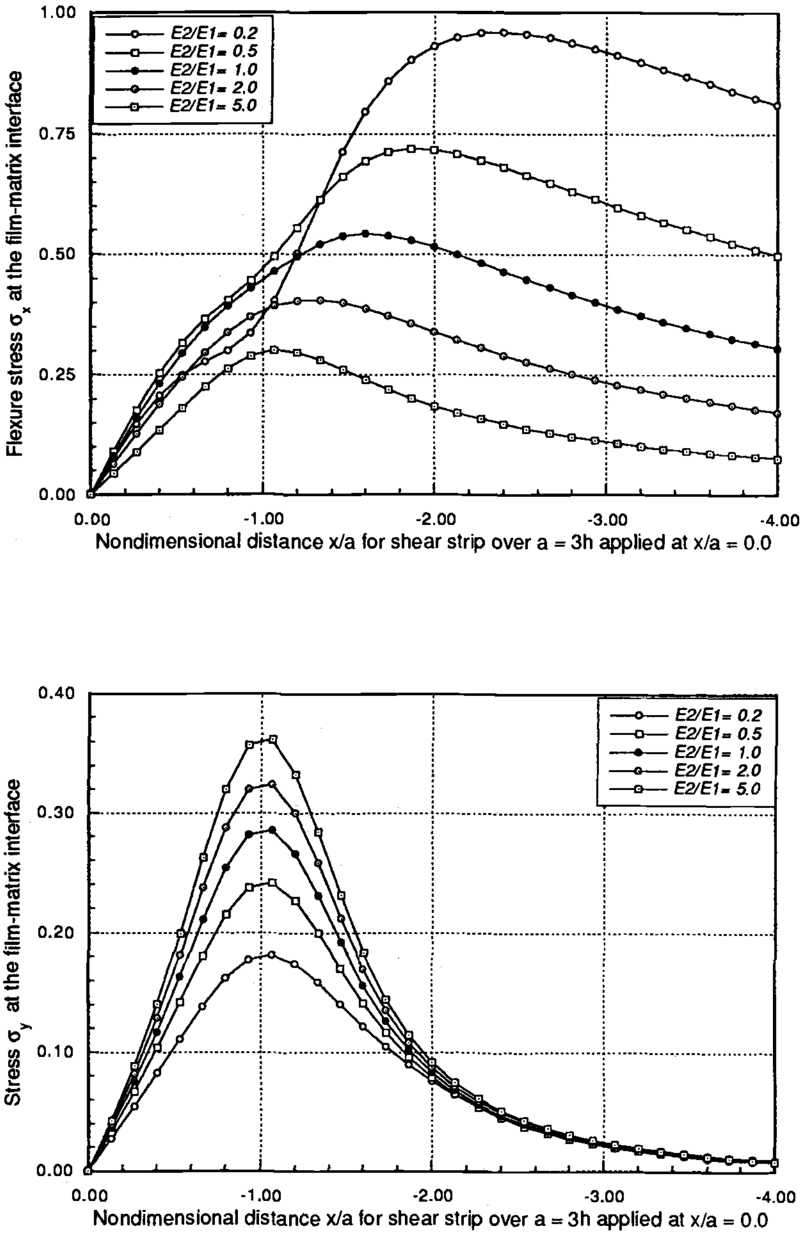

FIG. 7—*Calculated interface stresses, σ_x and σ_y, due to a unit tangential strip load applied at the origin. Narrow contact: contact width* = *3* h. *Flexural stress* (top) *is tensile in the wake of the contact for all substrate moduli. Higher flexure stresses for more compliant substrates. Lift-off stress* (bottom) *is greater with stiffer substrates* (h = *1* μm; μ = *0.33 for the film and the substrate).*

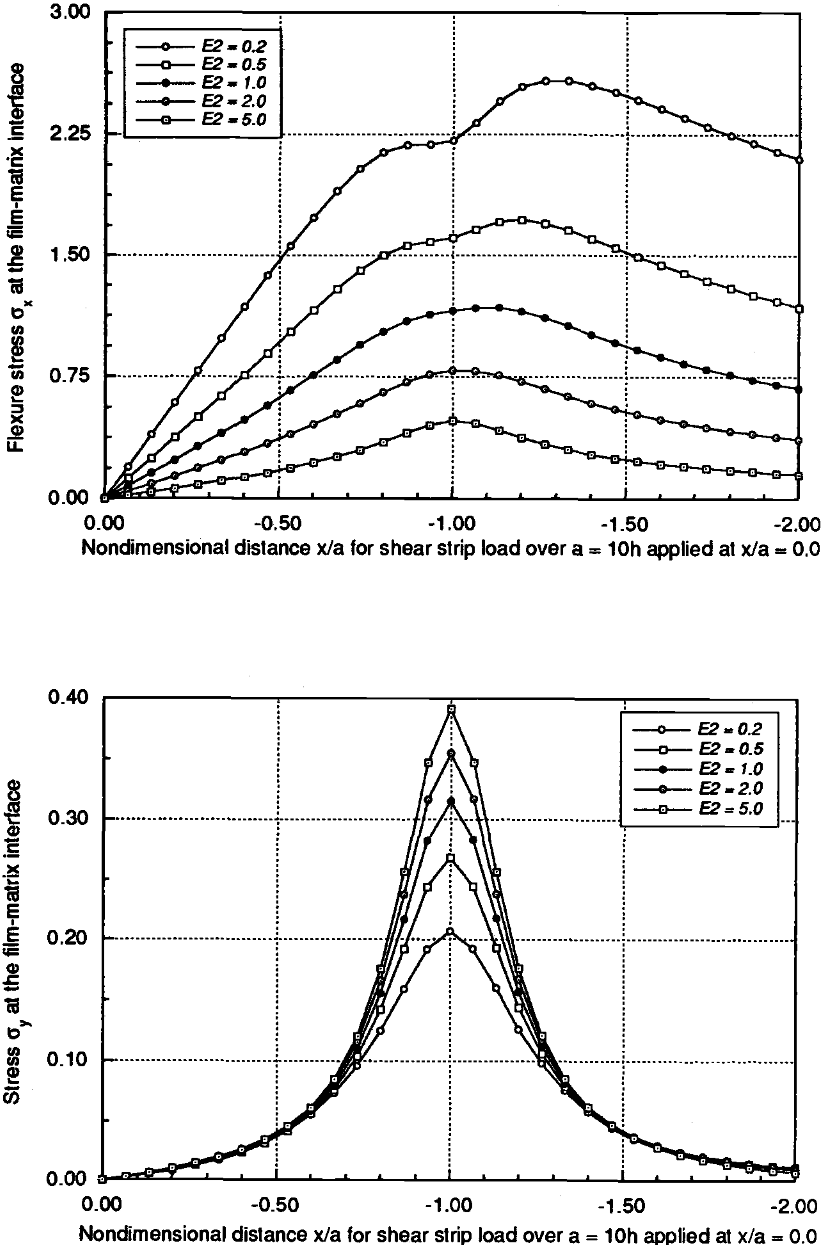

FIG. 8—*Calculated interface stresses, σ_x and σ_y, due to a unit tangential strip load applied at the origin. Wide contact: contact width = 10* h. *Flexural stress (*top*) is tensile in the wake of the contact and is much larger in wider contacts (compare with Fig. 7). Lift-off stress is tensile in the wake of the contact but is less strongly affected by the width of loading than the flexure stress (*bottom*) (*h *= 1 μm; μ = 0.33 for the film and the substrate).*

components are, in general, preferred over tensile stresses. Large, tensile flexure stresses at the film-substrate interface generated by the operating loads can at least be partially offset by compressive residual stresses. Film deposition conditions that consistently result in residual compressive stresses in hard coats are therefore preferred. It should, however, be recognized that when light alloy parts are coated, substrate yielding is likely to limit the maximum feasible residual stress.

Summary and Conclusions

A direct method is developed and applied in this study to calculate the stresses and displacements at the film-substrate interface on coated solids. It is based on the displacement formulation. Plane-strain deformation of a semi-infinite solid is used to model loaded contacts. The problem is formulated initially for homogenous solids and then extended to the analysis of coated composites. Problems involving line loads and strip loads acting along directions normal and parallel to the coated surface have been examined. Film thickness, the film-to-substrate elastic modulus ratio and the ratio of contact width to film thickness have been varied. Quantitative results have been obtained.

The results suggest that film flexure stresses can lead to film fracture when the contact dimensions are small, the contact stresses are high, and the substrate is much more compliant than the protective film. These problems can be handled by selecting a better combination of coating and substrate materials, changing the thickness of the coating, and modifying the film deposition conditions to induce residual compressive stresses in coated composites.

Shear tractions (line loads) are more insidious than normal tractions. Large shear tractions result in high bearing stresses, σ_y, that tend to lift the film off the substrate. Distributed shear tractions produce high flexure stresses in the film both in narrow and wide contacts. When stiffer substrates are used, lift-off stresses at the film-substrate interface can be a problem. In unlubricated applications where high friction is unavoidable (erosion, especially at high temperatures), film failure due to high flexure stresses and film lift-off will have to be avoided. Higher film thickness (still in the μm range) or multi-layer coatings may have to be used.

References

[1] Johnson, K. L., *Contact Mechanics*, Cambridge University Press, Cambridge, 1992.
[2] Sneddon, I. N., *Fourier Transforms*, McGraw-Hill, New York, 1951.
[3] Sneddon, I. N., *Mixed Boundary Value Problems in Potential Theory*, Amsterdam, North Holland, 1966.
[4] Gupta, P. K. and Walowit, J. A., *Journal of Lubrication Technology*, Vol. 96, 1974, pp. 250–257.
[5] Kannel, J. W. and Dow, T. A., *Journal of Tribology*, Vol. 108, 1986, pp. 403–409.
[6] Barkovich, D., Kingsley, S. C., and Ku, T. C., *International Journal of Engineering and Science*, Vol. 2, 1964, pp. 253–268.
[7] Ling, F. F., *Surface Mechanics*, Wiley-Interscience, New York, 1973.
[8] Wu, J. J. and Ling, F. F., *Developments in Mechanics*, Vol. 6, 1971, pp. 359–372.
[9] Meijers, P., *Applied Science and Research*, Vol. 18, 1968, pp. 353–383.

Arthur W. Ruff[1]

Nanoindentation and Instrumented Scratching Measurements on Hard Coatings

---

REFERENCE: Ruff, A. W., **"Nanoindentation and Instrumented Scratching Measurements on Hard Coatings,"** *Effect of Surface Coatings and Treatments on Wear, ASTM STP 1278,* S. Bahadur, Ed., American Society for Testing and Materials, 1996, pp. 124–146.

ABSTRACT: Elastic, plastic, and cracking properties of ZrO_2, a ZrO_2-metal composite, and a Ni-NiO composite, all plasma-sprayed as coatings on metallic substrates, have been studied. Data comparisons were made with bulk ZrO_2, bulk nickel, and single-crystal silicon as reference materials. A nanoindentation and scratching apparatus was used for the measurements. Three different indenter and scratching tool shapes were used: 200 μm radius sphere, Vickers four-sided pyramid, and a 45° wedge with a 0.5-mm radius curved edge. During indentation, over a load range of 10 mN to 1 N, continuous load versus depth data were obtained in each case to permit analysis for material hardness and elastic modulus. The loading curve data are used to calculate hardness, and the unloading curve data are used to calculate elastic modulus. The analytical models used are described and compared. An alternate method for deriving elastic modulus from the initial portion of the loading curve is described. Comparison among the results for different tool shapes will be discussed. During instrumented scratching over a similar load range, values for load, tool depth, and scratch-resisting force were continuously measured. The applied load was either held constant at one or more selected values, or linearly increased during scratching. This load variation permitted identification of critical loads for severe cracking damage of the brittle materials. Scanning electron microscope (SEM) studies were used to characterize the cracking damage. The critical load values depended on tool shape and material microstructure. The studies identified damage mechanisms in the hard coatings, and critical loads for damage initiation. Damage morphology typically involved local surface cracking, edge chipping, and plastic deformation. The relative proportions of cracking and plastic response seemed to vary with tool shape, material, and microstructure.

KEYWORDS: surface coatings, surface treatments, wear testing, ceramics, coatings, plasma-sprayed coatings, scratching, indentation, hardness, elastic modulus

Ceramic materials and coatings are of interest for thermal, mechanical, and corrosion protection of materials and devices in aggressive environments. Examples of current industrial uses include gas and steam turbine engine blades and vanes, nuclear reactor components, and low-heat-rejection internal combustion engines [*1*]. Ceramic material types include oxides, nitrides, and borides. These bulk materials and applied coatings are characterized by high hardness, good wear resistance, good thermal resistance, and low chemical reactivity [*2,3*]. However, hard ceramic materials tend to be brittle and thereby crack easily compared to more ductile but softer metals. As a compromise, metal-ceramic composites having better toughness are of considerable current interest.

If ceramic materials and coatings are to be used widely on mechanical system components, it will be necessary to carry out design calculations that can accurately predict properties or agree with actual measured performance in service. Usually, this involves development of a "material model," in computational form, so that dimensional details can be developed for the

---

[1] Guest scientist, Ceramics Division, National Institute of Standards and Technology, Gaithersburg, MD 20899.

component leading to suitable strength, thermal characteristics, etc. Properties data for the materials are needed as input in such a modeling effort [*4*]. Such properties data may not be readily on hand for new or complex materials, particularly for coatings of variable composition and microstructure. Therefore, it is necessary to have validated methods for measuring material properties, frequently on a small, local scale for materials of interest. This research has examined two measurement techniques that offer promise for this need: (1) instrumented, low load, indentation and (2) instrumented scratching.

Indentation testing has been widely used to measure the mechanical response of materials, including both plastic deformation and cracking [*5*]. Recently, it has become possible to perform controlled, instrumented indentations at depths of 20 nm or less [*6,7*]. Information on hardness and elastic modulus can be obtained by nanoindentation from regions very near the material surface. Similarly, controlled load-scratching techniques have been developed [*8,9*] and applied to measure additional mechanical responses of materials and coatings. Combined use of these two techniques should provide new insight into the near-surface mechanical properties of materials, and into the damaging effects of surface finishing of ceramics.

Experimental

Scratching and Indenting Apparatus

A specially designed nanoindentation and scratching system was used in these studies [*10, 11*]. It involves (Fig. 1) an electromagnetic driver with attached diamond tool (indenter) and a

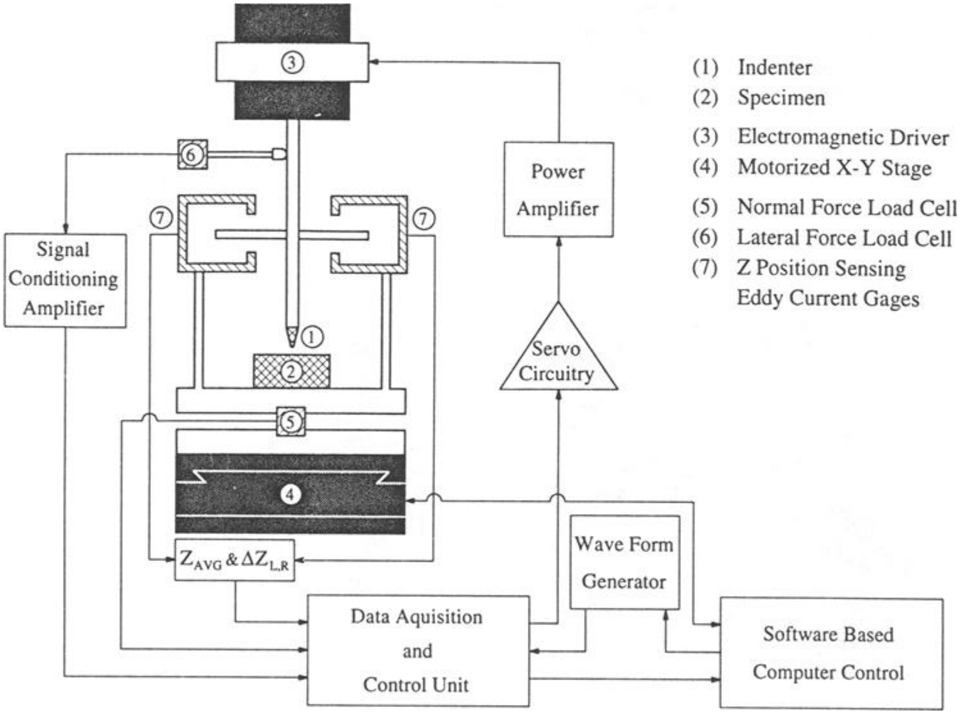

FIG. 1—*Schematic illustration of the indentation-scratching system.*

position-determining eddy current sensor. The sensor measures the relative displacement between the diamond tool and the test specimen. A computer-controlled digital waveform is fed to the driver to apply the load to the tool. Vertical position measurement sensitivity is about 1 nm, and loads are directly measured by a load cell to about 0.1 mN. Thermal drift of the system in the vertical direction is monitored and automatically corrected by the system software. A digitally-controlled X-Y position stage allows generation of multiple indentation patterns of any form, and also permits scratching by translation of the specimen during indenter loading.

The load-time waveform used for indentation in these studies was trapezoidal, typically ramping linearly from zero to maximum set load (range of 50 to 500 mN) in 60 s, then holding for 5 s, then ramping to zero load in 60 s. Surface contact (zero depth) was determined by the change in the indenter tip vibration amplitude as it moved into actual contact with the specimen surface. Scratching was conducted in this work at selected loads over the range of 10 to 500 mN, and scratch lengths of 0.1 to 0.5 mm. Either stepped (constant) or linear increasing load waveforms were used for the individual scratches. The ramping load type scratches were most useful to permit detection of threshold load values for cracking. The stepped-load scratches were used to examine uniformity of material response, for example, from grain to grain, at each load increment. In a typical test, motion would not start until the load had been increased to the desired value. At the conclusion of the scratch, stage motion would stop and the load would be ramped to zero. Scratching speed was in the range of 2 to 5 μm/s for all tests. A load cell measured the lateral force resisting the scratching of the material, and the eddy current sensor provided tool penetration data. Analysis of data recorded during testing along with post-test scanning electron microscope (SEM) observations of scratch damage morphology permitted conclusions to be drawn regarding the material response, which will be discussed later.

Two diamond tool shapes were used for indentation. One was a four-sided diamond pyramidal Vickers indenter with a tip angle of 136°, face-to-face. The shape of the tip apex (determined from scanning electron microscope (SEM) photographs) actually consisted of a short wedge-tip segment 300 nm in length. The other tool shape was spherical, with a radius of either 120 μm or 200 ± 1 μm. Two tool shapes were used for scratching studies. One was the Vickers pyramid, oriented edge-on to the scratching direction, and the other was a wedge-shaped diamond having a curved edge (0.5 mm radius), a −45° rake angle, and a 8° clearance angle. The

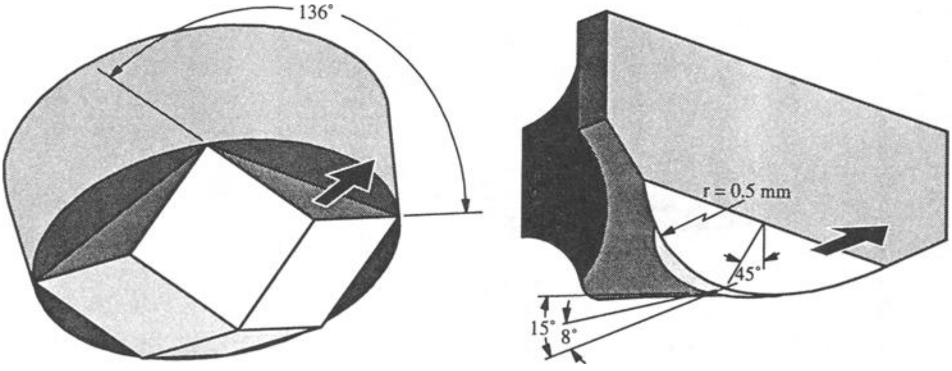

FIG. 2—*Schematic drawing of the two scratching tool shapes used,* (left) *pyramidal (Vickers) and* (right) *wedge-shaped, curved-edge.*

curved edge was oriented perpendicular to the sliding direction. This type of tool is often used in single-point diamond turning of crystalline materials. Illustrations of the scratching tools are shown in Fig. 2. The curved-edge scratching tool was expected to produce relatively more elastically stressed volume (because of a wider contact width and area), relatively higher compressive stresses ahead of the tool (because of the flat face-on orientation), and a lower average contact pressure for a given load. The Vickers diamond pyramid, moved along an edge, was expected to produce more shearing and lateral displacement of the material ahead of the tool. Wear of the pyramid tool tip was experienced, and necessitated occasional tool replacement. Wear of the curved-edge tool was not a problem.

Materials Tested

Several different hard materials were studied. Plasma-sprayed coatings of ZrO_2, a ZrO_2-metal composite, and a Ni-NiO composite, on metallic substrates were obtained. Typically, the specimen size was 10 by 10 by 2 mm, after being cut out of larger coupons. Both surface-section and cross-section orientations were prepared. For purposes of comparison, bulk tetragonal zirconia (containing 5% yttria for stabilization, sintered, and post-hipped), bulk 99.9% nickel, and single-crystal (111) oriented silicon specimens were obtained and measured. In all cases, it was necessary to abrasively polish the specimen surfaces through a range of diamond grit sizes from 15 μm down to 0.25 μm, in order to produce adequate smooth surfaces. Considerable porosity was present in the coatings studied, making it difficult to obtain smooth, uniform surfaces even after polishing. That porosity was a major problem in obtaining reproducible data for the coatings, and was the main factor in choosing a spherical indenter shape for indentation use in the study.

Results and Discussion

Indentation Measurements

Bulk Single-Crystal Silicon—An example of continuous loading-unloading indentation data from several tests using a 200-μm radius sapphire sphere on a (111) silicon single-crystal surface is shown in Fig. 3. The substantial amount of recovery of displacement seen on unloading is characteristic of a highly elastic material. Some cracking occurred in the silicon if the loads were sufficiently high, and that contributed to the unrecovered displacement of about 50 nm. Note that the elastic deflection of the apparatus is included in these data, amounting to about 60 nm at maximum load. Upon unloading, the data initially follow the expected elastic curve but then deviate increasingly as the load falls. Figure 4 shows more detail associated with one test. Several different elastic analyses of unloading have been proposed [*12–16*], along with other treatments that include elastic-plastic considerations [*17–19*]. The analysis method for sharp pyramidal indenters usually invokes a flat punch analogy, and rests on extrapolation of the initial unloading curve to obtain the total compliance (slope) and so-called plastic intercept [*13*]. Since the unloading curve is usually nonlinear, some judgment is required in the analysis. One particular extrapolation line for these data is shown in the figure, selected to best describe the initial unloading slope. Problems usually arise regarding the extent of data to include in the regression analysis, and the order of the regression fit used [*14*].

In this work, it was decided to avoid sharp indenter tips in view of the porosity and surface roughness associated with the specimens. The method of Doerner and Nix [*12*] was followed for the modulus analysis, modified to accommodate the spherical indenter. Figure 4 shows the details for one of these tests. Graphing the reciprocal unloading slope (compliance) versus

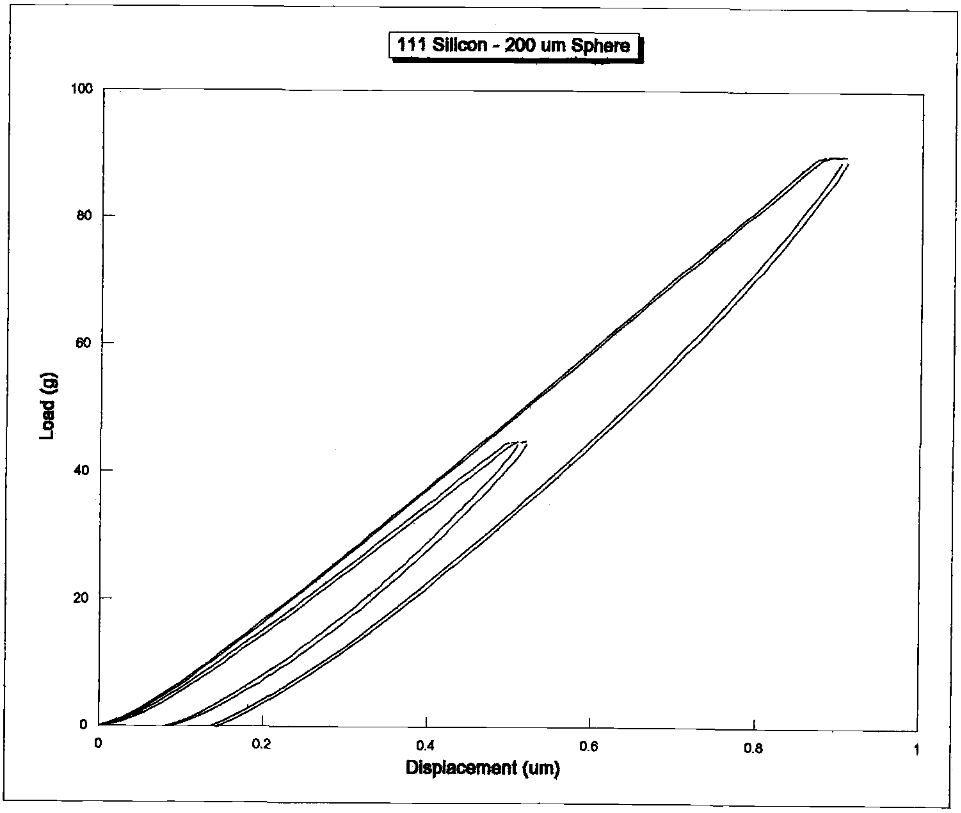

FIG. 3—*Load versus displacement plot of four indentation tests on (111) silicon surface using a 200-μm radius sapphire sphere.*

reciprocal square root of the intercept depth should lead to a straight line relationship whose slope is the combined modulus, E^* [*12*], where

$$1/E^* = (1 - v^2)/E + (1 - v_0^2)/E_0 \tag{1}$$

where E and v are the Young's modulus and Poisson's ratio for the specimen and (Subscript 0) indenter material, respectively. Figure 5 shows the analysis for tests on silicon. The known indentation machine compliance determines the y-intercept. As shown in Table 1, the analysis of four tests leads to an average elastic modulus of 150 ± 18 GPa[2], using Poisson's ratio of 0.223 for silicon, and appropriate elastic constants for the sapphire sphere.

An alternative analysis approach has been developed [*20*] that utilizes the initial portion of the loading data to calculate the elastic modulus. According to Hertz analysis, the relationship between load, P, and elastic deflection, h, for a ball-on-flat geometry is

$$P = 0.94\, E^*\, D^{1/2}\, h^{3/2} \tag{2}$$

---

[2] Mean value ± standard deviation.

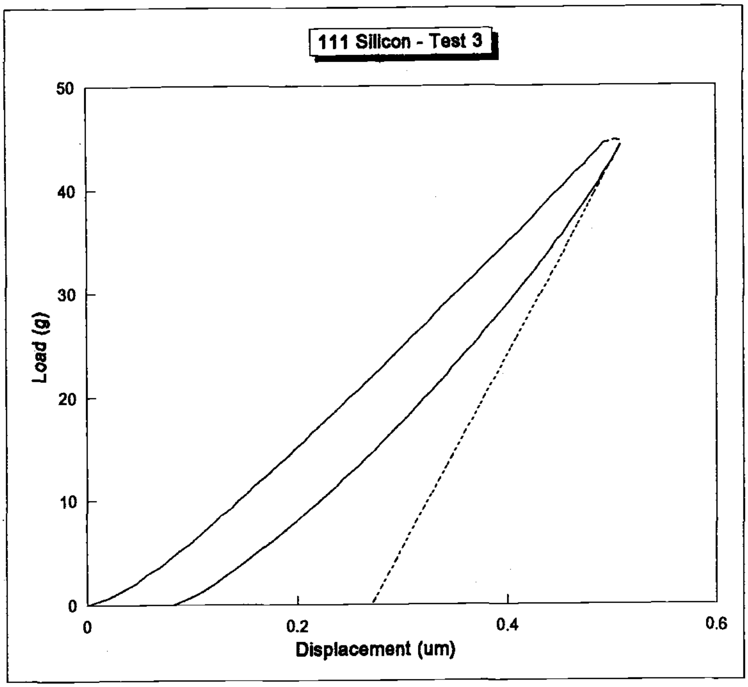

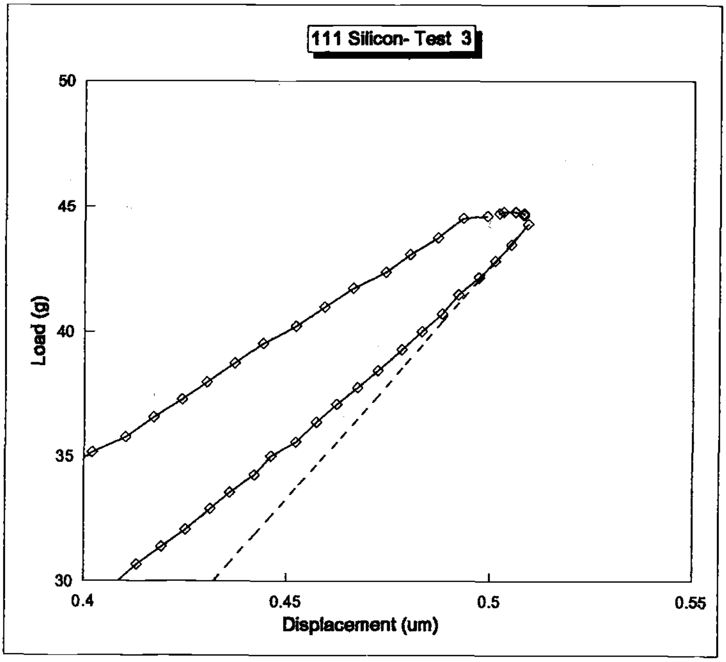

FIG. 4—*Load versus displacement for one test on (111) silicon showing* (top) *extrapolation of initial slope of unloading curve, used to calculate elastic modulus, and* (bottom) *details of initial unloading data.*

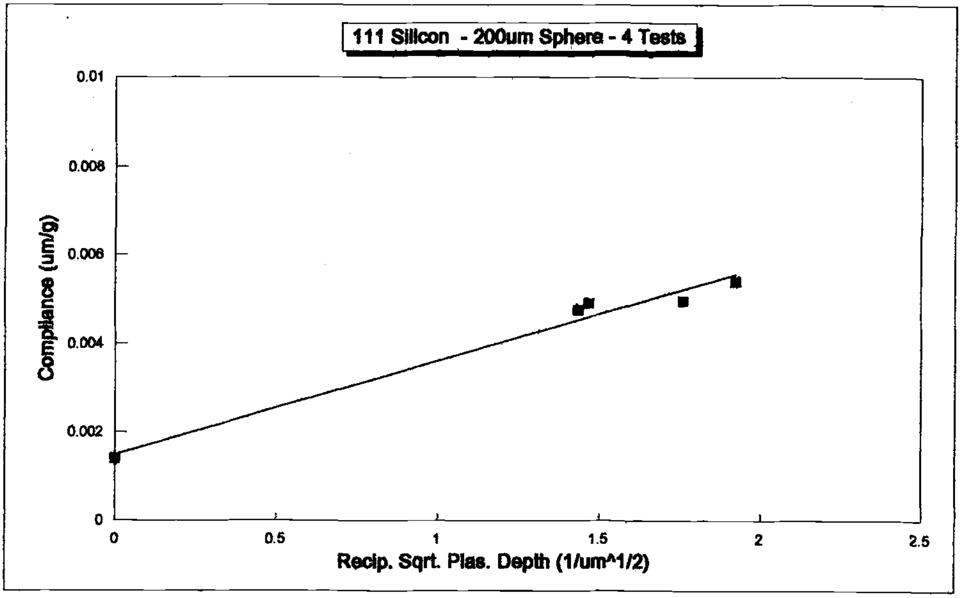

FIG. 5—*Plot of total compliance versus plastic depth from which the modulus value is obtained (see Table 1 for details).*

where E^* is the combined elastic modulus and D is the sphere diameter. A plot of P versus $h^{3/2}$ then allows the determination of E^*. This analysis for silicon, corrected for test machine compliance, leads to a modulus value of 150 ± 10 GPa that agrees within experimental uncertainty with the preceding unloading curve analysis.

In order to determine indentation hardness, a method similar to Field and Swain [*15*] for spherical indenters was followed. Hardness analysis (Meyer hardness) was carried out using the loading data from the same tests, as summarized in Table 2. The average hardness was 4.7 GPa (using projected surface area), with a ratio of contact radius-to-sphere radius (a/R) of

TABLE 1—*Elastic modulus results from unloading data analysis for four tests on (111) silicon (see Fig. 5 and text for details).*

Test	Unloading Slope, g/μm	Plastic Intercept, μm	Reciprocal Unloading Slope, μm/g	Square Root Reciprocal Plastic Intercept, 1/μm$^{1/2}$	Individual Elastic Modulus, GPa
1	201.68	0.322	0.00496	1.76	168
2	210.64	0.487	0.00475	1.43	136
3	185.15	0.270	0.00540	1.92	161
4	203.86	0.465	0.00491	1.47	132
			Average:	E^* (g/μm)	11.3
				E^* (GPa)	110
				E (GPa)	150

TABLE 2—*Hardness analysis for four tests on (111) silicon.*

Test	Condition	Load, g	Displacement, μm	Hardness (H), g/μm^2	Hardness (H), MPa
1	Loaded	44.81	0.510	0.070	686
	Unloaded	0	0.088	0.405	3972
2	Loaded	89.83	0.890	0.080	789
	Unloaded	0	0.140	0.511	5006
3	Loaded	44.62	0.499	0.071	698
	Unloaded	0	0.080	0.444	4351
4	Loaded	89.87	0.882	0.081	796
	Unloaded	0	0.13	0.550	5393
			Averages:	H(loaded), MPa	742
				H(final), MPa	4680
				Contact diameter, μm	33

0.083. Adler [*21*] has recently modeled spherical indentation noting that measured hardness increases with increasing (a/R). That dependence varies with material, and strictly must be measured in each case. Physically, the increase reflects the increasing levels of elastic-plastic accommodation under the indenter. In order to compare hardness measured with spheres at low loads with Vickers pyramid hardness, for example, at high loads, it is necessary to account for that strain accommodation difference. In the present case, following Adler, the hardness of 4.7 GPa would increase to an equivalent value of 8.4 GPa at a fully loaded value of $(a/R) = 0.5$. For comparison, Vickers hardness measurements over the load range of 1 to 2 N gave an average value of 9.3 GPa, about 10% higher than the adjusted value for the spherical indenter. (Most of the difference is based on the use of the surface projected area with the spherical indenter and the indent face area with the pyramid.)

It is possible to use the spherical indenter results on hardness to determine an estimated flow stress by using the well-known relationship [*22*] for plastically deforming materials

$$\text{flow stress} = \text{hardness}/3 \tag{3}$$

This leads to a flow stress value of about 2.8 GPa (at the deformation equivalent of $(a/R) = 0.5$). Alternatively, it is possible to utilize indentation results from a set of three differently shaped indenters to determine parameters in a material constitutive equation, as previously described for copper [*23*].

Table 3 summarizes these results on (111) silicon, as well as for the other materials that are discussed later.

Bulk Nickel—This material was in an annealed state with an average grain size about 3 μm. An example of continuous loading-unloading indentation data from one of the tests using a 200-μm radius sapphire sphere is shown in Fig. 6 (*top*). The recovery of displacement on unloading is less than for (111) silicon, as would be expected for a more ductile metal. An example of one residual indentation is shown in Fig. 6 (*bottom*). The observed diameter, 23.5 μm, is consistent with the calculated average diameter for six tests of 22.65 μm, using the set of final indentation depths recorded. Unloading analysis for six tests following the method described earlier for silicon gave an average elastic modulus of 106 ± 6 GPa, using Poisson's

TABLE 3—*Summary of measured elastic modulus, indentation hardness, and scratch damage mode for the materials studied. Average values ± standard deviation are given.*

Material	Elastic Modulus, GPa	Indentation Hardness, (H), GPa	Scratch Damage Mode
Silicon, (111) crystal	150 ± 18	8.4 ± 1.1	...
Nickel, polycrystalline	106 ± 6	2.9 ± 0.3	...
Nickel coating, plasma-sprayed, 15% porous	34 ± 5	2.8 ± 0.5	...
Zirconia, bulk, sintered, HIP'd, yttria stabilized, tetragonal	166 ± 35	5.8 ± 1.6	microfracture
Zirconia coating, plasma-sprayed, 15% porous	35 ± 5	2.6 ± 0.8	pore edge chipping, microfracture
Zirconia + metal coating, plasma-sprayed	59 ± 7	3.6 ± 0.4	ceramic phase: microfracture metal phase: deformation

ratio of 0.33. For comparison, analysis applied to the six loading curves [*20*] gave a value of 109 ± 10 GPa. Hardness analysis was carried out as described earlier for silicon. The average measured hardness was 1.7 GPa for $(a/R) = 0.10$. For comparison at an equivalent $(a/R) = 0.5$, the adjusted hardness would increase to 2.9 GPa.

Bulk Zirconia—The third reference material chosen was tetragonal-stabilized polycrystalline 95% zirconia – 5 mole % yttria specimens that had been previously used in an interlaboratory study on mechanical properties. Load versus displacement data from four of the tests are shown in Fig. 7 (*top*). As with silicon, a substantial recovery of displacement occurs on unloading, denoting a highly elastic material. Unloading analyses for the tests following the method described earlier gave an average elastic modulus of 166 ± 35 GPa, using Poisson's ratio of 0.3. Figure 7 (*bottom*) shows the detailed data at initial unloading for each of the tests along with the regression fits. Some variation was noted among the tests and was probably associated with actual material or surface topography differences. Hardness analysis was carried out as described earlier. The average measured hardness was 2.7 ± 0.8 GPa for $(a/R) = 0.10$. For comparison at an equivalent $(a/R) = 0.5$, the adjusted hardness would increase to 5.8 ± 1.6 GPa.

Nickel Coating—The nickel-nickel oxide coating[3] was plasma-sprayed (thickness = 0.3 mm) onto steel substrates and showed a typical microstructure for such a coating, as seen in a cross-section view in Fig. 8. Molten and partially-molten particles had impacted on the growing layers as the deposit thickened, leading to a lamellar morphology including considerable porosity (size range 2 to 10 μm) around the edges of the particles. While the cross section was polished prior to testing, it still retained considerable roughness due to the included porosity. A number of (spherical) indentation tests were carried out since considerable scatter was present in the data due to these microstructure variations. Load versus displacement data are shown for two of the tests in Fig. 9. For comparison, data from a test of bulk nickel under similar conditions are also plotted in the figure. Significant differences between the two materials are seen in both the loading and the unloading data. Most notable is the more plastic behavior of the bulk nickel, seen by the smaller displacement recovery upon unloading.

---

[3] Material supplied by C. Berndt, Stony Brook University, New York, 11794.

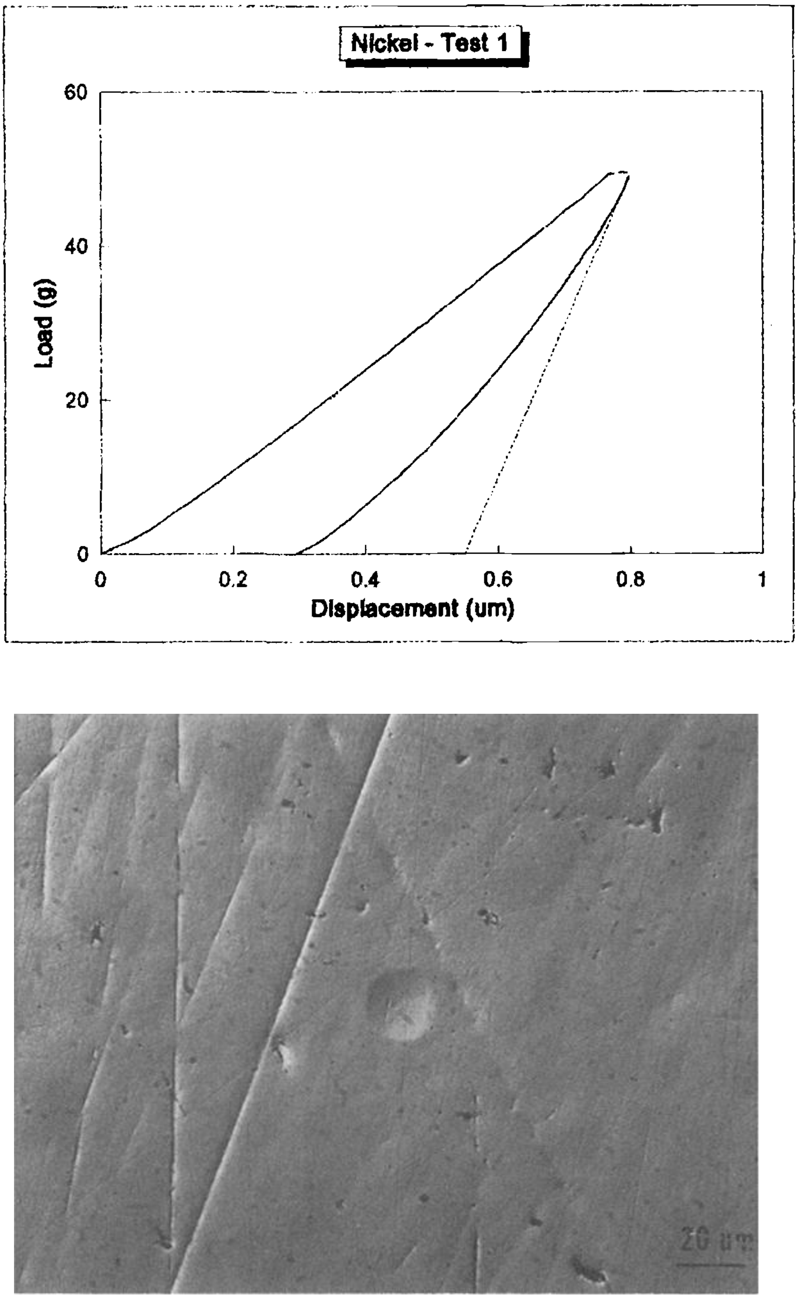

FIG. 6—(top) *Load versus displacement for one test on bulk nickel showing extrapolation of initial slope of unloading curve, used to calculate elastic modulus; and* (bottom) *optical micrograph showing a 1 N residual indentation.*

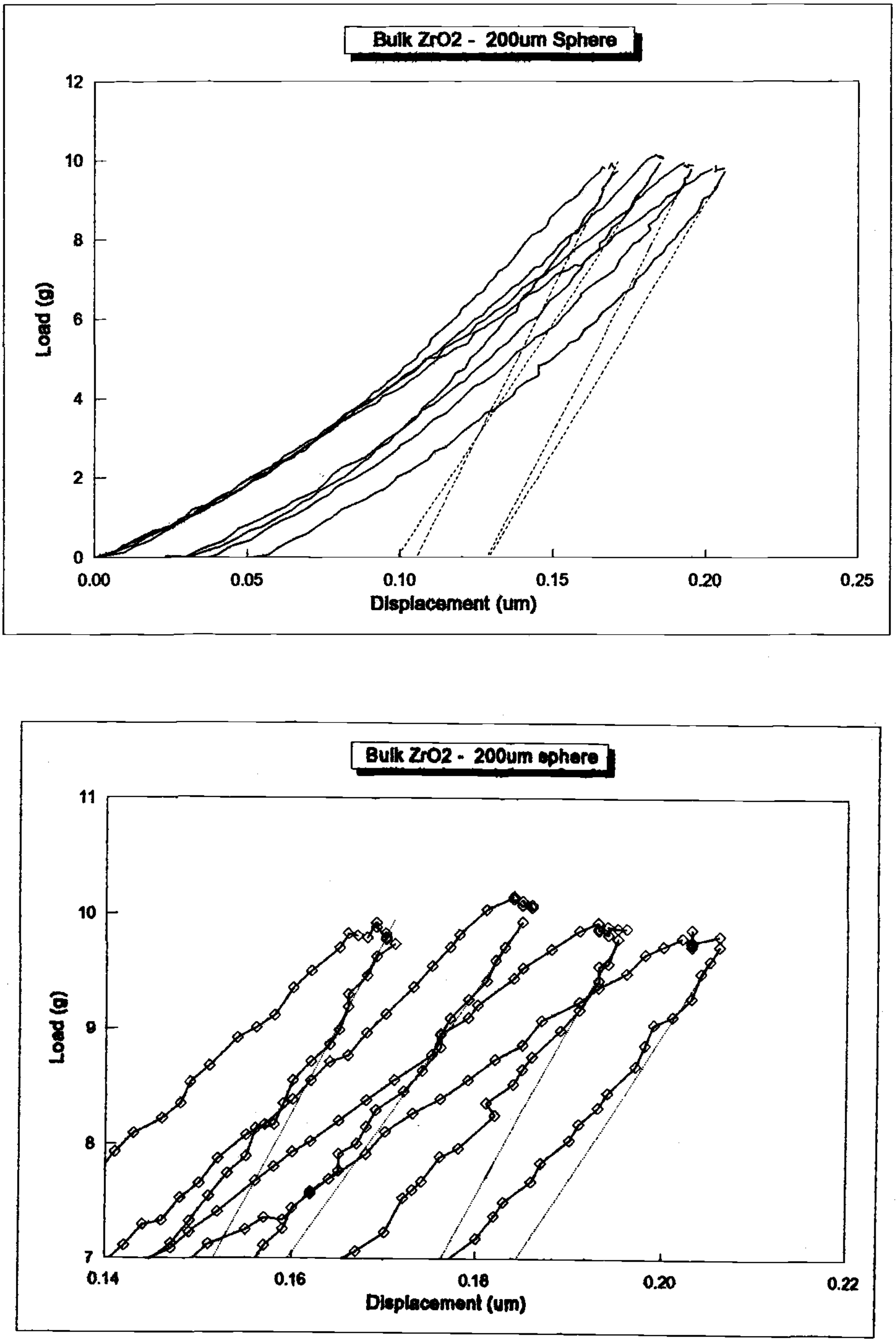

FIG. 7—*Results of four tests on bulk zirconia showing* (top) *load versus displacement data and elastic unloading extrapolations chosen for analysis, and* (bottom) *details at the initial unloading regions for each test.*

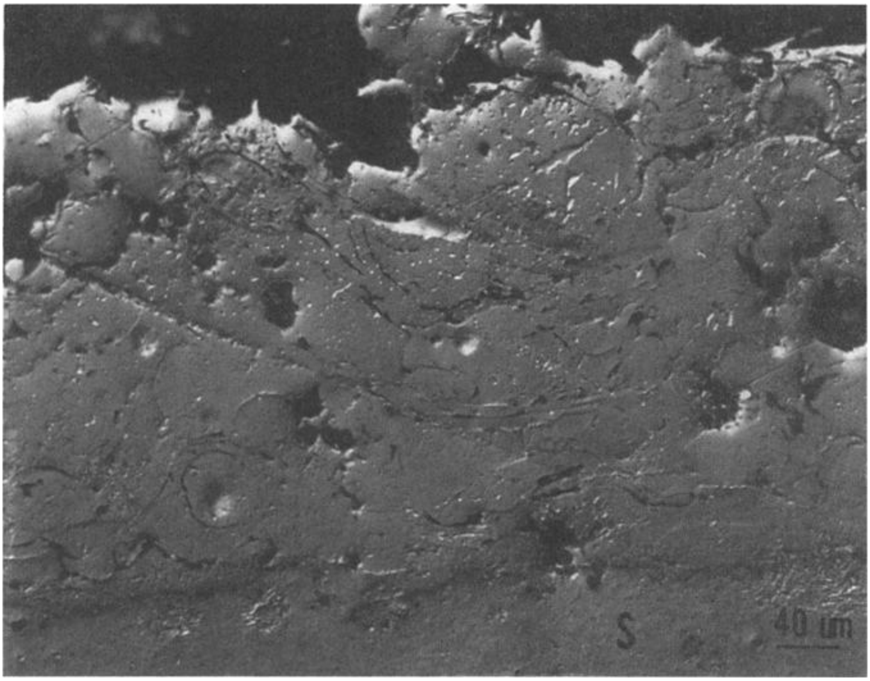

FIG. 8—*Micrograph showing the cross-section microstructure for the Ni/NiO coating. Dark regions are voids. The outer surface is at the top, and the steel substrate is marked S.*

Unloading analyses for the tests gave an average elastic modulus of 34 ± 5 GPa, using Poisson's ratio of 0.33. The relative variation is high because of actual material differences in the different locations due to porosity and metal-oxide proportions. This value is considerably less than the pure nickel result (106 GPa), believed due to specimen porosity, with some effect associated with the nickel-oxide phase present. Hardness analysis was also carried out. The average measured hardness was 1.6 ± 0.3 GPa for $(a/R) = 0.10$. For comparison at an equivalent $(a/R) = 0.5$, the adjusted hardness would increase to 2.8 ± 0.5 GPa. The result is close to the bulk nickel value of 2.9 GPa, probably reflecting a decrease associated with the porosity present and a compensating increase associated with an oxide particle hardening effect.

Zirconia Coating—This coating was commercially prepared[4] for a prior study of thermal barrier coatings of interest for gas turbine blade protection. It had a nominal porosity of 15% by volume and was sprayed onto a steel substrate with a metal-containing bond coat used in the initial deposit region. The coating thickness was 0.9 mm. The original surface was polished in order to produce smoother surface regions for indentation. However, as seen in Fig. 10, surface porosity was considerable. Note that indentations that fell even near to a pore would also be affected as the deformation expanded from the center of the indentation with increasing load. Because of this surface and material variability, considerable scatter was found in the indentation data. Figure 11 shows the results of two of the tests (spherical indenter) that indicate

---

[4] Specimen provided by Dr. K. Kreider, NIST.

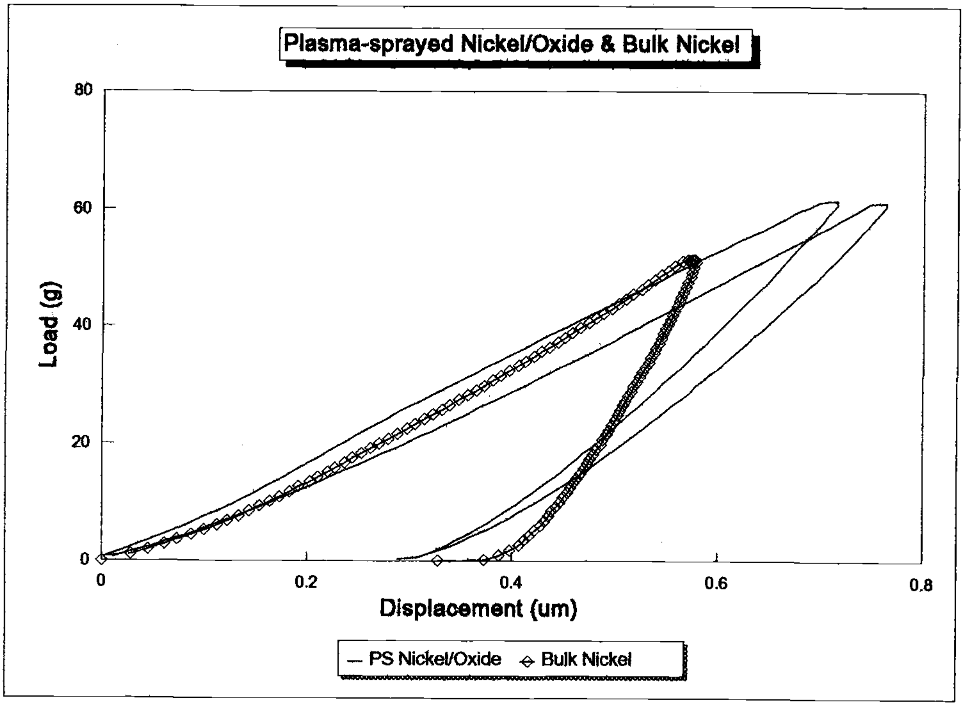

FIG. 9—*Load versus displacement for one test on bulk nickel and two tests on a Ni/NiO coating, shown on the same axes for comparison.*

the range of scatter. Figure 11 (*bottom*) shows detail near the peak load condition, and the extrapolations used for modulus determination.

Unloading analysis for the tests gave an average elastic modulus of 35 ± 5 GPa, using Poisson's ratio of 0.3. The relative variation is believed to be high because of the porosity. This value is considerably less than the pure zirconia result (166 GPa). Hardness analysis led to an average measured hardness of 1.7 ± 0.6 GPa for $(a/R) = 0.10$. For comparison at an equivalent $(a/R) = 0.5$, the adjusted hardness would increase to 2.6 ± 0.8 GPa, less than one-half of the value obtained for bulk zirconia. This lower hardness is believed due to specimen porosity.

Zirconia-Metal Composite Coating—This specimen, obtained from a commercial source, was studied as an example of plasma-sprayed coating technology involving an equal mixture of metal and ceramic particles. Considerable porosity was also found to be present. The coating was about 1 mm thick. The specimen was cross-sectioned, polished, and examined. An example of six of the indentation tests at two loads using the 200-μm sapphire sphere is shown in Fig. 12, along with an optical micrograph of a region of the cross-section surface. The observed scatter in the data can be attributed to the local variation in microstructure.

Analysis of the unloading data gave an average elastic modulus of 59 ± 7 GPa, using Poisson's ratio of 0.3. This value is significantly larger than the porous zirconia coating, but still considerably less than the pure zirconia (166 GPa). Hardness analysis led to an average measured hardness of 2.1 ± 0.2 GPa for $(a/R) = 0.10$. For comparison at an equivalent $(a/R) = 0.5$, the adjusted hardness would increase to 3.6 ± 0.4 GPa, somewhat more than one-half

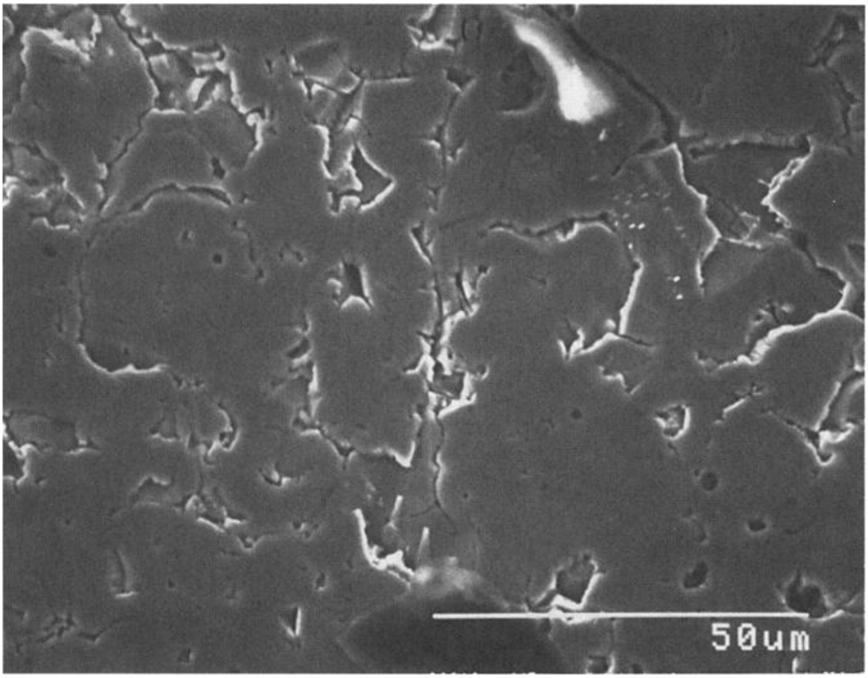

FIG. 10—*SEM micrograph showing the cross-section microstructure for the zirconia coating. Dark regions are pores. Bright edges correspond to particle boundaries with adjacent pores.*

of the value obtained for bulk zirconia, but larger than the hardness of the porous zirconia coating. It appears that metal addition, at a 50% level, increases both elastic modulus and indentation hardness, relative to the ceramic (zirconia) coating. This may be a result of better bonding within the deposit, and of the load-carrying capacity (elastic and plastic) of the metal particles.

Scratching Measurements—Single-point scratching has been used often as an additional technique to supplement indentation [*8,9*]. At light loads, it is a sliding contact process; at high loads, it becomes a material removal process. Scratching introduces a significantly different stress state in the material compared to indentation [*24–26*]. For hard, particularly brittle materials, scratching produces significant tensile stresses behind the contact, and these probe the resistance of the material to cracking [*27,28*]. Since many hard coatings are used in sliding contact situations, a scratching test should be useful to indicate differences in expected performance among materials of interest. Controlled, instrumented scratching tests were applied in this study to the two zirconia coatings and the bulk zirconia described earlier. It was of particular interest to determine the mode of local material failure in each case, and to determine, if possible, the critical load on the contact for initiation of severe failure.

Bulk Zirconia—The pyramidal tool was used for this material, oriented with one edge facing the direction of sliding. A load range of 10 to 250 mN, using a linear ramping function, was studied. One example of the test results is shown in Fig. 13. The upper photograph shows two scratches with a load range of 10 to 100 mN at the bottom, and 100 to 250 mN at the top. Details of the lower load range are seen in the SEM photograph below. The response to this tool appears largely "plastic," involving built-up edges to the scratch and associated loose debris

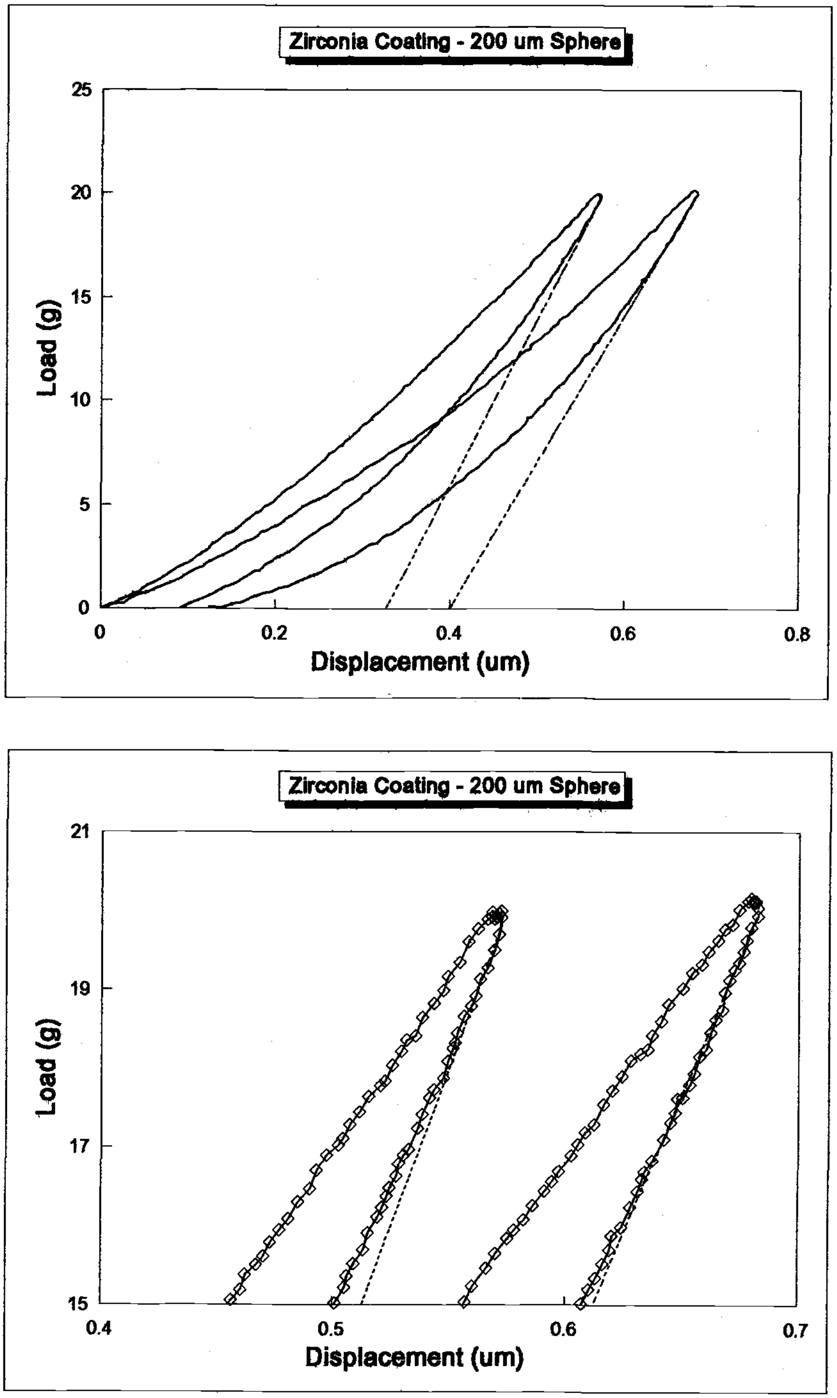

FIG. 11—*Results of two tests on zirconia coating showing* (top) *load versus displacement data and elastic unloading extrapolations chosen, and* (bottom) *details at the initial unloading regions for each test.*

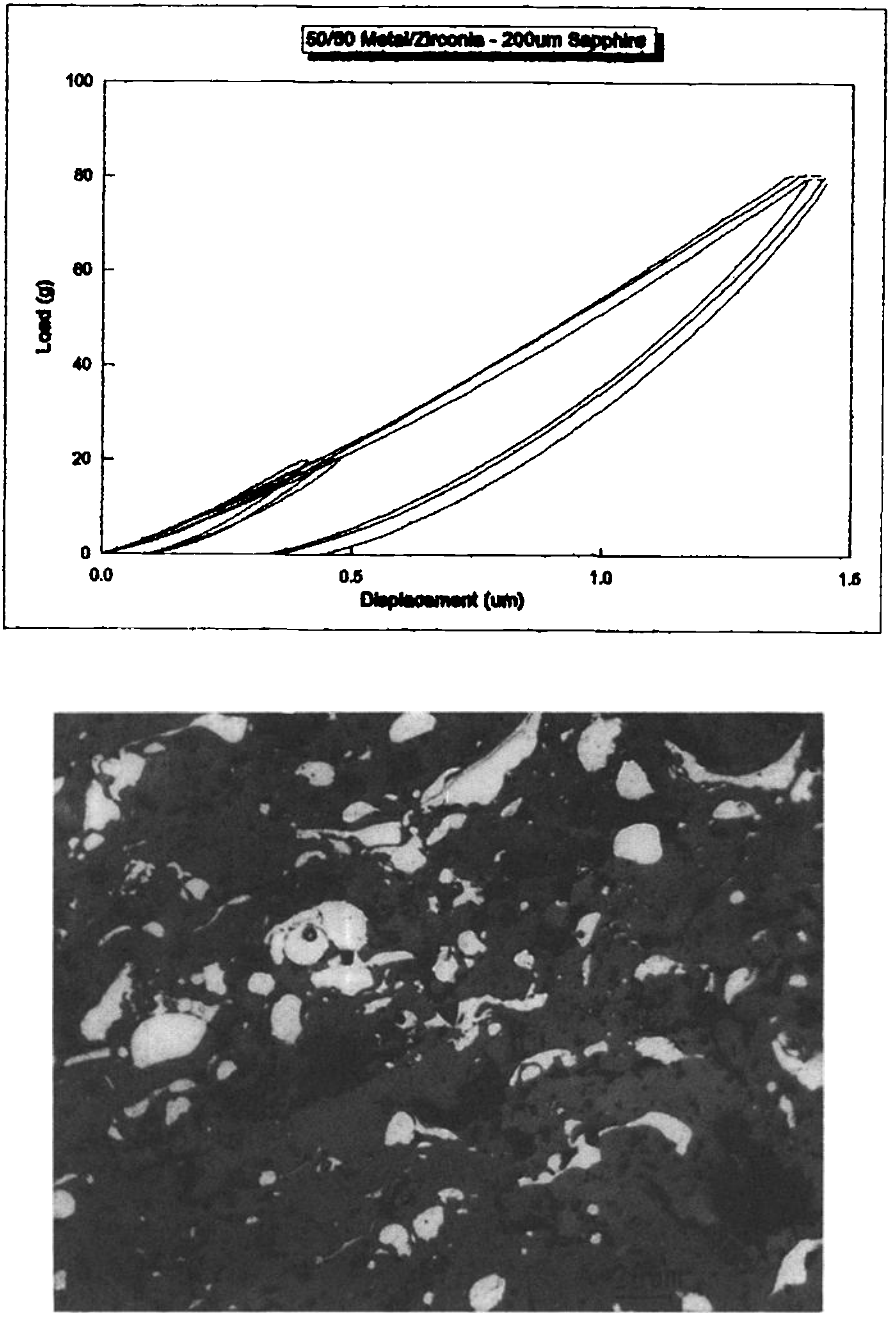

FIG. 12—(top) *Load versus displacement results from six tests on zirconia-metal composite coating.* (bottom) *Optical micrograph showing the cross-section microstructure for the coating. Dark regions are voids. Bright regions are metal particles. The remainder is zirconia.*

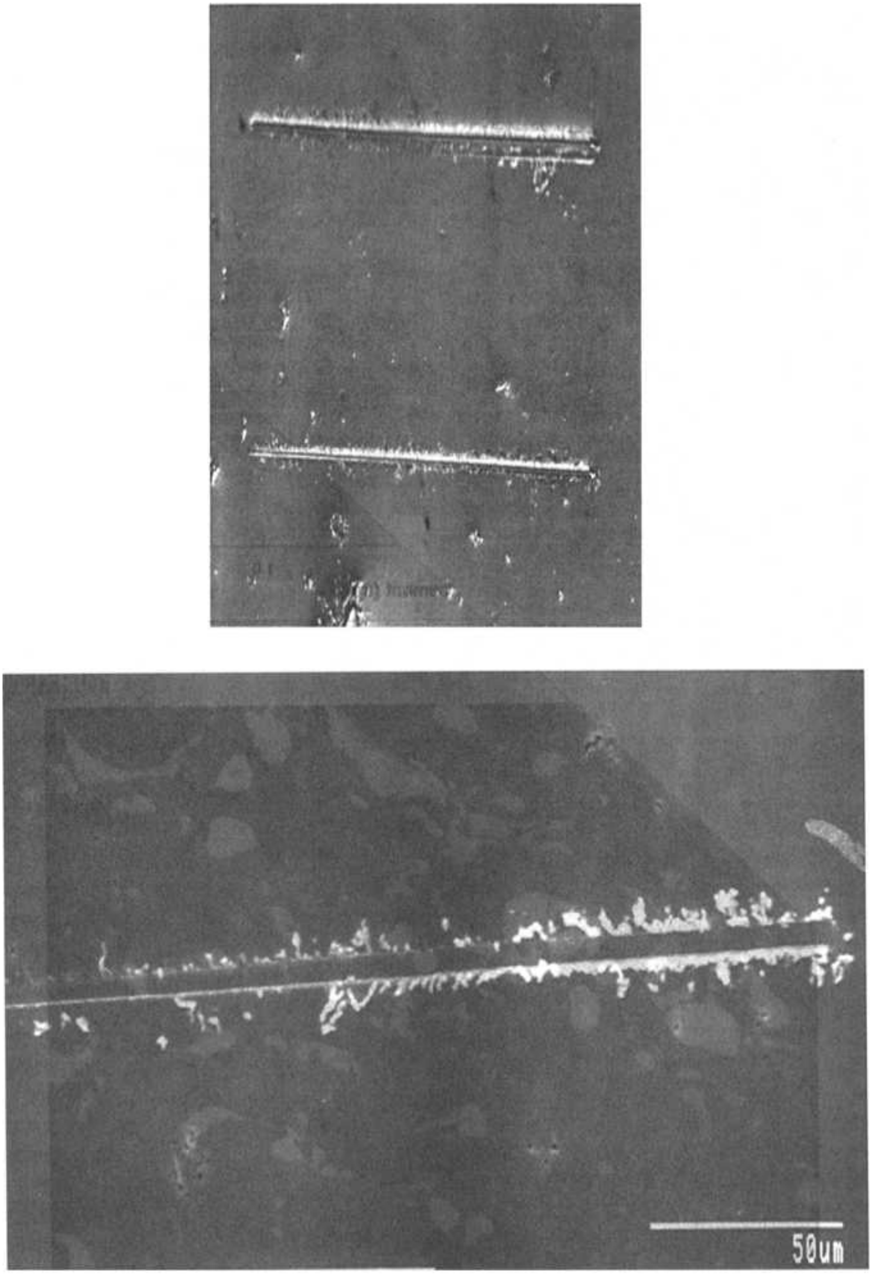

FIG. 13—*Pyramidal tool scratches in bulk zirconia:* (top) *optical micrograph showing two scratches; lower with load varying 10 to 100 mN, left to right; upper with load varying from 100 to 250 mN, left to right, and* (bottom) *SEM micrograph of lower scratch showing debris particles at the scratch edge.*

particles and flakes. The debris at the scratch sides appears to be created by local, micro-fracture processes as the tool progresses. No larger scale cracking is seen, up to 250 mN load, that is, any critical load for severe cracking would be higher. The damage associated with scratching appears to increase steadily with load. No particular failures are seen to be associated with the grain boundary regions in the material.

Zirconia Coating—Two different tool shapes were used on this material, the pyramidal tool oriented with one edge facing the direction of sliding, and the 45° wedge/curved-edge tool. With the latter tool, a linear-ramped load range of 10 to 250 mN was studied as well as a series of stepped loads over a similar range. An example of test results involving three separate pairs of scratches with the wedge tool, each 200 μm in length, is shown in the optical micrograph, Fig. 14. The left pair has load varying continuously from 10 mN at the top to 250 mN at the bottom (scratching direction downward). The center pair has a two-step load function with 120 mN over the upper half (100 μm long) and 170 mN over the lower half, and the right pair has a two-step load function with 70 mN over the upper half and 220 mN over the lower half. Arrows mark the beginning and end of each pair of scratches. The linear increasing load case (the two scratches at the left) shows a critical load for severe cracking to be about 140 mN. In agreement, the constant load scratch at 170 mN shows almost continuous cracking, as does the segment at 220 mN. However the porous regions in the microstructure show local damage at loads as low as 40 mN. In regions where there are no pores, loads as high as 120 mN may not lead to much cracking damage. Thus in this material, damage occurs at much lower loads where pores are located. More detail on this damage is seen in Fig. 15 (*top*) for the scratches with load change from 70 to 220 mN. Considerable edge chipping is seen at pore locations even at low loads. More widespread cracking damage appears to develop from the pore regions.

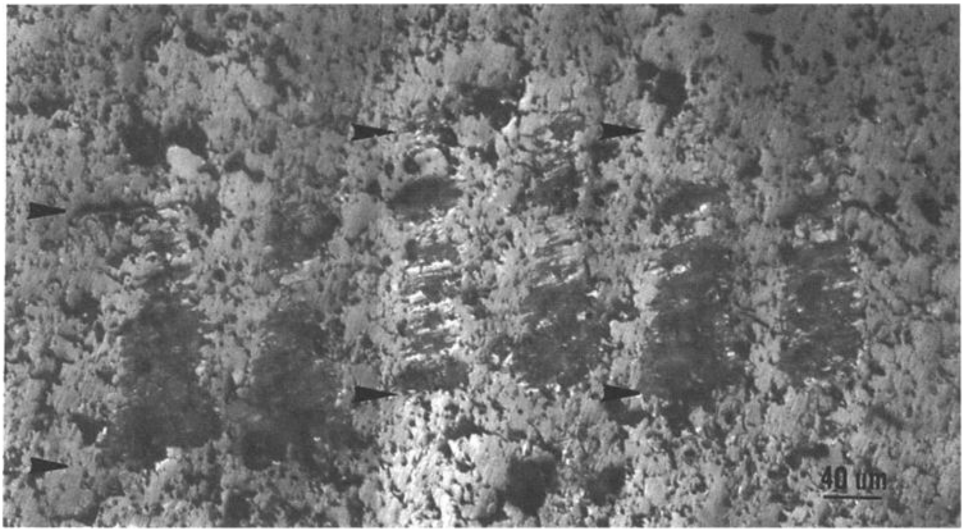

FIG. 14—*Optical micrograph of three pairs of radius tool scratches, each 200 µm long, in zirconia coating: left pair has load varying continuously from 10 mN at top to 250 mN at bottom; center pair has a two-step load function with 120 mN over upper half and 170 mN over lower half; right pair has a two-step load function with 70 mN over upper half and 220 mN over lower half. The arrows have been placed at the beginning and end of each pair of scratches. Scratching direction is downward.*

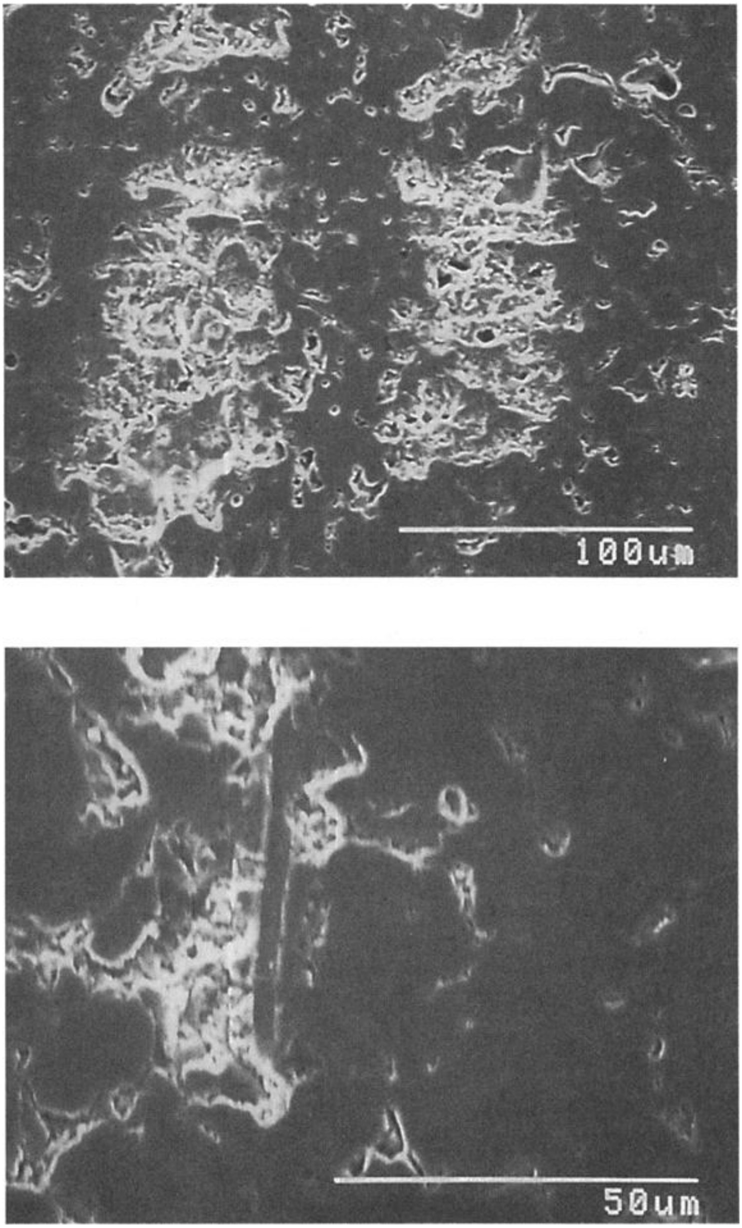

FIG. 15—(top) *SEM micrograph of the right pair of scratches showing details of cracking damage where the loads are 70 and 220 mN, and* (bottom) *SEM micrograph of Vickers scratch in zirconia coating over a load range of 180* (top) *to 220 mN* (bottom).

Figure 15 (*bottom*) shows the damage associated with a pyramidal tool scratch over a similar load range to that discussed earlier, again indicating the localization of damage at existing pores. Comparison with Fig. 13 shows the considerable difference from the behavior found in dense, bulk zirconia for this same tool shape.

Zirconia-Metal Composite Coating—The pyramidal tool was used over a linear ramped load range of 10 to 250 mN. An example of test results is shown in Fig. 16. The upper micrograph shows a scratch over the load range from 100 mN (at the left) to 250 mN (at the right). The measured load variation and tool depth are shown in the graph below the micrograph. The material response appears largely plastic, although edge chipping is seen at two intersected pores. Those two pore locations cause abrupt increases in tool depth, and because the system has a servo link between load and depth (to keep load more constant), the load temporarily decreases near the larger pore. It is also seen that when the tool crosses over two (marked) metal regions, the lower local hardness allows increased tool penetration. In the micrograph, the metal regions scratched show lateral material flow from the scratch that causes an uplift at the boundary with the neighboring zirconia regions. The uplift leads to bright edge contrast at parts of the boundary. There is some debris at the side of the scratch similar to the bulk zirconia specimen results. No large scale cracking is seen, up to 250 mN load, that is, any critical load for severe cracking would be higher in magnitude. It appears that this material falls between the dense zirconia and the porous zirconia in resisting scratching damage, even though it is also porous.

Summary and Conclusions

In summary, this study of several hard materials and coatings was intended to examine some promising methods for material property measurements. Instrumented microindentation was able to provide data on hardness and elastic modulus on selectable size scales depending on the microstructure. Instrumented scratch testing was able to provide data on coating scratch resistance, and damage mechanisms involving plastic and brittle behavior.

Several conclusions can be drawn from the experimental results described earlier concerning low-load indentation and scratching techniques.

1. Indentation measurements using load and displacement time-resolved data can provide hardness and elastic modulus values for hard, bulk materials that agree, typically within 10%, with values determined by more convention testing. The results vary somewhat depending on the analysis method used. Use of these methods with hard coatings, however, requires proper consideration of substrate effects. Those effects are relatively more substantial for thinner coatings and higher loads. Finite element analysis of the coating-substrate combination is important to proper data interpretation.
2. Instrumented scratching using load and displacement time-resolved data can determine local material damage and failure mechanisms, critical loads or pressures for cracking, and indicate the effects of pre-existing flaws. Since scratching produces different stressing conditions than does normal indentation, it provides a valuable adjunct to the results from indentation testing alone. For coated systems, instrumented scratching tests may be particularly appropriate where sliding contact applications are being considered. Two areas needing further work are analytical modeling of scratching stresses and the effect of tool shape.
3. Surface porosity and surface finishing damage can significantly affect hard-coating resistance to sliding contact. Conflicting requirements may appear, such as achieving low thermal conductivity by the introduction of volume porosity, while also achieving adequate resistance to loaded, sliding contacts.

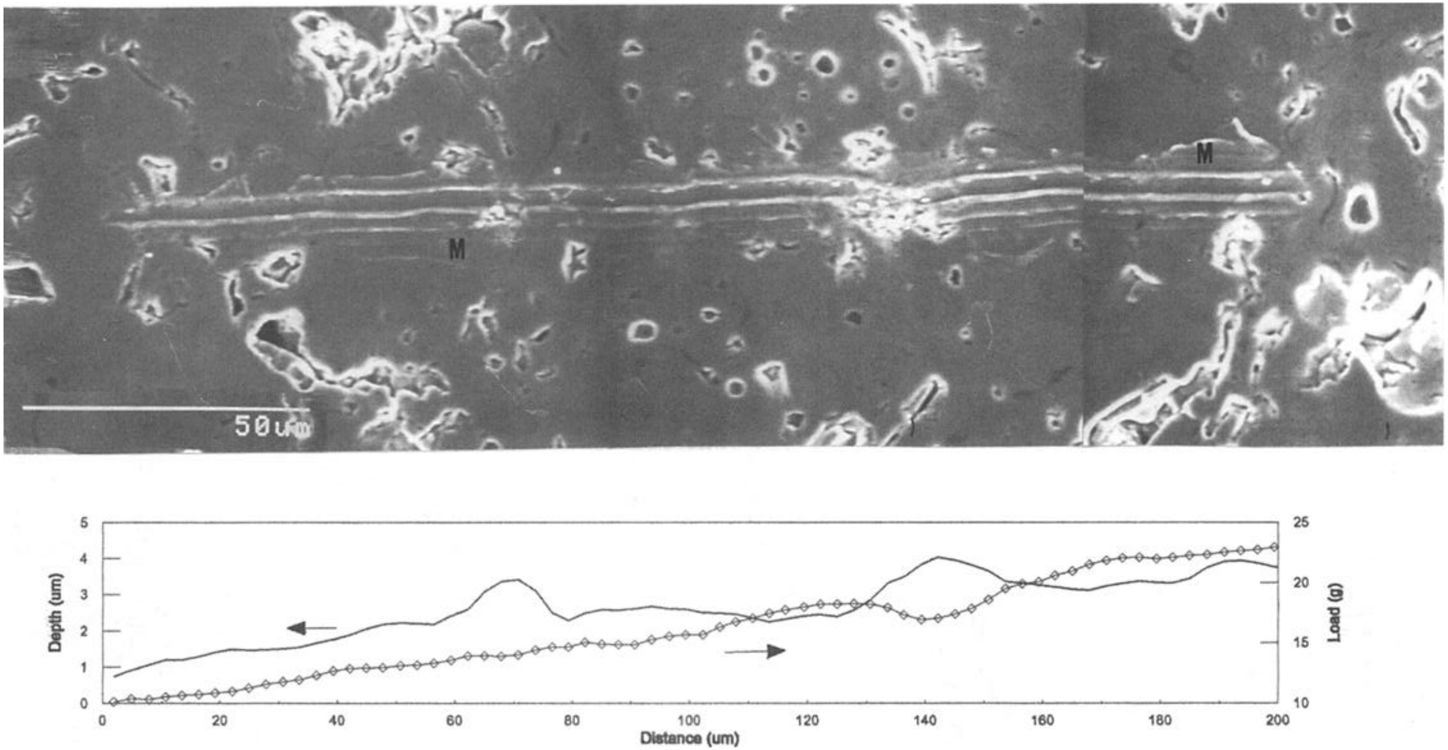

FIG. 16—(top) *SEM micrograph of Vickers scratch in zirconia-metal composite, and* (bottom) *applied load and tool penetration depth are shown for positions along the scratch. Several metal phase regions are marked as M.*

4. Further improvements to the indentation and scratching test methods and analyses would be beneficial for better hard-coating evaluation, particularly for the assessment of material microstructure effects.

Acknowledgments

Dr. H. Shin, University of Maryland, assisted in several phases of the research. Discussions of analysis methods and results with Professor R. Armstrong and Dr. L. Ramaswamy, University of Maryland, are gratefully acknowledged.

References

[*1*] *Wear Testing of Advanced Materials, ASTM STP 1167,* R. Divakar and P. J. Blau, Eds., American Society for Testing and Materials, Philadelphia, 1992.

[*2*] *Wear Test Selection for Design and Application, ASTM STP 1199,* A. W. Ruff and R. G. Bayer, Eds., American Society for Testing and Materials, Philadelphia, 1993.

[*3*] Budinski, K. G., *Surface Engineering for Wear Resistance,* Prentice Hall, Englewood Cliffs, NJ, 1988.

[*4*] *Tribological Modeling for Mechanical Designers, ASTM STP 1105,* K. C. Ludema and R. G. Bayer, Eds., American Society for Testing and Materials, Philadelphia, 1991.

[*5*] *Microindentation Techniques in Materials Science and Engineering, ASTM STP 889,* P. J. Blau and B. R. Lawn, Eds., American Society for Testing and Materials, Philadelphia, 1984.

[*6*] Newey, D., Wilkins, M. A., and Pollock, H. M., "An Ultra-Low Load Penetration Hardness Tester," Journal of Physics E: Scientific Instrumentation, Vol. 15, 1982, pp. 119–122.

[*7*] Pethica, J. B., Hutchings, R., and Oliver, W. C., "Hardness Measurement at Penetration Depths as Small as 20 nm," *Philosophical Magazine A,* Vol. 48, 1983, pp. 593–606.

[*8*] Jacobsson, S., Olsson, M., Hedenqvist, P., and Vingsbo, O., "Scratch Testing," *Friction, Lubrication, and Wear Technology: ASM Handbook,* Vol. 18, 1992, pp. 430–437.

[*9*] Wu, T. W., "Microscratch Test for Ultra-thin Films," *Proceedings,* Materials Research Society Symposium, Vol. 188, 1990, pp. 191–205.

[*10*] Chen, Y.-M., Ruff, A. W., and Dally, J. W., "Numerical Simulation of the Micro-indentation Process," *Proceedings,* ASME Symposium on Contact Problems and Surface Interactions in Manufacturing and Tribological Systems, New Orleans, American Society of Mechanical Engineers, 1993.

[*11*] Ruff, A. W., Shin, H., and Evans, C. J., "Chemo-mechanical Damage During Diamond Tool Scratching of CVD Silicon Carbide," *Proceedings,* ASME Symposium on Contact Problems and Surface Interactions in Manufacturing and Tribological Systems, New Orleans, American Society of Mechanical Engineers, 1993.

[*12*] Doerner, M. F. and Nix, W. D., "A Method for Interpreting the Data from Depth-sensing Indentation Instruments," *Journal of Materials Research,* Vol. 1, 1986, pp. 601–609.

[*13*] Oliver, W. C. and McHargue, C. J., "Characterizing the Hardness and Modulus of Thin Films using a Mechanical Properties Microprobe," *Thin Solid Films,* Vol. 161, 1988, pp. 117–122.

[*14*] Oliver, W. C. and Pharr, G. M., "An Improved Technique for Determining Hardness and Elastic Modulus using Load and Displacement Sensing Indentation Experiments," *Journal of Materials Research,* Vol. 7, 1992, pp. 1564–1583.

[*15*] Field, J. S. and Swain, M. V., "A Simple Predictive Model for Spherical Indentation," *Journal of Materials Research,* Vol. 8, 1993, pp. 297–306.

[*16*] Weppelmann, E. R., Field, J. S., and Swain, M. V., "Observation, Analysis, and Simulation of the Hysteresis of Silicon Using Ultra-Micro-Indentation with Spherical Indenters," *Journal of Materials Research,* Vol. 8, 1993, pp. 830–840.

[*17*] Armstrong, R. W. and Robinson, W. H., "Recovered Elastic and Plastic Deformation Behavior from a Continuous Indentation Hardness Test," *New Zealand Journal of Science,* Vol. 17, 1974, pp. 429–433.

[*18*] Hammond, B. L. and Armstrong, R. W., "Recovered Elastic and Plastic Strains at Residual Micro-Indentations in an MgO Crystal," *Philosophical Magazine Letters,* Vol. 57, 1988, pp. 41–47.

[*19*] Armstrong, R. W., Shin, H., and Ruff, A. W., "Elastic/Plastic Effects During Low-Load Hardness Testing of Copper," *Acta Metallurgica Materials,* Vol. 43, 1995, pp. 1037–1043.

[*20*] Armstrong, R. W., Ramaswamy, A. L., and Ruff, A. W., private communication.

[21] Adler, T. A., "Elastic-Plastic Indentation of Hard, Brittle Materials with Spherical Indenters," *Journal,* American Ceramic Society, in press.

[22] Tabor, D., *The Hardness of Metals,* Clarendon Press, Cambridge, UK, 1951.

[23] Chen, Y.-M, Ruff, A. W., and Dally, J. W., "A Hybrid Method for Determining Material Properties from Instrumented Micro-Indentation Experiments," *Journal of Materials Research,* Vol. 9, 1993, pp. 1314–1321.

[24] Kato, K., "Micro-Mechanisms of Wear—Wear Modes," *Wear,* Vol. 153, 1992, pp. 277–295.

[25] Kato, K., Diao, D. F., and Tsutumi, M., "The Wear Mechanism of Ceramic Coating Film in Repeated Sliding Friction," *Wear of Materials—1991,* American Society of Mechanical Engineers, New York, pp. 243–248.

[26] Adler, T. A. and Walters, R. P., "Wear and Scratch Hardness of 304 Stainless Steel Investigated with a Single Scratch Test," *Wear,* Vols. 162–164, 1993, pp. 713–720.

[27] Xie, Y. and Williams, J. A., "The Generation of Worn Surfaces by the Repeated Interaction of Parallel Grooves," *Wear,* Vol. 162, 1993, pp. 864–872.

[28] Ruff, A. W., Shin, H., and Evans, C. J., "Damage Processes in Ceramics Resulting from Diamond Tool Indenting and Scratching in Various Environments," *Wear,* Vols. 181–183, 1995, pp. 551–562.

Lin Li[1] *and Xue Qunji*[1]

Studies on the Characterization and Tribological Behavior of Self-Propagating High-Temperature Synthesis (SHS) Coatings of Chromium Cermet

---

REFERENCE: Li, L. and Qunji, X., **"Studies on the Characterization and Tribological Behavior of Self-Propagating High-Temperature Synthesis (SHS) Coatings of Chromium Cermet,"** *Effect of Surface Coatings and Treatments on Wear, ASTM STP 1278,* S. Bahadur, Ed., American Society for Testing and Materials, 1996, pp. 147–160.

ABSTRACT: A chromium cermet coating, about 150 μm thick, was formed on carbon steel with the gas transport self-propagating high-temperature synthesis (SHS) coating process. The present paper is concerned with the preparation method, property evaluation, and abrasive wear behavior of the SHS coatings. The experiment reveals that there is excellent adhesion between the coating and the substrate, with less matrix damage and good abrasive wear resistance compared with chemical vapor deposition (CVD)-Cr_7C_3 coatings. Investigations indicated that an intense metallurgical interaction, gradient composition distribution, and unique forming process are the major reasons for the superior performance of the SHS coatings. It is analytically shown that there is a relationship between the size of the abrasive, the coating thickness, and the abrasive wear resistance.

KEYWORDS: surface coatings, surface treatments, wear testing, combustion synthesis, gas transport, cermet coatings, diffusion, coating bonding, abrasion resistance, abrasion wear

Usually, wear resistance is a crucial factor in mechanical design, because many machine component failures are due to wear. One economical way to improve component life is to deposit ceramics or cermet hard coatings on soft or inexpensive materials such as steel, aluminum, etc. Up to now, great efforts have been made on surface techniques. Chemical vapor deposition (CVD) is one of the most important means [*1–4*]. The main advantages of CVD in engineering are the wide range of available coating materials (metallic, nonmetallic, and composite films) and excellent surface finishing (roughness less than 0.1 μm normally). However, the crucial forming conditions, consisting of more than 1000°C that can last for hours, can be difficult for many ordinary structural materials that can be seriously damaged during the procedure.

In recent years, a highly exothermic reaction, the self-propagating high-temperature synthesis (SHS) or simply, combustion synthesis, has been explored for making various advanced ceramic materials [*5–9*]. Once ignited, the reaction becomes self-sustaining and rapidly propagates through the reactant mixture in the form of a combustion wave at elevated temperature. The reactants are immediately converted into final products when the wave spreads over. As a principal branch of SHS technology, gas transport coatings deal with new processes in which thin coatings, 10 to 250 μm, are deposited onto various surfaces such as metal, ceramics, graphite, etc. The SHS coating process is situated, in principle, between gas phase condensation

---

[1] Assistant professor and professor, respectively, Lanzhou Institute of Chemical Physics, 730000, Lanzhou, China.

and diffusion saturation [*10*]. At present, work is concerned with alloy coatings, such as, iron-chromium-boron (Fe-Cr-B), iron-chromium-boron-aluminum (Fe-Cr-B-A1), chromium-nickel-aluminum-yttrium (Cr-Ni-A1-Y), etc. and limited ceramic coatings, such as, TiN, TiCN, etc. [*11*].

In this work, a chromium cermet coating and its characteristics and tribological behavior are investigated. Also, a comparison between a CVD coating and a SHS coating of similar composition is investigated.

Principles of Gas Transport SHS Coating

A typical SHS reaction-based thermite for synthesis of refractory phases can be written

$$AO + A1 + X \rightarrow AX + A1_2O_3 \qquad (1)$$

where

AO = oxide of Element A, usually being transition metals;
X = oxidizer, such as C, Si, B, N; and
AX = desired compound formed by A and X.

The most remarkable features of Eq 1 is the generated temperature above the melting point of alumna. One example of such reaction is as follows

$$MoO_3 + 2A1 + 2Si \rightarrow MoSi_2 + A1_2O_3 \qquad (2)$$

However, in a coarse-grained and uncompacted system, the initial contact area is so limited that the related solid reaction is nearly impossible or, at most, only at a very low rate. This is due to the fact that the reactive diffusion at the minimum contact surface has a huge energy barrier. Some additional agents, called gas transport agents (GTAs), are added to provide a gas transport action that can speed up the solid reaction. It can be explained as follows.

For a solid system where A(s) + B(s) → AB(s) at a lower temperature (T_1) zone, A(s) will first react with D(g) (GTA) to form a gaseous compound, AD(g). While at a higher temperature (T_2) zone, AD(g) will decompose and react with B(s) to form the AB(s) product, consequently. The general scheme of the reaction can be expressed as

$$A(s) + D(g) \rightarrow AD(g) \qquad \text{Zone 1 } (T_1) \qquad (3)$$

$$AD(g) + B(s) \rightarrow AB(s) + D(g) \qquad \text{Zone 2 } (T_2) \qquad (4)$$

Since the transferred A(s) reactant can be condensed on the surface of the other B(s) reactant by the AD(g) medium, the contact area can be greatly increased and the solid reaction can be started up successfully. The chemical nature of the gaseous carrier may be different for various reactants, but as a general rule, carbon can be transferred by hydrogen, and metal by halogens.

This principle can also be utilized to the SHS coating process. If B(s) is the element on the

TABLE 1—*Chemical composition of the substrate.*

C	Si	Mn	P	S	Cr	Ni	Fe
0.42 to 0.49	0.17 to 0.37	0.50 to 0.80	<0.04	<0.04	<0.25	<0.25	balance

TABLE 2—*Mechanical properties of the temper-treated substrate.*

Yielding Strength, MPa	Ultimate Strength, MPa	Strain, %	Vickers Hardness, GPa
500	700	17	4.1

substrate surface, the AB(s) compound will be produced in situ, as AD(g) reaches the surface. Further, if complex GTAs are used, the reactants that form the SHS procedure, such as those in Eq 1, can also be transferred, and a coating with the desired chemical products can be finally obtained. Since both the energy necessary for the gas transport reaction and the transferred chemicals come from the SHS reaction, this is called gas transport SHS coating process (or the "SHS coating" in this paper).

Experimental Procedures

Substrate Preparation

For practical consideration, a No. 45 carbon steel (AISI 1045) is chosen as the substrate material, and its original chemical composition and mechanical properties are given by Tables 1 and 2.

The size of the substrate is 24 mm in diameter and 10 mm in height. Prior to the coating process, the substrate is ground to a surface finish of 0.5 μm and followed by acetone ultrasonic cleaning.

SHS Coating Procedure

A previous investigation [*12*] demonstrated that the characteristics of SHS coatings, such as thickness, roughness, hardness, adhesion, microstructure, and so on, could be strongly influenced by the following factors: ambient pressure of the gas, batch size of the reactants, variety and amount of GTA, compact density of the charge, preheating temperature of substrates, etc. Therefore, the authors chose a set of process parameters (Table 3) and reactant mixture (Table 4) to optimize their research here.

The reactants are gently mixed with a blender protected with nitrogen gas for 20 h and then compacted with a die. Everything is then set up as shown in Fig. 1. The unit is evacuated at the end of preheating, which is necessary to attain the suitable temperature of the matrix, and is filled with argon to a desired pressure. A tungsten coil is subsequently used as an igniter that is electrified by a transformer (10 to 30 A). To be reliably initiated, the mixture is not directly ignited by the tungsten-igniter, but by a chemical furnace medium located on top of the compacted mixture. The medium is composed of aluminum powder, barium peroxide (BaO_2), and potassium chlorous ($KClO_3$) with a mass ratio of 1:4:0.7. The SHS coating process can be completed during a few seconds.

TABLE 3—*Used processing parameters for the SHS coatings.*

Medium gas	Ar
Ambient pressure, MPa	20
Batch size of the charge, g	8.0
Preheating temperature, °C	150
Compact porosity, %	45

TABLE 4—*Reactants used in SHS coating deposition.*

Chemicals	Purity, %	Particle Size, mesh	Mass Percentage, %
Chromium oxide, CrO_3	92.0	300	36
Chromium oxide, Cr_2O_3	98.0	300	27
Carbon black, C	99.9	800	9
Aluminum powders, Al	97.0	200	26
Yttrium oxide, Y_2O_3	99.9	400	0.8
Ammonium oxyhydrate, NH_3OH	98.0	400	0.4
Sodium chloride, NaCl	99.9	400	0.8

Preparation for the CVD Coating

The reaction for the preparation of CVD- Cr_7C_3 coatings is conducted by

$$7CrCl_2 + 7H_2 + 3C \rightarrow Cr_7C_3 + 14HCl \tag{5}$$

where the carbon comes from the treated steel. The coating is prepared at 1000°C and argon atmosphere with a low pressure CVD facility[2]. According to the report, the features of the prepared specimen are a coating thickness of 7 to 10 μm, surface hardness of 7.8 to 8.6 GPa, and forming phases of Cr_7C_3 + 45 to 55% Cr.

---

[2] The coating preparation was done at the factory of Jinwei Textile Machinery, Shanxi, China. The equipment was supplied by Bernex Corporation of Switzerland.

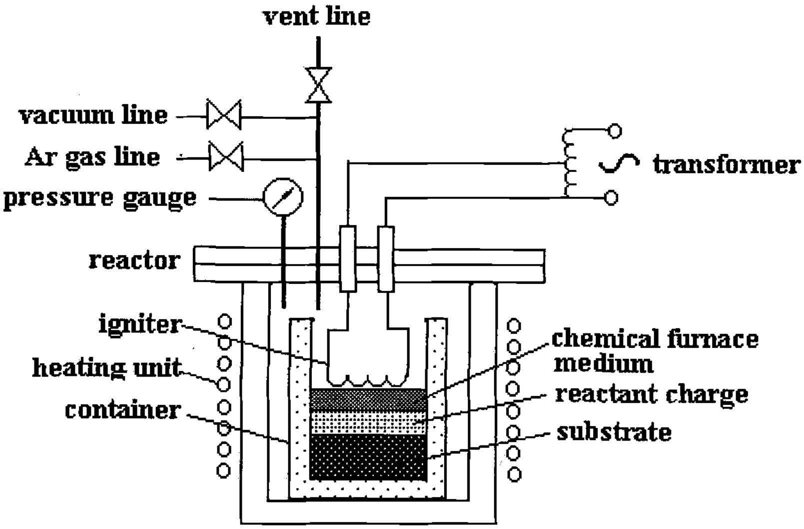

FIG. 1—*Schematic of the SHS coating deposition unit.*

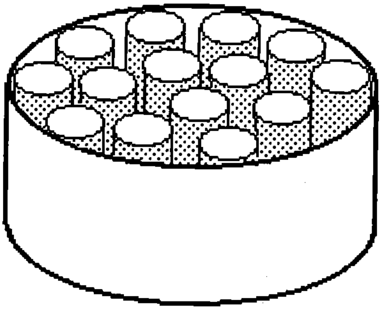

FIG. 2—*Schematic of pin specimens reformed from the coating specimen.*

Microstructure and Mechanical Properties Tests

X-ray diffraction (XRD, D/MAX-RB, Japan), electron probe microanalysis (EPMA-810Q, Japan), and scanning electron microscopy (SEM, JEM-1200 EXS, Japan) are employed for the microstructure examination of the SHS coatings.

The hardness of the specimen is measured in a microhardness tester, with a load of 20 g (MVK-1, Japan).

The bond strength evaluation of the coatings is carried out by a qualitative method, that is, by thermal quenching experiments. After 10 min in an air furnace at 950°C, the coated specimen is quenched in a saltwater solution (10% NaCl) and maintained there for 30 s. This is repeated until the coating peels. The maximum non-peeling cycles can be used as an indication of the dynamic bond strength.

Wear Tests

Wear tests are carried out using a pin-on-disk configuration. A piece of silicon-carbide (SiC) abrasive paper is fitted on a motorized disk. All tests used a 100-mm diameter fixed track, and the linear velocity can be changed by adjusting the revolution of the motor. The pin specimen is processed from the coated specimen by spark discharging (Fig. 2). Prior to the testing, the pin specimen is ground in situ with 600 grit SiC paper. The test variables selected are given in Table 5.

Wear rate is determined by the ratio of the mass loss to the sliding distance. Finally, the worn surface is examined with SEM.

TABLE 5—*Variables of abrasive wear test.*

Normal force, N	2.5, 15.0, and 35.0
Sliding velocity, m/s	0.3, 1.0, 2.1, and 4.5
Temperature, °C	25
Environment humidity	50%
Sliding distance, m	600
Type of motion	continuous sliding
SiC grit paper	#120 (115 μm size)

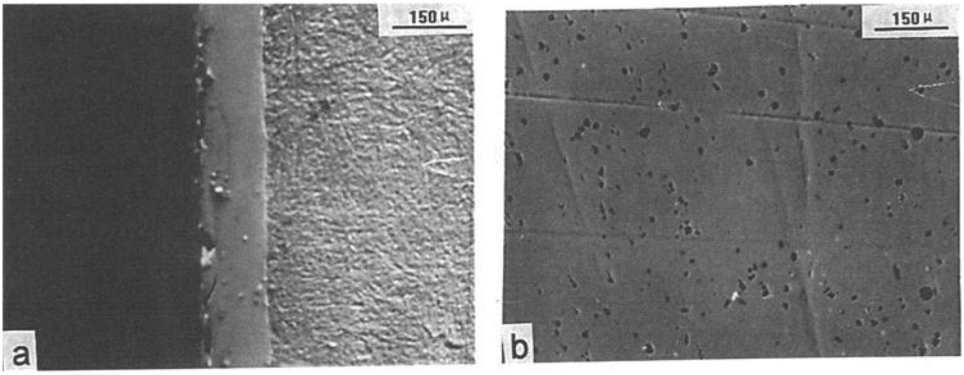

FIG. 3—*Micrographs of the SHS coating:* (a) *on the cross section and* (b) *on the coating surface.*

Results and Discussion

Microstructure of the SHS Coatings

The specimen takes on a layer of grayish white color as it is lightly polished and the original coating roughness approaches average roughness degree 1.2 μm. Figure 3 is a cross section micrograph showing a thickness of about 150 μm. Figure 4 shows the XRD plot for the surface layer. The XRD analysis indicates that the coating consists mainly of Cr_7C_3, chromium, Cr_3C_2, aluminum, and some other phases that are probably complex oxides of aluminum and carbon. The amount of the phases lowers in sequence.

The SHS coating, as with the other melt-coating processes such as plasma spraying and laser cladding, includes three regions: (1) the re-solidifying zone, (2) the transition zone, and (3) the thermally affected zone (Fig. 5*a*). The pores appearing on the first zone are due to the escape of gaseous impurities. At the second zone, a number of fine particles mingling with coarse dendrites forms an indistinct boundary. This result exhibits that a semi-melting condition has occurred and has formed a combination of solid ceramic particles with molten steel. This combination has been proved in thermal quenching to be one of the important reasons for

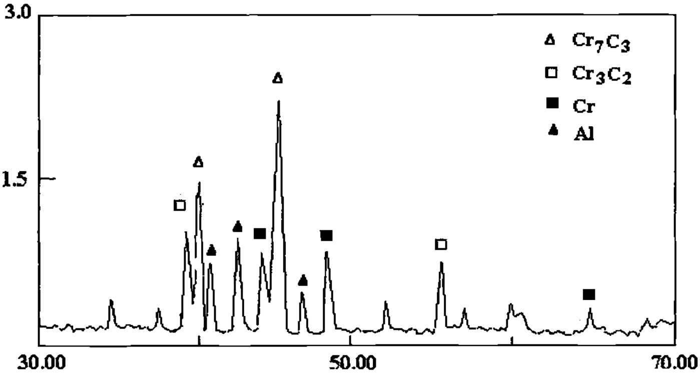

FIG. 4—*XRD plot for the SHS coating on the surface.*

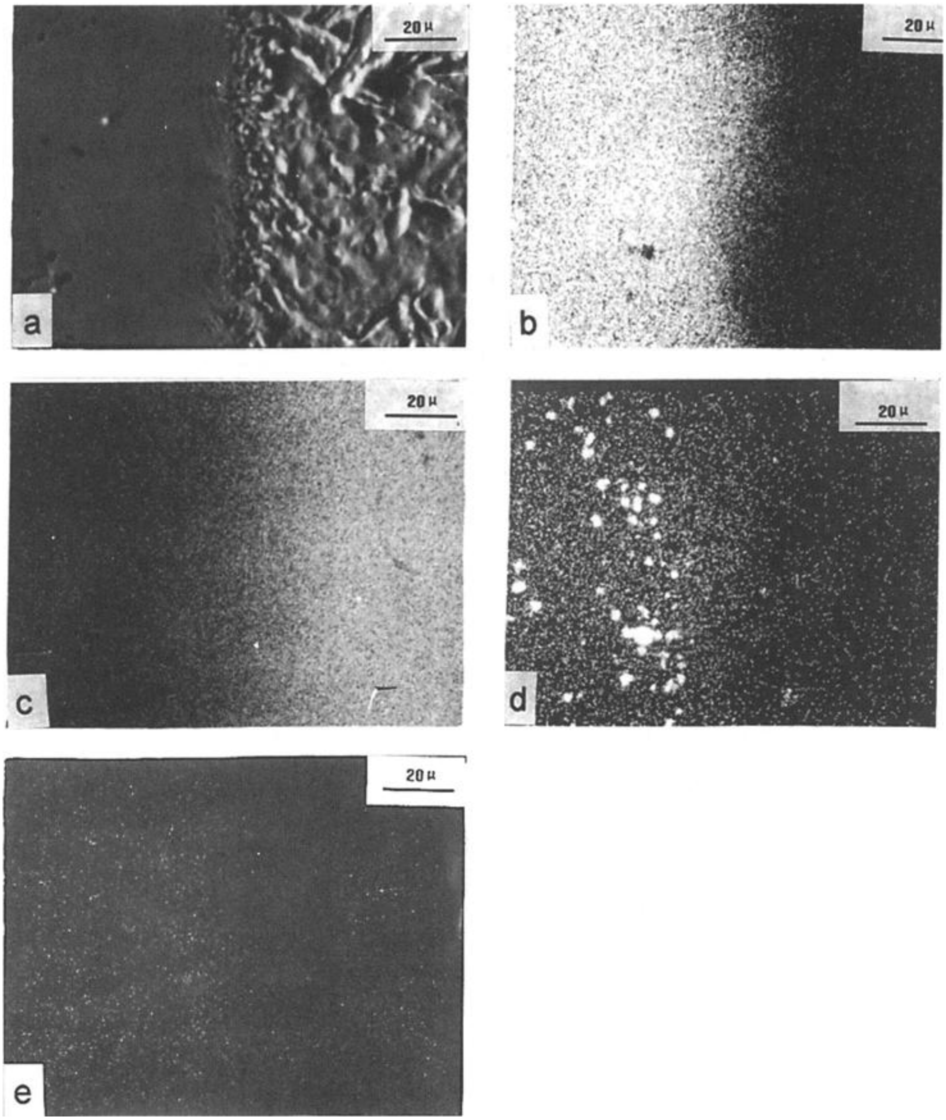

FIG. 5—*Microstructure of the SHS coating near the interface of the coating and substrate,* (a) *micrograph of SEM,* (b *through* e) *X-ray mapping of chromium, iron, aluminum, and carbon, respectively.*

excellent bond strength. The coarse microstructure that occurred in the third zone results in damage to the microstructure.

X-ray mapping of some elements (Figs. 5*b* to *e*) shows that there is a gradient composition distribution protruding into the substrate about 20 μm in depth. For clarity, the results are converted into a linear distribution plot in Fig. 6. It is clear that a mutual element diffusion has taken place during the processing.

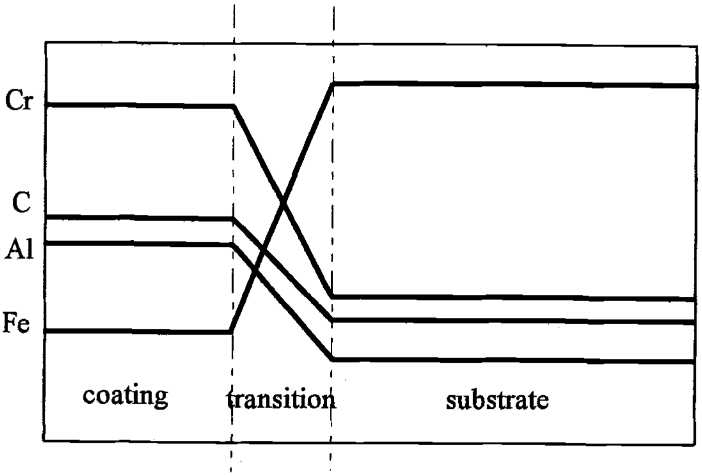

FIG. 6—*Schematic of elemental linear-distribution related to Figs. 5* b *through* e.

Physical Properties of the SHS Coating

Figure 7 shows the microhardness distribution versus the distance from the edge of the SHS and the CVD coatings. The coating thicknesses of about 150 to 170 μm (Fig. 7*a*) and about 10 to 12 μm (Fig. 7*b*) can be measured. The hardness value in the SHS coating surface is about 9.0 GPa and then approaches to its low point (2.5 GPa) that corresponds to the molten part of the steel. This value, however, increases to 3.0 GPa below the heat affected zone (about 3 mm in width) and remains constant for the rest of the substrate. The local damage to the substrate is attributed to the violent but transient combustion procedure. In contrast to the SHS coating, the CVD coating does not have a corresponding region, and its hardness remains at the lowest level throughout the whole substrate thickness (Fig. 7*b*). In other words, the substrate is subjected to the entire damage during the CVD process. It is impossible to completely avoid a hardness drop for substrate materials during the thermal coating processes, but the lower drop is obviously more favorable to the mechanical properties of the coated articles. In order to indicate the relative difference in hardness, a damage index, F, is probably effective, and is defined as

$$F = (H_b - H_a) / H_b \tag{6}$$

where H_b and H_a are the substrate hardness before and after the coating process, respectively.

Table 6 gives the damage index of both coatings. There is less damage for the SHS process (25%) than that for the CVD process (45%). This result can be attributed to heating patterns. For SHS, only the coated surface of the article contacts the exothermic procedure that only needs to last a few seconds. However, for CVD, the whole article needs to be heated to elevated temperatures and maintained for hours.

Thermal quenching reveals a huge bond strength difference between the SHS and CVD coatings. For SHS, the quenching cycle exceeds 40, but the coating layer is still intact even if some of the substrates are split by thermal stress. For CVD, the effective quenching cycle is never more than 8. As we know, the most important forms of coating bonding are the diffusion and metallurgical mechanisms. For diffusion, by forming some medium phases, that is, from

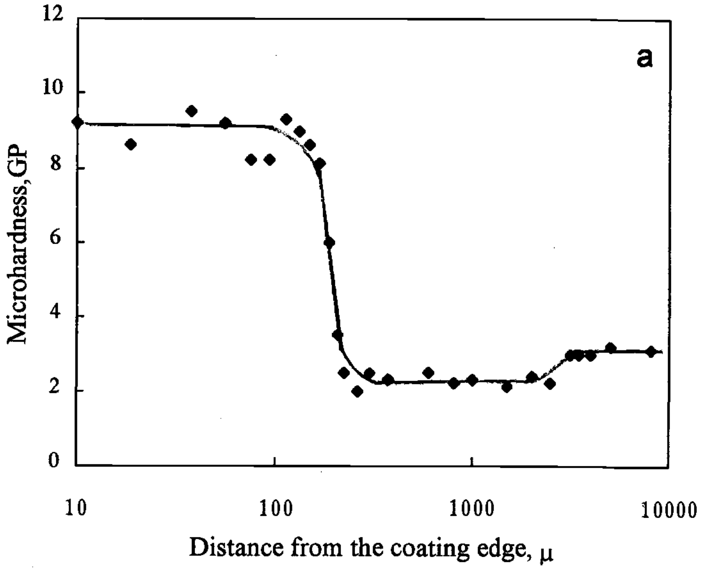

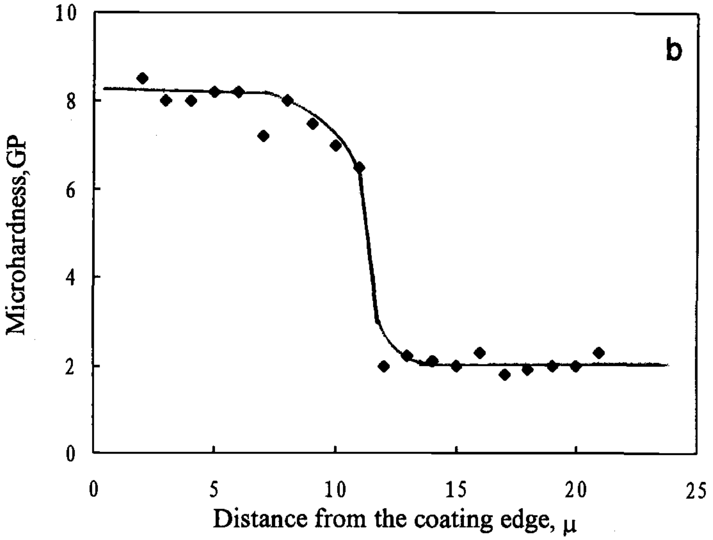

FIG. 7—*Microhardness distribution along with the distance of the coating edge:* (a) *for SHS and* (b) *for CVD.*

TABLE 6—*Damage index,* F, *of SHS and CVD coatings.*

Type	H_b, GPa	H_a, GPa	F, %
SHS	4.1	3.0	25
CVD	4.1	2.3	45

one kind of lattice to another the different materials are connected together. This procedure can be expedited at high temperature. However, the depth of the diffusion in solid state is still limited and, therefore, the related adhesion is also limited. The CVD coating is part of this case. For the metallurgical mechanism, since a melting condition occurs, alloys can be formed within a wide range by different materials in the boundary zone. To further increase the diffusion coefficient at the liquid state, these alloys have higher strength than do the medium phases for pure diffusion. In this case, there is higher adhesion. Obviously, the SHS coating belongs to this one. A strong exothermic reaction, more than 4000 K by theoretical calculation [*13*], is sufficient to melt the synthesized products and part of surface layer of the matrix (Fig. 5*a*) and form a gradient composition distribution in the zone (Figs. 5*b* through *e*). All of these determined the excellent bond strength.

Wear Studies

The abrasive wear rate variation with sliding velocity under variable loads for the SHS and the CVD specimens is shown in Fig. 8. Note that both the applied loads and the sliding velocity have a marked influence on the CVD coatings, and only the applied loads affect the SHS coatings.

For SHS, as applied loads increase, the wear rate increases approximately in proportion, but the effect of the velocity becomes less sensitive. These results agree with the general rules of abrasive wear. For the CVD coating, however, the situation is more complex. Under the lightest load (2.5 N), the wear plot is almost no different from that of the SHS, that is, the increase of the velocity results in a slight decrease of wear rate. In contrast, under the heavier loads (15 and 35 N), wear rate remarkably increases as a function of the increase of velocity.

Figure 9 shows the abrasion features of the worn surfaces by SEM. It is clear that the plough mechanism is essentially responsible for the material removal of both coatings. It is not difficult to see that there are considerable microfeature differences between the SHS and CVD under high velocity and heavy load (Figs. 9*b* and *d*) conditions. The observations indicated that the worn surfaces were still at the coated layers (Fig. 10*a* through *c*), but those (Fig. 10*d*) only partially worn were at the substrate surfaces, in other words, the coated CVD had been abraded completely. The SHS coatings are, therefore, far more suitable for being protective coatings under severe abrasion conditions than CVD coatings that are nearly economically impossible to use as thicker coatings. It is well known that abrasive wear resistance is not an intrinsic property of materials but that it depends on a tribological system [*14–16*]. Although many studies have investigated the effect of abrasive size on wear resistance, there are few studies concerning the relationship between abrasive size, coating thickness, and wear resistance. Two cases referring to the relative size between an abrasive and the coating thickness are considered, Fig. 10. In Fig. 10*a*, the size of the abrasive is far more than that of the coating, that is

$$D_a / D_m >> 1 \tag{7}$$

where D_a is the grain size of abrasive and D_m is the thickness of coated layer.

If the condition called "hard abrasive" is met, then

$$H_a / H_m > 1.1 \tag{8}$$

where H_a and H_m are the hardness of abrasive and the hardness of worn materials, respectively, the abrasive should have no problem being indented or even penetrated into the thin coating under heavy loads or high sliding velocities, or both. There is no question that in this case a serious wear consequence will be unavoidable. In contrast, in Fig. 10*b*, where the size of the

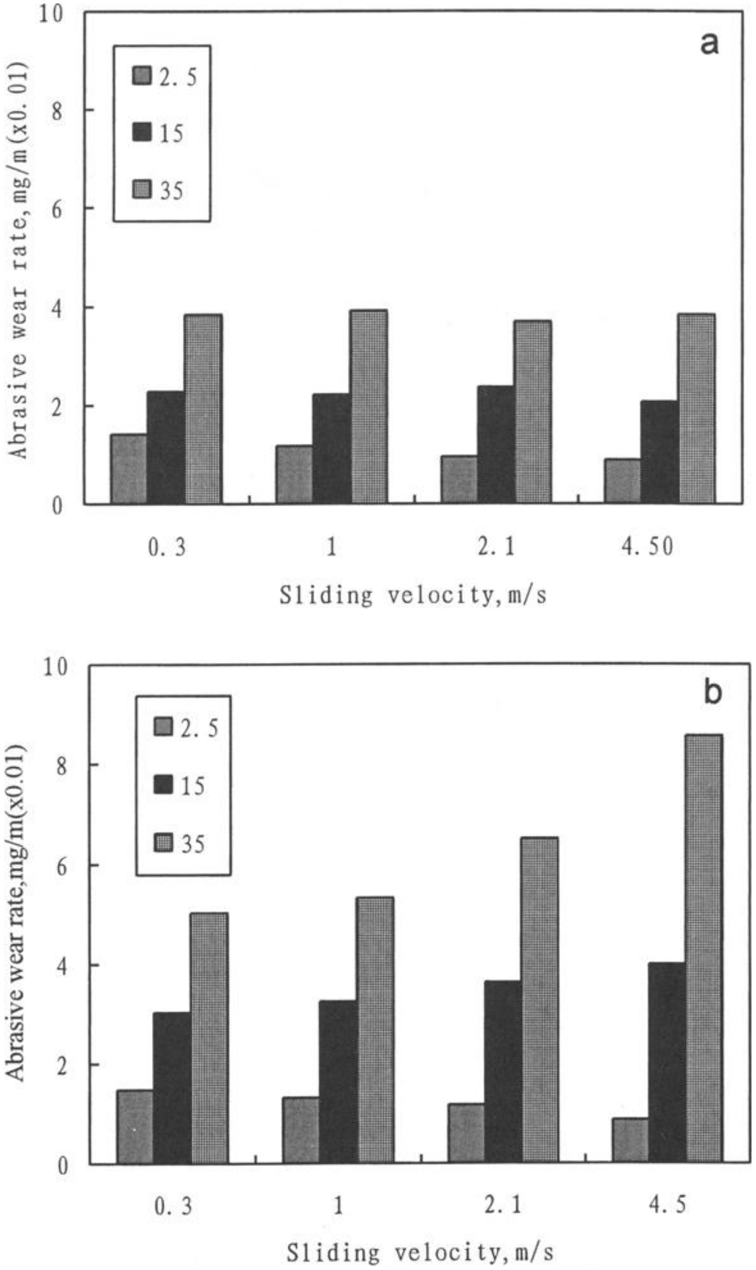

FIG. 8—*Effect of sliding velocity and applied loads on the variation of abrasive wear rate:* (a) *for SHS and* (b) *for CVD.*

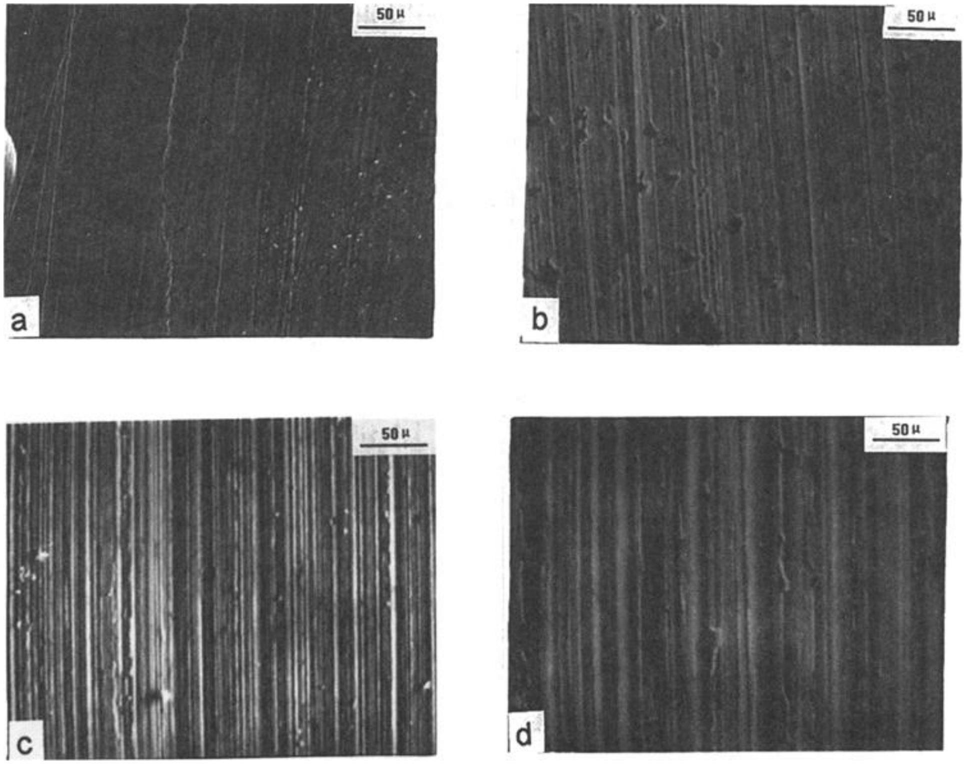

FIG. 9—*The abrasion features of the worn surface by SEM:* (a) *15 N, 1.0 m/s, SHS;* (b) *35 N, 4.5 m/s, SHS;* (c) *15 N, 2.1 m/s, CVD; and* (d) *35 n, 4.5 m/s, CVD.*

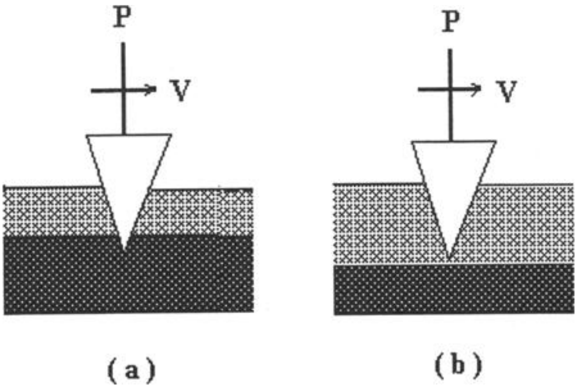

FIG. 10—*Schematics of the abrasive size and coating thickness effects on wear resistance:* (a) $D_a/D_m >> 1$ *and* (b) $D_a/D_m < 1$.

abrasive is less than or equal to the coating thickness, the wear mechanism is categorized for contact fatigue types in a surface microregion scale, even if the "hard abrasive" condition is still met [*17*]. Therefore, only a slight plough is produced. In the present study, where $H_a/H_m = 27/9 = 3$ and $D_a/D_m = 115/10 = 11$, it is easy to explain the results of the worn CVD coating. For the same reason, $H_a/D_m = 115/150 = 0.7$ for the results of the worn SHS coating.

Conclusions

Cermet coatings containing Cr_7C_3, chromium, Cr_3C_2, and aluminum of ~150 μm thickness can be obtained on No. 45 carbon steels by the SHS gas transport process. The coatings produced by this new process have excellent bonding capacity and less matrix damage compared with CVD coatings. Analysis indicates that the good physical performance can be attributed to the intense metallurgy interaction and the gradient composition distribution, while the good property process can be derived from the unique preparation method.

The SiC abrasive wear test (115 μm grit size) with variable load and sliding velocity shows that the SHS coatings have superior abrasive wear resistance to the CVD coatings, especially under high sliding velocity and heavy load conditions. The analysis shows that an interrelationship exists between the size of abrasive, the coating thickness, and the abrasive wear resistance. The superiority of the SHS coating over the CVD coating in abrasive wear resistance may depend on these relationships.

Acknowledgment

This project was supported by the National Natural Science Foundation of China.

References

[*1*] Aylett, B. and Tannahill, A. A., "Chemical Vapor Deposition of Metal Silicides from Organometallic Compounds with Silicon-Metal Bonds," *Vacuum,* Vol. 35, 1985, p. 435.

[*2*] Fix, R., Gordon, R. G., and Hoffman, D. M., "Chemical Vapor Deposition of Vanadium, Niobium and Tantalum Nitride Thin Films," *Chemical Materials,* Vol. 5, 1993, p. 614.

[*3*] Koumto, K., "Thermoelectric Properties of CVD Boron Carbide," *Bulletin,* American Ceramics Society, Vol. 73, 1994, p. 84.

[*4*] Racault, C., Langlais, F., and Bernad, C., "On the Chemical Vapor Deposition of Ti_3SiC_2 from $TiCl_4$-$SiCl_4$-CH_4-H_2 Gas Mixture," *Journal of Materials Science,* Vol. 29, 1994, p. 5023.

[*5*] Holt, J. B. and Munir, Z. A., "Combustion Synthesis of Titanium Carbide: Theory and Experiment," *Journal of Materials Science,* Vol. 21, 1986, p. 251.

[*6*] Munir, Z. A., and Anslmi-tamburini, V., "The Synthesis of High-Temperature Materials by Combustion," *Materials Science Report,* Vol. 3, 1989, p. 277.

[*7*] Merzhanov, A. G., "Self-Propagating High-Temperature Synthesis: Twenty Years of Search and Findings," *Combustion and Plasma Synthesis of High Temperature Materials,* Z. A. Munir and J. B. Holt, Eds., VCH, New York, 1990, p. 1.

[*8*] Subrahmanyam, J. and Vijayakumar, M., "Self-Propagating High-Temperature Synthesis," *Journal of Materials Science,* Vol. 27, 1992, p. 6249.

[*9*] Wang, L. L., Munir, Z. A. and Maximov, Y. M., "Thermite Reactions: Their Utilization in the Synthesis and Processing of Materials," *Journal of Materials Science,* Vol. 28, 1993, p. 3693.

[*10*] Kostgorov, E. P. and Dorozhevets, I. N., "Transport Reactions in SHS Combustion," *International Journal of Self-Propagating High-Temperature Synthesis,* Vol. 1, 1992, p. 33.

[*11*] Pampuch, R. and Stobierski, L., "Solid Combustion Synthesis of Refractory Carbides: Reaction Mechanisms and Properties of Products," *Ceramics Today—Tomorrow's Ceramics,* P. Vincenzini, Ed., Elsevier, Amsterdam, 1991, p. 1169.

[*12*] Lin, L. and Xue, Q., "Combustion Synthesis of Chromium Cermet Coatings," *Metal Materials and Engineering,* (in Chinese), Vol. 23, 1994, p. 80.

[*13*] Odawara, O., "Ceramic Lined Pipes Produced by a Centrifugal Thermite Process," *Transactions,* Japan Institute of Metals, Vol. 26, 1985, p. 578.
[*14*] Misra, A. and Finnie, I., "Some Observations on Two-Body Abrasive Wear," *Wear,* Vol. 68, 1981, p. 41.
[*15*] Misra, A. and Finnie, I., "Correlations between Two-Body and Three-Body Abrasive and Erosion of Metals," *Wear,* Vol. 68, 1981, p. 33.
[*16*] Moore, M. A.,"Laboratory Simulation Testing for Service Abrasion Wear Environments," *Wear of Materials,* Vol. 2, K. C. Ludema, Ed., American Society of Mechanical Engineers, New York, 1987, p. 673.
[*17*] Hesheng, S. and Qing, Z., *Abrasive Wear and Wear Resistance Materials,* (in Chinese), Mechanical Industry Publisher, Beijing, 1989, p. 72.

ISBN 0-8031-2036-2

ISBN 0-8031-2036-2